Computational Aerodynamics

ANDREW NING

Brigham Young University

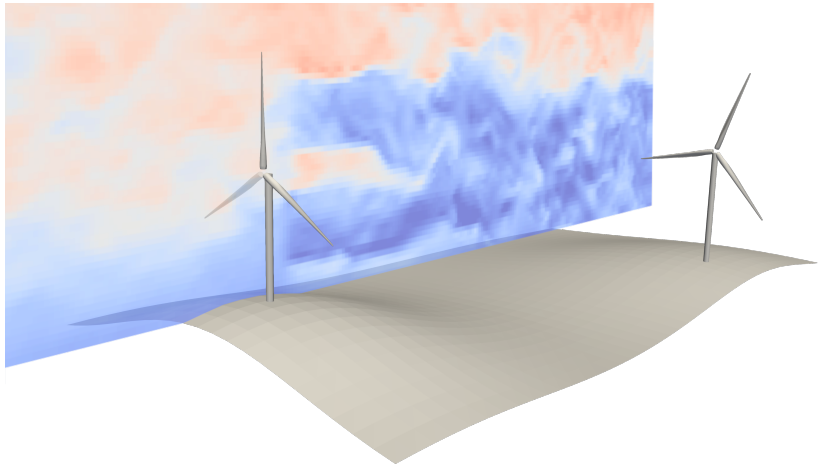

Compiled on Thursday 11th July, 2024 at 11:45

Publication
First electronic edition: January 2020.

Contents

Preface

This book is designed for graduate students to provide additional depth beyond an introductory course in aerodynamics. A major focus is on computational theory and implementation of modern aerodynamic methods.

Acknowledgements

The cover figure was provided by Denis-Gabriel Caprace. The layout of this book was greatly improved based, in part, on a template provided by Max Opgenoord. Judd Mehr transcribed some of the equations and figures from the author's lecture notes.

1 Fundamentals

This chapter reviews various concepts that are covered in an introductory fluids or aerodynamics course, but with greater depth. We begin with basic concepts including density, pressure, shear stress, the integration of pressure and shear stresses to compute forces and moments, and dynamic similarity. Following a brief math review, we derive the governing equations of fluid mechanics: mass and momentum balances (an energy balance is saved for a later chapter). These governing equations can be manipulated in many other useful forms, and we explore a few of these, as well as some additional considerations for translating and rotating frames of reference. Finally, we apply the integral form of our governing equation to see an alternative approach to computing forces, and to review control volume analyses.

By the end of this chapter you should be able to:

1. Understand fluid properties including density, pressure, and shear stress, and how to use these properties to compute forces and moments on objects of interest.
2. Use and explain the principle of dynamic similarity.
3. Read and use index notation for partial differential equations.
4. Interpret, use, and manipulate the Navier–Stokes equations in various forms.
5. Understand the far-field approach to computing forces and how to use control volume analyses.

1.1 Density

For solids, density is defined as mass per volume:

$$\rho = \frac{m}{V}. \tag{1.1}$$

However, the definition is not precise enough for a fluid as the size of the volume if not defined. If the control volume is large then the density may vary significantly at different locations within the volume.

The need for a small volume leads to the next most common definition of density:

$$\rho = \lim_{\Delta \forbidden{\mathcal{V}} \to 0} \frac{\Delta m}{\Delta \forbidden{\mathcal{V}}} . \tag{1.2}$$

However, this definition is also problematic because fluids are made up of individual molecules. Imagine freezing all of these particles, within some control volume, in order to make a density measurement. Suppose the volume is small enough so that there is only a couple of air particles in it and we sum up their mass and divide by the volume. Now suppose we make the volume a bit bigger so there is now a half dozen particle in it and we repeat the measurement. Because there are so few particles, as the volume changes size, the density measurement varies erratically as shown on the left side of Fig. 1.1.

As we increase the size of the control volume, eventually the number of particles contained within the volume is so large that the fluid acts like a continuum (we refer to this continuum volume as $\Delta \forbidden{\mathcal{V}}_c$). After this point, the density measurement begins to level out. For air at standard temperature and pressure the size of this control volume is a cube with sides approximately 1 micron in length. This control volume would have about 30 million air molecules in it. That is a large enough number that, statistically speaking, the density in the control volume is constant. However, if we continued to increase the volume then at some point our density measurements would change because of spatial variation as noted at the beginning of this section. So, a better definition of density is:

$$\rho = \lim_{\Delta \forbidden{\mathcal{V}} \to \Delta \forbidden{\mathcal{V}}_c} \frac{\Delta m}{\Delta \forbidden{\mathcal{V}}} . \tag{1.3}$$

If we operate at scales above $\Delta \forbidden{\mathcal{V}}_c$ we are said to employ the *continuum* assumption. This means that we can treat the fluid not as individual molecules, but as a continuous medium. Everything we consider in this book will assume that the fluid is a continuum. While this assumption is reasonable for most aerodynamic applications, it is not always a good assumption. For example, at very high altitudes, air molecules are spread out far enough that we can no longer reliably use the Navier-Stokes equations. Instead, we could use the Boltzman transport equations that use a statistical description to model particle transport.

One major categorization of fluids, related to density, is a distinction between *incompressible* versus *compressible*. No fluid can be truly incompressible, but it is a useful mathematical idealization. For now, we will

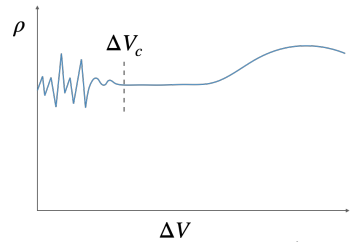

Fig. 1.1 Density variation with control volume size (logarithmic scale for control volume size). The behavior is erratic at small scales because there are few molecules in the control volume. At some point the number of particles is so large that the fluid acts like a continuum with a volume we denote as $\Delta \forbidden{\mathcal{V}}_c$.

think of incompressible as a fluid with constant density, but we will see shortly that is an overly restrictive definition of incompressibility.

1.2 Pressure

Pressure is defined as

$$p = \lim_{\Delta A \to 0} = \frac{\Delta F}{\Delta A}\,. \tag{1.4}$$

Again, we should keep in mind that the limit doesn't really go to zero, but rather to a small enough control volume to where the continuum assumption is still valid. But for simplicity we won't continue to make that distinction in the notation.

Let us first consider why a fluid creates pressure. One way to visualize the effect of pressure is to consider the individual air molecules bouncing off a solid surface. The momentum transfer of the molecules is proportional to their mass times their velocity. Since the force is momentum per unit time, the pressure is then proportional to the momentum flux:*

$$p \propto \rho V^2\,. \tag{1.5}$$

*In fluids, a flux of some quantity refers to the amount of that quantity that passes through some unit area per unit time. On in other words, it is the rate at which that quantity passes through a unit area.

For an ideal gas, temperature is proportional to the mean kinetic energy of the particles:

$$T \propto V^2. \tag{1.6}$$

Combining these equations yields:

$$p \propto \rho T. \tag{1.7}$$

For an *ideal gas* the proportionality constant is the *specific gas constant* R:

$$p = \rho R T. \tag{1.8}$$

For dry air the constant is:

$$R = 287.058 \frac{\mathrm{J}}{\mathrm{kg} \cdot \mathrm{K}} \tag{1.9}$$

We motivated pressure by imaging particles bouncing off a surface, but we know there is a pressure in a fluid away from surfaces as well. If there is no surface nearby to exchange momentum with, how is there a pressure? At first we might think the pressure arises because of collisions between the molecules, but this is not the case and in fact one of the assumptions for an ideal gas is that there are no interactions between particles. As long as there is a large number of particles, the situation is exactly the same as the case with a wall nearby as shown in Fig. 1.2. For any molecule leaving, if at equilibrium, then statistically

speaking another will be entering. The momentum flux through the control volume is the same (if the entering/leaving particle was straight on, then the change in momentum would be $2mV$ since the momentum has the same magnitude but with different signs in entering/leaving).

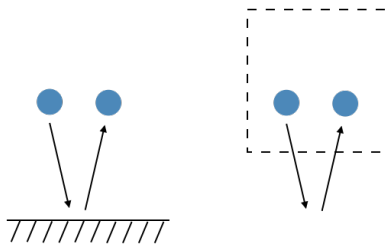

Fig. 1.2 Momentum transfer against a wall or momentum flux though a control volume is the same.

1.3 Shear Stress

Just like density and pressure, we can understand shear stresses better by starting from a molecular description of air. Imagine a bunch of faster moving air particles next to a bunch of slower moving air particles as shown in Fig. 1.3. The molecules exchange momentum causing the faster particles to slow down and the slower particles to speed up. On average the velocity profile would look something like that shown on the right of Fig. 1.3. The forces acting on the particles arise from shear stresses.

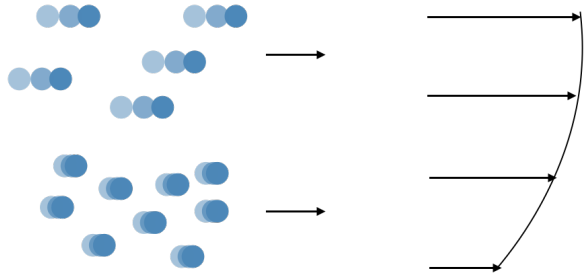

Fig. 1.3 Shear profile created from faster moving particles above lower moving particles.

Now let us consider fluid particles moving next to a solid object. The same principle applies. The molecules in the solid object have zero velocity. Because of the momentum exchange between particles the fluid particles next to the wall must then also have zero velocity on average (in the reference frame of the solid object). This is called the *no slip condition* and is depicted in Fig. 1.4.

The layer of slower moving air near a solid surface is called a

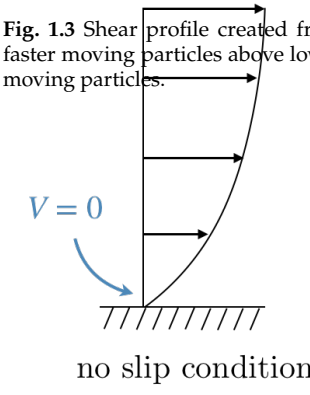

Fig. 1.4 The no slip condition requires that the velocity at a solid wall is zero.

boundary layer. This velocity gradient is proportional to shear stress:

$$\tau = \mu \frac{\partial V}{\partial y} \,, \tag{1.10}$$

where the proportionality constant μ is called the *dynamic viscosity* of the fluid.

Another common fluid categorization is *viscous* versus *inviscid*. An inviscid fluid is one where the viscosity is zero. A truly inviscid fluid doesn't exist, but is often a good mathematical approximation.

1.4 Forces and Moments

All aerodynamics forces and moments arise from just pressure and shear stresses (Fig. 1.5). Pressure can only act normal to a body, shear stresses act tangential to the surface but can have a component in the normal direction as well (more on this later). Once we know pressure and shear stress everywhere on the surface of a body we can integrate to get total forces.

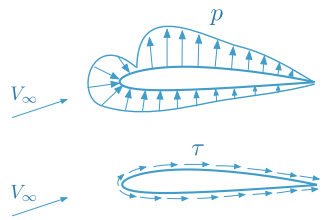

Fig. 1.5 top: pressure, bottom: shear stresses.

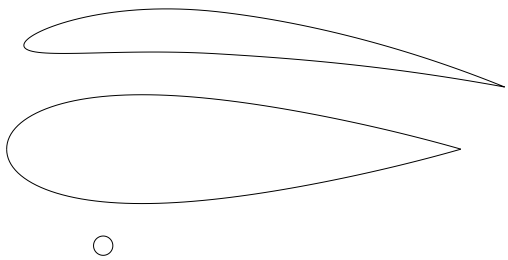

Fig. 1.6 A NACA 6409 airfoil at 5 degrees angle of attack, a NACA 0024 airfoil at 0 degrees angle of attack, and a cylinder at the scales of this figure, all have the same drag force for a Reynolds number of 1 million.

Pressure is very important to aerodynamic flows. A few examples will help illustrate. Consider the airfoils and cylinder depicted in Fig. 1.6. For a Reynolds number* of 1 million all of these shapes have the same amount of drag, which at first is a rather surprising result. The airfoils have low pressure drag because of their streamlined shape, but have significant skin friction drag (resulting from shear) because of their large surface area. The cylinder on the other hand has little skin friction drag, but because it is blunt it has a large wake with significant pressure drag. Even though the cylinder is much smaller the blunt shape creates drag as high as the much larger airfoils.

*We'll review Reynolds number later, but many aircraft have Reynolds number in the millions or tens of millions.

The significance of pressure drag is why aerodynamicists often mention the need for streamlined shapes. This also explains why many

World War I era planes had such poor performance. Lots of wire bracing, usually with biplanes, was required for structural reinforcement, but the blunt shapes of circular wires created a large amount of drag. Between the two world wars semi-monoconque designs (skin stiffened, like an eggshell) and high-strength aluminum allowed for sufficient structural strength without wire bracing and thus allowed for significant improvements in aerodynamic performance.

Example 1.1 Atmospheric pressure

Pressure plays such an important role in aerodynamics because the pressure in our atmosphere is quite high. At sea level the pressure is about 2,000 lbs/ft^2. A flat plate the size of an 8.5 × 11 in sheet of paper could carry approximately 65 pounds just by creating a 5% pressure differential from top to bottom.

In metric units, the sea level pressure is around 100 kPa, and so an A4 sheet of paper (210 × 297 mm) could carry a mass of about 32 kg from that 5% pressure differential.

When plotting pressure we generally use the nondimensional *pressure coefficient*:

$$C_p = \frac{p - p_\infty}{\frac{1}{2}\rho V_\infty^2}, \tag{1.11}$$

which is the gauge pressure divided by the dynamic pressure.[†] For the idealized inviscid flow around a cylinder we could plot the pressure as a function of the azimuthal angle of the cylinder as shown in Fig. 1.7. Because the cylinder is symmetric only one curve is shown to represent both the top and bottom half.

[†]Recall that gauge pressure is the pressure relative to atmospheric pressure. Dynamic pressure results from Bernoulli's equation, which we'll rederive in Section 1.9, and is a quantity that is frequently used in aerodynamic normalizations.

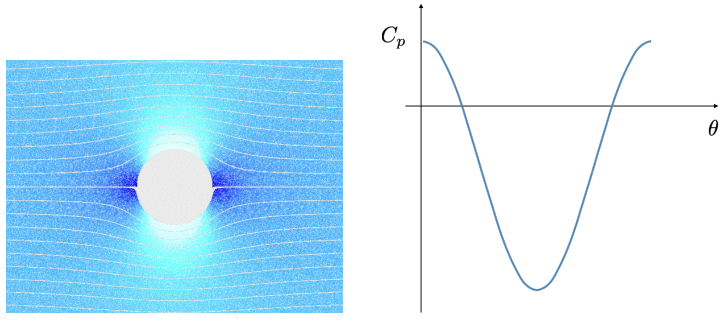

Fig. 1.7 Pressure coefficient around an idealized inviscid cylinder. Left is a public domain image.

Notice that the pressure starts high at the stagnation point, drops as the flow speeds up around the cylinder, and then recovers the same high pressure on the back side. Because the pressure distribution is perfectly symmetric, there is no drag in this inviscid scenario. The

curve is reminiscent of rolling a ball down a frictionless hill. In the absence of friction you would return to the same height, or in the fluids case you would return to the same high pressure.

The presence of viscosity, however, alters the flow field. The flow separates from the cylinder creating a large wake (much more on this behavior in Chapter 3). The pressure distribution does not recover to the same high pressure on the back side, and so the pressure imbalance results in a force imbalance that we call drag (Fig. 1.8). Notice that

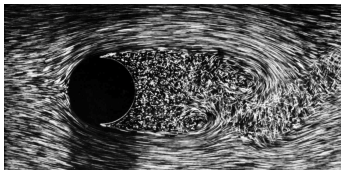

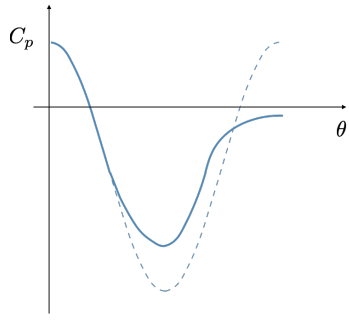

Fig. 1.8 Pressure coefficient around an viscous cylinder. Left image is a visualization of air bubbles in water.[1]

1. Van Dyke, *An album of fluid motion*, 1982.

on the forward half of the cylinder the pressure changes from high to low. We call this a *favorable pressure gradient* as the pressure accelerates the flow. On the back half of the cylinder, the flow moves from a low pressure region to a high pressure one. This is called an *adverse pressure gradient*. The fluid must work against the adverse pressure gradient, and in the presence of viscosity some energy is lost so it will not return all the around the cylinder. Instead the fluid decreases in momentum and eventually has zero velocity in the direction along the cylinder leading to flow separation. The void is filled in with a low pressure wake.

Most aerodynamic applications use streamlined bodies. The pressure coefficient distribution for a streamlined body called an airfoil is depicted in Fig. 1.9. An airfoil, however, is not symmetric, so we see

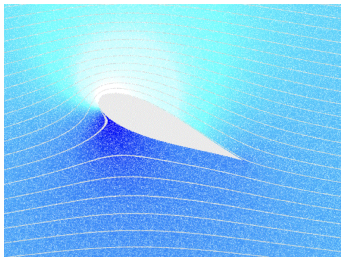

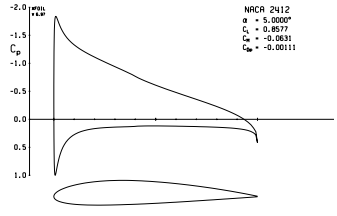

Fig. 1.9 Pressure coefficient around an airfoil. Left image is a public domain image, the right is generated from XFOIL.[2]

2. Drela, *XFOIL: An analysis and design system for low Reynolds number airfoils*, 1989.

two curves: one for the upper surface and one for the lower surface.

Also note that the y-axis plots the negative of the pressure coefficient. This is a common convention because the upper surface (or suction side) is associated with low pressures, whereas the lower surface (or pressure side) is associated with higher pressures. Thus, by plotting the negative of the pressure coefficient, the upper curve corresponds to the upper surface and lower curve corresponds to the lower surface.

The two curves start at the stagnation point (which for an inviscid, incompressible flow, corresponds to $C_p = 1$ as we will see in the next chapter). For the upper surface we see rapid acceleration into the low pressure region just aft of the nose, and then a long gradual pressure recovery, in an adverse gradient, towards the trailing edge. It is important that the pressure recovery in the adverse region is gradual, otherwise the flow will separate. As we will see later in this section, the inviscid force in the vertical direction is given by the area between these two curves (see c_n in Eq. 1.31). Thus, we see that most of the lift (which is not quite the same as the force in the vertical direction, as discussed below) is generated by the upper surface. This is generally true, and is primarily why many instruments for aircraft are located on the lower surface where disrupting the flow field is less consequential to lift production.

Shear stress, τ at the surface of the body is normalized by dynamic pressure and called the *skin friction coefficient*:

$$c_f = \frac{\tau}{\frac{1}{2}\rho V_\infty^2} \tag{1.12}$$

As discussed later in this chapter, the shear stress is a tensor and so has more components, but in two-dimensions at least we are generally just considered with this one component.

The integration of the pressure and shear stresses over a body results in forces and moments that could be resolved into any coordinate system. For aerodynamic bodies some common conventions are discussed below. By definition, we define drag (D) as the force in the direction of the freestream (depicted in Fig. 1.10), and lift (L) is always defined perpendicular to the freestream. The force normal to the body is called the normal force (N), and the force along the main reference line of the body is referred to as a tangential force or axial force (A). These forces are related by a simple coordinate transformation:

$$L = N\cos\alpha - A\sin\alpha \tag{1.13}$$

$$D = N\sin\alpha + A\cos\alpha. \tag{1.14}$$

Note also from the figure that the angle of attack is defined as the angle between the freestream and the reference line of the body, which for an airfoil would be the chord line.‡

‡The chord line is a line from the forward most part of the airfoil (nose) to the aft most part (tail), and an airfoil's chord refers to this distance. This, and other airfoil nomenclature will be discussed in more detail later in Section 2.8

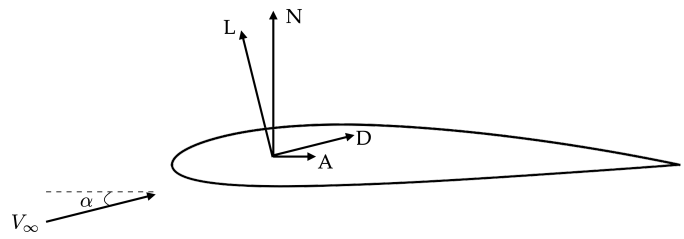

Fig. 1.10 Drag is in the direction of the freestream and lift acts perpendicular to the freestream.

As we will discuss in more detail in Section 1.5, nondimensional parameters are critically important in aerodynamics. The lift and drag are normalized as follows:

$$C_L = \frac{L}{\frac{1}{2}\rho V_\infty^2 S} \tag{1.15}$$

$$C_D = \frac{D}{\frac{1}{2}\rho V_\infty^2 S}\,, \tag{1.16}$$

where the symbol S is a reference area. Anything can be used for the reference area (it is just a reference), as long as one is consistent, but there are general conventions depending on the application. The force coefficients are meaningless without also defining what reference area was used.

For example, if you look up tables of drag coefficients for various objects they will always define what type of reference area should be used. Streamlined objects tend to use projected areas parallel to the freestream (because the drag scales more with the skin friction area), whereas blunt objects often use projected cross-sectional areas normal to the freestream (because the drag is more pressure dominant scaling with the projected frontal area).

The pitching moment is normalized as shown below, where c is an additional reference length (e.g., chord for an airfoil)

$$C_M = \frac{M}{\frac{1}{2}\rho V_\infty^2 S c}\,. \tag{1.17}$$

A moment causing the body to nose-up is typically considered positive.

In addition, to the 3D coefficients, we also have 2-D expressions for the aerodynamic coefficients. The symbols are lowercase to indicate 2D. These expressions for lift (ℓ), drag (d), and moment (m), per unit length, are respectively:

$$c_\ell = \frac{\ell}{\frac{1}{2}\rho V_\infty^2 c} \tag{1.18}$$

$$c_d = \frac{d}{\frac{1}{2}\rho V_\infty^2 c} \tag{1.19}$$

$$c_m = \frac{m}{\frac{1}{2}\rho V_\infty^2 c^2}\,. \tag{1.20}$$

The distinction between 2D and 3D coefficients is a frequent source of confusion for new students. Just keep in mind that 2D coefficients refer to forces or moments per unit length (i.e., the local value of a distributed load), whereas 3D coefficients refer to total forces and moments (i.e., a point load). We would use 2D coefficients for 2D cross-sections like airfoils, and 3D coefficidents for 3D objects like wings and full aircraft.

The lift coefficient is a function of angle of attack as shown in Fig. 1.11 (and potentially other nondimensional parameters like Reynolds number and Mach number). This curve shows the 2D lift coefficient for an airfoil, though the nature of the curve is similar for 3D bodies. For a positively cambered airfoil (not symmetric) the airfoil begins producing lift at a negative angle of attack called the *zero-lift angle of attack* (α_0). The lift then increases linearly with a slope m, called the lift curve slope. At some point, viscous effects dominate, the flow separates and the lift drops (a phenomenon called *stall*). The highest lift coefficient is called $c_{\ell max}$ (pronounced: c-ell-max). For the linear portion of the curve we can write:

$$c_\ell = m(\alpha - \alpha_0). \tag{1.21}$$

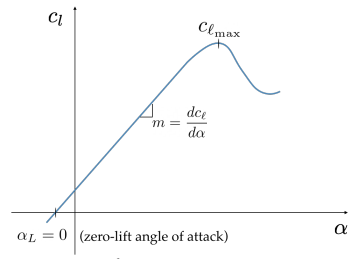

Fig. 1.11 Lift curve.

Similarly, we can plot the drag coefficient either as a function of angle of attack or as a function of lift coefficient as shown in Fig. 1.12 Drag generally varies quadratically with lift (and thus with angle of attack) over much of the drag polar.§

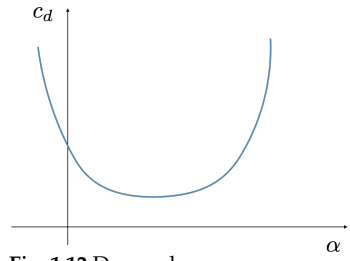

Fig. 1.12 Drag polar.

§Drag polar just refers to the curve or function describing drag as a function of lift.

Pitching moment coefficient is usually negative and relatively flat with respect to angle of attack for an airfoil Fig. 1.13. Although it may not appear that flat when plotted in isolation, i.e., on a small range for the y-axis. Positive camber, which leads to efficient lift generation, tends to create a nose-down pitching moment. This has implications for aircraft stability, with the conventional solution being an aft tail that lifts downward to counter this negative pitching moment. Airfoils can be designed to produce positive pitching moments, but are generally far less effective in producing lift.

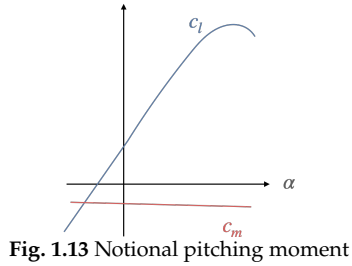

Fig. 1.13 Notional pitching moment versus angle of attack.

We now show explicitly how to integrate pressures and shear stresses along the surface to compute forces and moments. For simplicity, we focus on two-dimensions and use the coordinate system shown in Fig. 1.14. On the upper surface the pressure and shear over an incremental surface ds leads to the following local forces in the x-direction:

$$dF'_x = p_u ds \sin\beta + \tau ds \cos\beta, \tag{1.22}$$

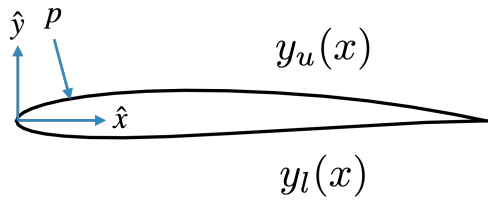

Fig. 1.14 Pressure and shear integration along a two-dimensional body. (TODO: show shear)

and y-direction:

$$dF'_y = -p_u ds \cos\beta + \tau ds \sin\beta, \tag{1.23}$$

and local pitching moment about the leading edge:

$$dM'_{le} = y_u dF'_x - x dF'_y, \tag{1.24}$$

where β is the local slope of the body (Fig. 1.15). Using the substitution:

$$\cos\beta = \frac{dx}{ds}, \tag{1.25}$$

and

$$\sin\beta = \frac{dy}{ds} = \frac{\frac{dy}{dx}dx}{ds}, \tag{1.26}$$

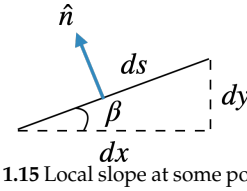

Fig. 1.15 Local slope at some point on the body.

and including the lower surface (which flips the positive direction on pressure) leads to the following total forces and moments per unit depth:

$$F'_x = \int_0^c \left(p_u \frac{dy_u}{dx} - p_l \frac{dy_l}{dx}\right) dx + \int_0^c (\tau_u + \tau_l)\, dx \tag{1.27}$$

$$F'_y = \int_0^c (p_l - p_u)\, dx + \int_0^c \left(\tau_u \frac{dy_u}{dx} + \tau_l \frac{dy_y}{dx}\right) dx \tag{1.28}$$

$$M'_{le} = \int_0^c \left[p_u \left(x + y_u \frac{dy_u}{dx}\right) - p_l \left(x + y_l \frac{dy_l}{dx}\right)\right] dx \tag{1.29}$$

$$+ \int_0^c \left[\left(y_u - x\frac{dy_u}{dx}\right)\tau_u + \left(y_u - x\frac{dy_u}{dx}\right)\tau_l\right] dx. \tag{1.30}$$

If we nondimensionalize we have:

$$\begin{aligned}
c_n &= \int_0^1 (C_{p_l} - C_{p_u})\, d\left(\frac{x}{c}\right) + \int_0^1 \left(c_{f_u}\frac{dy_u}{dx} + c_{f_l}\frac{dy_l}{dx}\right) d\left(\frac{x}{c}\right) \\
c_a &= \int_0^1 \left(C_{p_u}\frac{dy_u}{dx} - C_{p_l}\frac{dy_l}{dx}\right) d\left(\frac{x}{c}\right) + \int_0^1 \left(c_{f_u} + c_{f_l}\right) d\left(\frac{x}{c}\right) \\
c_{mle} &= \int_0^1 \left[C_{p_u}\left(\frac{x}{c} + \frac{y_u}{c}\frac{dy_u}{dx}\right) - C_{p_l}\left(\frac{x}{c} + \frac{y_l}{c}\frac{dy_l}{dx}\right)\right] d\left(\frac{x}{c}\right) \\
&\quad + \int_0^1 \left[\left(\frac{y_u}{c} - \frac{x}{c}\frac{dy_u}{dx}\right)c_{f_u} + \left(\frac{y_u}{c} - \frac{x}{c}\frac{dy_u}{dx}\right)c_{f_l}\right] d\left(\frac{x}{c}\right).
\end{aligned} \tag{1.31}$$

where c_n and c_a are the normal force coefficient and axial force coefficient corresponding to the y and x direction respectively, for our body-aligned coordinate system.

Again, we often rotate these forces to obtain lift and drag coefficients (Eq. 1.14):

$$\begin{aligned} c_\ell &= c_n \cos\alpha - c_a \sin\alpha \\ c_d &= c_n \sin\alpha + c_a \cos\alpha. \end{aligned} \tag{1.32}$$

1.5 Dynamic Similarity

Nondimensional numbers are critically important in fluids. They provide insight across problems of different scales. For example, a lift of 60 N doesn't mean much without context (is that a lot of lift or a little?). On the other hand, we can tell if a lift coefficient is large or small regardless of whether it is from a dragonfly or an airliner as the lift coefficient falls along a narrow range.

Nondimensional numbers also form the basis of wind tunnel testing, and similarity modeling in general. They provide critical insight by reducing the dimensionality of the problem, and highlight fundamental relationships. Let's illustrate with some examples.

Example 1.2 Nondimensional parameters for wind turbine power production

Consider a wind turbine. The data we explore could come from experimental measurements or computations, it doesn't matter, but in this case it is simulation data with added noise. As depicted in Fig. 1.16, we are interested in understanding the relationship between the power the turbine produces and two inputs: the incoming velocity V_∞ and the rotation speed Ω of the rotor.

For the purposes of this example, we let the inputs fall within the following ranges with uniform probability:

$$\begin{aligned} V_\infty &\in [5, 15]\ \text{m/s} \\ \Omega &\in [1, 30]\ \text{RPM} \end{aligned}. \tag{1.33}$$

We observe the output of many "experiments" in Fig. 1.17.

There appears to be very little structure in this data. In other words, if you were given a wind speed, you wouldn't be able to predict the power output (although it appears as if we could predict a maximum power, which is true). The same conclusion applies for the rotation speed. Imagine that you were given the assignment to create a predictive model for the turbine power as a function of two variables. So far, the data doesn't appear promising to allow this. What would you do?

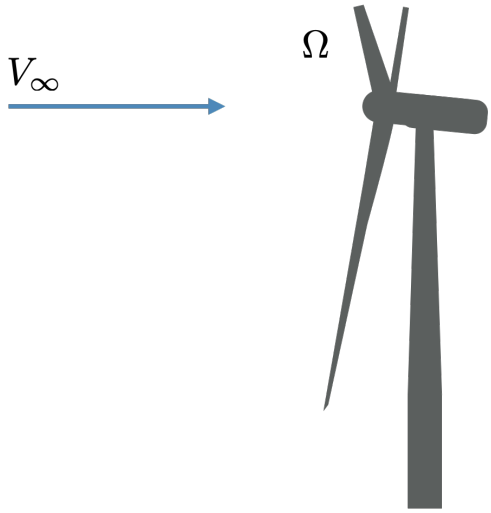

Fig. 1.16 A wind turbine with an incoming wind speed and a rotor rotation speed.

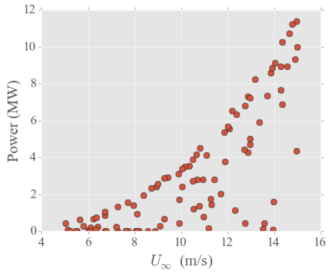

power vs windspeed

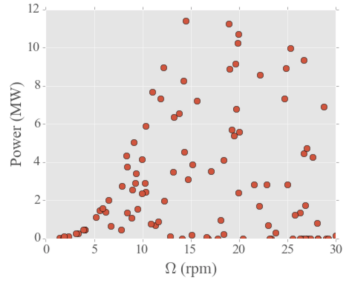

power vs rotation speed

Fig. 1.17 The power produced by the wind turbine as we randomly vary wind speed and rotation speed.

Perhaps, evaluating random samples obfuscated the results. Let's instead try holding the rotation speed constant, and just vary V_∞. In Fig. 1.18 we perform that experiment for four different rotation speeds.

This appears much more promising. Clear structure is visible. Perhaps we could create a polynomial fit for each rotation speed separately, and then a separate curve fit for the polynomial coefficients as a function of the rotation speeds. This is better though still rather problematic: it is fairly complex, and the curves seem to go to zero power at different points making interpolation challenging.

Formally, what we are trying to understand is a functional relationship to predict power as a function of all inputs (including some we are holding constant):

$$P = f(V_\infty, \Omega, \rho, R). \tag{1.34}$$

and perhaps other variables like viscosity. We would like to choose nondimensional parameters to simplify these functional relationships.

While the Buckingham-Pi theorem can help us formally quantify how many nondimensional parameters we need, most of the time it is straightforward to determine an appropriate set.* First, let's nondimensionalize the velocities.

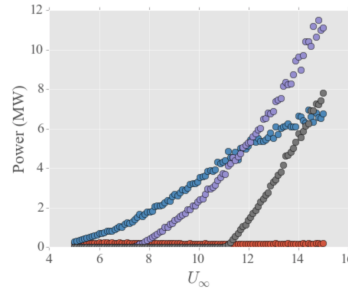

Fig. 1.18 Power as a function of windspeed for four different rotation speeds.

There are numerous possibilities but for wind turbines the standard convention for normalizing the speeds is to use the tip-speed ratio, which is a ratio of the blade tip speed relative to the freestream speed:

$$\lambda = \frac{\Omega R}{V_\infty}. \tag{1.35}$$

The power could also be nondimensionalized many ways, but the standard way is to use the freestream dynamic pressure times the rotor disk area (producing a force) then multiplying by the freestream velocity once more to obtain power. This is called the power coefficient:

$$C_P = \frac{P}{\frac{1}{2}\rho V_\infty^3 \pi R^2}. \tag{1.36}$$

All of the parameters have been used in the nondimensionalization so these are all the Pi groups. Our new equation now looks like:

$$C_P = f(\lambda). \tag{1.37}$$

Let's try plotting the data as suggested by this nondimensionalization. The data from the random inputs in Fig. 1.17 is shown in Fig. 1.19. and from the sequential inputs in Fig. 1.18 the results are shown in Fig. 1.20.

Now the relationship is very clear. Given a velocity V_∞ and rotation speed Ω we can now provide a quite good prediction for the wind turbine's power. Note that we are able to do this without knowing anything about the physics involved in the function f.

*The theorem isn't really important to us, but in brief, it states that if we have n variables, and d independent dimensions or units, then we should be able to reexpress our relationships in $n - d$ parameters. So in this case we have 5 variables and 3 dimensions (distance, time, mass), and so should be able to reexpress in terms of 2 nondimensional variables.

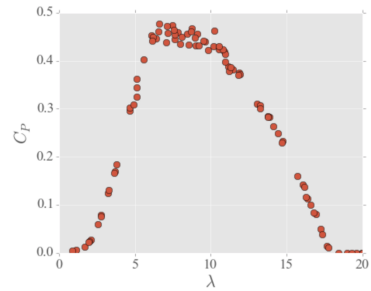

Fig. 1.19 Power coefficient as a function of tip speed.

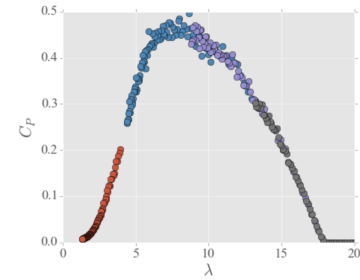

Fig. 1.20 Same figure but color coded by the rotation speed.

Imagine an object/vehicle that we wish to predict aerodynamic drag for. We could write the relationship generally as:

$$D = f(V_\infty, \rho, \mu, a, \alpha, \text{shape}). \tag{1.38}$$

where a is the speed of sound. Through nondimensionalization the function is reduced to:

$$C_D = f(\alpha, Re, M, \text{shape}^*). \tag{1.39}$$

where Re is the Reynolds number, M is the Mach number, and $shape^*$ means a nondimensional shape (the angle of attack could conceptually be grouped in shape, but we often wish to vary it with fixed shape). This equation means that if we have two identical shapes at different scales (e.g., a full scale aircraft, and a small model) if we match the Reynolds number and the Mach number then we can predict the drag of the full scale vehicle by performing tests on the small scale model.

The *Reynolds number* is defined as:

$$Re = \frac{\rho V l}{\mu} = \frac{V l}{\nu} \tag{1.40}$$

where l is an appropriate length scale for the object and ν is the kinematic viscosity (μ/ρ). It can be thought of as a ratio of inertial forces or pressure (Eq. 1.5) to viscous forces (Eq. 1.10). Reynolds number is unique in that most nondimensional numbers vary across a small range near 1. Reynolds number on the other hand spans many orders of magnitude from 1 to 100 million in this figure. Effectively, it should be thought of as operating on a log scale. This is seen for example in Fig. 1.21 showing the drag coefficient of a sphere as a function of Reynolds number.

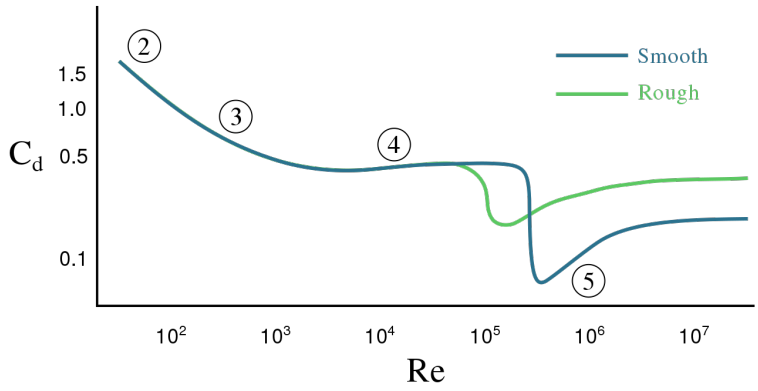

Fig. 1.21 Drag coefficient of a sphere as a function of Reynolds number. Public domain image.

Most aeronautics applications have Reynolds numbers in the millions or tens of millions, but small radio control aircraft or small low speed aircraft may have Reynolds numbers in the tens or hundreds of thousands. For an inviscid flow (an idealization) the Reynolds number is infinite (with zero viscosity).

Mach number is a ratio of fluid speed to the speed of sound:

$$M = \frac{V}{a} \tag{1.41}$$

A Mach number below 1 is *subsonic*, at 1 is *sonic*, and above 1 is *supersonic*. There are fundamental behavior changes in supersonic flow that we discuss more in Chapter 6. Sometimes we label other regimes like *transonic*, which means near sonic, as approximately M = 0.8–1.2 or *hypersonic* as M > 5. These latter two are rough guidelines as there is not a well-defined point where the fluid behavior changes as there is at the sonic point. Transonic flows are sometimes categorized separately as the fluid equations become highly nonlinear as discussed in Chapter 6, and hypersonic flows are sometimes categorized separately because of the massive aerodynamic heating that causes dissociation and ionization of the air molecules. For incompressible flow (again an idealization)

the Mach number is zero (with infinite speed of sound).

If we added gravity to the list of inputs in Eq. 1.38 then we would another nondimensional parameter, the Froude number. For unsteady flows we have another nondimensional parameter: the Strouhaul number. But for most steady aerodynamic flows buoyancy is negligible and so only Reynolds number and Mach number are of interest.

Now let us explore this concept a bit more rigorously from the governing equations. As a simple case, we will look at just the x component of the 2D incompressible Navier-Stokes equation[†]

[†]We'll go through governing equations in detail in Section 1.7.

$$u\frac{\partial u}{\partial x} + v\frac{\partial u}{\partial y} = -\frac{1}{\rho}\frac{\partial p}{\partial x} + \frac{\mu}{\rho}\left(\frac{\partial^2 u}{\partial x^2} + \frac{\partial^2 u}{\partial y^2}\right). \tag{1.42}$$

We would like to nondimensionalize this equation. The first term has two velocity terms in the numerator and one length in the denominator. We can multiply the whole equation as follows using V_∞ as a relevant velocity and c as a relevant length scale (e.g., the chord length of an airfoil):

$$\frac{c}{V_\infty^2}\left[u\frac{\partial u}{\partial x} + v\frac{\partial u}{\partial y} = -\frac{1}{\rho}\frac{\partial p}{\partial x} + \frac{\mu}{\rho}\left(\frac{\partial^2 u}{\partial x^2} + \frac{\partial^2 u}{\partial y^2}\right)\right]. \tag{1.43}$$

For convenience we define the following nondimensional variables:

$$u^* = \frac{u}{V_\infty}, \quad v^* = \frac{v}{V_\infty}, \quad x^* = \frac{x}{c}, \quad y^* = \frac{y}{c}. \tag{1.44}$$

We first focus on the first two terms, which nondimensionalize in a straightforward way:

$$u^*\frac{\partial u^*}{\partial x^*} + v^*\frac{\partial u^*}{\partial y^*} = -\frac{1}{\rho V_\infty^2}\frac{\partial p}{\partial x^*} + \frac{\mu c}{\rho V_\infty^2}\left(\frac{\partial^2 u}{\partial x^2} + \frac{\partial^2 u}{\partial y^2}\right). \tag{1.45}$$

For pressure we could nondimensionalize as follows:

$$p^* = \frac{p}{\rho V_\infty^2}. \tag{1.46}$$

Although convention is to use the pressure coefficient (Eq. 1.11):

$$p^* = C_p = \frac{p - p_\infty}{\frac{1}{2}\rho V_\infty^2}, \tag{1.47}$$

because it is only pressure differences that matters in computing loads. For the concept at hand it doesn't matter. Either way, the term p_∞ is constant and so drops out of the derivative leading to the same expression:

$$u^*\frac{\partial u^*}{\partial x^*} + v^*\frac{\partial u^*}{\partial y^*} = -\frac{\partial p^*}{\partial x^*} + \frac{\mu c}{\rho V_\infty^2}\left(\frac{\partial^2 u}{\partial x^2} + \frac{\partial^2 u}{\partial y^2}\right). \tag{1.48}$$

For the last term there is one velocity term in the numerator (and we already have a velocity in the denominator we can use to nondimensionalize). There are two length scales in the denominator and so we need to multiply and divide the last equation by c.

$$u^*\frac{\partial u^*}{\partial x^*} + v^*\frac{\partial u^*}{\partial y^*} = -\frac{\partial p^*}{\partial x^*} + \frac{\mu c^2}{\rho V_\infty^2 c}\left(\frac{\partial^2 u}{\partial x^2} + \frac{\partial^2 u}{\partial y^2}\right) \tag{1.49}$$

$$u^*\frac{\partial u^*}{\partial x^*} + v^*\frac{\partial u^*}{\partial y^*} = -\frac{\partial p^*}{\partial x^*} + \frac{\mu}{\rho V_\infty c}\left(\frac{\partial^2 u^*}{\partial x^{*2}} + \frac{\partial^2 u^*}{\partial y^{*2}}\right). \tag{1.50}$$

The equation is now nondimensional. We note that the factor appearing at the beginning of the last term is one over the Reynolds number:

$$u^*\frac{\partial u^*}{\partial x^*} + v^*\frac{\partial u^*}{\partial y^*} = -\frac{\partial p^*}{\partial x^*} + \frac{1}{Re}\left(\frac{\partial^2 u^*}{\partial x^{*2}} + \frac{\partial^2 u^*}{\partial y^{*2}}\right). \tag{1.51}$$

The insight from this equation, is that if we match Reynolds numbers for two similar geometries and boundary conditions, then all of the nondimensional fluid properties (velocity, pressure, density, etc.) will be identical in the entire flow field.

If we used the compressible Navier-Stokes equation then another parameter would emerge: the Mach number. If the unsteady term was added then the Strouhaul number would emerge, and if the gravity term was added then the Froude number would emerge.

Example 1.3 Matching Reynolds number

In practice, matching some of these parameters isn't so easy. Consider trying to match the Reynolds number between a full scale aircraft and a 1:20 scale model for use in a wind tunnel. The ratio of kinematic viscosity at 35,000 ft (typical altitude for a transport aircraft) as compared to sea level is about three ($\nu_{\text{fs}} = 3\nu_{\text{wt}}$). If we equate the Reynolds number of the full scale aircraft (fs) and the wind tunnel model (wt):

$$\frac{V_{\text{fs}} l_{\text{fs}}}{\nu_{\text{fs}}} = \frac{V_{\text{wt}} l_{\text{wt}}}{\nu_{\text{wt}}}, \tag{1.52}$$

we can solve for the requisite velocity ratio:

$$\frac{V_{\text{wt}}}{V_{\text{fs}}} = \frac{l_{\text{fs}}}{l_{\text{wt}}}\frac{\nu_{\text{wt}}}{\nu_{\text{fs}}} \tag{1.53}$$

$$= \frac{20}{1}\frac{1}{3} = 6.67. \tag{1.54}$$

This means that the velocity in the wind tunnel needs to be nearly seven times that of the aircraft's velocity! This is rather problematic. Some possible ways to help address this include using a pressurized tunnel (which can increase

density and thus reduce kinematic viscosity), or a cryogenic tunnel (which reduces temperature and thus reduces dynamic viscosity), but both of these solutions are expensive and generally require smaller tunnels which makes the problem harder (small models increase the necessary velocity ratio).

In practice, many wind tunnel experiments don't match Reynolds number. That isn't always as bad as it sounds. Revisit Fig. 1.21 and note how the drag changes relatively slowly across huge variations in Reynolds number. Because Reynolds number effectively operates on a log scale, one often only needs to match it within the same order of magnitude. In fact, we can often get away with not even getting close to matching Reynolds number as long as we are in the same flow regime (laminar or turbulent). The exception is near transition from laminar to turbulent flow (the steep drop in Fig. 1.21).‡

‡The other main exception is at very low Reynolds numbers, like in the tens or hundreds, but those are very rarely of interest in aerodynamics.

For our aircraft example in Ex. 1.3, the wind tunnel may be at too low of a Reynolds number to naturally have turbulent flow, whereas the full-scale aircraft will be turbulent much earlier. A common approach for wind tunnel testing in these scenarios is to intentionally trip the flow to be turbulent at the desired location by adding zigzag tape, or a roughness patch. Matching Reynolds number is generally only critical in the boundary layer where viscous effects are large, and so tripping the boundary layer can work reasonably well without actually matching the Reynolds number.

1.6 Vector Calculus and Index Notation

We first review a few concepts from vector calculus that we will need in deriving the governing equations and throughout the book. Next, we discuss index notation, which is often used with the governing equations of fluid dynamics to make derivations and expression easier.

1.6.1 Vector Calculus

These first few operators are expressed only in Carstesian coordinates for simplicity, but will introduce expressions in other coordinate systems later as needed. The *gradient* operator acts on a scalar and produces a vector:

$$\nabla p = \frac{\partial p}{\partial x}\hat{x} + \frac{\partial p}{\partial y}\hat{y} + \frac{\partial p}{\partial z}\hat{z}. \tag{1.55}$$

The gradient is a vector that points in the direction where the scalar field is increasing the fastest. So, for example, the gradient of temperature at

a given point in a fluid flow, would be a vector pointing in the direction in which temperature increases most rapidly.

Divergence is a scalar quantity that acts on vectors:

$$\nabla \cdot \vec{V} = \frac{\partial V_x}{\partial x} + \frac{\partial V_y}{\partial y} + \frac{\partial V_z}{\partial z}. \tag{1.56}$$

It can be thought of as a measure of how much something is expanding or contracting. If the vector $\vec{V}$ is velocity its divergence measures volume change per unit mass (or the rate of change of density). Thus, for incompressible flows the divergence is zero (we will derive this more rigorously shortly).

The *curl* is a vector quantity and it acts on vectors:

$$\nabla \times \vec{V} = \left(\frac{\partial V_z}{\partial y} - \frac{\partial V_y}{\partial V_z}\right)\hat{x} + \left(\frac{\partial V_x}{\partial z} - \frac{\partial V_z}{\partial V_x}\right)\hat{y} + \left(\frac{\partial V_y}{\partial x} - \frac{\partial V_x}{\partial V_y}\right)\hat{z}. \tag{1.57}$$

The curl measures the tendency of a vector field to create rotation. If the vector $\vec{V}$ is velocity then its curl is called *vorticity* ($\vec{\omega}$):

$$\vec{\omega} = \nabla \times \vec{V}. \tag{1.58}$$

Vorticity is an important aerodynamic quantity we will discuss later. It is related to rotation as vorticity is twice the angular velocity.

We can relate total divergence and curl with an interior to an integral along a boundary. *Stoke's theorem* relates the contour integral of a vector around a path to the curl (or rotation) of that vector inside the area.

$$\oint_C \vec{V} \cdot d\vec{\ell} = \int_A \left(\nabla \times \vec{V}\right) \cdot d\vec{A}. \tag{1.59}$$

Conceptually, this means that the net sum of all the rotation occurring within some two-dimensional area can be found by integrating along the boundary of that area.

The *divergence theorem* relates the flux of some vector leaving a control volume to the divergence of that vector inside the enclosed volume.

$$\int_A \vec{V} \cdot d\vec{A} = \int_{\forall} \left(\nabla \cdot \vec{V}\right) d\forall. \tag{1.60}$$

Conceptually, this means that the net sum of all the expansion inside a volume can be found by integrating the amount of fluid leaving the boundary.

Below we list a handful of vector calculus identities we will make use of where ϕ is an arbitrary scalar and $\vec{A}$ and $\vec{B}$ are arbitrary vectors:

$$\nabla \times (\nabla \phi) = 0 \tag{1.61}$$

$$\nabla \cdot (\nabla \times \vec{A}) = 0 \tag{1.62}$$

$$\nabla \times (\phi \vec{A}) = \phi(\nabla \times \vec{A}) + \nabla\phi \times \vec{A} \tag{1.63}$$

$$\frac{1}{2}\nabla(\vec{A} \cdot \vec{A}) = (\vec{A} \cdot \nabla)\vec{A} + \vec{A} \times (\nabla \times \vec{A}) \tag{1.64}$$

$$\nabla \times (\vec{A} \times \vec{B}) = \vec{A}(\nabla \cdot \vec{B}) - \vec{B}(\nabla \cdot \vec{A}) + (\vec{B} \cdot \nabla)\vec{A} - (\vec{A} \cdot \nabla)\vec{B}. \tag{1.65}$$

1.6.2 Index Notation

Index notation, also known as Einstein notation, or sometimes tensor notation, is a convenient representation often used in differential forms of fluid equations. In this notation a single index represents all three vector components. The same index may be used in separate terms indicating a free index that is repeated for all three vector components. Thus,

$$\frac{\partial(\rho u_i)}{\partial t} + \frac{\partial p}{\partial x_i} = 0. \tag{1.66}$$

is a shorthand for three equations:

$$\frac{\partial(\rho u_1)}{\partial t} + \frac{\partial p}{\partial x_1} = 0 \tag{1.67}$$

$$\frac{\partial(\rho u_2)}{\partial t} + \frac{\partial p}{\partial x_2} = 0 \tag{1.68}$$

$$\frac{\partial(\rho u_3)}{\partial t} + \frac{\partial p}{\partial x_3} = 0. \tag{1.69}$$

where the subscripts $1, 2, 3$ correspond to separate Cartesian directions, typically the x, y, z directions.

A repeated index, in the same term, represents a summation. Thus, $\partial u_i / \partial x_i$ is shorthand for:

$$\sum_{i=1}^{3} \frac{\partial u_i}{\partial x_i}. \tag{1.70}$$

or

$$\frac{\partial u_i}{\partial x_i} = \frac{\partial u_1}{\partial x_1} + \frac{\partial u_2}{\partial x_2} + \frac{\partial u_3}{\partial x_3} = \nabla \cdot \vec{V}. \tag{1.71}$$

We can combine the two types of indices (free index and summation index) as shown in the expression below:

$$\frac{\partial(\rho u_i)}{\partial t} + \frac{\partial(\rho u_i u_j)}{\partial x_j} = 0. \tag{1.72}$$

In this case index j is repeated in the same term, which indicates a summation. Whereas the index i appears once in each term and is thus the free index representing separate equations. There can only be one free index, but there can be multiple summations, generally indicated with additional indices. Written explicitly the above equations expands out to:

$$\begin{aligned}
\frac{\partial(\rho u_1)}{\partial t} + \frac{\partial(\rho u_1 u_1)}{\partial x_1} + \frac{\partial(\rho u_1 u_2)}{\partial x_2} + \frac{\partial(\rho u_1 u_3)}{\partial x_3} &= 0 \\
\frac{\partial(\rho u_2)}{\partial t} + \frac{\partial(\rho u_2 u_1)}{\partial x_1} + \frac{\partial(\rho u_2 u_2)}{\partial x_2} + \frac{\partial(\rho u_2 u_3)}{\partial x_3} &= 0 \\
\frac{\partial(\rho u_3)}{\partial t} + \frac{\partial(\rho u_3 u_1)}{\partial x_1} + \frac{\partial(\rho u_3 u_2)}{\partial x_2} + \frac{\partial(\rho u_3 u_3)}{\partial x_3} &= 0.
\end{aligned} \tag{1.73}$$

While this shorthand takes some getting used to, once we are familiar with it, we can express many equations more concisely and clearly. This shorthand becomes particularly useful once tensors are involved, and when combined with vector calculus operators, makes many of the derivations more straightforward. As one example that we'll need later in this chapter, here is the divergence theorem (Eq. 1.60) in index form:

$$\int_A u_j dA_j = \int_{\forall} \frac{\partial u_j}{\partial x_j} d\forall. \tag{1.74}$$

One function that is frequently used in index notation is the Kronecker delta, defined as:

$$\delta_{ij} = \begin{cases} 1 & \text{if } i = j \\ 0 & \text{if } i \neq j \end{cases}. \tag{1.75}$$

It is a function that takes in the two indices and returns a 1 or 0. A few useful properties, that are all straightforward to verify from its definition, are listed below. It is symmetric

$$\delta_{ij} = \delta_{ji}. \tag{1.76}$$

If summed over (we consider only three dimensional spaces, but it can be used in broader contexts):

$$\delta_{ii} = 3. \tag{1.77}$$

It contracts tensors as follows (recall the implied sum over i):

$$a_i \delta_{ij} = a_j. \tag{1.78}$$

In other words, multiplying it against a vector extracts the j^{th} component. Or with a more general tensor,

$$a_{ijk} \delta_{jl} = a_{ilk}. \tag{1.79}$$

Finally, multiplying two together gives:

$$\delta_{ij}\delta_{jk} = \delta_{ij}. \tag{1.80}$$

While this function may seem a bit abstract, we'll see it in use a few times this chapter.

1.7 Governing Equations

Sometimes we call the governing equations in fluid mechanics conservation laws. However, that is a bit of a misnomer. Momentum, for example, generally isn't conserved. Newton's second law doesn't say $dp/dt = 0$, but rather equates forces with changes in momentum. And while mass and energy are conserved in closed systems, in fluid mechanics we frequently use open control volumes (allow for transfer across boundaries and thus mass/energy changes within the volume), and so balance laws is perhaps a more apt terminology.

The balance laws in fluid mechanics are analogous to the principles of balancing your bank account, which we can write in a generic way as:

$$\text{accumulation} = \text{inflow} - \text{outflow} + \text{production}. \tag{1.81}$$

For finance, the accumulation is the total in your bank account, inflow is deposits, outflow is withdraws, and production is interest. The same idea works in fluids although we generally reorder, combine inflow/outflow, and speak of rates:

$$\text{rate of accumulation} + \text{rate of net outflow} = \text{rate of production}. \tag{1.82}$$

Let's apply this principle to the mass in a control volume. First, mass accumulates in a control volume as the change in time of the total mass integrated over the volume:

$$\frac{\partial}{\partial t}\int_{\forall} \rho d\forall. \tag{1.83}$$

The net outflow is an integral over the mass entering or leaving the surface area per unit time:

$$\int_A \rho \vec{V} \cdot d\vec{A} = 0. \tag{1.84}$$

Finally, mass cannot be produced within the control volume. Putting these pieces together yields:

$$\frac{\partial}{\partial t}\int_{\forall} \rho d\forall + \int_A \rho \vec{V} \cdot d\vec{A} = 0. \tag{1.85}$$

This is the integral form of the mass equation.

We can obtain the differential form through a few additional steps. For the first term we move the derivative inside the integral. Differentiation and integration commute (as long as the function and its derivative are continuous) and so we can swap the order. For the second term we apply the divergence theorem (Eq. 1.60):

$$\int_{\forall} \frac{\partial \rho}{\partial t} d\forall + \int_{\forall} \nabla \cdot \left(\rho \vec{V}\right) d\forall = 0. \tag{1.86}$$

Next, we combine the equations into one integral:

$$\int_{\forall} \left(\frac{\partial \rho}{\partial t} + \nabla \cdot \left(\rho \vec{V}\right)\right) d\forall = 0. \tag{1.87}$$

Because this equation must apply for every arbitrary control volume in the fluid, the integrand must be zero everywhere:

$$\frac{\partial \rho}{\partial t} + \nabla \cdot \left(\rho \vec{V}\right) = 0. \tag{1.88}$$

This is the differential form of the mass equation.

Let's now explore what the implications are for an incompressible flow. First, we need to understand what the total derivative of density looks like. The density in a fluid can vary with position and time:

$$\rho(x, y, z, t). \tag{1.89}$$

Let's take the derivative of this function with respect to time, realizing that the position x, y, z of the fluid particle can also vary with time.

$$\frac{d\rho}{dt} = \frac{\partial \rho}{\partial t} + \frac{\partial \rho}{\partial x}\frac{dx}{dt} + \frac{\partial \rho}{\partial y}\frac{dy}{dt} + \frac{\partial \rho}{\partial y}\frac{dz}{dt}. \tag{1.90}$$

Noting that $dx/dt = u$, the x-component of velocity, and similarly for the other components, we have:

$$\frac{d\rho}{dt} = \frac{\partial \rho}{\partial t} + \frac{\partial \rho}{\partial x}u + \frac{\partial \rho}{\partial y}v + \frac{\partial \rho}{\partial y}w. \tag{1.91}$$

Finally, we can write this in a generic vector notation (independent of coordinate system choice):

$$\frac{d\rho}{dt} = \frac{\partial \rho}{\partial t} + \nabla\rho \cdot \vec{V}. \tag{1.92}$$

In fluid mechanics we often give this total derivative the special name: material derivative or substantial derivative and often it is denoted

with a big D (although mathematically a little d has the same meaning, it is just a total derivative):

$$\frac{D()}{Dt} = \frac{\partial()}{\partial t} + \vec{V} \cdot \nabla(). \tag{1.93}$$

The first term in the total derivative tell us how a fluid property changes in time at a fixed point, whereas the second term tells us how a fluid property changes due to fluid motion. This is perhaps most easily visualized with temperature. Imagine a cold region of air transitioning towards hot region of air as shown in Fig. 1.22. Furthermore, let's assume for now that the entire volume of air is static (i.e., temperature is not changing in time). In this case the first term would be zero, but a fluid particle moving from the cold to the hot region would experience a change a temperature from the convective (second) term. Now imagine that the entire mass of air (both cold and hot regions) was heated up. Now the first term would be increasing even without moving. As we track the fluid particle the total change in temperature is due to the convective motion and the temporal change in temperature. The total derivative captures this full change.

Fig. 1.22 A temperature gradient from cold (blue) to hot (red).

With that background we can now understand that an incompressible flow means that the *total* derivative of density is zero:

$$\frac{D\rho}{Dt} = \frac{\partial \rho}{\partial t} + \nabla \rho \cdot \vec{V} = 0. \tag{1.94}$$

It is not actually necessary that both terms in the substantial derivative are zero, but rather only that their sum is zero. Thus, while all constant density flows are incompressible, not all incompressible flows need be constant density. Common examples of the latter are mixtures of two fluids (e.g., salt water with fresh water, or helium mixed with air). The density at a given fixed point changes in time, and if you moved between the two types of water the density also changes. However, the density following a given fluid particle does not change (if incompressible). Another way to state this is that the density is constant in a Lagrangian frame, not an Eulerian one.

Let's now go back to our mass balance equation and apply the definition of incompressibility. Repeating the mass balance equation (Eq. 1.88) gives:

$$\frac{\partial \rho}{\partial t} + \nabla \cdot \left(\rho \vec{V} \right) = 0 \,. \tag{1.95}$$

First, we apply the differential operator across the variables in the second term:

$$\frac{\partial \rho}{\partial t} + \nabla \rho \cdot \vec{V} + \rho \nabla \cdot \vec{V} = 0 \,. \tag{1.96}$$

We see that the first two terms are the substantial derivative, so this equation becomes:

$$\frac{D\rho}{Dt} + \rho\nabla\cdot\vec{V} = 0\,. \tag{1.97}$$

For an incompressible flow the substantial derivative of density is zero, thus the mass balance equation simplifies for an incompressible flow to:

$$\nabla\cdot\vec{V} = 0\,. \tag{1.98}$$

Again, if the density is constant we would arrive at this same conclusion, but we can also arrive at this conclusion for non-constant density flows that are still incompressible. We will use this formula multiple times throughout the book to apply incompressibility assumptions. This definition should make sense from what a divergence represents. This formula tells us that for an incompressible fluid, the volume of a particular quantity of fluid mass cannot expand or contract.

Let's now apply our balance law to momentum. The first, two terms (accumulation and net outflow) are nearly the same as that for mass, but are multiplied by another velocity to produce momentum. For now we won't worry about moving control volumes. For momentum, there are production terms, which come from forces (via Newton's second law). For aerodynamics these forces arise from pressure and shear stresses (the pressure term is negative since a positive pressure exerts an inward force whereas $d\vec{A}$ is positive out).

$$\frac{\partial}{\partial t}\int_{\forall}\rho\vec{V}d\forall + \int_A \rho\vec{V}\left(\vec{V}\cdot d\vec{A}\right) = -\int_A p d\vec{A} + \int_A \overleftrightarrow{\tau}\cdot d\vec{A}. \tag{1.99}$$

where $\overleftrightarrow{\tau}$ is the stress tensor.*

*We'll discuss the stress tensor in more detail in the next section. For now just note that it has two components, which you can think of as a direction and a face. So, for example, τ_{xy} would be a shear stress on the positive x face in the positive y direction (or equivalently a stress on the positive y face in the positive x direction).

We can put this equation in differential form using the divergence theorem in the same manner as in the mass balance. This is easiest to do using index notation. The integral equation becomes:

$$\frac{\partial}{\partial t}\int_{\forall}\rho u_i d\forall + \int_A \rho u_i u_j dA_j = -\int_A p dA_i + \int_A \tau_{ij} dA_j. \tag{1.100}$$

Applying the index form of the divergence theorem (Eq. 1.74) to this equation, and moving the derivative under the integral, results in:

$$\int_{\forall}\frac{\partial(\rho u_i)}{\partial t}d\forall + \int_{\forall}\frac{\partial(\rho u_i u_j)}{\partial x_j}d\forall = -\int_{\forall}\frac{\partial p}{\partial x_i}d\forall + \int_{\forall}\frac{\partial \tau_{ij}}{\partial x_j}d\forall. \tag{1.101}$$

Combining the integrals into one integral and noting that the equation must apply for any control volume and so the integrand must be zero,

gives the differential form of the momentum equation:

$$\frac{\partial(\rho u_i)}{\partial t} + \frac{\partial(\rho u_i u_j)}{\partial x_j} = -\frac{\partial p}{\partial x_i} + \frac{\partial \tau_{ij}}{\partial x_j}. \tag{1.102}$$

Note that since i appears once in each term it represents a vector equation (three equations in x, y and z). The index j appears twice in some terms indicating a summation over $j = 1 \ldots 3$. Explicitly, written out it would look like:

$$\begin{aligned}
\frac{\partial(\rho u_1)}{\partial t} + \frac{\partial(\rho u_1 u_1)}{\partial x_1} + \frac{\partial(\rho u_1 u_2)}{\partial x_2} + \frac{\partial(\rho u_1 u_3)}{\partial x_3} &= -\frac{\partial p}{\partial x_1} + \frac{\partial \tau_{11}}{\partial x_1} + \frac{\partial \tau_{12}}{\partial x_2} + \frac{\partial \tau_{13}}{\partial x_3} \\
\frac{\partial(\rho u_2)}{\partial t} + \frac{\partial(\rho u_2 u_1)}{\partial x_1} + \frac{\partial(\rho u_2 u_2)}{\partial x_2} + \frac{\partial(\rho u_2 u_3)}{\partial x_3} &= -\frac{\partial p}{\partial x_2} + \frac{\partial \tau_{21}}{\partial x_1} + \frac{\partial \tau_{22}}{\partial x_2} + \frac{\partial \tau_{23}}{\partial x_3} \\
\frac{\partial(\rho u_3)}{\partial t} + \frac{\partial(\rho u_3 u_1)}{\partial x_1} + \frac{\partial(\rho u_3 u_2)}{\partial x_2} + \frac{\partial(\rho u_3 u_3)}{\partial x_3} &= -\frac{\partial p}{\partial x_3} + \frac{\partial \tau_{31}}{\partial x_1} + \frac{\partial \tau_{32}}{\partial x_2} + \frac{\partial \tau_{33}}{\partial x_3}.
\end{aligned} \tag{1.103}$$

In vector notation we could write it as:

$$\frac{\partial(\rho \vec{V})}{\partial t} + \nabla \cdot (\rho \vec{V} \otimes \vec{V}) = -\nabla p + \nabla \cdot \overleftrightarrow{\tau}, \tag{1.104}$$

where $\otimes$ is the outer product.[†] As an aside these last three equations allow us a clearer comparison of index notation, explicitly written out form, and vector notation respectively. While index notation takes some getting use to it is the only one that retains both compactness and clarity. The vector form is just as compact as the index form, but it isn't clear which component differentiation should be with respect to, for each term, without some additional thought. Explicitly writing out the terms is very clear, but in derivations the amount of writing becomes quite cumbersome and makes it easier to introduce mistakes.

[†]The outer product operates on two vectors and produces a matrix: $(\vec{a} \otimes \vec{b})_{ij} = a_i b_j$ or in vector notation $\vec{a} \otimes \vec{b} = \vec{a}\vec{b}^T$, where $\vec{a}$ is a column vector and $\vec{b}^T$ is a row vector.

This equation is the *conservation form* of the momentum equation, and is a convenient form in many computational fluid dynamics applications. However, we typically simplify it by expanding the derivatives with the product rule (focusing on the just the left hand side):

$$\frac{\partial(\rho u_i)}{\partial t} + \frac{\partial(\rho u_i u_j)}{\partial x_j} = \tag{1.105}$$

$$\rho \frac{\partial u_i}{\partial t} + u_i \frac{\partial \rho}{\partial t} + u_i \frac{\partial(\rho u_j)}{\partial x_j} + \rho u_j \frac{\partial(u_i)}{\partial x_j}. \tag{1.106}$$

Next, we use the continuity equation (Eq. 1.88) in differential form:

$$\frac{\partial \rho}{\partial t} + \frac{\partial(\rho u_j)}{\partial x_j} = 0. \tag{1.107}$$

The second and third terms in Eq. 1.106 is exactly u_i times the continuity equation and so those two terms sum to zero. The remaining two terms are the definition of the total derivative:

$$\rho\frac{\partial u_i}{\partial t} + \rho u_j\frac{\partial (u_i)}{\partial x_j} = \rho\frac{Du_i}{Dt}. \tag{1.108}$$

Substituting this new left-hand side back into the momentum equations results in the following formula:

$$\rho\frac{Du_i}{Dt} = -\frac{\partial p}{\partial x_i} + \frac{\partial \tau_{ij}}{\partial x_j}, \tag{1.109}$$

or with the total derivative expanded:

$$\rho\frac{\partial u_i}{\partial t} + \rho u_j\frac{\partial u_i}{\partial x_j} = -\frac{\partial p}{\partial x_i} + \frac{\partial \tau_{ij}}{\partial x_j}. \tag{1.110}$$

This is known as the *convective form*. In vector form it would be:

$$\rho\frac{D\vec{V}}{Dt} = -\nabla p + \nabla\cdot\overleftrightarrow{\tau}, \tag{1.111}$$

or with the total derivative expanded:

$$\rho\frac{\partial\vec{V}}{\partial t} + \rho(\vec{V}\cdot\nabla)\vec{V} = -\nabla p + \nabla\cdot\overleftrightarrow{\tau}, \tag{1.112}$$

If we really want to be compact, we can define the total stress as the combination of pressure and shear stress:

$$\sigma_{ij} = -p\delta_{ij} + \tau_{ij}. \tag{1.113}$$

where δ_{ij} is the Kronecker delta (Eq. 1.75). Then the momentum equation becomes:

$$\rho\frac{Du_i}{Dt} = \frac{\partial \sigma_{ij}}{\partial x_j}. \tag{1.114}$$

The third balance law of fluid mechanics is energy, but we will save its discussion to Chapter 6. This equation requires additional thermodynamic variables and so it will be clearer when those are reviewed in the context of compressible flow.

1.8 Stress Tensor

The term that may be unfamiliar from the last section is the stress tensor τ. To formulate the stress tensor we need a relationship between

stresses and strains, which is called a *constitutive equation*. Stresses are related to the velocity gradients $\partial u_i/\partial x_j$: We can write the velocity gradient in the equivalent form:

$$\frac{\partial u_i}{\partial x_j} = \frac{1}{2}\left(\frac{\partial u_i}{\partial x_j} + \frac{\partial u_j}{\partial x_i}\right) + \frac{1}{2}\left(\frac{\partial u_i}{\partial x_j} - \frac{\partial u_j}{\partial x_i}\right). \tag{1.115}$$

Notice that the second and fourth terms cancel, and the first and second add back to the original relationship. This seems a rather unnecessary complication, but the usefulness is that the first two terms together form a symmetric tensor, and the last two form an antisymmetric tensor.* A tensor a_{ij} is antisymmetric if $a_{ij} = -a_{ji}$. For convenience we will express these two groupings as:

*Any rank 2 tensor can be decomposed into the sum of a symmetric and an antisymmetric tensor.

$$\frac{\partial u_i}{\partial x_j} = \epsilon_{ij} + \omega_{ij}. \tag{1.116}$$

The first term, the symmetric portion, we call the *strain tensor*.†

$$\epsilon_{ij} = \frac{1}{2}\left(\frac{\partial u_i}{\partial x_j} + \frac{\partial u_j}{\partial x_i}\right). \tag{1.117}$$

†Actually it is a rate of strain tensor as these are velocities, not deflections.

The strain tensor describes deformations. The antisymmetric, second term, is the *vorticity tensor* and it describes pure rotation. Like pure translations, pure rotation does not create stress. Thus, the stress tensor is related only to the strain tensor (the symmetric portion of the velocity gradients).

For a *Newtonian fluid* we assume that the stress-strain relationship is linear. Most fluids are quite accurately classified as linear, including air. However, there are non-Newtonian fluids where the stress-strain relationship is nonlinear and thus the viscosity varies with stress. Common examples are blood, ketchup, honey, and paint.

In the most general case the linear relationship mapping strains to stresses would look like:

$$\tau_{ij} = K_{ijkl}\epsilon_{kl}, \tag{1.118}$$

where K is a fourth-order tensor with $3^4 = 81$ constants relating the nine stress components ($\tau_{xx}, \tau_{xy}, \ldots$) to the nine strain components. However, because fluids are isotropic (fluid properties are the same in all directions) tensor theory shows that the most general isotropic fourth order tensor is as follows:[3]

$$K_{ijkl} = \lambda\delta_{ij}\delta_{kl} + \mu\delta_{ik}\delta_{jl} + \nu\delta_{il}\delta_{jk}, \tag{1.119}$$

3. Hodge, *On Isotropic Cartesian Tensors*, 1961.

where λ, μ and ν are all constants (down to 3 constants from the original 81), and the δ terms are all Kronecker deltas.

Because we know that the stress tensor is also symmetric we can exchange the ij components:

$$K_{ijkl} = K_{jikl} = \lambda\delta_{ji}\delta_{kl} + \mu\delta_{jk}\delta_{il} + \nu\delta_{jl}\delta_{ik}. \tag{1.120}$$

Comparing with the previous equation we see that the first term is identical, since the Kronecker delta is symmetric $\delta_{ij} = \delta_{ji}$. Comparing the latter two terms we see that $\mu = \nu$, and so a general isotropic, symmetric, fourth-order tensor is expressed as:

$$K_{ijkl} = \lambda\delta_{ij}\delta_{kl} + \mu\left(\delta_{ik}\delta_{jl} + \delta_{il}\delta_{jk}\right). \tag{1.121}$$

Note that there are now only two unique constants, μ and λ, which for a fluid we call the first and second coefficients of viscosity.‡

‡This is exactly the same situation with isotropic structural materials where the constitutive equation relating stress and strain requires only two constants: the modulus of elasticity E and Poisson's ratio ν. The shear modulus G is not an independent constant, any two of these three defines the other.

We now plug this general tensor relationship (Eq. 1.121) into the constitutive equation (Eq. 1.118):

$$\tau_{ij} = \left[\lambda\delta_{ij}\delta_{kl} + \mu\left(\delta_{ik}\delta_{jl} + \delta_{il}\delta_{jk}\right)\right]\epsilon_{kl}. \tag{1.122}$$

With the contraction rule of the Kronecker delta (Eq. 1.79), the stress tensor simplifies as:

$$\begin{aligned}\tau_{ij} &= \left[\lambda\delta_{ij}\delta_{kl} + \mu\left(\delta_{ik}\delta_{jl} + \delta_{il}\delta_{jk}\right)\right]\epsilon_{kl} \\ &= \lambda\delta_{ij}\delta_{kl}\epsilon_{kl} + \mu\left(\delta_{ik}\delta_{jl}\epsilon_{kl} + \delta_{il}\delta_{jk}\epsilon_{kl}\right) \\ &= \lambda\delta_{ij}\epsilon_{kk} + \mu\left(\epsilon_{ij} + \epsilon_{ji}\right) \\ &= \lambda\delta_{ij}\epsilon_{kk} + 2\mu\epsilon_{ij},\end{aligned} \tag{1.123}$$

where the last line was simplified because the strain tensor is symmetric. Finally, expanding the strain tensor explicitly (Eq. 1.117) gives the expression:

$$\tau_{ij} = \mu\left(\frac{\partial u_i}{\partial x_j} + \frac{\partial u_j}{\partial x_i}\right) + \lambda\left(\frac{\partial u_k}{\partial x_k}\right)\delta_{ij}. \tag{1.124}$$

The first coefficient of viscosity μ is the same one we're used to (Eq. 1.10). However, the second coefficient of viscosity λ is problematic because it adds another unknown that we don't have an equation for. Fortunately in many cases the last term in Eq. 1.124 is zero: inviscid flow (viscosity coefficients are zero), incompressible flow (the divergence $\partial u_k/\partial x_k = \nabla\cdot\vec{V} = 0$), or in boundary layers where viscous shear stresses are much larger than viscous normal stresses. However, for viscous compressible flows that term is not zero and we need a model to address it.

To motivate this model, let us consider the hydrostatic (h_{ij}) and deviatoric (d_{ij}) components of the stress tensor.§

§Any rank 2 tensor can be separated into the sum of a hydrostatic and a deviatoric tensor.

$$\tau_{ij} = h_{ij} + d_{ij} \,. \tag{1.125}$$

The hydrostatic value is just the average of the three diagonal components, and in matrix form is placed along the diagonals. This portion is invariant to rotation, and thus acts like pressure. The deviatoric component is just the original tensor minus the hydrostatic tensor.[¶] In this case the hydrostatic component is:

$$h_{ij} = \frac{1}{3}\text{trace}(\tau)\delta_{ij} \tag{1.126}$$

$$= \frac{1}{3}\tau_{kk}\delta_{ij} \,. \tag{1.127}$$

[¶] As another structural analogue, this is exactly the same process whereby von Mises stress is derived (via distortional energy theory). It is the deviatoric compoinent of the stress that is assumed to be related to failure.

Substituting in the definition of the stress tensor Eq. 1.124 gives:

$$h_{ij} = \frac{1}{3}\left(\mu\left(\frac{\partial u_k}{\partial x_k} + \frac{\partial u_k}{\partial x_k}\right) + \lambda\left(\frac{\partial u_l}{\partial x_l}\right)\delta_{kk}\right)\delta_{ij} \,. \tag{1.128}$$

We can simplify this since $\delta_{kk} = 3$ from the definition of the Kronecker delta (Eq. 1.75), and k and l are both dummy summation indices so we can make them both k and pull that term out:

$$h_{ij} = \left(\frac{2}{3}\mu + \lambda\right)\frac{\partial u_k}{\partial x_k}\delta_{ij} \tag{1.129}$$

$$= \kappa\frac{\partial u_k}{\partial x_k}\delta_{ij} \,. \tag{1.130}$$

Where $\kappa = 2/3\mu + \lambda$ is known as the *bulk viscosity*.

The deviatoric component is then:

$$\begin{aligned} d_{ij} &= \tau_{ij} - h_{ij} \\ &= \mu\left(\frac{\partial u_i}{\partial x_j} + \frac{\partial u_j}{\partial x_i}\right) - \frac{2}{3}\mu\left(\frac{\partial u_k}{\partial x_k}\right)\delta_{ij} \,. \end{aligned} \tag{1.131}$$

Stoke's hypothesis is that the bulk viscosity κ is zero. The rationale is that we expect the hydrostatic component of the shear stress to be zero. In other words the effective pressure, often called the mechanical pressure, is exactly the same as the thermodynamic pressure, which assumes that thermodynamic equilibrium occurs rapidly. The shear stress then only produces deviatoric components (only shear and no pure volume dilation/compression).

This hypothesis is widely used, and generally produces good results. Some theoretical arguments and limited experiments (it is difficult to measure the bulk viscosity) suggest that κ is negligible for some gases. However, in other scenarios have shown it to be quite large. More recent arguments suggest that it is not the bulk viscosity that is negligible but

4. Buresti, *A note on Stokes' hypothesis*, 2015.

rather that the product $\kappa \nabla \cdot \vec{V}$ (seen in Eq. 1.130) is typically negligible compared to the thermodynamic pressure.[4] Both assumptions result in the hydrostatic component vanishing (although the latter argument is more physically defensible). Using this hypothesis, the stress tensor retains only the deviatoric component:

$$\tau_{ij} = \mu \left(\frac{\partial u_i}{\partial x_j} + \frac{\partial u_j}{\partial x_i} \right) - \frac{2}{3} \mu \left(\frac{\partial u_k}{\partial x_k} \right) \delta_{ij} \,. \tag{1.132}$$

For an incompressible flow, the stress tensor portion simplifies considerably. First, the second term in the stress tensor vanishes because $\partial u_k / \partial x_k = \nabla \cdot \vec{V} = 0$ for an incompressible flow. Next, we need to take the derivative of the stress tensor since that is how it appears in the Navier-Stokes equations (Eq. 1.110). For an incompressible flow μ is constant (not true for compressible flows where μ is function of temperature) and so we can pull it out of the derivative.

$$\frac{\partial \tau_{ij}}{\partial x_j} = \mu \left(\frac{\partial^2 u_i}{\partial x_j^2} + \frac{\partial^2 u_j}{\partial x_i \partial x_j} \right) . \tag{1.133}$$

But since the divergence of the velocity field is zero for an incompressible flow ($\partial u_j / \partial x_j = 0$), the second term vanishes. Plugging this simplification into Eq. 1.110 yields the *incompressible momentum equation* (note that there is a summation over j on the last term even though the repeated index isn't explicitly shown because of the squared symbol):

$$\rho \frac{\partial u_i}{\partial t} + \rho u_j \frac{\partial u_i}{\partial x_j} = - \frac{\partial p}{\partial x_i} + \mu \frac{\partial^2 u_i}{\partial x_j^2} , \tag{1.134}$$

or in vector form:

$$\rho \frac{\partial \vec{V}}{\partial t} + \rho (\vec{V} \cdot \nabla) \vec{V} = - \nabla p + \mu \nabla^2 \vec{V} \,. \tag{1.135}$$

In this incompressible case, the vector notation doesn't have any ambiguities and so it is an often-used form.

For an incompressible flow there are only four unknowns: the three components of velocity and pressure (the density is either constant or known for the incompressible case). There are also four equations: mass and three momentum equations. For compressible flows we have two additional unknowns (e.g., temperature and density) and two additional equations: the energy equation and a thermodynamic equation of state (e.g., ideal gas equation). This topic will be discussed further in Chapter 6.

1.9 Bernoulli's Equation

Bernoulli's equation is well known because it is simple to use. To derive this equation we start with the incompressible momentum equation Eq. 1.135, and additionally assume that the flow is inviscid and steady to remove the viscous and time-dependent terms:

$$\rho(\vec{V}\cdot\nabla)\vec{V} = -\nabla p. \tag{1.136}$$

We use the vector identity (Eq. 1.64) to reexpress this equation as:

$$\rho\left(\frac{1}{2}\nabla(\vec{V}\cdot\vec{V}) - \vec{V}\times(\nabla\times\vec{V})\right) = -\nabla p \tag{1.137}$$

$$\frac{1}{2}\rho\nabla(\vec{V}\cdot\vec{V}) + \nabla p = \rho\vec{V}\times(\nabla\times\vec{V}). \tag{1.138}$$

We can bring $\rho/2$ under the differentiation, since it is a constant in this case, and we write $\vec{V}\cdot\vec{V} = u^2 + v^2 + w^2 = V^2$ to emphasize that the result is a scalar.

$$\nabla\left(\frac{1}{2}\rho V^2\right) + \nabla p = \rho\vec{V}\times(\nabla\times\vec{V}) \tag{1.139}$$

$$\nabla\left(\frac{1}{2}\rho V^2 + p\right) = \rho\vec{V}\times(\nabla\times\vec{V}). \tag{1.140}$$

We now take dot products of both sides with $\vec{V}$. Notice that the right hand-side will become zero since $\vec{V}\cdot(\vec{V}\times\square) = 0$ where $\square$ is any vector. That is because taking the cross product produces a vector orthogonal to $\vec{V}$, and the dot product of two orthogonal vectors is zero. We are left with:

$$\vec{V}\cdot\nabla\left(\frac{1}{2}\rho V^2 + p\right) = 0. \tag{1.141}$$

We may recall from vector calculus that the gradient of a function is everywhere orthogonal to its contour lines. The above expression states that the velocity vector is everywhere orthogonal to gradients of (incompressible) total pressure. But the gradient of total pressure is orthogonal to curves of constant total pressure. That means that curves of constant total pressure must be tangent to velocity contours (see **??**). In other words, the total pressure must be constant along a streamline:

$$p + \frac{1}{2}\rho V^2 = \text{constant along a streamline.} \tag{1.142}$$

Note that this is not a new equation. It is just an alternative, and often convenient, form of the momentum equation (with the additional restrictions of incompressible, inviscid, steady flow along a streamline).*

*In Chapter 6 we show that this equation could also be derived form the mechanical energy equation

1.10 Vorticity Equation

In this section we derive the vorticity equation, an alternative form of the Navier–Stokes equation useful in some contexts. We can derive the vorticity equation by taking the curl of the Navier-Stokes equation (Eq. 1.112).

$$\nabla \times \left(\frac{\partial \vec{V}}{\partial t} + (\vec{V} \cdot \nabla)\vec{V} = -\frac{1}{\rho}\nabla p + \frac{1}{\rho}\nabla \cdot \overleftrightarrow{\tau} \right). \tag{1.143}$$

We expand terms by recalling that vorticity is the curl of velocity (Eq. 1.58), and use some of the prior vector identities (Eqs. 1.61, 1.63, and 1.64) gives:

$$\frac{\partial \vec{\omega}}{\partial t} + \nabla \times \left(\frac{1}{2}\nabla(\vec{V} \cdot \vec{V}) - \vec{V} \times (\nabla \times \vec{V}) \right) = \frac{1}{\rho^2}\nabla\rho \times \nabla p + \nabla \times \left(\frac{1}{\rho}\nabla \cdot \overleftrightarrow{\tau} \right). \tag{1.144}$$

Let's now focus on the second term, which we'll call T_2 temporarily as shorthand:

$$T_2 = \nabla \times \left(\frac{1}{2}\nabla(\vec{V} \cdot \vec{V}) - \vec{V} \times (\nabla \times \vec{V}) \right) \tag{1.145}$$

$$= \nabla \times \left(\nabla \left(\frac{V^2}{2} \right) - \vec{V} \times \omega \right), \tag{1.146}$$

where V is the magnitude of $\vec{V}$. Since V^2 is just a scalar, this first term drops out by Eq. 1.61 leaving:

$$T_2 = \nabla \times \left(\omega \times \vec{V} \right). \tag{1.147}$$

We now expand the reamining term using Eq. 1.65:

$$T_2 = \vec{\omega}(\nabla \cdot \vec{V}) - \vec{V}(\cancel{\nabla \cdot \vec{\omega}}) + (\vec{V} \cdot \nabla)\vec{\omega} - (\vec{\omega} \cdot \nabla)\vec{V}, \tag{1.148}$$

where the second term dropped out by Eq. 1.62. We now put these terms back into the original equation to yield the vorticity equation.

$$\underbrace{\frac{\partial \vec{\omega}}{\partial t} + (\vec{V} \cdot \nabla)\vec{\omega}}_{D\vec{\omega}/Dt} = \underbrace{(\vec{\omega} \cdot \nabla)\vec{V}}_{\substack{\text{vortex stretching} \\ \text{and tilting}}} - \underbrace{\vec{\omega}(\nabla \cdot \vec{V})}_{\substack{\text{vortex stretching} \\ \text{due to} \\ \text{compressibility}}} + \underbrace{\frac{1}{\rho^2}\nabla\rho \times \nabla p}_{\text{baroclinic term}} + \underbrace{\nabla \times \left(\frac{1}{\rho}\nabla \cdot \overleftrightarrow{\tau} \right)}_{\substack{\text{vorticity diffusion} \\ \text{due to viscosity}}}. \tag{1.149}$$

The baroclinic term is zero if density is constant, or if incompressible and homogenous. It is also zero if density is only a function of pressure, which is called a *barotropic* fluid and includes many liquids. For aerodynamics, incompressible flows are almost always homogenous, so we will just call it incompressible. Using an incompressibility assumption also allows us to simplify the viscous term (as shown in Eq. 1.135):

$$\frac{D\vec{\omega}}{Dt} = (\vec{\omega} \cdot \nabla)\vec{V} + \nu\nabla^2\vec{\omega}. \tag{1.150}$$

The first term on the right-hand side is the vortex stretching and tilting term. If we look at just one direction, and temporarily leave out the vorticity diffusion term for clarity, we have:

$$\frac{D\omega_1}{Dt} = \omega_1\frac{\partial u_1}{\partial x_1} + \omega_2\frac{\partial u_1}{\partial x_2} + \omega_3\frac{\partial u_1}{\partial x_3} \tag{1.151}$$

The first term represents vortex stretching. An acceleration in the x direction ($\partial u_1/\partial x_1 > 0$) means that ω_1 is increased in its current direction. Thus, to conserve angular momentum, the vortex tube is contracted.* In other words the vortex tube is stretched—increased in vorticity magnitude but decreased in cross-sectional area. The second and third term represent vortex tiling. Looking at just the second term, if there is a shear in the velocity gradient ($\partial u_1/\partial x_2 \neq 0$), and ω_2 is nonzero, then there is change in ω_1. In other words, a vorticity vector that was aligned in the y direction, would now tilt toward the x direction.

*A vortex tube is analogous to a streamtube but for vortcity instead of velocity.

The last term, represents vorticity diffusion due to viscosity. It is perhaps more easily understood by comparing to the heat diffusivity equation:

$$\frac{dT}{dt} = k\nabla^2 T, \tag{1.152}$$

where T is temperature and k is the heat diffusivity. This equation describes how temperature spreads based on the heat diffusivity. This term in the vorticity equation has the same form, describing how vorticity spreads based on viscosity.

The vorticity equation can be a useful alternative to the incompressible Navier-Stokes equation as the vorticity vector is the only unknown (velocity can be computed from the vorticity). In other words, pressure is removed from the equation.

1.11 Translating and Rotating Reference Frames

In many cases the fluid behavior we measure and observe is occurring in a reference frame that is moving and/or is rotating. Some modifications

to our governing equations are required in these cases.

1.11.1 Translating Reference Frame

Imagine two reference frames: one fixed and one moving at a constant speed U relative to the fixed frame (Fig. 1.23). Both frames are inertial,

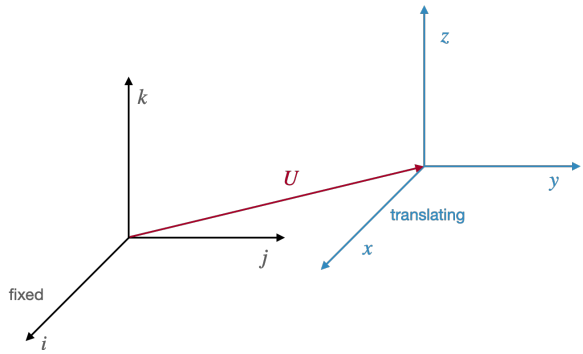

Fig. 1.23 An stationary frame and a translating frame.

and so we could apply our governing equations in whichever was more convenient. Often, we use a moving frame when analyzing a moving vehicle, like an aircraft, so that the problem has the potential to be steady (i.e., the airplane is fixed in that frame).

In some cases, however, we need to consider two frames at the same time that are moving with respect to each other. If $\vec{W}$ is the velocity as measured in the translating frame, what we will term the *relative velocity*, then the total velocity $\vec{V}$ in the fixed frame is:

$$\vec{V} = \vec{W} + \vec{U}. \tag{1.153}$$

Our differential equations are unchanged since we are in an inertial frame either way, but in in our integral equations we need to be careful to use the appropriate velocity vector for the net outflow term. In applying the balance equations in the fixed frame, we should use relative velocity $\vec{W}$ for the outflow since that measures how fast fluid is moving out of that volume, but should use the total velocity $\vec{V}$ for the momentum since that represents the actual momentum in that frame. The continuity equation (Eq. 1.85) becomes:

$$\frac{\partial}{\partial t}\int_{\forall} \rho d\forall + \int_A \rho \vec{W} \cdot d\vec{A} = 0, \tag{1.154}$$

and the momentum equation (Eq. 1.99) becomes:

$$\frac{\partial}{\partial t}\int_{\forall} \rho \vec{V} d\forall + \int_A \rho \vec{V}\left(\vec{W} \cdot d\vec{A}\right) = -\int_A p d\vec{A} + \int_A \overleftrightarrow{\tau} \cdot d\vec{A}. \tag{1.155}$$

1.11.2 Rotating Reference Frame

Fluid moving in a rotating reference frame introduces additional apparent forces. Imagine an inertial frame defined by the Cartesian coordinates $\hat{i}, \hat{j}, \hat{k}$, and a second rotating frame, rotating at some speed Ω relative to the inertial frame, defined by the Cartesian coordinates $\hat{x}, \hat{y}, \hat{z}$ (Fig. 1.24). We use the subscript I to refer to quantities measured relative to the inertial frame, and subscript R for quantities measured relative to the rotating frame. Then, from the perspective of the inertial frame, $\hat{i}$ is fixed. Mathematically this is expressed as:

$$\left(\frac{d\hat{i}}{dt}\right)_I = 0. \tag{1.156}$$

Similarly, from the perspective of the rotating frame, $\hat{x}$ is fixed.

$$\left(\frac{d\hat{x}}{dt}\right)_R = 0. \tag{1.157}$$

However, from the perspective of the inertial frame $\hat{x}$ is not fixed, it is rotating, and so its time derivative is not zero. We can show that this derivative is given by:*

$$\left(\frac{d\hat{x}}{dt}\right)_I = \vec{\Omega} \times \hat{x}. \tag{1.158}$$

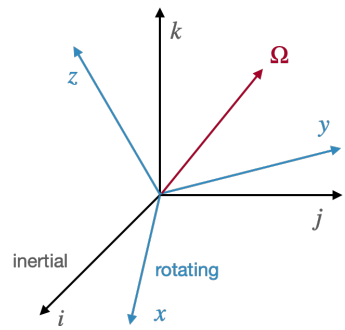

Fig. 1.24 An inertial frame and a rotating reference frame.

*This is shown in any dynamics textbook. It is easiest to derive by drawing out the geometry.

With that result, let us consider a position vector $\vec{r} = x\hat{x} + y\hat{y} + z\hat{z}$, which indicates the position of some fluid particle. We have chosen to represent the vector in the basis of the rotating coordinate frame, but it is the same vector for both frames (we are assuming the origins are coincident for this case). If we take derivatives in our rotating frame then we have:

$$\left(\frac{d\vec{r}}{dt}\right)_R = \dot{x}\hat{x} + \dot{y}\hat{y} + \dot{z}\hat{z}, \tag{1.159}$$

where the dot superscript indicates a time derivative (note that the unit vectors are fixed in this frame so the result is straightforward). These derivatives $(\dot{x}, \dot{y}, \dot{z})$ are unambiguous quantities because they are scalars and so are the same in any reference frame.

Let's now repeat the same derivative, but take derivatives in the inertial reference frame. Because the unit vectors $\hat{x}, \hat{y}, \hat{z}$ are not fixed in this reference frame, we have additional terms from the chain rule.

$$\begin{aligned}\left(\frac{d\vec{r}}{dt}\right)_I &= \dot{x}\hat{x} + x\left(\frac{d\hat{x}}{dt}\right)_I + \dot{y}\hat{y} + y\left(\frac{d\hat{y}}{dt}\right)_I + \dot{z}\hat{z} + z\left(\frac{d\hat{z}}{dt}\right)_I \\ &= \dot{x}\hat{x} + x(\vec{\Omega}\times\hat{x}) + \dot{y}\hat{y} + y(\vec{\Omega}\times\hat{y}) + \dot{z}\hat{z} + z(\vec{\Omega}\times\hat{z}). \\ &= \left(\frac{d\vec{r}}{dt}\right)_R + \vec{\Omega}\times\vec{r}\end{aligned} \tag{1.160}$$

Since the time derivative of position is velocity $\vec{v}$, we can write this more succinctly as:

$$\vec{v}_I = \vec{v}_R + \vec{\Omega} \times \vec{r}. \tag{1.161}$$

Thus, the velocity we measure in the relative frame needs to modified with an addition term.

We now repeat the process once more to determine accelerations. Note that Eq. 1.160 provides a general rule for any vector:

$$\left(\frac{d\square}{dt}\right)_I = \left(\frac{d\square}{dt}\right)_R + \vec{\Omega} \times \square\,, \tag{1.162}$$

where $\square$ is any vector. We now take derivatives of Eq. 1.160:

$$\left(\frac{d^2\vec{r}}{dt^2}\right)_I = \frac{d}{dt}_I \left(\frac{d\vec{r}}{dt}\right)_R + \frac{d\vec{\Omega}}{dt}_I \times \vec{r} + \vec{\Omega} \times \left(\frac{d\vec{r}}{dt}\right)_I. \tag{1.163}$$

We expand the first term on the right-hand side using Eq. 1.162

$$\vec{a}_I = \left(\frac{d^2\vec{r}}{dt^2}\right)_R + \vec{\Omega} \times \left(\frac{d\vec{r}}{dt}\right)_R + \frac{d\vec{\Omega}}{dt}_I \times \vec{r} + \vec{\Omega} \times \left(\frac{d\vec{r}}{dt}\right)_I. \tag{1.164}$$

We recognize the first term as $\vec{a}_R$, the acceleration as measured in the relative frame. For the third term $\vec{\Omega}$ is already defined in the inertial frame so the derivative is straightforward.

$$\vec{a}_I = \vec{a}_R + \vec{\Omega} \times \left(\frac{d\vec{r}}{dt}\right)_R + \dot{\vec{\Omega}} \times \vec{r} + \vec{\Omega} \times \left(\frac{d\vec{r}}{dt}\right)_I. \tag{1.165}$$

We now expand the last term using Eq. 1.160:

$$\vec{a}_I = \vec{a}_R + \vec{\Omega} \times \left(\frac{d\vec{r}}{dt}\right)_R + \dot{\vec{\Omega}} \times \vec{r} + \vec{\Omega} \times \left(\frac{d\vec{r}}{dt}\right)_R + \vec{\Omega} \times (\vec{\Omega} \times \vec{r}). \tag{1.166}$$

The second and fourth term are identical and so can be summed. If the rotation occurs at a constant rate, then the third term is zero. This leaves us with:

$$\vec{a}_I = \vec{a}_R + 2\vec{\Omega} \times \vec{v}_R + \vec{\Omega} \times (\vec{\Omega} \times \vec{r}). \tag{1.167}$$

We now see that, because of rotation, the acceleration as seen in the inertial frame differs from that of that in the rotating frame with two new terms (the dropped term should be reinserted if the rotation rate is not constant). The second term is called Coriolis acceleration, and the third term is called centripetal acceleration.

We can insert these accelerations as apparent forces (per unit mass) in the momentum equation (Eq. 1.111), with a negative sign since force

appears on the opposite side of acceleration in the momentum equation. The result is:

$$\frac{D\vec{V}}{Dt} = -\frac{1}{\rho}\nabla p + \frac{1}{\rho}\nabla\cdot\overleftrightarrow{\tau} - \underbrace{2\vec{\Omega}\times\vec{V}}_{\text{Coriolis}} - \underbrace{\vec{\Omega}\times(\vec{\Omega}\times\vec{r})}_{\text{centripetal}}. \tag{1.168}$$

Even though all fluid motion on the Earth is in a rotating frame, these last two terms are generally negligible. One notable exception is some large-scale atmospheric flows. There are also scenarios, within a boundary layer, where the flow speeds are slow enough that even though these extra forces are small their impact is important. One such case is discussed in Section 7.3.1.

1.12 Far Field Forces and Control Volume Analysis

In this section we are going to apply the integral form of our governing equations to yield some key insights. As discussed, if we want to determine the forces and moments on a body, we need to find the pressure and shear stress all along the body and integrate. In this section, we will see that there is an alternative approach. Through a control volume analysis we can determine the forces on a body by integrating in the far-field. This is a useful result that is the basis of some wind tunnel measurement techniques, and is directly used in several theorems related to the lift and drag of bodies as we will see. Generally, we can shortcut some of the steps shown in this analysis, but we will be fully rigorous this first time.

Consider, a body with a control volume as shown in Fig. 1.25. The outer surface is far away from the body. The figure is not two control volumes (one around the body and one in the far field), but rather one control volume, which we have created by making a small cut to allow a continuous shape that wraps around the body from the far field control volume. In other words, as defined, the control volume contains only fluid (not the body).

We now apply the integral form of the momentum equation to this control volume (Eq. 1.99). The standard equation is shown below, but in this case we will assume the flow is steady so the time dependent term drops off.

$$\cancel{\frac{\partial}{\partial t}\int_{\forall}\rho\vec{V}d\forall} + \int_A \rho\vec{V}\left(\vec{V}\cdot d\vec{A}\right) = -\int_A p d\vec{A} + \int_A \overleftrightarrow{\tau}\cdot d\vec{A}. \tag{1.169}$$

All of the remaining integrals are only surface integrals so we combine them into one integral and we redefine $d\vec{A}$ as $\hat{n}dA$ for convenience.

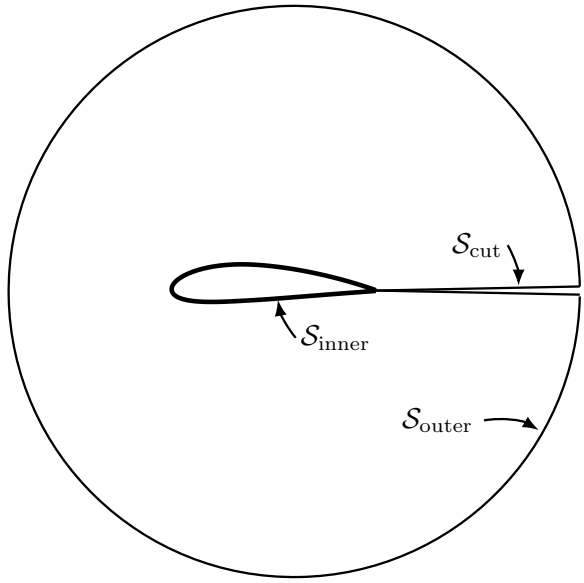

Fig. 1.25 A control volume with a branch cut so that the volume contains only fluid on the interior.

By convention the surface normal always points "out" of the control volume:

$$\int_A \left(\rho \vec{V}\left(\vec{V}\cdot\hat{n}\right) + p\hat{n} - \overleftrightarrow{\tau}\cdot\hat{n}\right) dA = 0. \tag{1.170}$$

Next, we divide the surface integration into three parts: integration along the inner surface, integration along the outer surface, and integration along the cut surface. The integration along the cut surface will go to zero. The reason is that the velocity and pressure must vary continuously and so we be identical on either side of the cut. However, the unit normal $\hat{n}$ will change sign from one side of the cut to the other and so the sum of those integrals will cancel:

$$\int_{S_{\text{inner}}} (\,)dA + \int_{S_{\text{outer}}} (\,)dA + \cancel{\int_{S_{\text{cut}}} (\,)dA} = 0. \tag{1.171}$$

Let's look at the remaining terms. For the inner surface $\hat{V}\cdot\hat{n}$ must be zero since fluid cannot pass through the body (and the control volume is right against the body). This is called the *no flow through* condition, which is true for a solid body whether the flow is viscous or inviscid (no slip occurs only for viscous flows).

$$\int_{S_{\text{inner}}} \left(\cancel{\rho \vec{V}\left(\vec{V}\cdot\hat{n}\right)} + p\hat{n} - \overleftrightarrow{\tau}\,\hat{n}\right) dA. \tag{1.172}$$

What remains is the the definition for the body force (i.e., the integral of pressure and shear stress over the body is the force that acts on the

body):

$$\int_{S_{\text{inner}}} \left(p\hat{n} - \overleftrightarrow{\tau} \cdot \hat{n} \right) dA = \vec{F}_b. \tag{1.173}$$

This integral represents the force on the fluid, but usually we care about the force of the fluid on the body. Thus, we would need a negative sign. However, because of the way we have defined our control volume, "out" for the control volume points into the body. This is opposite of our convention for positive pressures. Thus, we need another negative sign and so the two signs cancel out.

For the outer surface we are far enough away from the body that any shear stresses would be negligible.

$$\int_{S_{\text{outer}}} \left(\rho \vec{V} \left(\vec{V} \cdot \hat{n} \right) + p\hat{n} - \cancel{\overleftrightarrow{\tau} \cdot \hat{n}} \right) dA. \tag{1.174}$$

If we put this all together we are left with:

$$\vec{F}_b = -\int_{S_{\text{outer}}} \left(\rho \vec{V} \left(\vec{V} \cdot \hat{n} \right) + p\hat{n} \right) dA. \tag{1.175}$$

This is a significant result! It means that we can determine the forces on the body just by measuring velocities and pressures in a domain surrounding the body. Furthermore, if the outer boundary is unconfined (e.g., not in a wind tunnel) then the pressure term also goes to zero, and in that case we only need the velocity term.

Now that we've done it rigorously we note that you would get the exact same result by using just one outer control volume with no cut. In this case, we would consider the body force as an internal force acting in the control volume that we need to include with the other forces (pressure and shear stress). We will also need to include a negative sign because the equation uses the force of the body on the fluid and F_b is the force of the fluid on the body. This approach is easier, and one we will shortcut to from now on. However, it is worth rigorously justifying that we can include a body in a control volume when all the governing equations are for the fluid only.

Example 1.4 Control volume analysis for far-field drag analysis.

Consider flow around a cylinder (2D) in an unconfined domain. The Reynolds number is large enough such that the wake width is reasonably steady. Assume 2-dimensional, incompressible flow with the wake velocity profile shown in Fig. 1.26.

We will compute the 2D drag coefficient of the cylinder based on projected area (i.e., diameter) using two different control volumes.

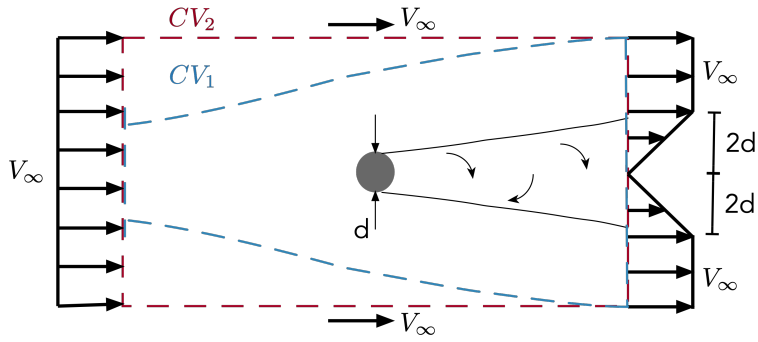

Fig. 1.26 Velocity profile upstream and downstream of a cylinder. (TODO: don't show the control volumes when redoing this)

Let's start with control volume 1 as shown in Fig. 1.27. The side boundaries follow streamlines of the flow field. We've labeled some unknowns lengths as h as l. We apply the mass balance using Eq. 1.85, but in this case it is steady

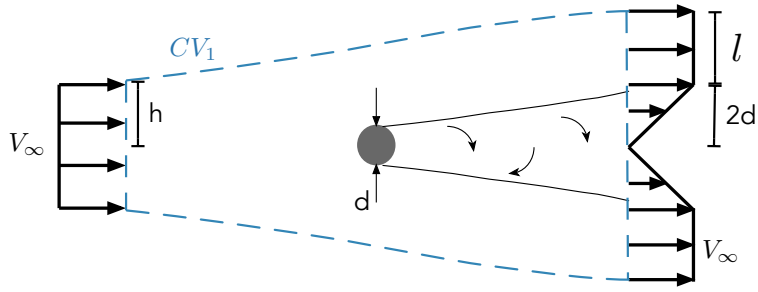

Fig. 1.27 Control volume 1 follows streamlines on the side boundaries.

and incompressible, so it reduces to:

$$\int_A \vec{V} \cdot d\vec{A} = 0. \tag{1.176}$$

There is no mass flow through the sides by definition because they are streamlines. Thus, the mass balance (per unit depth) is:

$$\int_{in} \vec{V} \cdot d\vec{A} + \int_{out} \vec{V} \cdot d\vec{A} = 0 \tag{1.177}$$

$$-V_\infty(2h) + V_\infty(2l) + 2\int_0^{2d} \frac{V_\infty y}{2d} dy = 0 \tag{1.178}$$

$$-V_\infty(2h) + V_\infty(2l) + \frac{V_\infty}{d}\left[\frac{y^2}{2}\right]_0^{2d} = 0 \tag{1.179}$$

$$-V_\infty(2h) + V_\infty(2l) + 2V_\infty d = 0 \tag{1.180}$$

$$-h + l + d = 0. \tag{1.181}$$

We now apply the momentum equation (Eq. 1.99), removing the unsteady term:

$$\int_A \rho\vec{V}(\vec{V}\cdot d\vec{A}) = -\int_A p d\vec{A} + \int_A \overleftrightarrow{\tau}\cdot d\vec{A}.$$

The viscous stresses are negligible along the boundaries, and the volume is unconfined, so the pressure along the boundary should be atmospheric. Thus, the pressure and stress terms are zero for the boundary. The cylinder creates a force on the fluid in the $-x$ direction (from pressure and viscous stresses). Thus, the x-component of the momentum equation simplifies to:

$$\int_A \rho V_x(\vec{V}\cdot d\vec{A}) = -D'. \tag{1.182}$$

Again, there is no momentum flux across streamlines so

$$\int_{in} \rho V_x(\vec{V}\cdot d\vec{A}) + \int_{out} \rho V_x(\vec{V}\cdot d\vec{A}) = -D' \tag{1.183}$$

$$\rho V_\infty(-V_\infty 2h) + 2\left[\rho V_\infty(V_\infty l) + \int_0^{2d} \rho\left(\frac{V_\infty y}{2d}\right)\left(\frac{V_\infty y}{2d}\right)dy\right] = -D' \tag{1.184}$$

$$-2\rho V_\infty^2 h + 2\left[\rho V_\infty^2 l + \frac{\rho V_\infty^2}{4d^2}\int_0^{2d} y^2 dy\right] = -D' \tag{1.185}$$

$$-2\rho V_\infty^2 h + 2\left[\rho V_\infty^2 l + \frac{\rho V_\infty^2}{4d^2}\left(\frac{8d^3}{3}\right)\right] = -D' \tag{1.186}$$

$$\Rightarrow D' = 2\rho V_\infty^2 h - 2\rho V_\infty^2 l - \frac{4\rho V_\infty^2 d}{3} \tag{1.187}$$

$$= 2\rho V_\infty^2\left(h - l - \frac{2d}{3}\right). \tag{1.188}$$

From conservation of mass we have $h - l = d$ (Eq. 1.181) so:

$$D' = \frac{2}{3}\rho V_\infty^2 d. \tag{1.189}$$

The definition of the 2D drag coefficient based on diameter is

$$c_d = \frac{D'}{\frac{1}{2}\rho V_\infty^2 d} \tag{1.190}$$

$$= \frac{\frac{2}{3}\rho V_\infty^2 d}{\frac{1}{2}\rho V_\infty^2 d} \tag{1.191}$$

$$= \frac{4}{3}. \tag{1.192}$$

Let's now try a different control volume and see if we can get the same result. This time we'll use a rectangular control volume as shown in Fig. 1.28.

There will be mass flow out the sides, as depicted in the figure, because they are not streamlines. We know nothing about the mass flow other than they

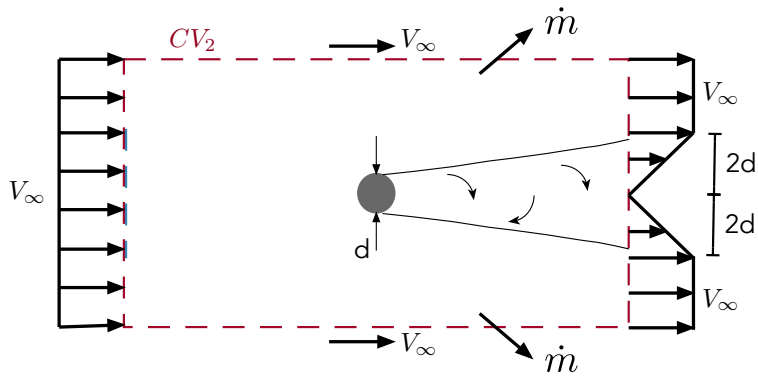

Fig. 1.28 Control volume 2 is a rectangle.

will be the same top and bottom because of symmetry. We assume the flow is out, but the sign will tell us if our assumption was correct or not (in this case it is obvious). We also make the assumption that the sides are far enough away that the x component of velocity at the side boundaries is approximately V_∞.

Applying a mass balance gives:

$$\int_A \rho \vec{V} \cdot d\vec{A} = 0 \tag{1.193}$$

$$-\rho V_\infty 2(2d + l) + \rho V_\infty 2(l + d) + 2\dot{m}_{side} = 0 \tag{1.194}$$

$$\Rightarrow \dot{m}_{side} = \rho V_\infty d. \tag{1.195}$$

The density was left in for convenience (just so the last term is a mass flow rate). The first term is from the inlet, the second term is from the outlet and is the same as CV1, and the last term is from the sides.

For momentum, the outlet is the same as before, but the inlet and sides differ. The velocity in the x-direction at the sides is V_∞. (Note that the magnitude of the vertical component of the velocity, which we don't know, doesn't matter because we only need to solve the x-component of momentum.)

$$\int_A \rho V_x(\vec{V} \cdot d\vec{A}) = -D' \tag{1.196}$$

$$\rho V_\infty(-V_\infty 2(2d + l)) + 2\rho V_\infty^2 l + \frac{4\rho V_\infty^2 d}{3} + 2V_\infty \dot{m}_{side} = -D'. \tag{1.197}$$

Substituting in the mass flow rate found from continuity (Eq. 1.195) results in:

$$D' = 2\rho V_\infty^2(2d + l)) - 2\rho V_\infty^2 l - \frac{4\rho V_\infty^2 d}{3} - 2\rho V_\infty^2 d \tag{1.198}$$

$$= \rho V_\infty^2(4d + 2l - 2l - 4/3d - 2d) \tag{1.199}$$

$$= \frac{2}{3}\rho V_\infty^2 d. \tag{1.200}$$

This is exactly the same result for drag as before (Eq. 1.189), so we will get the same drag coefficient: $c_d = 4/3$.

2D Potential Flow

2

For low Mach number flows, incompressibility is a justifiable assumption. Furthermore, outside the boundary layer, many aerodynamic applications can reasonably be assumed to be inviscid, which is required for irrotational flow. When a flow is both incompressible and irrotational then the governing equations simplify drastically and is known as *potential flow*.* Instead of the complexity of the nonlinear Navier-Stokes equations we end up with a single linear partial differential equation known as Laplace's equation. This simplification allows us to rapidly solve for potential flow fields around complex geometries enabling broad design exploration. The fast run times of potential-flow-based computational methods has led to their widespread use in aerodynamic applications, particularly in preliminary design.

*Compressible potential flows have some utility as will be discussed in Chapter 6, but the incompressible counterparts are far more useful.

In this chapter we focus on two-dimensional behavior, and will look at three-dimensional applications in Chapter 4. We first define terms and derive the equations of potential flow. Next, we explore basic solutions to Laplace's equation. These are of interest because Laplace's equation is linear and so we can build up complex flows from the superposition of basic solutions. We then discuss the uniqueness challenge in lift computation, and then explore distributions of solutions that will allow for general shapes. This capability enables us to explore thin airfoil theory and 2D panel methods. The numerical methods portion of thin airfoil theory is not of much utility anymore, but the analytic results of theory are highly useful and well known. Finally, we explore two different 2D panel code implementations allowing us to solve for the potential flow around any airfoil shape.

By the end of this chapter you should be able to:

1. Identity and use elementary solutions of Laplace's equations to simulate basic flow fields.
2. Use both numerical integration and the Kutta-Joukowski theorem to compute forces in potential flow.
3. Understand and apply key takeaways from thin airfoil theory.
4. Write a basic inviscid 2D panel code to simulate flow around arbitrary airfoil shapes.

2.1 Irrotational and Incompressible Flow

We call a flow field *irrotational* if the velocity field is curl-free:

$$\nabla \times \vec{V} = 0. \tag{2.1}$$

From the definition of vorticity,

$$\vec{\omega} = \nabla \times \vec{V}, \tag{2.2}$$

we see that irrotationality is equivalent to the vorticity being zero everywhere.

If irrotational, then we can always represent the velocity field as a scalar potential function ϕ:

$$\vec{V} = \nabla \phi. \tag{2.3}$$

That is because the curl of any gradient is always zero (Eq. 1.61):

$$\nabla \times \nabla \phi = 0. \tag{2.4}$$

One benefit of this form is that ϕ is a scalar and so it simplifies our representation from a three-dimensional velocity field to a one-dimensional scalar function.

You might also recall from vector calculus that an irrotational field is conservative, meaning that line integrals are path independent. That also implies that any contour integral will be zero. To see this, let us split any contour at an arbitrary point. The line integrals along paths A and B, as illustrated in Fig. 2.1, are equal by path independence. So if we traverse contour C, which goes forward along A and backward

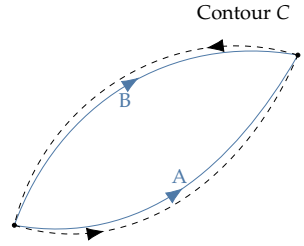

Fig. 2.1 Two different path integrals and a contour integral (which goes along A then backwards along B.)

along B, the total integral will be zero. We also note that because it is the gradient of ϕ that matters (Eq. 2.3), the potential is only defined up to an arbitrary constant.

As a familiar analogue, gravity is a conservative force. It is an irrotational force field, and so has a gravitational potential associated with the force (where the gradient of the potential is the force just like Eq. 2.3). Contour integrals around any arbitrary contour are zero (meaning no net work was done). The particular value of the gravitational potential is not of significance, but rather the differences between two points is what matters (i.e., a gradient), and so enables one to define a potential energy relative to some shared reference point.

Shear stresses from viscosity always introduces rotation (except in some contrived cases), whereas an inviscid flow does not. Thus, we need an inviscid flow in order for the flow to be irrotational. Inviscid flow is a necessary but not a sufficient condition to irrotationality. However, if the flow starts irrotational, *and* the fluid is inviscid, then it will remain irrotational. For many aerodynamic cases we have a constant freestream (which is irrotational) and so outside the boundary layer the flow field will be irrotational.

The most broadly useful reason for identifying an irrotational flow occurs if the flow is both irrotational *and* incompressible. For aerodynamics, incompressibility is a reasonable assumption for low Mach numbers, approximately less than $M = 0.3$. Recall that for an incompressible flow continuity requires that the velocity field is divergence free:

$$\nabla \cdot \vec{V} = 0. \tag{2.5}$$

If we now substitute in the vector potential for irrotational flow (Eq. 2.3) we have:

$$\nabla \cdot \nabla\phi = 0, \tag{2.6}$$

or

$$\nabla^2\phi = 0. \tag{2.7}$$

This is Laplace's equation. In Cartesian coordinates this equations is expressed as:

$$\frac{\partial^2\phi}{\partial x^2} + \frac{\partial^2\phi}{\partial y^2} + \frac{\partial^2\phi}{\partial z^2} = 0. \tag{2.8}$$

Laplace's equation is a very useful equation that shows up in many fields. We could solve Laplace's equation on a grid in a similar (but much simpler) manner to what is done with computational fluid dynamics (discussed in Chapter 8). However, that isn't necessary. The

reason why it is so useful is that it is a *linear* PDE. Linearity allows us to construct complex solutions by combining elementary ones. If we have two vector fields that satisfy Laplace's equation, then their sum also satisfies Laplace's equation (the principle of *superposition*). There are many known solutions to Laplace's equation that are relevant to flow fields. This means that we can build up complex flow fields from simple vector fields that are known solutions to the governing equations. In this manner we can, for example, analyze the flow over a complicated aircraft shape, using a superposition of known vector field solutions by adjusting their strengths appropriately to satisfy the boundary conditions. This is the basis of panel methods that are widely used in applied aerodynamics.

Note that the above derivation only needed to assume that the flow was incompressible and irrotational. It applies in 2D and 3D and for both steady and unsteady flows. However, in this chapter we will focus on 2D steady flows. While the assumptions of incompressible and irrotational flow may seem restrictive, most aerodynamic applications avoid significant flow separation, and so those assumptions are often appropriate for low-speed flows outside the boundary layer (which is typically quite thin as many aerodynamic applications occur at high Reynolds numbers). As we will learn in Chapter 3 we can add boundary layer theory to our potential flow models and in Chapter 6 we extend the methods into flow fields that are moderately compressible. Thus, potential flow methods are actually relevant to a broad cross-section of aerodynamics and are especially appealing because of their fast computational performance.

2.2 Stream Function Interpretation

There is an alternative way to come to the same governing equations using stream functions, at least in two dimensions. By construction, a streamline automatically satisfies continuity for an incompressible flow. The incompressible continuity equation (Eq. 1.98) in 2D is:

$$\frac{\partial u}{\partial x} + \frac{\partial v}{\partial y} = 0. \tag{2.9}$$

If we define a stream function ψ by the following relationships:

$$u = \frac{\partial \psi}{\partial y}, v = -\frac{\partial \psi}{\partial x}, \tag{2.10}$$

then plugging them into Eq. 2.9 we see that continuity is automatically satisfied since the mixed partials must be equal:

$$\frac{\partial^2\psi}{\partial y\partial x} - \frac{\partial\psi}{\partial x\partial y} = 0. \tag{2.11}$$

Lines of constant ψ (contour lines) are tangential to the velocity vector, and by definition are streamlines of the flow field, hence the name *stream* function. We can show this by first recalling from vector calculus that the gradient of a function is always orthogonal to its contour lines. So if the gradient of ψ is everywhere orthogonal to the local velocity vector then contour lines of ψ must be tangential to velocity vectors as illustrated in Fig. 2.2. In other words we must show that:

$$\nabla\psi \cdot \vec{V} = 0. \tag{2.12}$$

Using Eq. 2.10 we find:

$$\begin{aligned}
\nabla\psi \cdot \vec{V} &= \left(\frac{\partial\psi}{\partial x}\hat{x} + \frac{\partial\psi}{\partial y}\hat{y}\right) \cdot (u\hat{x} + v\hat{y}) && (2.13)\\
&= \left(\frac{\partial\psi}{\partial x}\hat{x} + \frac{\partial\psi}{\partial y}\hat{y}\right) \cdot \left(\frac{\partial\psi}{\partial y}\hat{x} - \frac{\partial\psi}{\partial x}\hat{y}\right) && (2.14)\\
&= \frac{\partial\psi}{\partial x}\frac{\partial\psi}{\partial y} - \frac{\partial\psi}{\partial y}\frac{\partial\psi}{\partial x} && (2.15)\\
&= 0. && (2.16)
\end{aligned}$$

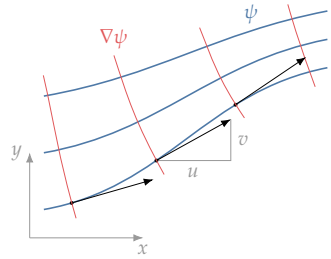

Fig. 2.2 Streamlines are always tangential to the local velocity

Note that this only works in two-dimensions.

If we use the definition of irrotationality (Eq. 2.1) with our defined stream function condition (Eq. 2.10):

$$\begin{aligned}
&\frac{\partial v}{\partial x} - \frac{\partial u}{\partial y} = 0 \Rightarrow\\
&\quad \frac{\partial^2\psi}{\partial x^2} + \frac{\partial^2\psi}{\partial y^2} = 0\,,
\end{aligned} \tag{2.17}$$

we obtain Laplace's equation.

In other words, the potential formulation automatically satisfies irrotationality ($\vec{V} = \nabla\phi$) and we impose continuity to get Laplace's equation. The stream function does the opposite. It automatically satisfies continuity, and we impose irrotationality to get Laplace's equation. The downside of the stream function approach is that, as outlined, it only works in 2D. Describing three-dimensional flows requires two stream functions. The potential form automatically works in 3D, and is simpler with just one function so is widely used.

The main usefulness of introducing the stream function is to note that both the potential and stream functions satisfy the Cauchy Riemann equations (used frequently in complex analysis):

$$\frac{\partial \phi}{\partial x} = \frac{\partial \psi}{\partial y} \tag{2.18}$$

$$\frac{\partial \phi}{\partial y} = -\frac{\partial \psi}{\partial x}. \tag{2.19}$$

This means that potential lines and streamlines are orthogonal (see Fig. 2.3):

$$\nabla\phi \cdot \nabla\psi = \frac{\partial \phi}{\partial x}\frac{\partial \psi}{\partial x} + \frac{\partial \phi}{\partial y}\frac{\partial \psi}{\partial y} \tag{2.20}$$

$$= \frac{\partial \phi}{\partial x}\left(-\frac{\partial \phi}{\partial y}\right) + \frac{\partial \phi}{\partial y}\frac{\partial \phi}{\partial x} \tag{2.21}$$

$$= 0. \tag{2.22}$$

This concept is sometimes helpful to attribute some physical significance to potential lines.

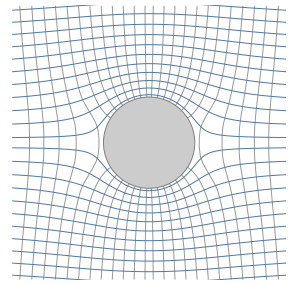

Fig. 2.3 Streamlines depicted using — and potential lines depicted using — are always orthogonal in 2D. TODO: Map the colors referred in the caption correctly for dark mode to work

2.3 Pressure Field

Before moving on we note that the prior equations discuss resolving the velocity field, and generally we would like the pressure field as well. This can be accomplished most easily with Bernoulli's equation. This equation was derived in Section 1.9, but for an irrotational flow the equation is even more broadly applicable. We back up to Eq. 1.140, before making the along-the-streamline assumption, and see that the right-hand-side of the equation will always be zero for irrotational flow (since $\nabla \times \vec{V} = 0$):

$$\nabla\left(\frac{1}{2}\rho V^2 + p\right) = 0. \tag{2.23}$$

If the gradient is everywhere zero, it means that the term in parentheses must be constant everywhere.

$$p + \frac{1}{2}\rho V^2 = \text{constant everywhere (if also irrotational).} \tag{2.24}$$

So, for potential flow, Bernoulli's equation can be applied between any two-points in the flow field, not just along streamlines.

This fact allows us to derive a more useful version of the pressure coefficient for potential flow. The pressure coefficient was introduced

earlier (Eq. 1.11), and is defined as:

$$C_p = \frac{p - p_\infty}{\frac{1}{2}\rho V_\infty^2}. \tag{2.25}$$

In potential flow we can apply Bernoulli's equation between any two points in the field:

$$p_\infty + \frac{1}{2}\rho V_\infty^2 = p + \frac{1}{2}\rho V^2 \tag{2.26}$$

$$p - p_\infty = \frac{1}{2}\rho V_\infty^2 - \frac{1}{2}\rho V^2. \tag{2.27}$$

Substituting into the pressure coefficient definition results in:

$$C_p = 1 - \left(\frac{V}{V_\infty}\right)^2. \tag{2.28}$$

Thus, we can quickly compute the pressure field at any point, once we have resolved the velocity field. Note that for potential flow, $C_p = 1$ at a stagnation point.

2.4 Elementary Solutions to the 2D Laplace Equation

We will now derive and describe elementary solutions to the 2D Laplace equation. These elementary solutions are useful to us because the governing equation is linear, and so these simple solutions become building blocks towards more complex solutions.

In this chapter we focus on two-dimensional solutions and so the governing equations are:

$$\frac{\partial^2\phi}{\partial x^2} + \frac{\partial^2\phi}{\partial y^2} = 0, \tag{2.29}$$

or in polar coordinates:

$$\frac{\partial^2\phi}{\partial r^2} + \frac{1}{r}\frac{\partial\phi}{\partial r} + \frac{1}{r^2}\frac{\partial^2\phi}{\partial\theta^2} = 0. \tag{2.30}$$

2.4.1 Uniform Flow

The simplest solution comes from the Cartesian version of Laplace's equation (Eq. 2.29) where we assume that each term is zero separately. In other words:

$$\frac{\partial^2\phi}{\partial x^2} = 0, \quad \frac{\partial^2\phi}{\partial y^2} = 0. \tag{2.31}$$

We pick the first equation and integrate twice to obtain:

$$\phi = kx + c, \tag{2.32}$$

where k and c are constants. The second term (derivatives with respect to y), works similarly and so a general solution is:

$$\phi = k_1 x + k_2 y + c. \tag{2.33}$$

Recall that the potential is only defined up to an arbitrary constant, since it is only the gradient that matters, so we can set $c = 0$ without a loss in generality.

These two constants are the two components of velocity for uniform flow:

$$\phi(x, y) = ux + vy, \tag{2.34}$$

or in terms of an angle of attack:

$$\phi(x, y) = V_\infty \cos(\alpha) x + V_\infty \sin(\alpha) y. \tag{2.35}$$

We can verify that this potential field represents a uniform flow by resolving the velocity components (Eq. 2.3), or in 2D:

$$\vec{V} = \nabla\phi = \frac{\partial\phi}{\partial x}\hat{x} + \frac{\partial\phi}{\partial y}\hat{y}. \tag{2.36}$$

In this case the result is:

$$u = V_\infty \cos\alpha \tag{2.37}$$

$$v = V_\infty \sin\alpha, \tag{2.38}$$

which we can immediately recognize as the components of velocity of uniform flow at an incidence angle of α as depicted in Fig. 2.4.

Additionally, if we visualize the scalar potential ϕ for the uniform flow as a surface, we see that it represents an inclined slope as shown in Fig. 2.5. You can visualize how the fluid flows from higher to a lower potential, much like how a ball would roll downhill from a higher to a lower elevation. The gradient of the potential function indicates the direction and velocity of flow, with fluid particles moving along the steepest descent of the potential surface. The potential function is typically depicted as a 2D contour plot as shown in Fig. 2.6.

The stream function representation is less commonly used, but it is particularly convenient if plotting streamlines is desired, and it is used in some panel codes. We can convert from the potential form to the

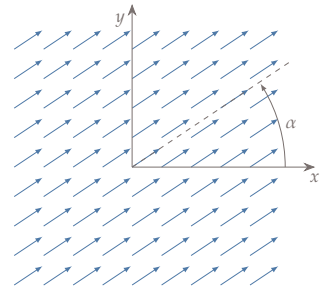

Fig. 2.4 Velocity field of uniform flow at an incidence angle α.

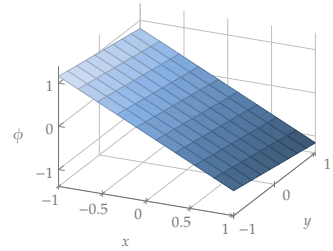

Fig. 2.5 Surface plot of scalar potential of a uniform flow.

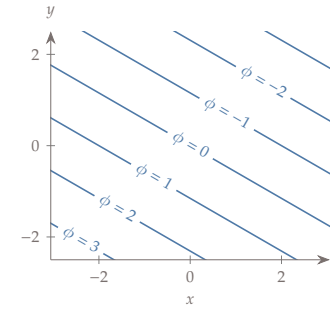

Fig. 2.6 Contour plot of scalar potential of a uniform flow.

stream function form by using the Cauchy-Reimann conditions. Using the first condition (Eq. 2.18) yields:

$$\frac{\partial \psi}{\partial y} = V_\infty \cos \alpha. \tag{2.39}$$

Integrating gives:

$$\psi(x, y) = V_\infty \cos(\alpha) y + \mu(x), \tag{2.40}$$

where $\mu(x)$ is some unknown function of x (like an integration constant, but it is potentially a function of x since we integrated with respect to a partial derivative). Using the second condition (Eq. 2.19) gives:

$$-\frac{d\mu}{dx} = V_\infty \sin \alpha, \tag{2.41}$$

from which we integrate:

$$\mu(x) = -V_\infty \sin(\alpha) x + c. \tag{2.42}$$

We again drop the arbitrary constant c. The stream function for uniform flow is then:

$$\psi(x, y) = V_\infty \cos(\alpha) y - V_\infty \sin(\alpha) x. \tag{2.43}$$

2.4.2 Source

For the next elementary solution, we assume a purely radial solution: $\phi = R(r)$. The polar form of the equations will be simpler in this case (Eq. 2.30). Because there is no θ dependence, the last term drops out, and our partial derivatives become total derivatives. Plugging in our assumed form for ϕ (where $R' \equiv dR/dr$) results in:

$$R'' + \frac{1}{r} R' = 0 \tag{2.44}$$

$$\frac{R''}{R'} = -\frac{1}{r}. \tag{2.45}$$

Integrating both sides yields:

$$\ln R' = -\ln r + c, \tag{2.46}$$

with c as an arbitrary constant. Exponentiating both sides gives:

$$R' = e^{(-\ln r)} e^c \tag{2.47}$$

$$= A e^{(\ln \frac{1}{r})} \tag{2.48}$$

$$= \frac{A}{r}, \tag{2.49}$$

where $A = e^c$ is a new arbitrary constant. We integrate once again to get our solution (where we again discard the last additive constant):

$$R = A \ln r. \tag{2.50}$$

By convention, we normalize the constant A as $\Lambda/(2\pi)$ for reasons we'll see in a moment, and so the final solution is:

$$\phi(r) = \frac{\Lambda}{2\pi} \ln r. \tag{2.51}$$

Similar to the uniform flow, the scalar potential can be visualized as a surface or contour plot as shown in Figs. 2.7 and 2.8. The parameter Λ is a free parameter we can choose for different strength sources.

The gradient in polar coordinates is:

$$\vec{V} = \nabla\phi = \frac{\partial\phi}{\partial r}\hat{r} + \frac{1}{r}\frac{\partial\phi}{\partial\theta}\hat{\theta}. \tag{2.52}$$

So in our case the velocity components are:

$$V_r = \frac{\Lambda}{2\pi r} \tag{2.53}$$

$$V_\theta = 0. \tag{2.54}$$

We see that the velocity field is purely radial. We call this solution a *source* (or if Λ is negative we sometimes refer to it as a *sink*), and the velocity field is depicted in Fig. 2.9. The parameter Λ is a free parameter we can choose for different strength sources.

Note that the center point is a singularity by observing the $1/r$ behavior for the induced velocity (Eq. 2.53). In fact, we often refer to sources, and the other solutions we will discuss next as *singularities*. This terminology reminds us to take care when evaluating velocities at or very near to their centers.

To obtain the stream function we use the Cauchy-Reimann equations in polar form:

$$\frac{\partial\phi}{\partial r} = \frac{1}{r}\frac{\partial\psi}{\partial\theta} \tag{2.55}$$

$$\frac{\partial\psi}{\partial r} = -\frac{1}{r}\frac{\partial\phi}{\partial\theta}. \tag{2.56}$$

For the source these two conditions yield:

$$\frac{\Lambda}{2\pi r} = \frac{1}{r}\frac{\partial\psi}{\partial\theta} \tag{2.57}$$

$$\frac{\partial\psi}{\partial r} = 0. \tag{2.58}$$

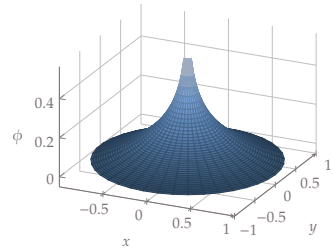

Fig. 2.7 Surface plot of scalar potential for a source.

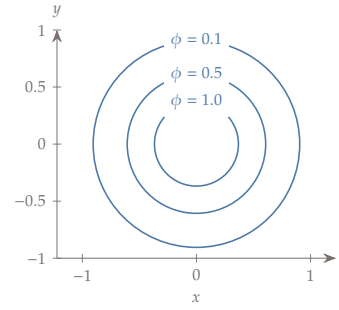

Fig. 2.8 Contour plot of scalar potential for a source.

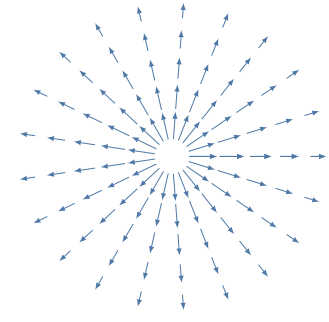

Fig. 2.9 Velocity field for a source.

Integrating the first equation gives:

$$\psi(r,\theta) = \frac{\Lambda}{2\pi}\theta + \mu(r). \tag{2.59}$$

Applying the second gives:

$$\frac{d\mu}{dr} = 0 \Rightarrow \mu = c. \tag{2.60}$$

Dropping the arbitrary constant our stream function is:

$$\psi(\theta) = \frac{\Lambda}{2\pi}\theta. \tag{2.61}$$

If we take a volumetric flux through any circle surrounding the source (see contour A of Fig. 2.10) we get:

$$\int_A \vec{V}\cdot d\vec{A} = \int_0^{2\pi} \frac{\Lambda}{2\pi r}\hat{r}\cdot r d\theta \hat{r} = \Lambda. \tag{2.62}$$

So, Λ, which we call the *source strength*, is just the volumetric flux or volume flow rate (and hence the 2π was included in the previous definition for convenience).

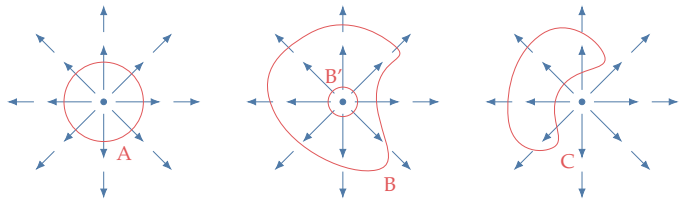

Fig. 2.10 Three different contours to evaluate the volumetric flux.

Since the radius cancelled out in the above derivation, the flow rate would be the same for any size circle, and in fact will be the same for any contour that surrounds the center of the source. To see this, consider the second figure in Fig. 2.10. We can transform our integral using the divergence theorem (Eq. 1.60), which transforms an integral on the boundary to one on the interior:

$$\int_A \vec{V}\cdot d\vec{A} = \int_{\forall} \left(\nabla\cdot\vec{V}\right) d\forall. \tag{2.63}$$

If we apply this to contour B we can divide the interior integral to two parts, where we have created a new circular control volume called B' (also shown in the figure):

$$\int_B \left(\nabla\cdot\vec{V}\right) d\forall = \int_{B-B'} \left(\nabla\cdot\vec{V}\right) d\forall + \int_{B'} \left(\nabla\cdot\vec{V}\right) d\forall. \tag{2.64}$$

The integral over $B - B'$ means we integrate the volume between the two contours. Because the flow is incompressible, $\nabla \cdot \vec{V}$ is zero everywhere, except at the singularity. So the integral over $B - B'$ vanishes:

$$\int_B \left(\nabla \cdot \vec{V}\right) d\forall = \int_{B'} \left(\nabla \cdot \vec{V}\right) d\forall = \Lambda. \tag{2.65}$$

We are left just with the integral over a circular region, which is exactly the same as our first case.

For contour C (Fig. 2.10) the divergence of the velocity is zero everywhere in the control volume, so the above equation shows that the volumetric flux is zero for any contour that does not enclose the center of the source.

$$\int_C \left(\nabla \cdot \vec{V}\right) d\forall = 0. \tag{2.66}$$

Physically this means that, for an incompressible flow, the volume of fluid entering a control volume per unit time must equal that leaving the control volume. And, when the contour surrounds the center of the source, a volume of flow per unit time of magnitude Λ is being injected into the control volume. It also shows that the flow field is divergence free (incompressible) everywhere as desired (except right at the singularity).

2.4.3 Vortex

For the next solution, instead of a purely radial solution, we assume a purely azimuthal one: $\phi = T(\theta)$. Using Eq. 2.30 we get:

$$T'' = 0, \tag{2.67}$$

where $T' = dT/d\theta$. This is easily integrated to (again dropping the arbitrary additive constant):

$$T = k\theta, \tag{2.68}$$

where k is a constant. Like the source we define a new normalized constant: $k = \Gamma/(2\pi)$ and so the potential is

$$\phi(\theta) = \frac{\Gamma}{2\pi}\theta. \tag{2.69}$$

The scalar potential visualized as a surface plot is a helix as shown in Figs. 2.11 and 2.12 and indicates that the fluid swirls in a circular motion.

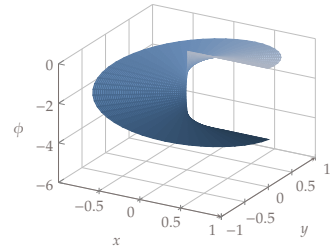

Fig. 2.11 Surface plot of scalar potential for a vortex.

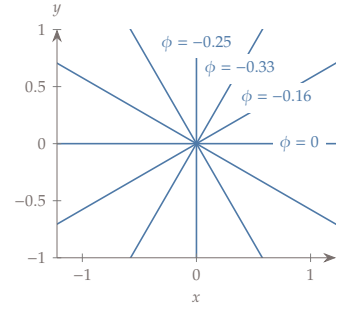

Fig. 2.12 Contour plot of scalar potential for a vortex.

Taking the gradient (Eq. 2.52) gives the following velocity components:

$$V_r = 0 \tag{2.70}$$

$$V_\theta = \frac{\Gamma}{2\pi r}. \tag{2.71}$$

We see that the velocity field is purely tangential (Fig. 2.13), and we call this solution a *vortex*. The vortex strength Γ is a free parameter we choose corresponding to different strength vortices.

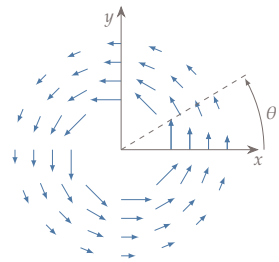

Fig. 2.13 Velocity field for a point vortex centered at $(0, 0)$.

The Cauchy-Reimann conditions (Eqs. 2.55 and 2.56) are:

$$0 = \frac{\partial \psi}{\partial \theta} \tag{2.72}$$

$$\frac{\partial \psi}{\partial r} = -\frac{1}{r}\frac{\Gamma}{2\pi}. \tag{2.73}$$

Integrating gives the stream function:

$$\psi(r) = -\frac{\Gamma}{2\pi}\ln r. \tag{2.74}$$

For a source, we evaluated the volumetric flux or the volume flow rate generated by the source. For a vortex we do something similar, but because this is a rotating rather than diverging flow we evaluate a quantity known as *circulation*:

$$\Gamma = \oint \vec{V} \cdot d\vec{l}. \tag{2.75}$$

Note that this is a contour integral around a closed path. Circulation is usually defined with the symbol Γ. It is no accident, as we will see, that we used the same symbol for the point vortex strength.

Consider the following three scenarios for a contour integral around a vortex shown in Fig. 2.14, which are analogous to the scenarios we considered for a source. We can easily perform the integral for contour A since the tangential velocity of the vortex (Eq. 2.71) aligns perfectly with our circular contour:

$$\Gamma = \int_0^{2\pi} \frac{\Gamma}{2\pi r} r d\theta = \Gamma. \tag{2.76}$$

Again, we see that the choice of a normalizing constant of 2π was intentional. The circulation of a point vortex is Γ, the vortex strength. The second and third cases follow exactly the same logic as in the source case, except that we use Stoke's theorem (Eq. 1.59) rather than the divergence theorem:

$$\Gamma = \oint \vec{V} \cdot d\vec{l} = \int_S \left(\nabla \times \vec{V}\right) \cdot d\vec{A}, \tag{2.77}$$

and use the fact that the flow is irrotational ($\nabla \times \vec{V} = 0$) everywhere except at the singularity. So again, we find that circulation is Γ for any shaped contour that surrounds the center of the point vortex, and is zero for any contour that does not.

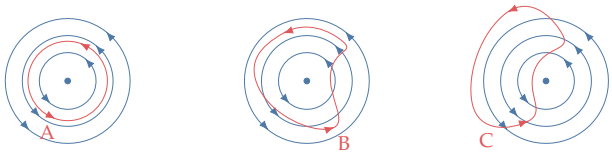

$\int_A \vec{V} \cdot d\vec{l} = \Gamma$ $\int_B \vec{V} \cdot d\vec{l} = \Gamma$ $\int_C \vec{V} \cdot d\vec{l} = 0$

Fig. 2.14 Three different contours to evaluate the circulation around a vortex.

This transformation also shows us that circulation is related to the concept of vorticity. Circulation can be interpreted as the net integral of vorticity within some boundary and so tells us about the net rotation of fluid inside the boundary. The concept of circulation plays a significant role in aerodynamics and we will see it many more times in this book, including later in this chapter.

2.4.4 Doublet

For our final elementary solution we assume a more general solution with both radial and tangential dependence $\phi = R(r)T(\theta)$, and we use the standard method of separation of variables. Substituting ϕ into Laplace's equation (Eq. 2.30) where $R' = dR/dr$ and $T' = dT/d\theta$ results in:

$$R''T + \frac{1}{r}R'T + \frac{1}{r^2}RT'' = 0 \tag{2.78}$$

$$\left(\frac{r^2R'' + rR'}{R}\right) + \frac{T''}{T} = 0. \tag{2.79}$$

We see that the second term has no radial dependence, and so for this equation to hold everywhere the first term must also have no radial dependence (i.e., it must a constant for all r). We set the left hand side to a yet unknown positive constant m^2 and so the second term must be equal to $-m^2$ (we will see shortly that we correctly guessed the sign choice).

Let's start with the second term since it is easier:

$$\frac{T''}{T} = -m^2 \tag{2.80}$$

$$T'' + m^2T = 0. \tag{2.81}$$

This is a standard second-order homogenous ODE, which we solve by assuming a general solution of $T(\theta) = e^{r\theta}$. Plugging this into the equation we get $r^2 + m^2 = 0$ or $r = \pm im$ and so our general solution is:

$$T(\theta) = Ae^{im\theta} + Be^{-im\theta} \tag{2.82}$$

$$T(\theta) = A(\cos(m\theta) + i\sin(m\theta)) + B(\cos(m\theta) - i\sin(m\theta)). \tag{2.83}$$

Grouping constants the general solution is:

$$T(\theta) = C\cos(m\theta) + D\sin(m\theta). \tag{2.84}$$

If we had chosen a positive constant (m^2) for this term then our solution would have had positive and negative exponentials, neither of which is physically appropriate in this case since we should have a periodic solution in terms of θ.

Let's now go back to the first term:

$$\frac{r^2R'' + rR'}{R} = m^2 \tag{2.85}$$

$$r^2R'' + rR' - m^2R = 0. \tag{2.86}$$

This ODE is known as a Cauchy-Euler equation (note that the exponent of r matches the order of the derivative with respect to r in each term), specifically a second-order version. It has known solutions of r^k for any integer k. If we plug this trial solution in we get:

$$r^2k(k-1)r^{k-2} + rkr^{k-1} - m^2r^k = 0 \tag{2.87}$$

$$k(k-1)r^k + kr^k - m^2r^k = 0 \tag{2.88}$$

$$k(k-1) + k - m^2 = 0 \tag{2.89}$$

$$k^2 - m^2 = 0. \tag{2.90}$$

With the result $k = \pm m$. Thus, we have general solutions of the form:

$$R(r) = Ar^m + Br^{-m}. \tag{2.91}$$

Combining our two equations we now have (again eliminating the arbitrary additive constant):

$$\phi = R(r)T(\theta) = (Ar^m + Br^{-m})(C\cos(m\theta) + D\sin(m\theta)), \tag{2.92}$$

for any integer m. The first term Ar^m is not physically relevant in our case because as $r \to \infty$ the potential becomes larger and larger as does the velocity (in the case $r = 1$ the velocity remains finite). However, for physical consistency in our fluid application we need the velocity from all of these solutions, except uniform flow, to decay to zero as $r \to \infty$

so that in the farfield we are left with just uniform flow. Thus, we set $A = 0$.

If we choose $m = 0$ we recover a source (compare Eq. 2.86 with $m = 0$ and Eq. 2.44) and a vortex (compare Eq. 2.81 with $m = 0$ and Eq. 2.67). We now move up to the next higher order solution $m = 1$.

$$\phi = \frac{1}{r}(C\cos(\theta) + D\sin(\theta)). \tag{2.93}$$

We will choose $D = 0$ for simplicity as the cosine term already provides periodicity. Furthermore, we normalize the remaining constant by 2π.

$$\phi(r,\theta) = \frac{\mu\cos\theta}{2\pi r} = \frac{\mu x}{2\pi r^2}. \tag{2.94}$$

This defines a dipole oriented in the $-x$ direction as shown in Fig. 2.15.

Taking the gradient we find the velocity components as:

$$V_r = -\frac{\mu\cos(\theta)}{2\pi r^2} \tag{2.95}$$

$$V_\theta = -\frac{\mu\sin(\theta)}{2\pi r^2}. \tag{2.96}$$

This solution is known as a *doublet* with strength μ.

Using the Cauchy-Reimann equations (Eqs. 2.55 and 2.56) for the doublet gives:

$$-\frac{\mu\cos\theta}{2\pi r^2} = \frac{1}{r}\frac{\partial\psi}{\partial\theta} \tag{2.97}$$

$$\frac{\partial\psi}{\partial r} = \frac{1}{r}\frac{\mu\sin\theta}{2\pi r}. \tag{2.98}$$

Integrating the first condition gives:

$$\psi(r,\theta) = -\frac{\mu\sin\theta}{2\pi r} + \mu(r). \tag{2.99}$$

Differentiation and substituting into the second condition gives:

$$\frac{\mu\sin\theta}{2\pi r^2} + \frac{d\mu}{dr} = \frac{\mu\sin\theta}{2\pi r^2}. \tag{2.100}$$

Which implies $d\mu/dr = 0$ and so μ is an arbitrary constant. The final stream function is then:

$$\psi(r,\theta) = -\frac{\mu\sin\theta}{2\pi r}. \tag{2.101}$$

Our general equation permits even higher order solutions (Eq. 2.92 with $m = 2, 3, \ldots$), but for aerodynamic flows these four: uniform flow, source, vortex, doublet, are all that are of practical interest.

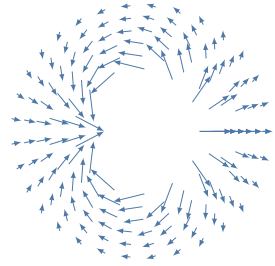

Fig. 2.15 Velocity field induced by a doublet centered at $(0, 0)$.

2.5 Superposition for Basic Flow Fields

Now that we have some building blocks in place, we will put them together to produce more interesting flow fields. Recall that because Laplace's equation is linear, if we have any two solutions their sum is also a solution. This means that we can place any number of sources, vortices, and doublets, at any location, and the resulting flow field will also be a solution to Laplace's equation. Because the velocity of all the singularities decays to zero in the farfield, we will automatically satisfy a farfield boundary condition of uniform flow. Thus, the only boundary condition we need to worry about is flow tangency around some geometry. In this section we do not pick the geometry beforehand, but rather will just combine some solutions and look at the resulting shape. In future sections we will see how to choose positions and strengths appropriately to satisfy boundary conditions for a desired shape.

Example 2.1 Half of a Rankine oval.

We begin with a combination of uniform flow and a point source. We set the uniform flow with a freestream speed of 0.5 m/s and set the source strength to $\Lambda = \pi$ m^2/s, with its center at the origin. We wish to find the location of the stagnation point, and plot the resulting streamlines.

Since we know that the source exerts a velocity radially in all directions, along the x axis its induced velocity will be purely in the x direction. This induced velocity varies from very large as we approach to source, to very small as move far from the source. So somewhere on the axis, to the left of the source, its velocity will exactly cancel with the freestream. Along the x axis then, the contribution of the freestream and the source is:

$$V_\infty + \frac{\Lambda}{2\pi x} = 0. \tag{2.102}$$

We solve for x:

$$x = -\frac{\Lambda}{2\pi V_\infty}. \tag{2.103}$$

In our case this gives:

$$x = -1 \text{ m}. \tag{2.104}$$

So the stagnation point is one meter to the left of the origin. Perhaps the easiest way to visualize the flow field is to compute the stream function on a grid, and plot it as a contour plots (the contour lines of the stream function are streamlines). The streamlines for this case are shown in Fig. 2.16.

We notice that there is a *dividing streamline* that separates the flow emitted from the source and that of the freestream. To ensuring the dividing streamline is plotted we can compute the value for the stream function at the stagnation point (-1, 0). The result is:

$$\psi = V_\infty y + \frac{\Lambda}{2\pi}\theta = \theta/2, \tag{2.105}$$

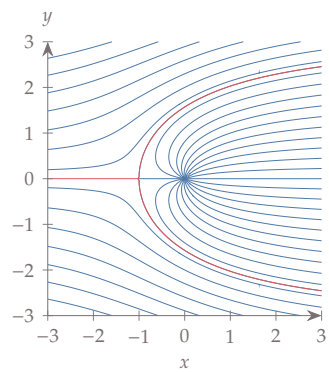

Fig. 2.16 Streamlines for the half Rankine oval, which is uniform flow around a source.

which in this case has two solutions: $\pi/2$ and $-\pi/2$ corresponding to the streamlines on the upper and lower half of the oval.

A streamline, by definition, has no flow across it. Thus, we could imagine replacing the interior of that dividing streamline with a solid body then the outer flow automatically satisfies flow tangency around that body. In other words, uniform flow plus a source allow us to solve for the flow field around this infinite oval-shaped body (known as a Rankine oval, or rather half of one). We can of course move the source, and change its strength, to alter the shape of the half oval.

Example 2.2 Rankine oval.

An infinite body is not of practical interest, so we now add a sink with the same strength (opposite sign). In this case we place the sink at $(1, 0)$. The stagnation points occur when:

$$V_\infty + \frac{\Lambda}{2\pi x} - \frac{\Lambda}{2\pi(x-1)} = 0. \tag{2.106}$$

Rearranging results in the quadratic equation:

$$x^2 - x - \frac{\Lambda}{2\pi V_\infty} = 0. \tag{2.107}$$

For our specific case we use the quadratic formula to find the stagnation points:

$$x = \frac{1 \pm \sqrt{5}}{2} \approx -0.618 \text{ and } 1.618. \tag{2.108}$$

More generally, we use a numerical approach, discretize the domain as before and create a contour plot of streamlines (Fig. 2.17). We need to be careful to evaluate r and θ relative to the center of the source/sink, and in this case the sink is offset from the origin so we compute θ as:

$$\theta = \tan^{-1}\left(\frac{y - y_c}{x - x_c}\right). \tag{2.109}$$

where (x_c, y_c) is the center of the singularity. This figure is plotted on the same domain size as the previous, so we see that the sink pulls in the flow field significantly. Again, we can see that the flow outside the oval represents potential flow (incompressible, inviscid flow) over the body (Rankine oval) since flow tangency is automatically satisfied. The flow field inside the oval is not of any practical interest and so can be ignored. It can be considered a byproduct of creating the desired exterior flow field.

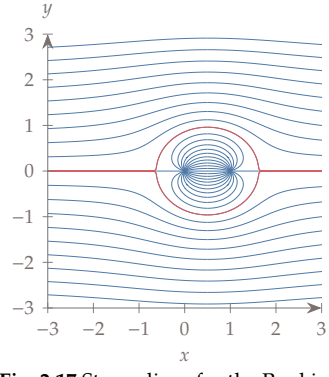

Fig. 2.17 Streamlines for the Rankine oval, created by uniform flow around a source and sink of equal strength.

Example 2.3 Flow Around a Cylinder.

One interpretation of a doublet is that it is the limit of bringing an equal strength source and sink pair infinitely close together (creating a higher order singularities from multiple lower order ones). This is perhaps an interesting side note, but motivates the shape we should expect when combining uniform flow and a doublet. If we revisit the prior example, moving the source and sink pairs further apart elongates the oval, while bringing them together contracts it. In the limit of bringing them together (a doublet), we expect a perfect circle.

We place a doublet at the origin of strength $\kappa = \pi\ \mathrm{m}^3/\mathrm{s}$, keep $V_\infty = 0.5\ \mathrm{m/s}$ as before, and plot the resulting streamlines in Fig. 2.18. We can calculate the radius of the cylinder analytically by considering the dividing streamline. The stagnation point occurs along the x axis ($\theta = \pi$) when the freestream velocity cancels the radial velocity produced from the doublet (see Eq. 2.95 with $\theta = \pi$ and an additional negative sign because the positive radial direction to the left of the doublet is in the negative x direction):

$$V_\infty - \frac{\kappa}{2\pi R^2} = 0. \tag{2.110}$$

Solving for R gives the radius of the produced cylinder:

$$R = \sqrt{\frac{\kappa}{2\pi V_\infty}}. \tag{2.111}$$

We can adjust κ to create any desired radius. In our case the radius is 1 m.

We can now, for example, compute the velocity along the surface of the cylinder where $r = R$. We will do this in cylindrical coordinates so we need to rotate our uniform flow as shown in Fig. 2.19.

$$V_\infty \hat{x} = V_\infty \cos\theta \hat{r} - V_\infty \sin\theta \hat{\theta}. \tag{2.112}$$

We now add the velocities from the doublet at $r = R$, recalling from Eq. 2.111 that $\kappa = 2\pi V_\infty R^2$. First, the radial velocity (see Eq. 2.95) equals zero:

$$V_r = V_\infty \cos\theta - \frac{\kappa \cos(\theta)}{2\pi R^2} \tag{2.113}$$

$$= V_\infty \cos\theta - \frac{(2\pi V_\infty R^2)\cos(\theta)}{2\pi R^2} \tag{2.114}$$

$$= 0. \tag{2.115}$$

This is expected because this was our dividing streamline and so satisfies the flow tangency boundary condition around the cylinder body.

The tangential velocity is:

$$V_\theta = -V_\infty \sin\theta - \frac{\kappa \sin(\theta)}{2\pi R^2} \tag{2.116}$$

$$= -V_\infty \sin\theta - \frac{(2\pi V_\infty R^2)\sin(\theta)}{2\pi R^2} \tag{2.117}$$

$$= -2V_\infty \sin\theta. \tag{2.118}$$

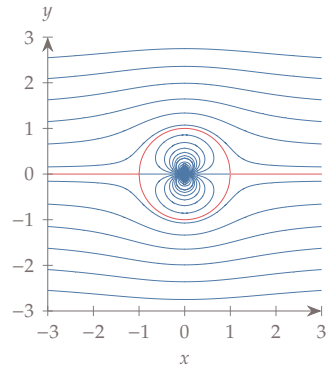

Fig. 2.18 Streamlines around a cylinder, created by uniform flow plus a doublet.

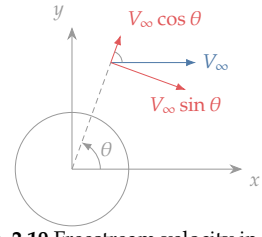

Fig. 2.19 Freestream velocity in cylindrical coordinates.

We plot this as a function of x/R where $x = \cos\theta$ so $x/R = -1$ corresponds to the front of the cylinder, and $x = 1$ to the back. The magnitude of the tangential velocity is plotted in Fig. 2.20 We see that after stagnation at the leading edge of the cylinder, we reach a maximum velocity of twice the freestream at the top of the cylinder, after which we slow down and stagnate at the back end. Recall that this is potential flow, and in real flow a blunt body would separate far earlier and thus not reach stagnation on the trailing end.

The corresponding pressure coefficient we compute using Eq. 2.28 and the result is shown in Fig. 2.21.

$$C_p = 1 - 4\sin^2\theta. \tag{2.119}$$

Note that the pressure coefficient is 1 at the stagnation points as expected.

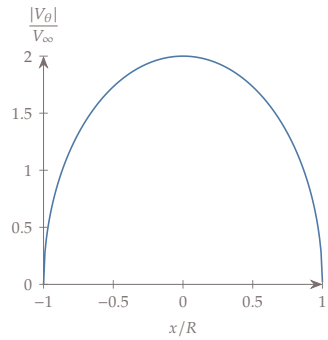

Fig. 2.20 Tangential velocity along the cylinder surface.

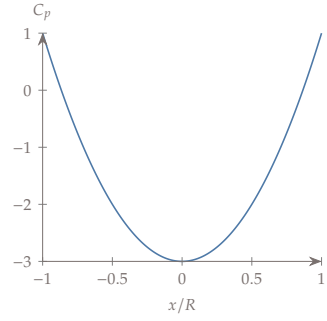

Fig. 2.21 Pressure coefficient along the cylinder surface.

In all of our prior examples the flow fields were symmetric left to right and top to bottom. In the next case we will find that the flow field is no longer symmetric top to bottom, and that a net vertical force is produced. This is accomplished by adding vortices, which are associated with lift generation. This connection will be discussed further in a subsequent section, but for now we just explore an example.

Example 2.4 Lifting cylinder.

We continue with the prior example of a cylinder (source plus doublet), but now add a vortex at the center of the cylinder. We try three different vortex strengths and visualize the effect on the flow field: $\Gamma = -2, -5, -8$ m^2/s Figs. 2.22 to 2.24. We use negative values of circulation because the positive direction of θ, as defined from conventional polar coordinates, results in a negative lift assuming a freestream from left to right as is commonly used. Notice that as the vortex strength increases the stagnation points move towards the bottom of the cylinder, and eventually the stagnation points move off the body ($\Gamma = -8$).

For the first case, $\Gamma = -2$ we plot the pressure coefficient. We previously computed the tangential velocity as Eq. 2.118, to which we add the velocity from the vortex Eq. 2.71 using our particular cylinder radius from Eq. 2.111:

$$V_\theta = -2V_\infty \sin\theta + \frac{\Gamma}{2\pi R} \tag{2.120}$$

$$= -2V_\infty \sin\theta + \frac{\Gamma}{2\pi}\sqrt{\frac{2\pi V_\infty}{\kappa}} \tag{2.121}$$

$$= -2V_\infty \sin\theta + \Gamma\sqrt{\frac{V_\infty}{2\pi\kappa}}. \tag{2.122}$$

The pressure coefficient (Eq. 2.28) is then:

$$C_p = 1 - \left(-2\sin\theta + \frac{\Gamma}{\sqrt{2\pi V_\infty \kappa}}\right)^2. \tag{2.123}$$

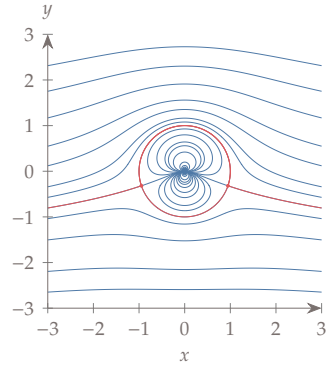

Fig. 2.22 Streamlines around a lifting cylinder for $\Gamma = -2$ m^2/s.

and is plotted in Fig. 2.25.

We notice two things from this figure. First, we see that there are two curves. In all our previous cases, the pressure coefficient was symmetric top to bottom so there was only one curve (i.e., there was no net vertical force). Second, we notice that the y-axis plots $-C_p$ rather than C_p. This is common practice in aerodynamics. This is because for lifting bodies the upper surface will have more negative pressure coefficients, and so it is visually convenient to make the upper plot correspond to the upper surface and vice-versa. The separation between the two plots indicates higher pressures below and lower pressures above, thus a net vertical force. In this case, because the angle of attack is zero, that net vertical force is precisely the lift.

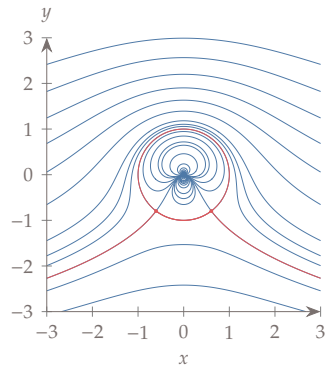

Fig. 2.23 Streamlines around a lifting cylinder for $\Gamma = -5$ m^2/s.

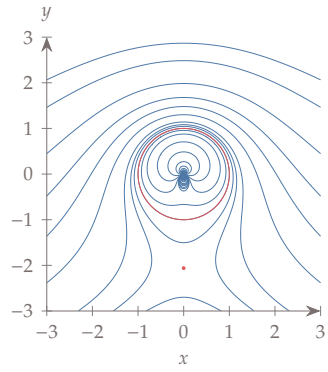

Fig. 2.24 Streamlines around a lifting cylinder for $\Gamma = -8$ m^2/s.

In the prior examples all of our singularities resided inside the body. This is convenient as we avoid issues of evaluating near singularities for the exterior flow field of interest. More often, as we'll see in subsequent sections, we place singularities on the body. Another usage of singularities is to simulate wakes. In this case the singularities are not fixed in location, but rather convect with the flow field. We'll see a couple examples of that type of usage next.

Example 2.5 Ground effect.

In Chapter 4 we will see that a lifting wing produces a pair of counter-rotating vortices in its wake as depicted in Fig. 2.26. As a first approximation, we can represent the wake vortices as two point vortices of equal strength as shown in Fig. 2.27. If these are the only features in the flow field, then the right vortex induces a downward velocity on the left vortex, and similarly the left vortex induces a downward velocity on the right vortex. So, the vortex pair descends downward forever (a real vortex pair does descend but also undergoes viscous decay).

In this example, we are interested in observing the behavior of this wake when interacting with flat ground. The behavior of a lifting body near the ground is called *ground effect*. A common trick in potential flow to simulate flat ground is to use the *method of images*. If we take any of the 2D singularities we've discussed, and mirror them over the ground plane, then we will automatically satisfy the inviscid boundary condition of flat ground (no-flow-through or flow tangency). Mirroring involves duplicating the singularity on the opposite side of the ground, the same distance away from the ground. Sources/sinks maintain their sign, but vortices flip their sign (e.g., like a mirror, or imagine folding a piece of paper over the "ground" line). This technique also works in three dimensions.

An example is shown in **??** for a source and for a vortex, where the normal components of velocity cancel at any location on the ground because of symmetry. So in this case, we mirror our two vortices as shown in Fig. 2.28 and thus simulate four vortices instead of two.

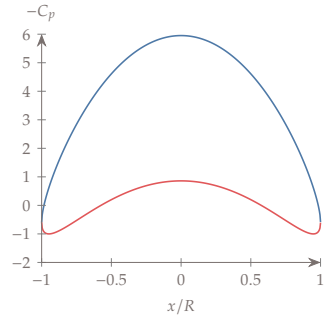

Fig. 2.25 Pressure coefficient for a lifting cylinder.

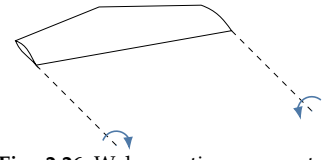

Fig. 2.26 Wake vortices generated from a lifting wing.

One way to explore ground effect is to consider a frame of reference moving with the airplane, and so our wake vortex pair, and its mirrored pair, are fixed. From Fig. 2.29 we see that the net impact of the mirrored vortex on the wing is an upward force. This effective rising air, reduces the amount of lift the airplane must create on its own, and as we will find in Chapter 4, this means that the airplane will have less drag. This is the main benefit of ground effect and is why some migrating birds fly close to ground/sea and why some transport aircraft concepts have been proposed to take advantage of this behavior.

For our purposes, we are interested in the wake behavior, in other words, a ground-fixed frame that observes the wake vortex in its descent. The presence of the ground will modify the wake trajectory from its normal straight downward path. The states that fully define our wake are the x, y positions of all of the vortices:

$$s = \begin{bmatrix} x_1 \\ y_1 \\ \vdots \\ x_4 \\ y_4 \end{bmatrix}. \tag{2.124}$$

We also know the state rates (i.e., velocities) imposed on each vortex in the x and y directions:

$$\dot{s} = \begin{bmatrix} u_1 \\ v_1 \\ \vdots \\ u_4 \\ v_4 \end{bmatrix}. \tag{2.125}$$

The velocities are functions of the states:

$$\dot{s} = f(s), \tag{2.126}$$

which is the equation of a first-order ordinary differential equation (ODE).

Let us now more clearly define that function f. We previously derived the velocity magnitude induced by a vortex in Eq. 2.71, but now need to be more careful about defining a vector relationship so we can get the directions correct in a numerical implementation. Consider some arbitrary vortex located at position (x_0, y_0) and we with to evaluate the velocity induced at some other arbitrary position (x, y).

First, we define the vector r as the distance from the vortex center to the evaluation point:

$$\vec{r} = (x - x_0)\hat{x} + (y - y_0)\hat{y}. \tag{2.127}$$

The direction of positive circulation is given by the right-hand rule: we curl our fingers in the way the induced velocity field curls, and our thumb points in the direction of positive circulation. From Fig. 2.30, this means that our circulation is in the positive z direction: $\vec{\Gamma} = \Gamma\hat{z}$.

Using the right-hand rule we can see then that $\vec{\Gamma} \times \hat{r}$ points in the direction of our induced velocity. Notice that we normalized r so that the magnitude of

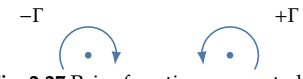

Fig. 2.27 Pair of vortices generated by a lifting wing.

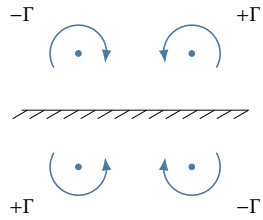

Fig. 2.28 A wing in ground effect simulated by a set of mirror vortices.

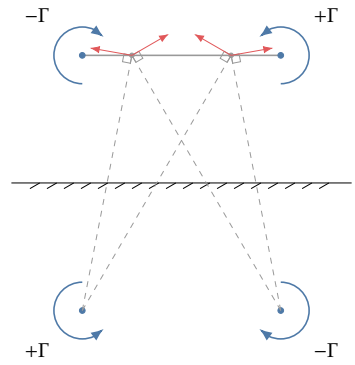

Fig. 2.29 Effective upwash on wing due to ground effect.

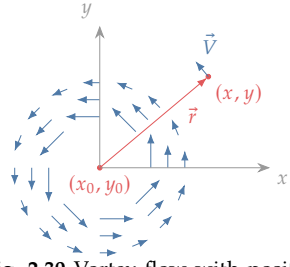

Fig. 2.30 Vortex flow with positive circulation strength. Circulation is $\vec{\Gamma} = \Gamma\hat{z}$

V_θ is unchanged. Thus, we can reexpress the tangential velocity induced by a vortex (Eq. 2.71) as:

$$\vec{V} = \frac{\vec{\Gamma} \times \hat{r}}{2\pi r} = \frac{\vec{\Gamma} \times \vec{r}}{2\pi r^2}. \tag{2.128}$$

Since we know the strengths of each vortex, and their positions at some given instant in time, we can compute the velocity induced at vortex i. The velocity induced at vortex i from some other vortex j is:

$$\vec{V}_{ij} = \frac{\vec{\Gamma}_j \times \vec{r}_{ij}}{2\pi r_{ij}^2}, \tag{2.129}$$

where $\vec{r}_{ij} = (x_i - x_j)\hat{x} + (y_i - y_j)\hat{y}$. The total velocity induced at vortex i from all other vortices is then:

$$\vec{V}_i = \sum_{\substack{j=1 \\ j \neq i}}^{4} \vec{V}_{ij}. \tag{2.130}$$

Notice that we omit the contribution of a vortex on itself (as it is zero, but if we tried to evaluate it we would get a singularity).

We have now fully defined the ODE and can use any standard ODE solver to obtain the trajectory of a pair of vortices in ground effect.

Example 2.6 Ground effect - Numerical problem

A pair of vortices of equal and opposite strength $\Gamma = 4.0\ \text{m}^2/\text{s}$ are 3.0 m apart and at a height of 1.0 m from the ground as shown in Fig. 2.31. Find the distance between the vortex pair and height from ground after 20 s.

We start by setting the initial coordinates for the vortex pair at $(1.5, 1.0)$ and $(-1.5, 1.0)$. This ensures the vortices are separated at a distance of 3.0 m. If the ground is at $y = 0.0$, then the corresponding mirrored vortices that represent the ground will be at $(1.5, -1.0)$ and $(-1.5, -1.0)$ respectively. This setup is depicted in Fig. 2.32.

We shall use a basic time-marching approach to simulate the motion of these vortices. Using Eq. 2.130, we may find the induced velocity by all vortices on each of the vortices in the domain. For a small enough timestep, say one-tenth of a second, the local velocity can then be used to update the position of each vortex (i.e., the states) at every timestep of the simulation using

$$\vec{r}_{i+1} = \vec{r}_i + \vec{V}_i \, \Delta t, \tag{2.131}$$

where the subscript i and $i + 1$ denote the current timestep and the next one. This approach is known as Euler's method and is an approximation because the velocity vector $\vec{V}$ changes continuously and does not follow straight lines during time intervals.

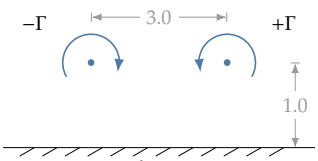

Fig. 2.31 Pair of vortices in ground effect.

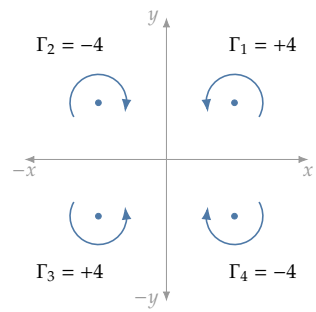

Fig. 2.32 Setup of the ground effect simulation.

At the initial timestep, the induced velocities by each vortex on the upper right vortex at (1.5, 1.0) are given in Table 2.1 in the form (V_x, V_y), where $\vec{V} = V_x\hat{x} + V_y\hat{y}$.

Vortex location	Velocity induced
$(-1.5, +1.0)$	$(0.0, -0.212)$
$(-1.5, -1.0)$	$(-0.098, 0.147)$
$(-1.5, -1.0)$	$(0.318, 0.0)$

Table 2.1 Velocity induced on vortex located at (1.5, 1.0).

After time-marching the differential equation for 20 s, the locations of the actual vortices will be at $(8.474, 0.834)$ and $(-8.474, 0.834)$. Hence, the separation distance after 20 s is 16.95 m and height from ground is 0.834 m. Fig. 2.33 depicts the trajectory of the pair of vortices in ground effect over a duration of 20 s. The convergence of the solution should be verified by decreasing the timestep (and a time step is too large will cause numerical instability). This is especially relevant when using non-adaptive low-accuracy methods like the first-order Euler scheme described here.

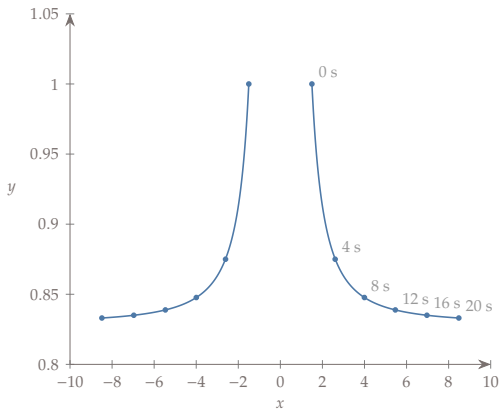

Fig. 2.33 Trajectory of a vortex pair in ground effect.

The method of images is a technique that can be used generally, even in three-dimensions. However, the computational cost can be fairly high as it doubles the number of singularities and this is an n-body problem (the number of interactions between the singularities scales as n^2). The last example of this section, uses the same methodology as the ground effect example, but in this scenario there is no solid body at all. We simply use vortices to represent a flow field.

Example 2.7 Leapfrogging vortices

Vortex rings are fun to look at, but also have practical significance. They

can propel themselves quite far when moving through a quiescent fluid. There are various interesting videos of vortex rings* including those formed by a volcano, dolphins, plates in a pool, helicopters, etc. If you picture a toroidal vortex intersecting a 2D plane you will have two vortices (like the left pair shown in Fig. 2.34). From our understanding of vortices we can see how it is self-propelling. Consider the left pair of vortices (e.g., one ring vortex). The top vortex induces a velocity on the bottom vortex towards the right. Simultaneously, the top vortex induces a velocity on the top vortex to the right. Thus, it pushes itself forward.

*https://youtu.be/Sj9irzI-Pzw?si=0yIgv_--8VoR9PMP

With two vortices next to each other, things become even more interesting. The leapfrogging vortex behavior has been demonstrated experimentally as well as in various simulations.† It is also of practical interest in the wakes of propellers. A propeller wake is not a set of perfect vortex rings, but it is fairly close and similar leapfrogging behavior is observed.

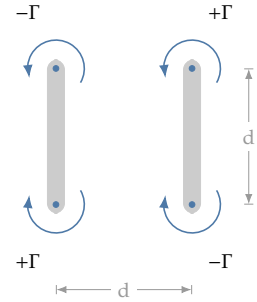

Fig. 2.34 Leapfrogging vortices.

Let's model the trajectory for vortices of circulation strength $\Gamma = 2.0\ \mathrm{m}^2/\mathrm{s}$, placed at a distance $d = 1.5$ m from each other. We'll simulate the trajectory for a time span of 20 s and use a timestep $\Delta t = 0.002$ s. The vortices are placed in the four quadrants and numbered as shown in Fig. 2.35. The following tables show the values of position and velocity as 2D vectors, of the form (x, y), at the first two timesteps for reference (again using a forward Euler method). They may be used to prescribe the initial coordinates and to verify intermediate results.

†https://youtu.be/SPBMEXX5xBI?si=TZqrCHSU4nO-d4gt

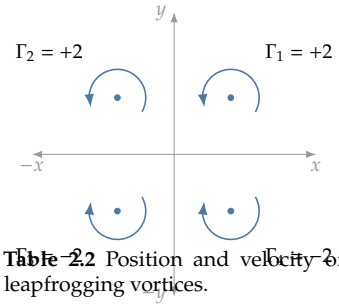

Fig. 2.35 Setup of the leapfrogging vortices simulation.

Timestep	P1	P2	P3	P4
0^{th}	$(0.750, 0.750)$	$(-0.750, 0.750)$	$(-0.750, -0.750)$	$(0.750, -0.750)$
1^{st}	$(0.751, 0.750)$	$(-0.749, 0.749)$	$(-0.749, -0.749)$	$(0.751, -0.750)$
Timestep	V1	V2	V3	V4
0^{th}	$(0, 0)$	$(0, 0)$	$(0, 0)$	$(0, 0)$
1^{st}	$(0.318, 0.106)$	$(0.318, -0.106)$	$(0.318, 0.106)$	$(0.318, -0.106)$

Table 2.2 Position and velocity of leapfrogging vortices.

Figure 2.36 shows the trajectory after 20 s of simulation time. As in the previous example, we use only a first-order method and so the step size of our simulation has to be kept small enough to avoid instability. The leapfrogging behavior is even clearer if you generate an animation.

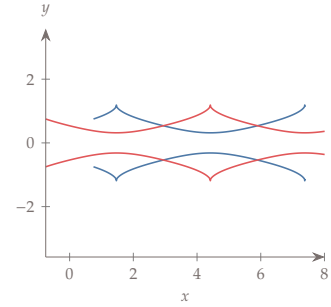

Fig. 2.36 Trajectory of leapfrogging vortices.

2.6 Lift

In Ex. 2.4 we found that adding a vortex to a cylinder lead to lift production. Vortices are intrinsically related to lift. In that previous example we computed the lift through numerical integration, but in this section we will discuss an alternate relationship applicable for potential flow. We also noted from that example that we could change

the vortex strength to anything we wanted and still have flow around a cylinder, each with a different lift. This highlights a nonuniqueness problem that we will need to address, i.e., which solution is correct for given input conditions?

We start by considering an arbitrary control volume and arbitrary 2D lifting body as shown in Fig. 2.37. We align the x-axis with the freestream velocity and thus write the velocity generically at any point, in Cartesian coordinates, as:

$$\vec{V} = (V_\infty + u, v, w)\,. \tag{2.132}$$

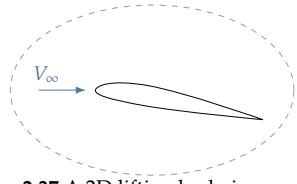

Fig. 2.37 A 2D lifting body in an arbitrary control volume.

We apply a momentum balance to this control volume (similar to Eq. 1.175) with the assumptions of steady flow and no shear stresses (which we have already assumed with potential flow).

$$\int_A \rho\vec{V}\left(\vec{V}\cdot\hat{n}\right)dA = -\int_A p\hat{n}dA - \vec{F}. \tag{2.133}$$

We rearrange to solve for $\vec{F}$, the force the fluid exerts on the body:

$$\vec{F} = -\int_A \left(\rho\vec{V}\left(\vec{V}\cdot\hat{n}\right) + p\hat{n}\right)dA. \tag{2.134}$$

We will apply the divergence theorem to the integral, and in this case it will be clearer in index notation, so we repeat the divergence theorem in index notation (Eq. 1.74):

$$\int_A u_j dA_j = \int_{\forall} \frac{\partial u_j}{\partial x_j} d\forall. \tag{2.135}$$

The force equation is transformed as:

$$F_i = -\int_A \rho u_i u_j dA_j - \int_A p dA_i \tag{2.136}$$

$$= -\int_{\forall} \frac{\partial \rho u_i u_j}{\partial x_j} d\forall - \int_{\forall} \frac{\partial p}{\partial x_i} d\forall \tag{2.137}$$

$$= -\int_{\forall} \left(\rho u_i \frac{\partial u_j}{\partial x_j} + \rho u_j \frac{\partial u_i}{\partial x_j} + \frac{\partial p}{\partial x_i}\right) d\forall. \tag{2.138}$$

Or back in vector notation as:

$$\vec{F} = -\int_{\forall} \left(\rho\vec{V}(\nabla\cdot\vec{V}) + \rho(\vec{V}\cdot\nabla)\vec{V} + \nabla p\right) d\forall. \tag{2.139}$$

The first term is zero for incompressible flow ($\nabla\cdot\vec{V} = 0$), leaving:

$$\vec{F} = -\int_{\forall} \left(\rho(\vec{V}\cdot\nabla)\vec{V} + \nabla p\right) d\forall. \tag{2.140}$$

We now make use of the vector identity (Eq. 1.64) repeated here in terms of velocity:

$$\frac{1}{2}\nabla(V^2) = (\vec{V}\cdot\nabla)\vec{V} + \vec{V}\times\omega. \tag{2.141}$$

We are left with:

$$\vec{F} = -\int_{\not{V}}\left(\frac{1}{2}\rho\nabla(V^2) - \rho\vec{V}\times\vec{\omega} + \nabla p\right)d\not{V} \tag{2.142}$$

$$= -\int_{\not{V}}\nabla\left(\frac{1}{2}\rho V^2 + p\right)d\not{V} + \int_{\not{V}}\rho\vec{V}\times\vec{\omega}d\not{V}. \tag{2.143}$$

The first term is zero for potential flow as we showed in Eq. 2.23 so we are left with:*

$$\vec{F} = \int_{\not{V}}\rho\vec{V}\times\vec{\omega}d\not{V}. \tag{2.144}$$

*The Lamb vector, $\vec{l} = \vec{\omega}\times\vec{V}$, shows up in various places in fluid mechanics, one of which is its associated with a far-field force as seen here.

If restrict ourselves to two-dimensions then the only nonzero component of vorticity is in the z direction (out of the page): $\vec{\omega} = (0, 0, \omega_z)$. Using the velocity definition (Eq. 2.132) we can then express the force as:

$$\vec{F} = \int_A (\rho v\omega_x\hat{x} - \rho(V_\infty + u)\omega_z\hat{y})\,dA. \tag{2.145}$$

Note that we rewrote the volume integral as an area integral (over the interior, not the boundary) since we restricted to two-dimensions. Since we have aligned our axes with the freestream, the y and x components of the force corrrespond to lift and drag forces respectively (per unit depth):

$$L' = -\rho V_\infty\int_A \omega_z dA - \rho\int_A u\omega_z dA \tag{2.146}$$

$$D' = \rho\int_A v\omega_z dA. \tag{2.147}$$

The first integral is precisely the definition of circulation (Eq. 2.77).

$$L' = -\rho V_\infty\Gamma - \rho\int_A u\omega_z dA \tag{2.148}$$

$$D' = \rho\int_A v\omega_z dA. \tag{2.149}$$

The remaining integrals are challenging as they require integration over the entire domain. We would like to use the divergence theorem to change them to integrals over just the boundary. To do so we need

to manipulate the terms to involve differentials. Let's expand the first integrand:

$$u\omega_z = u(\nabla \times \vec{V})_z \tag{2.150}$$
$$= u\left(\frac{\partial v}{\partial x} - \frac{\partial u}{\partial y}\right) \tag{2.151}$$
$$= u\left(\frac{\partial v}{\partial x} - \frac{\partial u}{\partial y}\right) + v(\nabla \cdot \vec{V}). \tag{2.152}$$

We were able to add that last term since the divergence of the velocity is zero. This addition will be helpful in consolidating our terms into differentials.

$$u\omega_z = u\left(\frac{\partial v}{\partial x} - \frac{\partial u}{\partial y}\right) + v\left(\frac{\partial u}{\partial x} + \frac{\partial v}{\partial y}\right) \tag{2.153}$$
$$= u\frac{\partial v}{\partial x} + v\frac{\partial u}{\partial x} - \left(u\frac{\partial u}{\partial y} - v\frac{\partial v}{\partial y}\right) \tag{2.154}$$
$$= \frac{\partial}{\partial x}(uv) - \frac{1}{2}\frac{\partial}{\partial y}(u^2 - v^2). \tag{2.155}$$

If we define the following vector:

$$\vec{U}_L = \left(uv, -\frac{1}{2}(u^2 - v^2), 0\right), \tag{2.156}$$

then we can reexpress the above term as a divergence:

$$u\omega_z = \nabla \cdot \vec{U}_L. \tag{2.157}$$

We similarly expand the drag term:

$$v\omega_z = v\left(\frac{\partial v}{\partial x} - \frac{\partial u}{\partial y}\right) \tag{2.158}$$
$$= v\left(\frac{\partial v}{\partial x} - \frac{\partial u}{\partial y}\right) - u\left(\frac{\partial u}{\partial x} + \frac{\partial v}{\partial y}\right) \tag{2.159}$$
$$= v\frac{\partial v}{\partial x} - u\frac{\partial u}{\partial x} - v\frac{\partial u}{\partial y} - u\frac{\partial v}{\partial y} \tag{2.160}$$
$$= \frac{1}{2}\frac{\partial}{\partial x}(v^2 - u^2) - \frac{\partial}{\partial y}(uv) \tag{2.161}$$
$$= \nabla \cdot \vec{U}_D, \tag{2.162}$$

where

$$\vec{U}_D = \left(\frac{1}{2}(v^2 - u^2), -uv, 0\right). \tag{2.163}$$

Plugging these back into our lift and drag equations and using the 2D divergence theorem gives:

$$L' = -\rho V_\infty \Gamma - \rho \int_A u\omega_z dA \tag{2.164}$$

$$= -\rho V_\infty \Gamma - \rho \int_A \nabla \cdot \vec{U}_L dA \tag{2.165}$$

$$= -\rho V_\infty \Gamma - \rho \oint \vec{U}_L \cdot \hat{n} ds. \tag{2.166}$$

Similarly,

$$D' = \rho \oint \vec{U}_D \cdot \hat{n} ds. \tag{2.167}$$

We now have transformed our lift and drag calculations so that the integrals are only along the boundary of the domain. All the terms in $\vec{U}_L$ and $\vec{U}_D$ involve products of u and v. Recall that we have already pulled out V_∞ in the velocity definition so u and v represents deviations from the freestream. While those deviations will be potentially large throughout the domain, at the boundary they will be much smaller (and their products will be smaller still). As we make the domain larger, which we are free to do without any changes in the above derivation, then those terms will go to zero leaving:

$$L' = -\rho V_\infty \Gamma \tag{2.168}$$

$$D' = 0. \tag{2.169}$$

First, we find that the drag in 2D potential flow is always zero. This is true even when the flow field is not symmetric fore and aft like the flow field in Fig. 2.38. When integrating pressures, i.e., using Eqs. 1.31 and 1.32, we won't get exactly zero drag, but this just numerical error and those results will asymptote towards zero as discretization error and other sources of numerical error are reduced. The prediction of zero drag for any body in potential flow is known as *D'Alembert's Paradox* and it historically led to some rifts in theoretical and empirical fluid mechanics. We will resolve sources of drag in future chapters as we discuss boundary layers, three-dimensional effects, and compressible flow.

Next, we observe that for positive lift (assuming inflow from the left), the circulation should be in the $-z$ direction as shown in Fig. 2.38. Conceptually we could think of the circulation as accelerating the incoming flow over the upper surface and decelerating it on the lower surface, consistent with the direction shown. Or perhaps we could

think of it as turning the flow downward towards the trailing edge, and thus generating lift as a reaction to the net downward moving air. Because we usually have positive lift, we typically define the positive

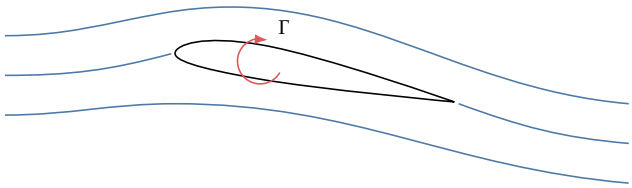

Fig. 2.38 Circulation around a lifting body.

direction for circulation in the $-z$ direction. Of course, any convention can be used as long as one is clear. Both conventions will be useful depending on the context.

With positive circulation defined in the $-z$ direction we rewrite the forces as:

$$L' = \rho V_\infty \Gamma \tag{2.170}$$

$$D' = 0. \tag{2.171}$$

Or, to be explicit on the directions we can write it in vector notation as:

$$\vec{L}' = \rho \vec{V}_\infty \times \vec{\Gamma}. \tag{2.172}$$

where we recall that a positive circulation is given by the right-hand rule (fingers curl in the direction of rotation and the thumb points in the direction of positive circulation). Notice that the force is by definition a lift force (and there is no drag), since the genereated force is perpendicular to the incoming velocity (Fig. 2.39).

This equation is called the *Kutta-Joukowski theorem* and is a well-used equation in aerodynamics. It provides a simple relationship between lift and circulation, and so for cases where circulation is easy to obtain it provides a useful and potentially more accurate alternative to numerical integration of pressures to obtain lift.

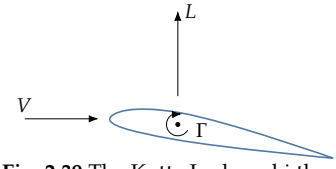

Fig. 2.39 The Kutta Joukowski theorem defines the direction of the lift force based on the incoming velocity and the circulation.

We still have a major problem with our lift calculation. From Ex. 2.4 you will recall that we could change the circulation of the vortex at the center of the cylinder and generate many solutions. For a given cylinder radius and freestream conditions, there are an infinite number of solutions. As we change the vortex strength, flow tangency and far-field freestream conditions are always satisfied, but the circulation and thus the lift does not have a unique solution.

This problem is general to any two-dimensional geometry, and also is not restricted to potential flow, but any inviscid and incompressible flow (whether rotational or irrotational). For example, the flow

fields in Fig. 2.40 both satisfy our governing equatioxns and boundary conditions.

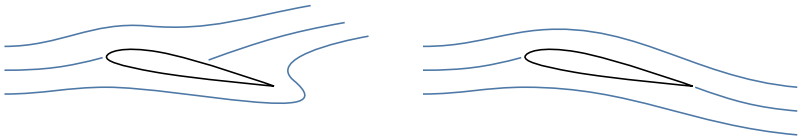

Fig. 2.40 Two different solutions to a potential flow field.

Historically, this problem has been addressed with the *Kutta condition*. Comparing the two velocity fields in Fig. 2.40, we would say that the left one is unphysical. A sharp turn in the flow around the sharp corner at the trailing edge, would require an infinitely large adverse pressure gradient. Even a tiny amount of viscosity would make such a rapid change impossible leading to flow separation. So, the argument is that the nonuniqueness is only resolved by viscosity and since we are using an inviscid model we need to create an ad hoc criterion (the Kutta condition) in order to impose a realistic flow field.

The Kutta condition is expressed in several ways. For a sharp trailing edge, we see that maintaining flow tangency on the upper and lower surfaces all the way to the trailing edge implies that the trailing edge must be a stagnation point (Fig. 2.41). For a blunt trailing edge we might instead impose that the tangential velocities are equal on the upper and lower surface at the trailing edge (normal velocities are zero by no-flow-through condition):

$$V_{tu} = V_{tl} \text{ at the trailing edge.} \tag{2.173}$$

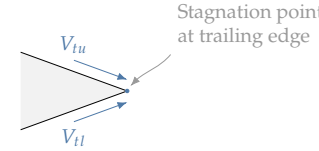

Fig. 2.41 The Kutta condition at a sharp trailing edge.

This condition tends to be used even for sharp trailing-edges as no airfoil is perfectly sharp. If the velocities are equal, then the pressures will be equal (see Bernoulli's equation for potential flow Eq. 2.24) and so there will be no flow around the trailing edge ensuring that it leaves the trailing edge smoothly like the right side of Fig. 2.40. Enforcing this criteria allows us to compute a unique value for the circulation and thus the lift.

There are various problems with this criterion however. It is really only defensible for a sharp trailing edge, and it is unclear what to do for a rounded trailing edge or more general geometries. It also is apparent that the criteria is unphysical for unsteady flows (where the velocity can and does wrap around the trailing edge at a given instant in time).

Recent work has resolved this nonuniqueness with a first-principles-based derivation rather than with ad hoc criterion.[5] Interestingly, the derivation shows that momentum conservation alone is sufficient to resolve the nonuniqueness, without any considerations of viscosity as

5. Gonzalez and Taha, *A variational theory of lift*, 2022.

has been commonly argued.

The derivation uses Gauss' principle of least constraint. We consider the fluid as a collection of particles with Newton's laws applied to each particle i:

$$m_i a_i = F_i + R_i. \tag{2.174}$$

The forces are split up into those that do work (F_i) and those that do not (R_i), which we also call constraints. Gauss' variational principle asserts an alternative statement of Newton's equations that nature minimizes the following quantity:

$$\min \sum_i \frac{1}{2} m_i \left(a_i - \frac{F_i}{m_i} \right)^2. \tag{2.175}$$

Note that only the forces that do work appear in this equation.

For inviscid problems, the governing equations are the Euler equations (Eq. 1.135 but with zero viscosity):

$$\rho \vec{a} = -\nabla p. \tag{2.176}$$

So we must first determine whether the pressure force does work or not. We integrate the work (actually rate of work) done by the pressure force over the volume:

$$W = \int \nabla p \cdot \vec{V} d\forall. \tag{2.177}$$

Next, we use the following vector calculus identity:

$$\nabla \cdot (\phi \vec{A}) = \phi (\nabla \cdot \vec{A}) + \nabla \phi \cdot \vec{A}. \tag{2.178}$$

to express the work as:

$$W = \int \nabla \cdot (p\vec{V}) - p(\nabla \cdot \vec{V}) d\forall. \tag{2.179}$$

If incompressible ($\nabla \cdot \vec{V} = 0$), then the second term disappears. The remaining term we transform with the divergence theorem (Eq. 1.60).

$$W = \int p\vec{V} \cdot d\hat{A}, \tag{2.180}$$

which is zero by the no-flow through condition (we assume the external domain is unbounded). So for an inviscid and incompressible flow, whether rotational or not, pressure does no work but simply is a constraint to satisfy continuity.

Then, if we neglect gravity, as appropriate for most aerodynamic applications, the F_i term is zero so Gauss' principle (Eq. 2.175) reduces to minimizing the following:

$$\min \sum_i \frac{1}{2} m_i a_i^2. \tag{2.181}$$

It turns out, that because total kinetic energy must also be conserved, that this expression is equivalent to minimizing total curvature.† In our continuum context, we replace the discrete mass with an integral, and write out the acceleration term (substantial derivative) from the momentum equation:

†Wikipedia, Hertz's principle of least curvature

$$\min \frac{1}{2}\rho \int \left(\frac{\partial u_i}{\partial t} + u_j \frac{\partial u_i}{\partial x_j} \right)^2 d\forall. \tag{2.182}$$

While the derivation is a bit obscure, the end result is intuitive. It means that of all the possible resulting flow fields around a body, the flow field will deviate in such a way to minimize curvature. This criterion reduces to the Kutta condition for a sharp trailing edge, but now generalizes to any geometry.

Fortunately, most aerodynamic bodies have reasonably sharp trailing edges, and relatively modest angles of attack, so the Kutta condition will work fine (for steady flows). In the remainder of the text we will use the simpler geometric Kutta condition, although for more general cases one would need to impose this minimization criteria instead.

2.7 Source and Vortex Distributions

We've seen that we can combine point sources, point vortices, and point doublets to produce some useful flow fields, but the types of geometries we can represent are rather limited. To obtain continuously varying shapes, like airfoils, we need continuous distributions. While sources and vortices can be distributed along arbitrary curves, in this section we consider only straight line segments. Note that doublets could also be distributed along lines, but for our purposes source and vortex distributions will suffice (doublets are heavily used in three dimensions). Distributed sources and vortices are analogous to distributed loads from statics (a force per unit length) in contrast to point forces.

We will start with sources, and use q to represent the source strength per unit length. We will distribute these sources along some general coordinate s, which follows a straight line but need not be aligned within our coordinate axes. See for example Fig. 2.42.

Fig. 2.42 Source distribution along a line segment.

Recall that a point source creates only radial velocity (Eq. 2.53) where Λ is the strength of the source and r is the radial distance from the center of the source:

$$V_r = \frac{\Lambda}{2\pi r}. \tag{2.183}$$

Since we will be dealing with multiple sources it will be more convenient to decompose the radial velocity into x and y components:

$$u = \frac{\Lambda \cos\theta}{2\pi r} \tag{2.184}$$

$$v = \frac{\Lambda \sin\theta}{2\pi r}. \tag{2.185}$$

To make things simpler for now, let us align our line segment with the x axis, and the start of the line segment (left side) will coincide with the origin. We now consider an infinitesimal point source at some arbitrary location s along this source distribution (Fig. 2.43). This infinitesimal point source has a strength $d\Lambda = q\,ds$. We are interested in computing the velocity it induces at some arbitrary location (x, y). We express all variables in Cartesian coordinates, using Fig. 2.43, $\cos\theta = (x-s)/r$, $\sin\theta = y/r$, and $r = \sqrt{(x-s)^2 + y^2}$:

$$du = \frac{q(x-s)}{2\pi[(x-s)^2 + y^2]} ds \tag{2.186}$$

$$dv = \frac{qy}{2\pi[(x-s)^2 + y^2]} ds. \tag{2.187}$$

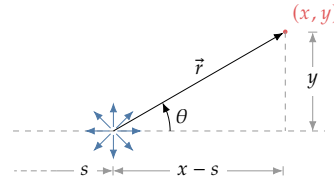

Fig. 2.43 Conversion from polar to cartesian coordinates in describing relative position of evaluation point and the source.

To compute the total velocity induced at point x, y, we need to integrate across all the infinitesimal sources along this distribution:

$$u_s(x,y) = \frac{1}{2\pi} \int q(s) \frac{x-s}{(x-s)^2 + y^2} ds \tag{2.188}$$

$$v_s(x,y) = \frac{1}{2\pi} \int q(s) \frac{y}{(x-s)^2 + y^2} ds. \tag{2.189}$$

Note that as we evaluate the velocity at points that cross the source sheet ($y \to 0$), the velocity u is continuous where v is not. This should match our physical intuition as we inspect the direction of the velocities induced by the sources.

We now repeat the process for vortices. Recall that the velocity induced by a vortex is (Eq. 2.71):

$$V_\theta = \frac{\Gamma}{2\pi r}. \tag{2.190}$$

where Γ is the point vortex strength. However, it will be convenient to reverse the direction of our vortex because this is the typical direction of

circulation for a lifting body (assuming inflow from the left as discussed around Fig. 2.38).

$$V_\theta = -\frac{\Gamma}{2\pi r}. \tag{2.191}$$

We again break the tangential velocity into x and y components:

$$u = \frac{\Gamma \sin\theta}{2\pi r} \tag{2.192}$$

$$v = -\frac{\Gamma \cos\theta}{2\pi r}. \tag{2.193}$$

Let us now consider a line vortex distribution with strength per unit length γ (Fig. 2.44). Note the direction of the vortices is consistent with the sign change we made earlier.

Fig. 2.44 Vortex distribution along a line segment.

The strength of an infinitesimal vortex is $d\Gamma = \gamma ds$, and again we integrate along the line distribution:

$$u_v(x,y) = \frac{1}{2\pi}\int \gamma(s)\frac{y}{(x-s)^2+y^2}ds \tag{2.194}$$

$$v_v(x,y) = -\frac{1}{2\pi}\int \gamma(s)\frac{x-s}{(x-s)^2+y^2}ds. \tag{2.195}$$

The velocities induced from the vortex distribution look similar to those from the source distribution but have some minor differences. Note that when crossing the vortex sheet ($y \to 0$) the velocity v is continuous whereas u is discontinuous. Again, this should make sense physically as you consider the flow field induced by vortices.

2.8 Airfoils

Having laid the basics of potential flow, we can now explore more complex geometries. In two-dimensions, the most common geometry of interest in aerodynamics is an airfoil, which forms the cross-sectional shape of wings and blades.

For subsonic conditions, an airfoil typically consists of a rounded nose that transitions into a tapered rear edge, as illustrated in Fig. 2.45. The *leading edge* is the forward most point, whereas the *trailing edge* is the aft most point. A straight line segment joining the leading edge to the trailing edge is called the *chord* of the airfoil. The chord serves as a fundamental reference length for airfoil geometry and is used in various aerodynamic normalizations. The local thickness is the distance between the upper and lower surfaces and the maximum thickness is simply referred to as the airfoil's *thickness*. An important parameter for an airfoil is its thickness-to-chord ratio, written as t/c. A typical t/c

for aircraft airfoils is between 6-14%. The inclination of the chord with respect to the freestream direction is called the angle of attack.

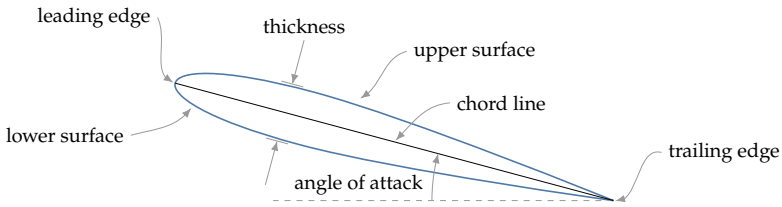

Fig. 2.45 Symmetric airfoil

While we will generally use the terms upper and lower surface, some applications prefer the terms suction and pressure surface (referring to the typically low pressure and high pressure side respectively). While the terms upper and lower have obvious meanings on most aircraft wings, it is a less apt description when discussing airfoils that rotate across many orientations like those on wind turbines or propeller blades, or when describing configurations like the spoiler of a racecar where the "upper" surface is on the bottom of the wing.

Some airfoils, like the one shown in Fig. 2.46, are unsymmetric between the top and bottom halves, and are called cambered airfoils. The curve that is exactly halfway between the upper and lower surfaces is called the *camber line*. The local camber is the distance between the chord line and the camber line. For a symmetric airfoil, the camber line coincides with the chord line.

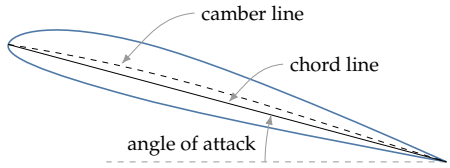

Fig. 2.46 Cambered airfoil

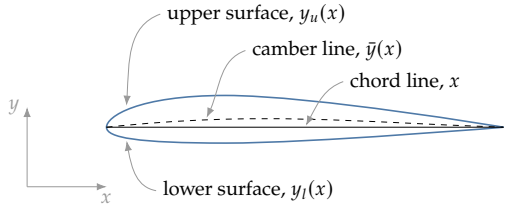

Fig. 2.47 Definitions of upper and lower surfaces, camber line, and the chord length c.

Airfoils are defined for unit chord (which of course can then be scaled to any desired size), and with the chord line aligned with the x axis. The airfoil geometry can then be defined by a function for the

upper surface $y_u(x)$ and the lower surface $y_l(x)$ where $0 < x < 1$. With that given shape we can compute the thickness distribution as shown in Fig. 2.47:

$$y_t(x) = y_u(x) - y_l(x)\,, \tag{2.196}$$

and the camber distribution:

$$y_c(x) = \frac{y_u(x) + y_l(x)}{2}\,. \tag{2.197}$$

If given thickness and camber we can solve for the outer shape by rearranging these equations:

$$y_u(x) = y_c(x) + \frac{1}{2}y_t(x) \tag{2.198}$$

$$y_l(x) = y_c(x) - \frac{1}{2}y_t(x)\,. \tag{2.199}$$

Sometimes when we refer to thickness or camber we mean the maximum thickness or camber, normalized by chord. Hence,

$$\text{thickness, } \frac{t}{c} = \frac{\max\left[y_t(x)\right]}{c} \tag{2.200}$$

$$\text{camber, } \frac{\bar{y}}{c} = \frac{\max y_c(x)}{c}\,. \tag{2.201}$$

It is important to clarify that some practitioners define the thickness distribution as normal to the camber line rather than normal to the chord line (see **??**). While either definition is perfectly valid, the normal-to-camber definition leads to some challenges in numerical computation. Going from a given camber and thickness distribution to the outer shape is straightforward in either approach (though a bit more challenging in the normal-to-camber definition since we need to recompute the normal direction at each x position).

However, the inverse problem is much more difficult in the normal-to-camber approach. Most airfoils are defined by a discrete set of points defining its outer shape. Because we then don't know the continuous shape ($y_u(x)$ and $y_l(x)$), we need to estimate it with a curve fit (more on this later). That estimate will drives out computation of the normal direction, which will likely not be consistent for the upper and lower surfaces, thus requiring some iteration. In other words, in the normal-to-camber definition, solving for the thickness distribution and the camber line requires knowing the normal directions, which in turn requires knowing the camber line, thus creating a circular dependency. This problem doesn't occur with the normal-to-chord definition since the normal direction is always $\hat{y}$.

Another challenge with the normal-to-camber definition occurs in design applications. As the thickness is varied, the location of the leading edge can change (see **??**). If the leading edge moves, then the chord length changes, which typically requires a rescaling of the whole airfoil to maintain unit chord. It also indirectly changes the angle of attack. Such global or indirect changes to the geometry, based on small localized perturbations at the nose, are undesirable in most optimization applications. Since our focus is numerical methods we prefer the normal-to-chord definition and will use that exclusively in this book.

To define an airfoil then we need to know $y_u(x)$ and $y_l(x)$, or equivalently $y_c(x)$ and $y_t(x)$. There are a few families of airfoils that define these distributions through continuous equations (we will discuss NACA airfoils next as one such example), but these are rare. More commonly, airfoils are defined discretely with $y_u(x)$ and $y_l(x)$ specified indirectly via a table of (x, y) points. Even though most of our methods are computational, and thus will require a discrete representation in the end, the coordinates provided for most airfoils are too coarse for reliable calculations and so we seek a continuous representation from which we can sample any desired level of discretization. Thus, we need to fit a provided set of coordinate points with a continuous function. One such approach will be discussed later in this section.

2.8.1 NACA airfoils

A well-known series of airfoils are the NACA four and five-digit airfoils. These were developed during the late 1920s by the National Advisory Committee for Aeronautics (NACA), which was the predecessor to NASA. These airfoils have a system of numerical designation to identify each airfoil's critical geometric properties.

The four-digit series airfoils are definxed using four digits where each digit represents the following:

1. First digit describes the maximum camber as a percentage of the chord.

2. Second digit describes the distance of maximum camber from the airfoil leading edge in tenths of the chord.

3. Last two digits describe the maximum thickness of the airfoil as a percent of the chord.

For example, the NACA 2412 airfoil has a maximum camber of 2% chord length, located at 40% chord from the leading edge with

a maximum thickness of 12% of the chord. A symmetric airfoil like NACA 0012 has two leading zeros to signify no camber.

The geometry of these airfoils are also described using simple expressions in terms of the chordwise distance from the leading edge. The thickness of four-series symmetric airfoils are given by the expression,

$$y_t(x) = 10\tau \left(0.2969\sqrt{x} - 0.1260x - 0.3516x^2 + 0.2843x^3 - 0.1015x^4\right), \tag{2.202}$$

where x is the position along the chord varying from 0 to 1 and where τ is the maximum thickness as a fraction of the chord and corresponds to the last two digits of the airfoil designation divided by 100. The maximum thickness of these airfoils occur at 30% of the chord from the leading edge. This expression produces an airfoil of finite thickness at the trailing edge. In some computational applications, including many in this chapter, a sharp trailing edge (zero-thickness) is desired. One way to obtain that is to change the third coefficient (0.3516) to 0.3537.

For cambered airfoils, in addition to the thickness expression, the following expression for the camber line is also necessary:

$$y_c(x) = \begin{cases} \dfrac{m}{p^2}\left(2px - x^2\right), & 0 \le x \le p \\ \dfrac{m}{(1-p)^2}\left(1 - 2p + 2px - x^2\right), & p \le x \le 1 \end{cases} . \tag{2.203}$$

Here, m is the maximum camber as a fraction of the chord, which is the first digit in the airfoil designation divided by 100. The parameter p is the location of maximum camber, which is the second digit in the designation divided by 10.

The NACA airfoil definition of thickness assumes the normal-to-camber definition, however as discussed previously, in this book will always use the normal-to-chord definition. This will introduce slight variations in the geometry as compared to the original definition.

While the NACA four-series are well known airfoils, and are still used in simpler geometries like stabilizers, they are rather limited and thus not generally useful for design. There most common usage is for verification, or initial testing of computation methods since the geometry has a simple definition. The NACA five-digit airfoils have similar definitions and are documented in several resources,[6] though are used even less frequently.

6. Abbott and Doenhoff, *Theory of Wing Sections*, 1959.

2.8.2 Airfoil Curve Fit: Class Shape Transformation Function

In the most common case, we don't have an equation to define the airfoil shape, but rather a set of discrete points. However, these points

are often too coarse for high-quality analysis or design. A simple linear interpolation might look ok, but that will not permit finer discretizations of the geometry, which are needed to obtain good convergence.

Instead, we need to fit the provided points with continuous and smooth functions, from which we can sample any desired discretization. Many such methods exist ranging from airfoil specific parameterizations to general approaches. One popular approach is the class shape transformation (CST) method also known as Kulfan parameterization.[7]

7. Kulfan, *Universal Parametric Geometry Representation Method*, 2008.

The CST method is designed specifically to create airfoil geometries. It begins with a class function, whose functional form is designed to create a round nose and a sharp trailing edge*:

$$C(x) = \sqrt{x}(1-x). \tag{2.204}$$

*Other class functions can be used, for example, rounded on both ends or sharp on both ends.

This class function is multiplied by a shape function, which can be any smooth function, but typically is a polynomial represented in the Bernstein basis.† A Bernstein polynomial of order n is given by:

$$\sum_{j=0}^{n} a_{n,j} x^j (1-x)^{n-j}, \tag{2.205}$$

†A general polynomial can be written as $\sum_j w_j f_j(x)$ where w_j are weights and f_j are polynomial basis functions. The familar power basis is $f_i(x) \in \{1, x, x^2, x^3, \ldots\}$. Bernstein polynomials are an alternative basis with nice geometric properties that form the bases of B-splines.

where $a_{n,j}$ are binomial coefficients:

$$a_{n,j} = \frac{n!}{j!(n-j)!}. \tag{2.206}$$

We add weights to these polynomials to form our shape function:

$$S(x) = \sum_{j=0}^{n} w_j a_{n,j} x^j (1-x)^{n-j}, \tag{2.207}$$

The final representation of the airfoil shape is given separately for the upper and lower surfaces as:

$$\hat{y}(x) = C(x)S(x) + \Delta y_{TE} x \tag{2.208}$$

$$= \sqrt{x}(1-x) \sum_{j=0}^{n} w_j a_{n,j} x^j (1-x)^{n-j} + \Delta y_{TE} x, \tag{2.209}$$

where Δy_{TE} is an offset to allow for a blunt trailing edge.

To fit a given set of points we solve a least squares problem (assuming we have more data points than weights, which should always be the case unless the airfoil discretization was *extremely* poor). We first need to choose how many weights we will use. Too few won't allow enough degrees of freedom to provide a good fit (underfitting), too many will

induce spurious oscillations (overfitting). Some testing is needed to determine an appropriate number, but a typical amount is around 4–8 per surface.

In constructing the fits we need to do each surface separately. Given data points (x_i, y_i) for $i = 1 \dots m$ (on the upper surface, for example) we solve the least squares problem:

$$\min_{w_u} \sum_{i=1}^{m} (\hat{y}(x_i; w_u) - y_i)^2, \tag{2.210}$$

where $\hat{y}$ is our function estimate shown in Eq. 2.209, and

$$w_u = [w_0, w_1, w_2, \dots, w_n]_u \tag{2.211}$$

are the weights for the upper surface with $n + 1$ as the number of weights we selected. We can rewrite this in vector format as:

$$\min_{w_u} \|A w_u - b\|_2^2, \tag{2.212}$$

with

$$A_{ij} = \sqrt{x_i}(1 - x_i) a_{n,j} x_i^j (1 - x_i)^{n-j}, \tag{2.213}$$

for $i = 1 \dots m$, $j = 0 \dots n$, and

$$b_i = y_i - \Delta y_{TE} x_i, \tag{2.214}$$

for $i = 1 \dots m$. This procedure is then repeated for the lower surface, which has its own set of weights. Once all the weights are computed we can construct the functions $y_u(x)$ and $y_l(x)$ using Eq. 2.209.

Example 2.8 Fitting airfoil coordinates with the CST method.

In this example we use the SG6043 wind turbine airfoil as tabulated in the UIUC Airfoil Database.[‡] First, we separate the data into upper and lower surfaces, and add the point $(0, 0)$ to both surfaces to form the leading edge. Let's also modify the last x coordinate 0.999999 to 1.0.[§]

[‡] https://m-selig.ae.illinois.edu/ads/coord/sg6043.dat

[§] It is common to need to do some data cleanup of airfoil coordinates (e.g., duplicated rows, a subset of rows that are reversed.)

The upper surface has the following coordinates:

$$\begin{aligned} x_u = [&0.0, 2.4 \times 10^{-5}, 0.001496, 0.005277, 0.011416, 0.019828, 0.030622, \\ &0.043757, 0.059198, 0.076936, 0.096866, 0.118895, 0.142926, 0.168817, \\ &0.196447, 0.225671, 0.25633, 0.288269, 0.321306, 0.355272, 0.389995, \\ &0.425276, 0.460955, 0.496847, 0.532761, 0.568537, 0.603962, 0.638892, \\ &0.673195, 0.706663, 0.739215, 0.770741, 0.801008, 0.829794, 0.856884, \\ &0.882072, 0.905161, 0.925966, 0.944288, 0.960071, 0.973434, 0.984387, \\ &0.992735, 0.998105, 1.0] \end{aligned} \tag{2.215}$$

$$y_u = [0.0, 0.000942, 0.00741, 0.014355, 0.021706, 0.029159, 0.03659, 0.043981, 0.05117, 0.058094, 0.06473, 0.070995, 0.076839, 0.082199, 0.087021, 0.091274, 0.094905, 0.09788, 0.100174, 0.101752, 0.102599, 0.10269, 0.10201, 0.100592, 0.098415, 0.095505, 0.091903, 0.087606, 0.082684, 0.077173, 0.071138, 0.064777, 0.05824, 0.051648, 0.045099, 0.038683, 0.032475, 0.026547, 0.020916, 0.015523, 0.010465, 0.006072, 0.002712, 0.000656, 0.0] \tag{2.216}$$

In this example we use 4 parameters per surface (so $n = 3$). Following the methodology of this section we get:

$$w_u = [0.209966, 0.281403, 0.275871, 0.383838]. \tag{2.217}$$

The methodology is the same for the lower surface. The coordinates are not written out for brevity, but are available at the previously noted website, and the resulting weights are:

$$w_l = [-0.091172, 0.069681, -0.033338, 0.203912]. \tag{2.218}$$

Figure 2.48 shows the fit for 4 parameters. Zooming in on small regions shows that there are some noticeable discrepancies, which are improved as we move up to 8 parameters.

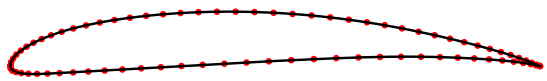

Fig. 2.48 CST fit for the SG6043 airfoil with 4 parameters.

The CST approach is just one of many possible approaches to curve fitting. It is not always the best approach for shape optimization, i.e., changing the shape while evaluating an aerodynamics or multiphysics model. B-splines, for example, provide some compelling advantages as they are more general. Every CST function is a Bézier curve (and thus can be represented as a B-spline), but the opposite is not true. Changing B-splines control points also provide a more intuitive mapping to the shape allowing for better bound constraints. B-splines also allow for localized changes, as opposed to only global, and permit knot insertion to maintain lower order splines but with high degree of control. That said, when optimizing for data fit rather than optimizing under a physics model, as we are doing in this section, CST is often an excellent choice. This is because the restrictive (as compared to B-splines), but always airfoil-like, nature of the design space becomes advantageous in

the presence of limited data (many airfoil data sets are disappointingly coarse, especially near the nose where curvature is high and small changes can be impactful).

2.8.3 Discrete Sampling of Airfoil Shape

With continuous functions defining our airfoil, $y_u(x)$ and $y_(x)$, we now need to choose the x points to sample at for a discrete representation of the airfoil. A simple approach is to uniformly sample between 0 and 1. However, this is generally not efficient. Typical airfoils change rapidly in y near the leading and trailing edge, with relatively little change near the middle. Thus, a more effective strategy is to non-uniformly space by clustering points towards the leading and trailing edges.

One widely-used approach is *cosine spacing*. We use the transformation

$$x = \frac{1}{2}(1 - \cos\theta) \tag{2.219}$$

where θ is uniformly sampled from 0 to π. The 1/2 just provides appropriate scaling so that x varies from 0 to 1.

Example 2.9 Discretizing an airfoil shape.

We use the SG6043 airfoil, fit with CST, from the prior example. Figure 2.49 compares linear versus cosine spacing with 20 pts per surface. Twenty points is too few for practical usage, but makes it easier to see the figure without zooming in. Notice how, for a given number of points, the nose and tail are much better resolved with cosine spacing.

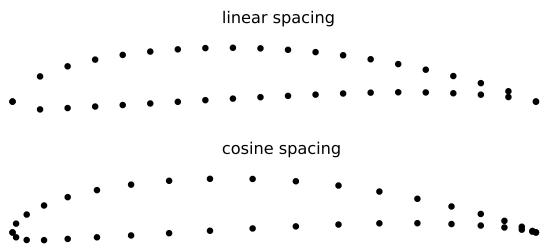

Fig. 2.49 Linear versus cosine spacing with 20 pts per side.

2.9 Thin Airfoil Theory

We are now ready to tackle the problem of flow around general shapes like an airfoil. As opposed to the initial examples where we just combined singularities and observed the resulting flow pattern, we are interested in the inverse: given a geometry what should be the strengths and positions of the singularities in order to create a flow field that satisfies flow tangency around the geometry?

Thin airfoil theory is the first method we will explore with this goal in mind. These are two main outcomes of thin airfoil theory: 1) numerical solutions for general shapes, and 2) some analytic relationships. The first outcome is no longer particularly useful. Thin airfoil theory requires some simplifying assumptions, and with modern computing capabilities, such assumptions are no longer needed for numerical solutions. The second outcome is widely useful as analytic relationships provide unique insight that is hard to extract from numerical solutions. We present both outcomes, as their derivations are intertwined, though one should pay more attention to the analytic relationships that result. We'll discuss better numerical methods in subsequent sections.

2.9.1 Boundary Conditions

In Section 2.7 we derived the velocities induced by source distributions and vortex distributions. To generate an airfoil we will combine freestream flow, with a source distribution $q(s)$along the chord line, and a vortex distribution $\gamma(s)$ along the chord line. We have already seen that vortices are necessary for lift, and previous examples have hinted that sources are particularly effective at creating thickness. Our aim is to solve for the distribution of $q(s)$ and $\gamma(s)$ to satisfy our boundary conditions.

The first boundary condition is that the induced velocity must go to zero in the farfield (so we are left with only freestream). This boundary condition is automatically satisfied by the choice of singularities (sources and vortices). The other boundary condition we need to satisfy is flow tangency. We require that the total velocity vector is tangent to the airfoil surface, or in other words that the normal component of velocity is zero (no flow-through condition). Mathematically we can say that the slope of the airfoil is related to the local velocity as (Fig. 2.50):

$$\frac{v}{u} = \frac{dy}{dx}. \tag{2.220}$$

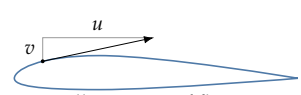

Fig. 2.50 Illustration of flow tangency condition.

Using the definitions for the airfoil shape in terms of camber and thickness (Eqs. 2.198 and 2.199) we can express the flow tangency

condition as:

$$\frac{v}{u} = \frac{d\bar{y}}{dx} \pm \frac{1}{2}\frac{dt}{dx}, \tag{2.221}$$

where the plus sign corresponds to the upper surface and negative to the lower surface.

We will subdivide our velocity into three terms associated with freestream, sources, and vortices.

$$u = V_\infty \cos\alpha + u_s + u_v \tag{2.222}$$

$$v = V_\infty \sin\alpha + v_s + v_v. \tag{2.223}$$

The resulting boundary condition is then:

$$\frac{V_\infty \sin\alpha + v_s + v_v}{V_\infty \cos\alpha + u_s + u_v} = \frac{d\bar{y}}{dx} \pm \frac{1}{2}\frac{dt}{dx}. \tag{2.224}$$

In order to solve this problem analytically three simplifications are made. All of these assumptions are based on small disturbances, or in other words assume that the airfoil is *thin*, and has a small angle of attack, thus the name *thin airfoil theory*. The first assumption is that α is small enough to where we can approximately $\sin\alpha \approx \alpha$ and $\cos\alpha \approx 1$. This assumption is actually not necessarily for the analytic solutions, but is conventionally done, simplifies the equations, and is consistent with the other assumptions and so it used here:

$$\frac{V_\infty \alpha + v_s + v_v}{V_\infty + u_s + u_v} = \frac{d\bar{y}}{dx} \pm \frac{1}{2}\frac{dt}{dx}. \tag{2.225}$$

The second assumption is that the x-components of the induced velocity are much smaller than the freestream velocity and so can be neglected *in the boundary condition*.

$$\frac{V_\infty \alpha + v_s + v_v}{V_\infty} = \frac{d\bar{y}}{dx} \pm \frac{1}{2}\frac{dt}{dx}. \tag{2.226}$$

The final simplification is to use the exact airfoil slope, but impose the boundary condition at $y = \pm 0$ rather than at the actual surface (y_u, y_l). The resulting boundary condition is then:

$$(v_s + v_v)_{y=\pm 0} = V_\infty \left(\frac{d\bar{y}}{dx} \pm \frac{1}{2}\frac{dt}{dx} - \alpha \right). \tag{2.227}$$

Because vortices are necessary for lift, and for an airfoil, camber and angle of attack result in lift generation, it makes sense to associate those terms with vortices. Furthermore, sources can be used to create

thickness. Thus, we separate this equation into two equations to satisfy separately (which can then be added by superposition):

$$v_s(y=0) = \pm V_\infty \frac{1}{2}\frac{dt}{dx} \tag{2.228}$$

$$v_v(y=0) = V_\infty \left(\frac{d\bar{y}}{dx} - \alpha\right). \tag{2.229}$$

2.9.2 Induced Velocities

Let's now work out the induced velocities from the sources and vortices. Previously, we derived the induced velocity for a line of sources (Eqs. 2.188 and 2.189), but now we need to evaluate the integrals as $y \to 0$. The first, we can evaluate directly, the second is less straightforward, so we'll leave in the form of a limit for now.

$$u_s(x, y=0) = \frac{1}{2\pi}\int_0^c \frac{q(s)}{(x-s)} ds \tag{2.230}$$

$$v_s(x, y\to 0^+) = \frac{1}{2\pi}\lim_{y\to 0^+}\int_0^c q(s)\frac{y}{(x-s)^2+y^2} ds. \tag{2.231}$$

The second integral is zero everywhere except when $x = s$. Thus, $q(s)$ becomes $q(x)$, an evaluation at a single point, and can come out of the integral. Additionally, because the function is zero everywhere else we can extend the limits of integration to $-\infty$ to ∞ without changing the solution

$$v_s(x, y\to 0^+) = \frac{q(x)}{2\pi}\int_{-\infty}^{\infty} \frac{y}{(x-s)^2+y^2} ds. \tag{2.232}$$

We divide the top and bottom of the integrand by y^2:

$$v_s(x, y\to 0^+) = \frac{q(x)}{2\pi}\int_{-\infty}^{\infty} \frac{1/y}{\left(\frac{x-s}{y}\right)^2+1} ds, \tag{2.233}$$

and introduce the change of variables $z = (x-s)/y$ and $ds = -y dz$:

$$v_s(x, y\to 0^+) = \frac{q(x)}{2\pi}\int_{\infty}^{-\infty} \frac{-1}{z^2+1} dz. \tag{2.234}$$

After switching the limits of integration:

$$v_s(x, y\to 0^+) = \frac{q(x)}{2\pi}\int_{-\infty}^{\infty} \frac{1}{z^2+1} dz, \tag{2.235}$$

the integrand has a known solution:

$$v_s(x, y \to 0^+) = \frac{q(x)}{2\pi}\left[\tan^{-1} z\right]_{-\infty}^{\infty}. \tag{2.236}$$

Finally, evaluating the integral gives:

$$v_s(x, y \to 0^+) = \frac{q(x)}{2}. \tag{2.237}$$

The solution is the same if we approach from $y \to 0^-$ except with a negative sign. Thus, we arrive at:

$$v_s(x, y \to \pm 0) = \pm\frac{q(x)}{2}. \tag{2.238}$$

The vortex line has the same types of integral but reversed in order for u and v:

$$u_v(x, y = 0) = \pm\frac{\gamma(x)}{2} \tag{2.239}$$

$$v_v(x, y = 0) = -\frac{1}{2\pi}\int_0^c \frac{\gamma(s)}{x - s} ds. \tag{2.240}$$

We can now plug these into the boundary conditions (Eqs. 2.228 and 2.229):

$$\pm\frac{q(x)}{2} = \pm V_\infty \frac{1}{2}\frac{dt}{dx} \tag{2.241}$$

$$-\frac{1}{2\pi}\int_0^c \frac{\gamma(s)}{x - s} ds = V_\infty\left(\frac{d\bar{y}}{dx} - \alpha\right). \tag{2.242}$$

The first equation shows that we can determine the source distribution simply from the known airfoil thickness distribution:

$$q(x) = V_\infty \frac{dt}{dx}. \tag{2.243}$$

In other words, for any symmetric airfoil at zero angle of attack, we directly generate the source distribution that will produce flow over its shape just by knowing the airfoil thickness distribution. The vortex distribution needed for a given angle of attack and camber distribution is not as simple, and requires solving an integral equation:

$$\frac{1}{2\pi}\int_0^c \frac{\gamma(s)}{x - s} ds = V_\infty\left(\alpha - \frac{d\bar{y}}{dx}\right). \tag{2.244}$$

2.9.3 Symmetric Airfoil

The integral equation is easiest to solve if the airfoil is symmetric. For a symmetric airfoil the camber is zero and so the integral equation simplifies to:

$$\int_0^c \frac{\gamma(s)}{x-s} ds = 2\pi V_\infty \alpha. \tag{2.245}$$

To solve this equation we will use a coordinate transformation. This is the same type of transformation used in cosine spacing (Eq. 2.219):

$$x = \frac{c}{2}(1-\cos\theta)\,, \quad \theta = 0\ldots\pi \tag{2.246}$$

$$s = \frac{c}{2}(1-\cos\phi) \tag{2.247}$$

$$ds = \frac{c}{2}\sin\phi d\phi. \tag{2.248}$$

With this transformation the integral becomes:

$$\int_0^\pi \frac{\gamma(\phi)\sin\phi}{\cos\phi-\cos\theta} d\phi = 2\pi V_\infty \alpha. \tag{2.249}$$

A useful integral that we will use again later when we discuss finite wing theory is:

$$\int_0^\pi \frac{\cos(n\phi)}{\cos\phi-\cos\theta} d\phi = \pi\frac{\sin(n\theta)}{\sin\theta}. \tag{2.250}$$

For convenience, we enumerate two solutions below. For $n = 0$:

$$\int_0^\pi \frac{1}{\cos\phi-\cos\theta} d\phi = 0, \tag{2.251}$$

and for $n = 1$,

$$\int_0^\pi \frac{\cos\phi}{\cos\phi-\cos\theta} d\phi = \pi. \tag{2.252}$$

Referring back to Eqs. 2.249 and 2.252 we see by inspection that

$$\gamma(\phi) = \frac{2V_\infty\alpha}{\tan\phi} \tag{2.253}$$

is a solution. However, referring to Eq. 2.251 we see that adding on a second term like that shown below is also a solution:

$$\gamma(\phi) = \frac{2V_\infty\alpha}{\tan\phi} + \frac{k}{\sin\phi}, \tag{2.254}$$

where k is an arbitrary constant. This last equation is the most general solution. However, it presents a problem. Since the equation is satisfied for any value of k that means that γ has an infinite number of solutions that satisfy the boundary conditions. As expected we are running into the nonuniqueness problem, and will use the simple sharp-trailing-edge Kutta condition to determine an appropriate value for k.

2.9.4 Kutta Condition

Referring back to Eq. 2.239 we see that the predicted velocity is discontinuous at the trailing edge (Fig. 2.51) unless $\gamma(c) = 0$. Note that this does not result in a stagnation point, as we need to add the thickness contribution. The thickness-induced tangential velocity (Eq. 2.230) is symmetric top and bottom, so this requirement means that the flow speed on upper and lower surfaces are equal at the trailing edge, which is the Kutta condition we discussed earlier (Eq. 2.173).

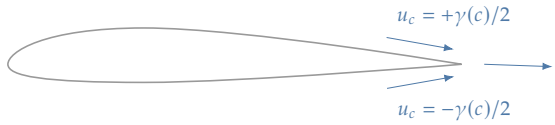

Fig. 2.51 A depiction of the Kutta condition and the discontinuous jump in u_c unless $\gamma(c) = 0$.

Using our coordinate transformation (Eq. 2.246) the Kutta condition is $\gamma(\pi) = 0$. Referring back to our equation for the vortex distribution:

$$\gamma(\phi) = \frac{2V_\infty \alpha}{\tan\phi} + \frac{k}{\sin\phi}, \tag{2.255}$$

we can see that at $\phi = \pi$ the circulation is infinite unless:

$$k = 2V_\infty \alpha. \tag{2.256}$$

Inserting this into the above equation yields:

$$\gamma(\phi) = \frac{2V_\infty \alpha}{\sin\phi}(1 + \cos\phi). \tag{2.257}$$

We can see that $\gamma(\pi) = 0$ by applying L'Hopital's rule. While this removes the infinite velocities at the trailing edge, there are still infinite velocities at the leading edge. This is just a consequence of the fact that at the leading edge the small disturbance assumption, on which thin airfoil theory is based, is clearly violated. Riegel's correction, a simple ad-hoc correction, can help alleviate the velocity spike (briefly discussed later).

While we did the derivation in a transformed coordinate system, we now wish to transform back to our original coordinate system. We can rearrange Eq. 2.246 as:

$$\cos\phi = 1 - \frac{2x}{c}. \tag{2.258}$$

Then with that definition, and the aid of Fig. 2.52, we can write an expression for $\sin\phi$ in terms of x (just using the Pythagorean theorem):

$$\sin\phi = 2\left[\frac{x}{c}\left(1 - \frac{x}{c}\right)\right]^{1/2}. \tag{2.259}$$

The resulting circulation distribution for a symmetric airfoil is then:

$$\gamma(x) = 2V_\infty \alpha \frac{\sqrt{1 - x/c}}{\sqrt{x/c}}. \tag{2.260}$$

2.9.5 Cambered Airfoil

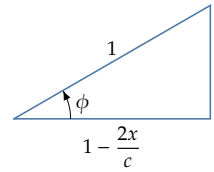

Fig. 2.52 Diagram to help transform from cosine coordinate system back to original coordinate system.

The cambered case is a bit more difficult, but we start with the same equation (Eq. 2.244), include camber this time, and apply the same coordinate transformation (Eq. 2.246):

$$\int_0^\pi \frac{\gamma(\phi)\sin\phi}{\cos\phi - \cos\theta} d\phi = 2\pi V_\infty(\alpha - b(\theta)), \tag{2.261}$$

where

$$b(\theta) = \frac{d\bar{y}}{dx}(x(\theta)). \tag{2.262}$$

We also need the Kutta condition:

$$\gamma(\pi) = 0. \tag{2.263}$$

To find a solution we use the same form we found from the symmetric solution (Eq. 2.257), but with additional terms using a Fourier sine series. We know that with enough terms in a Fourier series we can satisfy any solution. In order to ensure that the Kutta condition can be meet we chose a form of the equation that automatically satisfies it:

$$\gamma(\phi) = 2V_\infty \left[A_0 \frac{(1 + \cos\phi)}{\sin\phi} + \sum_n A_n \sin(n\phi) \right], \tag{2.264}$$

where A_i are Fourier coefficients. By plugging into our governing equation Eq. 2.261, and using the integral in Eq. 2.250, we can compute the coefficients from the known camber distribution as follows:

$$A_0 = \alpha - \frac{1}{\pi}\int_0^\pi b(\theta) d\theta \tag{2.265}$$

$$A_n = \frac{2}{\pi}\int_0^\pi b(\theta)\cos(n\theta) d\theta. \tag{2.266}$$

The evaluation process is then:

1. Get the camber line shape of the airfoil $\bar{y}$.
2. Differentiate to get $d\bar{y}/dx$.

3. Perform a variable substitution in terms of θ (Eq. 2.246).

4. Evaluate the above integrals to get the Fourier coefficients.

The Fourier series converges even if the camber line does not have a continuous slope (e.g., flaps and slats). Once we have the coefficients then we have a known solution for $\gamma(\phi)$ (Eq. 2.264).

2.9.6 Pressure

Again, numerical solution of thin airfoil theory is rarely used these days, but if desired, for a more accurate pressure distribution one should retain all of the terms in the velocity magnitude computation:

$$\begin{aligned} V^2 &= u^2 + v^2 \\ &= (V_\infty \cos\alpha + u_s + u_v)^2 + (V_\infty \sin\alpha + v_s + v_v)^2. \end{aligned} \tag{2.267}$$

Previously, we dropped some terms in the application of the boundary condition in order to have integrals we could solve analytically, but dropping terms is not necessary in this equation. The pressure coefficient can then be computed as normal for potential flow (Eq. 2.28).

As hinted at earlier, one problem with thin airfoil theory is that it leads to unrealistically large velocities near the leading edge because the small disturbance assumption is not justified there. One way to address this is to use Riegel's correction. The method is simple, the velocity is just multiplied by the cosine of the local airfoil slope angle β:

$$V_{mod} = V\cos\beta. \tag{2.268}$$

Note that at the leading edge where $\beta = 90°$ this correction allows for a stagnation point. In terms of our airfoil camber and thickness we can rewrite this equation as:

$$V_{mod} = V\frac{1}{\sqrt{1 + \left(\frac{d\bar{y}}{dx} \pm \frac{1}{2}\frac{dt}{dx}\right)^2}}. \tag{2.269}$$

This modified velocity is used in the pressure coefficient calculation:

$$C_p = 1 - \left(\frac{V_{mod}}{V_\infty}\right)^2. \tag{2.270}$$

A comparison of a pressure distribution with and without Riegel's correction is shown in Fig. 2.53. The correction not only appears more physical, but tends to compare much more favorably as compared to a panel code or experimental data.

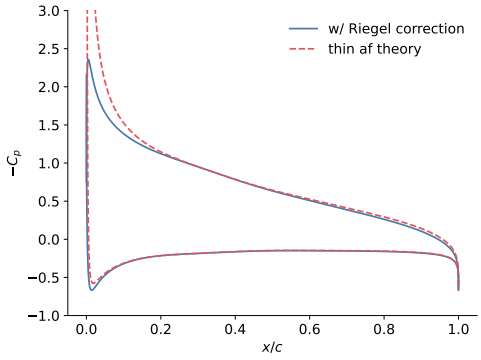

Fig. 2.53 Comparison to a pressure distribution with and without Riegel's correction.

2.9.7 Forces and Moments

With known pressures we can integrate along the surface to compute forces and moments as shown in Section 1.4. Or, in this case it is easier to use the Kutta-Joukowski theorem (Eq. 2.172). The total circulation is given by the integrating the vorticity:

$$\Gamma = \int_0^c \gamma(s) ds. \tag{2.271}$$

To perform the integral we use our coordinate transformation (Eq. 2.248):

$$\Gamma = \int_0^c \gamma(s) ds \tag{2.272}$$

$$= \frac{c}{2} \int_0^\pi \gamma(\phi) \sin\phi d\phi. \tag{2.273}$$

We then substitute the general solution for the vortex distribution (Eq. 2.264) into the integral:

$$\Gamma = \frac{c}{2} \int_0^\pi 2V_\infty \left[A_0 \frac{(1+\cos\phi)}{\sin\phi} + \sum_n A_n \sin(n\phi) \right] \sin\phi d\phi \tag{2.274}$$

$$= V_\infty c \left[A_0 \int_0^\pi (1+\cos\phi) d\phi + \sum_n A_n \int_0^\pi \sin\phi \sin(n\phi) d\phi \right] \tag{2.275}$$

$$= V_\infty c \left[A_0 \left(\phi + \sin\phi\right)_0^\pi + \sum_n A_n \int_0^\pi \sin\phi \sin(n\phi) d\phi \right] \tag{2.276}$$

$$= V_\infty c \left[A_0 \pi + \sum_n A_n \int_0^\pi \sin\phi \sin(n\phi) d\phi \right]. \tag{2.277}$$

From the orthogonality of the Fourier terms:

$$\int_0^\pi \sin(n\theta)\sin(m\theta) = 0 \text{ for } n \neq m, \tag{2.278}$$

we see that the last integral vanishes for every term in the Fourier series except $n = 1$.

$$\Gamma = V_\infty c \left[A_0 \pi + A_1 \int_0^\pi \sin^2 \phi d\phi \right] \tag{2.279}$$

$$= V_\infty c \left[A_0 \pi + A_1 \frac{\pi}{2} \right] \tag{2.280}$$

$$= V_\infty c \pi \left[A_0 + \frac{A_1}{2} \right]. \tag{2.281}$$

To get the lift we then use the Kutta-Joukowski theorem (Eq. 2.172):

$$L' = \rho V_\infty \Gamma \tag{2.282}$$

$$L' = \rho V_\infty^2 c \pi \left[A_0 + \frac{A_1}{2} \right] \tag{2.283}$$

We already know from the Kutta-Joukowski derivation that the drag is zero:

$$D' = 0, \tag{2.284}$$

though integrating the pressure distribution will lead to the same conclusion.

Let's analyze the equations in a bit more detail to see what insights the analytic expression can offer. As usual, we will want to nondimensionalize the lift:

$$c_l = \frac{L'}{\frac{1}{2}\rho V_\infty^2 c} = 2\pi \left(A_0 + \frac{A_1}{2} \right) \tag{2.285}$$

$$= 2\pi \left[\alpha - \frac{1}{\pi} \int_0^\pi b(\theta)(1 - \cos\theta) d\theta \right]. \tag{2.286}$$

If we compare this with the standard form for the lift curve prior to stall (Eq. 1.21),

$$c_l = m(\alpha - \alpha_0), \tag{2.287}$$

we notice the remarkable and useful result that no matter what shape the (thin) airfoil is *the theoretical lift curve slope is always* 2π. In other words:

$$m = 2\pi. \tag{2.288}$$

In practice, the lift curve slope of real airfoils is generally a bit less than 2π because of viscous effects, but is still quite close. The second part of the equation gives the zero lift angle of attack:

$$\alpha_0 = \frac{1}{\pi} \int_0^\pi b(\theta)(1 - \cos\theta) d\theta, \tag{2.289}$$

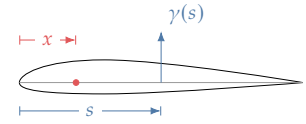

Fig. 2.54 Pitching moment about an arbitrary location x from a differential lift produced at location s.

which would be zero for an uncambered airfoil ($b(\theta) = 0$) as expected.

The pitching moment can be derived about an arbitrary point x as shown in Fig. 2.54. The integral is:

$$M(x) = -\rho V_\infty \int_0^c \gamma(s)(s - x)ds. \tag{2.290}$$

where the negative sign is used since a pitch up is considered a positive moment. Using our coordinate transformations (Eqs. 2.246 to 2.248) results in:

$$M(x) = -\frac{\rho V_\infty c^2}{4} \int_0^\pi \gamma(\phi) \sin\phi(\cos\theta - \cos\phi)d\phi \tag{2.291}$$

$$= \frac{\rho V_\infty c}{2} \left[\cos\theta \int_0^\pi \gamma(\phi) \sin\phi d\phi - \int_0^\pi \gamma(\phi) \sin\phi \cos\phi d\phi\right]. \tag{2.292}$$

The first integral is the same as the one we evaluated for lift earlier (Eq. 2.273), excepting the constant $c/2$ term and evaluates to Eq. 2.281 (times $2/c$).

$$M(x) = -\frac{\rho V_\infty c^2}{4} \left[\cos\theta\, 2V_\infty \pi \left(A_0 + \frac{A_1}{2}\right) - \int_0^\pi \gamma(\phi) \sin\phi \cos\phi d\phi\right]. \tag{2.293}$$

Let's consider only the second integral now:

$$\int_0^\pi \gamma(\phi) \sin\phi \cos\phi d\phi \tag{2.294}$$

$$= 2V_\infty \left[A_0 \int_0^\pi \cos\phi(1 + \cos\phi) + \sum_n A_n \int_0^\pi \sin\phi \cos\phi \sin(n\phi)\right] \tag{2.295}$$

$$= 2V_\infty \left[A_0 \frac{\pi}{2} + A_1 \int_0^\pi \cos\phi \sin\phi \sin(\phi) + A_2 \int_0^\pi \cos\phi \sin\phi \sin(2\phi)\right. \tag{2.296}$$

$$\left. A_3 \int_0^\pi \cos\phi \sin\phi \sin(3\phi) + \ldots\right]. \tag{2.297}$$

The A_1 term integrates to zero, as does A_3 and all higher order terms. The A_2 term integrates to $\pi/4$.

$$\int_0^\pi \gamma(\phi) \sin\phi \cos\phi d\phi = 2V_\infty \left[A_0 \frac{\pi}{2} + A_2 \frac{\pi}{4}\right]. \tag{2.298}$$

We now plug this result back into Eq. 2.293 yielding:

$$M(x) = -\frac{\rho V_\infty c^2}{4}\left[\cos\theta\, 2V_\infty \pi\left(A_0 + \frac{A_1}{2}\right) - 2V_\infty\left(A_0\frac{\pi}{2} + A_2\frac{\pi}{4}\right)\right] \tag{2.299}$$

$$= -\frac{\rho V_\infty^2 c^2 \pi}{2}\left[\cos\theta\left(A_0 + \frac{A_1}{2}\right) - \left(A_0\frac{1}{2} + A_2\frac{1}{4}\right)\right] \tag{2.300}$$

$$= -\frac{\rho V_\infty^2 c^2 \pi}{2}\left[A_0\left(\cos\theta - \frac{1}{2}\right) + A_1\frac{\cos\theta}{2} - \frac{A_2}{4}\right]. \tag{2.301}$$

Let's now express this in terms of x using our inverse transformation (Eq. 2.258):

$$M(x) = -\frac{\rho V_\infty^2 c^2 \pi}{2}\left[A_0\left(\frac{1}{2} - \frac{2x}{c}\right) + A_1\left(\frac{1}{2} - \frac{x}{c}\right) - \frac{A_2}{4}\right]. \tag{2.302}$$

Now for convenience, we distribute a $c/2$ from the outside term through the parenthesis:

$$M(x) = -\rho V_\infty^2 c\pi\left[A_0\left(\frac{c}{4} - x\right) + A_1\left(\frac{c}{4} - \frac{x}{2}\right) - A_2\frac{c}{8}\right]. \tag{2.303}$$

The definition of the aerodynamic center is the point about which the pitching moment is independent of angle of attack $dM/d\alpha = 0$. The only Fourier coefficient that depends on angle of attack is A_0:

$$A_0 = \alpha - \frac{1}{\pi}\int_0^\pi b(\phi)d\phi. \tag{2.304}$$

So from the moment equation we can see that the point at which $dM/d\alpha = 0$ is when $x = c/4$. This is another highly useful result from thin airfoil theory, namely that *the airfoil quarter chord is the theoretical location of the aerodynamic center*:

$$x_{ac} = \frac{c}{4}. \tag{2.305}$$

We can also compute the pitching moment coefficient about the aerodynamic center, but that depends on the specific airfoil shape.

$$M_{ac} = M(x = c/4) = -\rho V_\infty^2 c\pi\left[A_1\frac{c}{8} - A_2\frac{c}{8}\right] \tag{2.306}$$

$$= -\frac{\rho V_\infty^2 c^2 \pi}{8}(A_1 - A_2) \tag{2.307}$$

$$c_{m\mathrm{ac}} = \frac{M_{ac}}{\frac{1}{2}\rho V_\infty^2 c^2} \tag{2.308}$$

$$= -\frac{\pi}{4}(A_1 - A_2). \tag{2.309}$$

By far the most useful results from thin airfoil theory are these two: the lift curve slope is 2π and the quarter chord is the aerodynamic center. These results are widely used in aerodynamics. There are various other minor analytic solutions that can sometimes be useful, for example in verification studies, or as parts of broader aerodynamic methods. A few such examples are shown below.

Example 2.10 Parabolic camber

Let's consider an example of an airfoil with parabolic camber as shown in Fig. 2.55 and given in equation form as:

$$\bar{y} = 4\epsilon \frac{x}{c}(c - x), \tag{2.310}$$

where ϵ is a free parameter signifying the maximum camber.

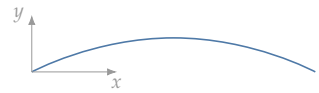

Fig. 2.55 A parabolic camber line.

We now follow the steps outlined at the end of Section 2.9.5. With the camber line defined we now differentiate:

$$\frac{d\bar{y}}{dx} = 4\epsilon \left(1 - \frac{2x}{c}\right), \tag{2.311}$$

then apply the variable substitution $x = \frac{c}{2}(1 - \cos\phi)$:

$$b(\phi) = 4\epsilon \cos\phi. \tag{2.312}$$

We now perform the integrals for the Fourier coefficients:

$$A_0 = \alpha - \frac{4\epsilon}{\pi} \int_0^\pi \cos\phi d\phi \tag{2.313}$$

$$= \alpha \tag{2.314}$$

$$A_1 = \frac{8\epsilon}{\pi} \int_0^\pi \cos^2(\phi) d\phi \tag{2.315}$$

$$= 4\epsilon \tag{2.316}$$

$$A_2 = \frac{8\epsilon}{\pi} \int_0^\pi \cos(\phi)\cos(2\phi) d\phi \tag{2.317}$$

$$= 0. \tag{2.318}$$

Similarly, $A_n = 0$ for all $n \geq 2$.

Finally, using the equation for lift we have:

$$L' = \pi\rho V_\infty^2 c(\alpha + 2\epsilon), \tag{2.319}$$

or normalizing:

$$c_l = 2\pi(\alpha + 2\epsilon). \tag{2.320}$$

This equation provides a simple back-of-the envelope estimate for the lift of a cambered airfoil with parabolic, or at least roughly parabolic camber.

Example 2.11 NACA 4-series camber

The equation for the camber line of a NACA four-series airfoil is given in Eq. 2.203, which we can differentiate:

$$\frac{dy_c}{dx} = \begin{cases} \frac{2m}{p^2}(p-x), & 0 \le x \le p \\ \frac{2m}{(1-p)^2}(p-x), & p \le x \le 1 \end{cases}, \tag{2.321}$$

and then apply the coordinate transformation:

$$b(\theta) = \begin{cases} \frac{2m}{p^2}\left(p - \frac{c}{2}(1-\cos\theta)\right), & 0 \le \theta \le \theta_p \\ \frac{2m}{(1-p)^2}\left(p - \frac{c}{2}(1-\cos\theta)\right), & \theta_p \le \theta \le \pi \end{cases}, \tag{2.322}$$

where θ_p is such that $p = \frac{c}{2}(1-\cos\theta_p)$.

Equation 2.289 provides the zero-lift angle of attack. However, since the camber slope is different before and after the maximum camber position p, the integral also has to be split as:

$$\alpha_0 = \frac{1}{\pi}\int_0^{\theta_p} b(\theta)(1-\cos\theta)\,d\theta + \frac{1}{\pi}\int_{\theta_p}^{\pi} b(\theta)(1-\cos\theta)\,d\theta. \tag{2.323}$$

The numerator of the camber slope is the same and the common term of the integral can be shown to be:

$$\frac{1}{\pi}\int 2m\left(p\,(1-\cos\theta) - \frac{c}{2}(1-\cos\theta)^2\right)d\theta \tag{2.324}$$

$$= \frac{2m}{\pi}\left[p\,(\theta - \sin\theta) - \frac{c}{8}\,(6\theta - 8\sin\theta + \sin 2\theta)\right]. \tag{2.325}$$

Evaluating the integral in Eq. 2.323, and rearranging the expression, we obtain the zero-lift, angle in radians, to be

$$\alpha_0 = \left(\frac{-m}{\pi}\right)\frac{\pi p^2\,(3-4p) + (1-2p)\left((3-4p)\,\theta_p + (2p-3)\sin\theta_p\right)}{2p^2(1-p)^2}, \tag{2.326}$$

where $\theta_p = \cos^{-1}(1-2p)$.

Since we already know the lift curve slope, we now have an analytic expression (with the assumptions of thin-airfoil theory) for the lift curve of any NACA four-series airfoil (using Eq. 2.287).

Example 2.12 Lumped Vortex Method

The following example is a bit of an aside, but uses the results of thin airfoil theory and will be useful in Chapter 4. Let's consider a lumped vortex model as shown in Fig. 2.56. Rather than using a distribution of vortices, we want to lump all the vorticity into one point vortex. This model will be used later when we need a simple way to model the camber and will use results of thin airfoil theory to do so. With only one point vortex we can only satisfy the flow tangency boundary condition at one point (the control point denoted by x). The question then is where should we place the point vortex (distance a), and where should we place the control point (distance b)?

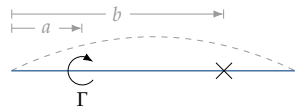

Fig. 2.56 A lumped vortex model and a control point marked with x.

In Eq. 2.229 we derived that the flow tangency boundary condition for the vertical velocity is:

$$v_v = V_\infty \left(\frac{d\bar{y}}{dx} - \alpha \right). \tag{2.327}$$

For a point vortex we know that the induced velocity is given by $V_\theta = \Gamma/(2\pi r)$ or in this case the velocity of the vortex induced at the control point where we will impose the boundary condition is:

$$-\frac{\Gamma}{2\pi(b-a)} = V_\infty \left(\frac{d\bar{y}}{dx} - \alpha \right). \tag{2.328}$$

As we know nothing about the airfoil at this stage, we will assume a parabolic camber as that seems reasonably flexible will still retaining simplicity. Example 2.10 provides the camber line slope for parabolic camber, which is given by the following equation when evaluated at the control point:

$$\left. \frac{d\bar{y}}{dx} \right|_{x=b} = 4\epsilon \left(1 - \frac{2b}{c} \right). \tag{2.329}$$

Similarly, that same example solved for the lift of a parabolic camber airfoil, which we can relate to circulation through the Kutta-Joukowski theorem:

$$L' = \pi\rho V_\infty^2 c(\alpha + 2\epsilon) = \rho V_\infty \Gamma. \tag{2.330}$$

Solving for Γ and using some algebra on the above equation results in the following:

$$\left(\frac{c}{b-a} \right) \alpha + \left(\frac{2c}{b-1} \right) \epsilon = (2)\,\alpha - \left(8 \left(1 - 2\frac{b}{c} \right) \right) \epsilon. \tag{2.331}$$

For this equation to be satisfied the coefficients in front of α must be equal, as must the coefficients in front of ϵ. This gives two equations for two unknowns:

$$a = \frac{1}{4}c \tag{2.332}$$

$$b = \frac{3}{4}c. \tag{2.333}$$

Thus, using the results of thin airfoil theory suggests that we should put the vortex at the quarter chord, and place the control point at three-quarters chord.

2.10 2D Panel Methods

Thin airfoil theory is quite clever, but comes with a few significant limitations. The most problematic limitation is the assumption of small disturbances. This means that near stagnation points, which exist for all airfoils, the pressure distributions are not well predicted. Significant inaccuracies may also exist for airfoils with high camber or large thickness.

We still use the same key idea that the flow is modeled as a sum of freestream, and source/vortex/doublet distributions. But unlike thin airfoil theory, we place the source/vortex/doublet distributions on the surface of the body rather than at the chord line. We will also use exact boundary conditions rather than approximate ones.

In the following equation, we show only source and vortex distributions for brevity (doublet distributions are widely used in 3D):

$$\phi = V_\infty \cos(\alpha)x + V_\infty \sin(\alpha)y + \int \frac{q(s)}{2\pi} \ln r ds + \int \frac{\gamma(s)}{2\pi} \theta ds. \quad (2.334)$$

The above integrals are difficult to evaluate on arbitrary shapes so a common simplification is to approximate the airfoil with straight line segments. These segments form the *panels*, and they will be numbered as shown in Fig. 2.57. With that simplification the equation becomes a summation of integrals that occur over flat panels:

$$\phi = V_\infty \cos(\alpha)x + V_\infty \sin(\alpha)y + \sum_{i=1}^{N} \int_{\text{panel } i} \left[\frac{q(s)}{2\pi} \ln r + \frac{\gamma(s)}{2\pi} \theta \right] ds. \quad (2.335)$$

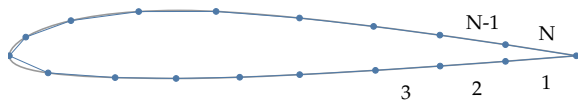

Fig. 2.57 An airfoil discretized into straight line panels.

The integral equations developed in this chapter can be applied on each panel leading to a system of linear equations. The resulting methodology is called a *panel method*.

There are many variations of panel methods. For example, the singularity distributions on a given panel can be of constant strength per unit length, or might vary linearly, quadratically, or in some other manner. The panels are often flat segments but can instead be curved (e.g., B-splines). One can use just vortices, just doublets, a combination of sources and vortices, or a combination of sources and doublets. The formulation can be based on the potential function or the stream

function. The type of boundary condition can also vary. A *Dirichlet* boundary condition specifies values of the function (ϕ or ψ) on the boundary, whereas a *Neumann* boundary condition, specifies derivatives of the function (e.g., $\partial\phi/\partial n = V_n$). A mixed boundary condition is also possible. There are also varied considerations on how to model the wake (when adding viscous considerations), flaps, jets, etc.

Not all choices are equally efficient, but the distinctions in numerical performance advantages are less important in 2D than they are in 3D since 2D panel codes require far less computational effort. Still, some choices lead to simpler implementation, more robust numerical behavior, or cleaner coupling with viscous methods.

Two approaches are described in the following sections. First, we describe a method developed by Hess and Smith of Douglas Aircraft in 1966,[8] which resulted in the first practical panel method. The methodology is well described by Moran and we follow a similar derivation.[9] The approach uses a combination of constant sources, and constant vortices with a Neumann boundary condition of zero normal flow. Next, we describe the inviscid portion of XFOIL,[2] which is the most widely used 2D panel code today. It uses linear vortices (it also uses constant sources but those are used to enforce consistency with the viscous solution, which is not needed here), and a Dirichlet boundary condition on the stream function around the airfoil.

8. Hess and Smith, *Calculation of potential flow about arbitrary bodies*, 1967.

9. Moran, *An Introduction to Theoretical and Computational Aerodynamics*, 1984.

2. Drela, *XFOIL: An analysis and design system for low Reynolds number airfoils*, 1989.

2.11 Hess-Smith Panel Method

As noted the Hess/Smith model uses constant source and vortex distributions. In other words, the source strength per unit length ($q(s)$) is constant on a given panel, but can vary from panel to panel. These strengths will be varied to satisfy flow tangency at control points, one for each panel (N strengths and N boundary conditions). The vortex strength ($\gamma(s)$) be constant over the entire airfoil (and thus constant on each panel). This leads to one additional unknown to satisfy the one additional equation: the Kutta condition.

A panel with constant source/vortex strength produces infinite velocities at the ends of each panel and so control points cannot be at the end points. The midpoint is the most logical choice—either the midpoint of the panel or the midpoint of the actual surface. For this model it works better (and is simpler) to have the control points at the midpoints of the panel. This is because numerical errors can occur if the control point is too close to a singularity. Similarly, the Kutta condition is applied at the control points at the middle of the trailing edge panels highlighted in Fig. 2.58. This means that the Kutta condition is not

quite at the trailing edge. The real flow, with viscosity, does not have a stagnation point right at the trailing edge anyway, so it turns out this approximation fortuitously often yields better predictions than a more numerically accurate boundary condition would.

Fig. 2.58 Location of control points (x) and direction of normal for an arbitrary panel, and the controls points (x) on the trailing edge-panels for the Kutta condition.

Let us consider a generic panel as described in Fig. 2.59. From known end point locations (x_i, y_i), we need to determine the control point locations, the angle, and the normal and tangent vectors. Because we chose to model control points at the center of the panels they are easily computed:

$$\bar{x}_i = \frac{x_i + x_{i+1}}{2} \tag{2.336}$$

$$\bar{y}_i = \frac{y_i + y_{i+1}}{2}. \tag{2.337}$$

One must always be careful in computing angles to ensure the appropriate branch/quadrant is obtained. In this case we don't actually need the panel inclination angle θ, but rather will compute $\sin\theta$ and $\cos\theta$ directly to avoid the quadrant issues. These can be computed as:

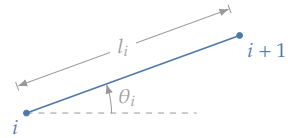

Fig. 2.59 Nomenclature for a generic panel i.

$$\sin\theta_i = \frac{y_{i+1} - y_i}{l_i} \tag{2.338}$$

$$\cos\theta_i = \frac{x_{i+1} - x_i}{l_i}, \tag{2.339}$$

where l_i is the length of the panel:

$$l_i = \sqrt{(x_{i+1} - x_i)^2 + (y_{i+1} - y_i)^2}. \tag{2.340}$$

Based on our numbering scheme (Fig. 2.57) the body is to the right when progressing from i to $i+1$ and the surface normal always points out (away from the body). Thus, the normal and tangential vectors are given by:

$$\hat{t}_i = \cos\theta_i \hat{x} + \sin\theta_i \hat{y} \tag{2.341}$$

$$\hat{n}_i = -\sin\theta_i \hat{x} + \cos\theta_i \hat{y}. \tag{2.342}$$

The velocity at panel i will be the velocity calculated at control point i:

$$u_i \equiv u(\bar{x}_i, \bar{y}_i) \tag{2.343}$$

$$v_i \equiv v(\bar{x}_i, \bar{y}_i). \tag{2.344}$$

With that setup we can now write our Neumann boundary condition (a condition on the derivative of the potential function, which is a condition on velocity) in equation form. The no-flow-through, or flow tangency, condition is:

$$\vec{V} \cdot \hat{n} = 0. \tag{2.345}$$

Using the normal vectors defined earlier (Eq. 2.341) we can express this as:

$$-u_i \sin\theta_i + v_i \cos\theta_i = 0, \tag{2.346}$$

which is applied at each panel. Next we use the Kutta condition that the tangential velocity at the trailing edge is the same on the upper and lower surfaces as shown in Eq. 2.173. In our case, we need these velocities to have opposite signs just because of the way the panels are ordered Fig. 2.57 (and so the positive tangential direction is upstream for panel 1):

$$V_{t1} = -V_{tn}, \tag{2.347}$$

or using our panel notation:

$$u_1 \cos\theta_1 + v_1 \sin\theta_1 = -u_N \cos\theta_N - v_N \sin\theta_N. \tag{2.348}$$

To build up the solution we need to be able to compute the influence of a panel on another panel. To start, we compute u^*_{sij} and v^*_{sij}, which are the x and y components of velocity at panel i induced by a source distribution at panel j (see Fig. 2.60).

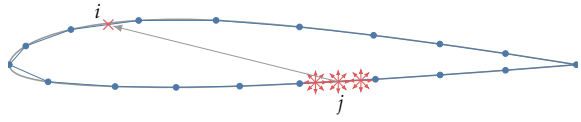

Fig. 2.60 Computing induced velocity at panel i from a line source distribution along panel j.

To determine the velocities, we need to consider a generic panel j as shown in Fig. 2.61. For convenience, we use a rotated coordinate system aligned with the panel (x^*, y^*). In the rotated coordinate system, we already know the how to compute the velocities. This is exactly what we derived previously in Section 2.7: the velocities induced by a line source distribution over a finite segment (Eqs. 2.188 and 2.189), except in this case the source strength is constant over the panel.

$$u^*_{sij} = \frac{q_j}{2\pi} \int_0^{l_j} \frac{x^* - s}{(x^* - s)^2 + (y^*)^2} ds \tag{2.349}$$

$$v^*_{sij} = \frac{q_j}{2\pi} \int_0^{l_j} \frac{y^*}{(x^* - s)^2 + (y^*)^2} ds. \tag{2.350}$$

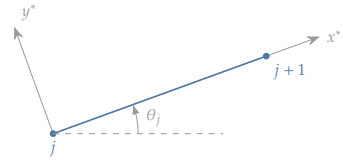

Fig. 2.61 A rotated coordinate system aligned with an arbitrary panel j.

With q out of the integral, both of these integrals can be solved analytically (recall that x^* and y^* are constants in the integral as they are just an evaluation point). To simplify the results we will make use of some geometric relationships by referring to the variables defined in Fig. 2.62. The tangential velocity is:

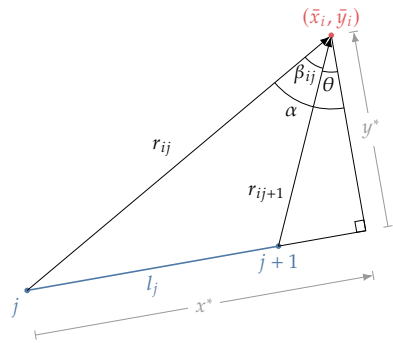

Fig. 2.62 A depiction of the geometry for an evaluation point on panel i from singularities integrating across panel j.

$$
\begin{aligned}
u^*_{sij} &= -\frac{q_j}{4\pi}\int_0^{l_j} \frac{-2(x^*-s)}{(x^*-s)^2+(y^*)^2}ds \\
&= -\frac{q_j}{4\pi}\left[\ln\left((x^*-s)^2+(y^*)^2\right)\right]_0^{l_j} \\
&= -\frac{q_j}{4\pi}\ln\left[\frac{(x^*-l_j)^2+(y^*)^2}{(x^*)^2+(y^*)^2}\right] \\
&= -\frac{q_j}{2\pi}\ln\left[\frac{\sqrt{(x^*-l_j)^2+(y^*)^2}}{\sqrt{(x^*)^2+(y^*)^2}}\right] \\
&= -\frac{q_j}{2\pi}\ln\left(\frac{r_{ij+1}}{r_{ij}}\right).
\end{aligned}
\tag{2.351}
$$

The second integral is the same integral we came across in thin airfoil theory (Eq. 2.232), but with different limits. We use the same

change of variables $z = (x^* - s)/y^*$ so $dz = -ds/y^*$:

$$\begin{aligned} v^*_{sij} &= \frac{q_j}{2\pi}\int_0^{l_j} \frac{1/y^*}{\left(\frac{x^*-s}{y^*}\right)^2+1} ds \\ &= \frac{q_j}{2\pi}\int_{x^*/y^*}^{(x^*-l_j)/y^*} \frac{-1}{z^2+1} dz \\ &= \frac{q_j}{2\pi}\int_{(x^*-l_j)/y^*}^{x^*/y^*} \frac{1}{z^2+1} dz \\ &= \frac{q_j}{2\pi}\left[\tan^{-1} z\right]_{(x^*-l_j)/y^*}^{x^*/y^*} \\ &= \frac{q_j}{2\pi}\left(\tan^{-1}\left(\frac{x^*}{y^*}\right) - \tan^{-1}\left(\frac{x^*-l_j}{y^*}\right)\right) \\ &= \frac{q_j}{2\pi}(\alpha - \theta) \\ &= \frac{q_j}{2\pi}\beta_{ij}. \end{aligned} \tag{2.352}$$

The vortices use the same integrals, with slightly different signs. We summarize all four results as:

$$\begin{aligned} u^*_{sij} &= -q_j \frac{1}{2\pi}\ln\left(\frac{r_{ij+1}}{r_{ij}}\right) \\ v^*_{sij} &= q_j \frac{\beta_{ij}}{2\pi} \\ u^*_{vij} &= \gamma \frac{\beta_{ij}}{2\pi} \\ v^*_{vij} &= \gamma \frac{1}{2\pi}\ln\left(\frac{r_{ij+1}}{r_{ij}}\right). \end{aligned} \tag{2.353}$$

Again, we need to take care when computing the angle β. There are various trigonometry approaches we could use, but we may run into problems for large angles. Consider two vectors starting from a common point as shown in Fig. 2.63. The definitions of the cross and dot product yield:

$$\vec{a} \times \vec{b} = |a||b| \sin\theta \tag{2.354}$$

$$\vec{a} \cdot \vec{b} = |a||b| \cos\theta \tag{2.355}$$

If we divide these two equations and solve for θ we get:

$$\theta = \tan^{-1} \frac{\vec{a} \times \vec{b}}{\vec{a} \cdot \vec{b}} \tag{2.356}$$

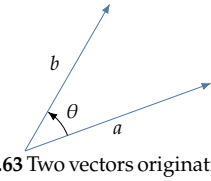

Fig. 2.63 Two vectors originating from a common origin.

Using our geometry leads to the following equation for β:

$$\beta_{ij} = \begin{cases} \tan^{-1}\left(\dfrac{(x_j - \bar{x}_i)(y_{j+1} - \bar{y}_i) - (y_j - \bar{y}_i)(x_{j+1} - \bar{x}_i)}{(x_j - \bar{x}_i)(x_{j+1} - \bar{x}_i) + (y_j - \bar{y}_i)(y_{j+1} - \bar{y}_i)}\right) & \text{if } i \neq j \\ \pi & \text{if } i = j \end{cases} \tag{2.357}$$

We now need to decide how to handle the β_{ii} case (both indices are the same). The angle approaches π or $-\pi$ depending on which direction you approach from. In our case, we always come from the outside based on the way we defined our geometry and the fact that we only care about external flow so that is why $\beta_{ii} = \pi$. We need to make sure we force this. If we rely on the first equation to compute the self-induction then some panels will evaluate to something close to π and others close to $-\pi$ based on small numerical errors.

While this equation is a bit long, it is reliable. If we use the `atan2` function then the domain is $(-\pi, \pi]$, so the correct quadrant will be preserved. Note that this formula works equally well in three dimensions.

Recall that we computed all the velocities in the rotated (starred) coordinate system (Fig. 2.61). We need to rotate the velocities back to the original x, y coordinate system:

$$\begin{aligned} u_{ij} &= u^*_{ij} \cos\theta_j - v^*_{ij} \sin\theta_j \\ v_{ij} &= u^*_{ij} \sin\theta_j + v^*_{ij} \cos\theta_j \end{aligned} \tag{2.358}$$

Then, to get the total velocity at panel i, we need to add the freestream velocity and the contributions of the sources and vortices across all panels. In doing so it will be helpful to write out the velocities as products of the singularity strength times the velocity per unit strength, e.g., $u_{sij} = q_j \hat{u}_{sij}$ for the first equation in Eq. 2.353, and so on for the other velocity components.

$$\begin{aligned} u_i &= V_\infty \cos\alpha + \sum_{j=1}^{N} u_{sij} + \sum_{j=1}^{N} u_{vij} \\ &= V_\infty \cos\alpha + \sum_{j=1}^{N} (u^*_{sij} \cos\theta_j - v^*_{sij} \sin\theta_j) + \sum_{j=1}^{N} (u^*_{vij} \cos\theta_j - v^*_{vij} \sin\theta_j) \\ &= V_\infty \cos\alpha + \sum_{j=1}^{N} q_j (\hat{u}_{sij} \cos\theta_j - \hat{v}_{sij} \sin\theta_j) + \gamma \sum_{j=1}^{N} (\hat{u}_{vij} \cos\theta_j - \hat{v}_{vij} \sin\theta_j) \end{aligned} \tag{2.359}$$

$$
\begin{aligned}
v_i &= V_\infty \sin\alpha + \sum_{j=1}^{N} v_{sij} + \sum_{j=1}^{N} v_{vij} \\
&= V_\infty \sin\alpha + \sum_{j=1}^{N} (u^*_{sij} \sin\theta_j + v^*_{sij} \cos\theta_j) + \sum_{j=1}^{N} (u^*_{vij} \sin\theta_j + v^*_{vij} \cos\theta_j) \\
&= V_\infty \sin\alpha + \sum_{j=1}^{N} q_j (\hat{u}_{sij} \sin\theta_j + \hat{v}_{sij} \cos\theta_j) + \gamma \sum_{j=1}^{N} (\hat{u}_{vij} \sin\theta_j + \hat{v}_{vij} \cos\theta_j)
\end{aligned}
\tag{2.360}
$$

Recall that the flow tangency boundary condition is (Eq. 2.346):

$$
-u_i \sin\theta_i + v_i \cos\theta_i = 0 \tag{2.361}
$$

Substituting in the above velocities and using sine and cosine sum and difference formulas results in:

$$
\begin{aligned}
&\sum_{j=1}^{N} q_j \left[-\hat{u}_{sij} \sin(\theta_i - \theta_j) + \hat{v}_{sij} \cos(\theta_i - \theta_j) \right] \\
&+ \gamma \sum_{j=1}^{N} \left[-\hat{u}_{vij} \sin(\theta_i - \theta_j) + \hat{v}_{vij} \cos(\theta_i - \theta_j) \right] = V_\infty \sin(\theta_i - \alpha)
\end{aligned}
\tag{2.362}
$$

We see that this is a linear set of equations for the unknowns q_j and γ:

$$
\sum_{j=1}^{N} A_{i,j} q_j + A_{i,N+1} \gamma = b_i \tag{2.363}
$$

where

$$
A_{i,j} = -\hat{u}_{sij} \sin(\theta_i - \theta_j) + \hat{v}_{sij} \cos(\theta_i - \theta_j) \tag{2.364}
$$

$$
A_{i,N+1} = -\hat{u}_{vij} \sin(\theta_i - \theta_j) + \hat{v}_{vij} \cos(\theta_i - \theta_j) \tag{2.365}
$$

$$
b_i = V_\infty \sin(\theta_i - \alpha). \tag{2.366}
$$

We can combine the unknowns into one vector $x = [q1, q2, \ldots, q_N, \gamma]$, then Eq. 2.363 becomes:

$$
\sum_{j=1}^{N+1} A_{ij} x_j = b_i, \tag{2.367}
$$

or in matrix-vector form:

$$
Ax = b. \tag{2.368}
$$

Referring back to Eq. 2.353 for the definitions of $\hat{u}$ and $\hat{v}$ we have the following (note we moved the 2π that divides every term on the left-hand side over to the right-hand side for conciseness):

$$
\begin{aligned}
A_{ij} &= \left[\ln\left(\frac{r_{ij+1}}{r_{ij}}\right)\sin(\theta_i-\theta_j)+\beta_{ij}\cos(\theta_i-\theta_j)\right] \text{ for } i\in 1\dots N, j\in 1\dots N \\
A_{iN+1} &= \sum_{j=1}^{N}\left[\ln\left(\frac{r_{ij+1}}{r_{ij}}\right)\cos(\theta_i-\theta_j)-\beta_{ij}\sin(\theta_i-\theta_j)\right] \text{ for } i\in 1\dots N \\
b_i &= 2\pi V_\infty \sin(\theta_i-\alpha) \text{ for } i\in 1\dots N
\end{aligned}
\tag{2.369}
$$

We can expand the sum and difference formulas as:

$$\sin(\theta_i-\theta_j)=\sin\theta_i\cos\theta_j-\cos\theta_i\sin\theta_j \tag{2.370}$$

$$\cos(\theta_i-\theta_j)=\cos\theta_i\cos\theta_j+\sin\theta_i\sin\theta_j. \tag{2.371}$$

With these expansions we never need to explicitly compute θ, but rather just use the formulas shown in Eqs. 2.338 and 2.339 for $\sin\theta_i$ and $\cos\theta_i$. Alternatively, we can compute each θ_i directly, but we must use the `atan2` function. This is because $\sin^{-1}(0.5)$, for example, has multiple solutions, and the default implementation does not account for which quadrant we are. The function `atan2` on the other hand, looks at the signs of the components to determine the quadrant, and thus return a unique angle.

Now we have to enforce the Kutta condition (Eq. 2.348) and follow essentially the same procedure. The result is the following linear equation:

$$\sum_{j=1}^{N} A_{N+1,j}q_j + A_{N+1,N+1}\gamma = b_{N+1}. \tag{2.372}$$

where

$$
\begin{aligned}
A_{N+1,j} &= \sum_{k=1 \text{ and } N} \left[\beta_{kj} \sin(\theta_k - \theta_j) - \ln\left(\frac{r_{kj+1}}{r_{kj}}\right) \cos(\theta_k - \theta_j) \right] \text{ for } j \in 1 \ldots N \\
A_{N+1,N+1} &= \sum_{k=1 \text{ and } N} \left(\sum_{j=1}^{N} \left[\beta_{kj} \cos(\theta_k - \theta_j) + \ln\left(\frac{r_{kj+1}}{r_{kj}}\right) \sin(\theta_k - \theta_j) \right] \right) \\
b_{N+1} &= -2\pi V_\infty \left[\cos(\theta_1 - \alpha) + \cos(\theta_N - \alpha) \right]
\end{aligned}
\tag{2.373}
$$

Now we can assemble the no-flow-through conditions and the Kutta condition in one large matrix:

$$
\begin{bmatrix}
A_{11} & \cdots & A_{1N} & A_{1,N+1} \\
\vdots & & \vdots & \vdots \\
A_{N1} & \cdots & A_{NN} & A_{N,N+1} \\
A_{N+1,1} & \cdots & A_{N+1,N} & A_{N+1,N+1}
\end{bmatrix}
\begin{bmatrix}
q_1 \\ \vdots \\ q_N \\ \gamma
\end{bmatrix}
=
\begin{bmatrix}
b_1 \\ \vdots \\ b_N \\ b_{N+1}
\end{bmatrix}.
\tag{2.374}
$$

This is a linear system that we can solve for q and γ. With known source and vortex strengths we then compute the pressure coefficient. We know the normal velocity is zero at each panel so we just need to compute the tangential velocity. We use Eq. 2.341, plugin the velocity contributions Eqs. 2.359 and 2.360, and the velocities per unit strength

(Eq. 2.353)

$$
\begin{aligned}
V_{ti} &= u_i \cos\theta_i + v_i \sin\theta_i \\
&= \left(V_\infty \cos\alpha + \sum_{j=1}^{N} q_j(\hat{u}_{sij}\cos\theta_j - \hat{v}_{sij}\sin\theta_j) + \gamma \sum_{j=1}^{N} (\hat{u}_{vij}\cos\theta_j - \hat{v}_{vij}\sin\theta_j) \right) \cos\theta_i \\
&\quad + \left(V_\infty \sin\alpha + \sum_{j=1}^{N} q_j(\hat{u}_{sij}\sin\theta_j + \hat{v}_{sij}\cos\theta_j) + \gamma \sum_{j=1}^{N} (\hat{u}_{vij}\sin\theta_j + \hat{v}_{vij}\cos\theta_j) \right) \sin\theta_i \\
&= V_\infty \cos(\theta_i - \alpha) \\
&\quad + \sum_{j=1}^{N} \left[q_j \left(\hat{u}_{sij}\cos(\theta_i - \theta_j) + \hat{v}_{sij}\sin(\theta_i - \theta_j) \right) + \gamma \left(\hat{u}_{vij}\cos(\theta_i - \theta_j) + \hat{v}_{vij}\sin(\theta_i - \theta_j) \right) \right] \\
&= V_\infty \cos(\theta_i - \alpha) \\
&\quad + \sum_{j=1}^{N} \left[q_j \left(\frac{-1}{2\pi} \ln\left(\frac{r_{ij+1}}{r_{ij}} \right) \cos(\theta_i - \theta_j) + \frac{\beta_{ij}}{2\pi} \sin(\theta_i - \theta_j) \right) \right. \\
&\quad \left. + \gamma \left(\frac{\beta_{ij}}{2\pi} \cos(\theta_i - \theta_j) + \frac{1}{2\pi} \ln\left(\frac{r_{ij+1}}{r_{ij}} \right) \sin(\theta_i - \theta_j) \right) \right]
\end{aligned}
\tag{2.375}
$$

The final result is then:

$$
\begin{aligned}
V_{ti} &= V_\infty \cos(\theta_i - \alpha) \\
&\quad + \frac{1}{2\pi} \sum_{j=1}^{N} \left[q_j \left(\beta_{ij} \sin(\theta_i - \theta_j) - \ln\left(\frac{r_{ij+1}}{r_{ij}} \right) \cos(\theta_i - \theta_j) \right) \right] \\
&\quad + \frac{\gamma}{2\pi} \sum_{j=1}^{N} \left[\beta_{ij} \cos(\theta_i - \theta_j) + \ln\left(\frac{r_{ij+1}}{r_{ij}} \right) \sin(\theta_i - \theta_j) \right]
\end{aligned}
\tag{2.376}
$$

The pressure coefficient is then given by (since the normal velocity is zero):

$$
C_p(\bar{x}_i, \bar{y}_i) = 1 - \left(\frac{V_{ti}}{V_\infty} \right)^2 . \tag{2.377}
$$

and is assumed to be constant over a given panel.

Finally, we need to go from pressure distribution to forces and moments. The Kutta-Joukowski theorem (Eq. 2.172) is the most straightforward estimate of lift (and always predicts zero drag as it should in this case). We have already solved for γ which is the vortex strength per unit length. Recall that we assumed a uniform distribution of vorticity on each panel, and that value was the same on all panels. Thus, the vortex strength for a given a panel is γl_i and the total circulation is

$$\Gamma = \gamma \sum_i l_i. \tag{2.378}$$

Then we compute the Kutta-Joukowski theorem and the definition of the lift coefficient:

$$c_l = \frac{L'}{q_\infty c} = \frac{2\Gamma}{V_\infty c}. \tag{2.379}$$

Alternatively, we can compute the forces/moments using integration as discussed in Section 1.4. This approach if necessary for computing pitching moment. Each panel has some pressure (with a uniform distribution in this method), and we can convert that to a normal/axial force, and then rotate to lift/drag using the angle of attack.

For the normal force we use **??**, but eliminate the viscous terms.

$$c_n = \int_0^1 \left(C_{p_l} - C_{p_u}\right) d\left(\frac{x}{c}\right) \tag{2.380}$$

$$= -\frac{1}{c}\int_{\text{upper}} C_p dx + \frac{1}{c}\int_{\text{lower}} C_p dx \tag{2.381}$$

Since we've ordered panels clockwise (Fig. 2.57), a clockwise integrations means that we integrate backwards along the lower surface and so negate the sign of its integral (which also allows us to consolidate the two terms):

$$c_n = -\frac{1}{c}\int_{\text{clockwise}} C_p dx \tag{2.382}$$

We now change the integral to a sum over integrals over each panel. But on a given panel the pressure coefficient is constant so the calculation simplifies to:

$$c_n = \sum_i -\frac{1}{c}\int_{\text{panel}} C_p dx \tag{2.383}$$

$$= \sum_i -C_{p_i}\frac{\Delta x_i}{c} \tag{2.384}$$

For the axial force we use **??** and follow the same procedure (noting that the slope of a given panel is constant):

$$c_a = \sum_i C_{p_i} \frac{\Delta y_i}{c}. \tag{2.385}$$

We can now rotate the normal/axial force to the lift/drag force as shown previously in Eq. 1.32 and repeated here:

$$c_\ell = c_n \cos\alpha - c_a \sin\alpha \tag{2.386}$$

$$c_d = c_n \sin\alpha + c_a \cos\alpha. \tag{2.387}$$

The last calculation we need to make is for the pitching moment about the quarter chord. The pitching moment about the leading edge (see also Eq. 1.24) is found by computing the contributions to the moment from these two forces on each panel (see Fig. 2.64):

$$c_{mle} = \frac{1}{c} \sum_i (-\bar{x}_i c_{ni} + \bar{y}_i c_{ai}). \tag{2.388}$$

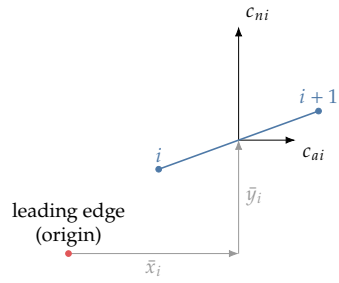

Fig. 2.64 Pitching moment about leading edge.

The extra chord in the denominator is needed because of the normalization of pitching moment: $c_m = M'/(q_\infty c^2)$ relative to the normalization of the axial and normal force coefficients. Finally, as seen in Fig. 2.65, we can translate the pitching moment to any point, though most typically we report the moment about the quarter chord because that is the theoretical aerodynamic center as we found in Section 2.9.

$$c_{mqc} = c_{mle} + \frac{c}{4} c_n. \tag{2.389}$$

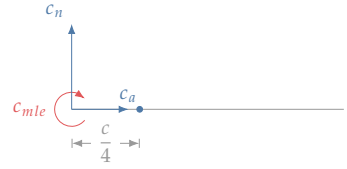

Fig. 2.65 Translating moment to quarter chord.

Example 2.13 Simple diamond-like airfoil

Let's consider a simple example, a diamond airfoil, though one that is not symmetric just so we can distinguish the different calculations. The airfoil coordinates, going clockwise from trailing edge to trailing edge as illustrated in Fig. 2.66, are:

x	y
1.0	-0.001
0.5	-0.03
0	0
0.5	0.07
1.0	0.001

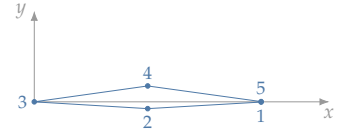

Fig. 2.66 Example diamond airfoil.

and the angle of attack is 5° with $V_\infty = 1$. Obviously, this is an extremely crude airfoil, but the small number of points will make it easier to compare

intermediate calculations. Note that the trailing edge is not sharp (starting point and ending point are not coincident), as is typical of real airfoils. However, a sharp trailing edge would work similarly.

Below we list various intermediate values to facilitate checking your implementation:

$$\beta = \begin{bmatrix} 3.14159 & -0.0785988 & -0.308866 & -2.74616 \\ -0.0785927 & 3.14159 & -2.75393 & -0.306408 \\ -0.206405 & -2.74813 & 3.14159 & -0.184398 \\ -2.74038 & -0.208942 & -0.184432 & 3.14159 \end{bmatrix} \tag{2.390}$$

$$r = \begin{bmatrix} 0.25042 & 0.25042 & 0.75016 & 0.264216 & 0.250544 \\ 0.750131 & 0.25045 & 0.25045 & 0.264055 & 0.750171 \\ 0.750864 & 0.258312 & 0.252438 & 0.252438 & 0.75077 \\ 0.25265 & 0.258438 & 0.75084 & 0.252369 & 0.252369 \end{bmatrix} \tag{2.391}$$

$$A = \begin{bmatrix} 3.14159 & 0.0509606 & 0.22325 & 2.70437 & 1.68373 \\ 0.0509482 & 3.14159 & 2.71002 & 0.224962 & -1.67066 \\ 0.292234 & 2.69843 & 3.14159 & 0.11985 & 1.62492 \\ 2.69279 & 0.290581 & 0.119917 & 3.14159 & -1.63755 \\ -0.508959 & -0.0515339 & 0.0341423 & 0.480173 & 12.3651 \end{bmatrix} \tag{2.392}$$

$$b = \left[0.184268, 0.921515, 0.325508, -1.39815, 0.154831\right]^T \tag{2.393}$$

$$q = \left[1.83240, 2.23520, -2.00285, -2.05088\right]^T \tag{2.394}$$

$$\gamma = 0.182433 \tag{2.395}$$

$$V_t = \left[-1.02996, -0.681357, 1.41886, 1.02996\right]^T \tag{2.396}$$

$$C_p = \left[-0.060819, 0.535753, -1.01316, -0.060819\right]^T \tag{2.397}$$

$$c_l \text{ (Kutta-Joukowski)} = 0.733875 \tag{2.398}$$

$$c_l \text{ (integration)} = 0.775771 \tag{2.399}$$

$$c_{m\,qc} = -0.0026017. \tag{2.400}$$

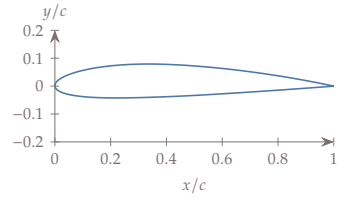

Fig. 2.67 NACA 2412 airfoil.

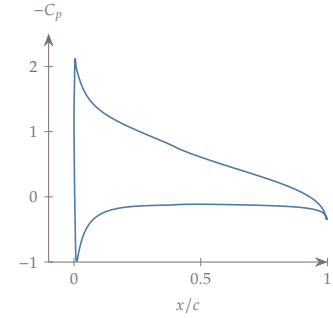

Fig. 2.68 Pressure coefficient distribution over a NACA 2412 airfoil in inviscid flow.

Example 2.14 NACA 4-series airfoil

We shall now investigate the inviscid lift generated by an actual airfoil using the panel method described above. For this example, we use a unit chord NACA 2412 airfoil, the definition of which is given in Eq. 2.203.

To keep the discretization simple, let's model the upper and lower surfaces with 200 equispaced points each (which is 398 panels). Note how we require a considerably large number of points primarily to resolve the leading edge curvature of the airfoil accurately. Example 2.16 explores how many panels are needed for convergence.

Using the inviscid panel method described above, we can obtain the pressure distribution over the airfoil at an angle of attack of 5°. The pressure coefficient distribution obtained from such a solution is given in Fig. 2.68.

The lift coefficient corresponding to this solution is,

$$c_l \text{ (Kutta-Joukowski)} = 0.8562 \tag{2.401}$$

$$c_l \text{ (integration)} = 0.8544. \tag{2.402}$$

We may also compare this lift coefficient with thin airfoil theory results using the expression for zero-lift angle we derived in Eq. 2.326. Substituting for $m = 0.02$ and $p = 0.4$, we get the zero-lift angle of attack to be $\alpha_0 = -0.0363$ radians ($or\ -2.1°$). We also found that the lift curve slope for any thin-airfoil is 2π per radian. Hence, the lift coefficient at 5° is,

$$c_l = 2\pi(\alpha - \alpha_0) = 2\pi\left(5\frac{\pi}{180} - (-0.0363)\right) = 0.7757. \tag{2.403}$$

The lift coefficient obtained using thin-airfoil theory is around 10% off from the lift coefficient obtained using the panel solver integration method. This is due to thin-airfoil theory not accounting for the thickness of the airfoil. If we were to plot the lift coefficient at 5° for various NACA airfoils of the same camber and decreasing thickness, for example NACA 2410, 2408, 2406, and so on, we can observe that the values converge towards thin-airfoil results. This trend is depicted in Fig. 2.69.

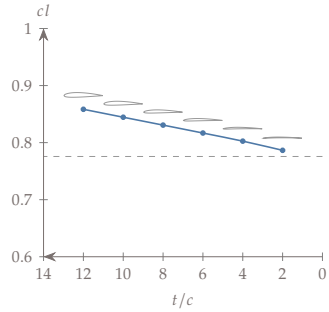

Fig. 2.69 Convergence of lift coefficient towards thin-airfoil results as thickness of airfoils decrease.

2.12 Linear Vortex Panel Method

XFOIL uses a stream function formulation with flat panels and linearly varying vortex distributions along each panel. Once coupled with the viscous solution, source distributions are used along the airfoil and its wake. But since we are focused on the inviscid case for now, we will not discuss those aspects in this section.

The main difference from the prior case is integrating a linear distribution rather than a constant one. We adopt the same panel-aligned coordinate system (Fig. 2.61). If s is the coordinate that varies from 0 to l along the panel, a linear distribution of vorticity strength is defined as:

$$\gamma(s) = \gamma_j + (\gamma_{j+1} - \gamma_j)\frac{s}{l_j}, \tag{2.404}$$

where γ_j and γ_{j+1} define the as yet unknown vortex strengths (per unit length) at the endpoints. We will make significant reuse of the same geometric relationships (Fig. 2.62).* The main difference is that point i corresponds to another node at the end of another panel, rather than the center of another panel. This is because we've decided to define

*XFOIL numbers the panels in the opposite direction from the prior section, but we'll keep the ordering as is for internal consistency in this text.

vorticity strength as a linear distribution, and so those distributions are defined by the values at the endpoint of each node.

The other main difference is that we use a Dirichlet boundary condition on the stream function, rather than a Neumann boundary condition on the potential function. We first need to obtain an expression for the stream function, which is a combination of the freestream and the contributions from the vorticity distributions across all panels:

$$\psi(x, y) = \psi_\infty(x, y) + \psi_v(x, y). \tag{2.405}$$

The freestream portion is straightforward (Eq. 2.43), which we evaluate at the i^{th} panel:

$$\psi_{\infty_i} = V_\infty \cos(\alpha) y_i - V_\infty \sin(\alpha) x_i. \tag{2.406}$$

The vortex portion from a single panel is adapted from Eq. 2.74 with an integration across the linear variation in vorticity. Note that we negate the positive direction as defined in polar coordinates, following the discussion surrounding Fig. 2.38 where we noted that positive lift is associated with the opposite convention for positive circulation:

$$\psi_{vij} = \frac{1}{2\pi} \int_0^{l_j} \gamma(s) \ln(r) ds \tag{2.407}$$

$$= \frac{\gamma_j}{2\pi} \int_0^{l_j} \ln(r) ds + \frac{(\gamma_{j+1} - \gamma_j)}{2\pi l_j} \int_0^{l_j} s \ln(r) ds. \tag{2.408}$$

Let's take these integrals one at a time. Recall that $r = \sqrt{(x^* - s)^2 + y^{*2}}$, so:

$$dr = -\frac{(x^* - s)}{r} ds, \tag{2.409}$$

or

$$ds = -\frac{r}{(x^* - s)} dr. \tag{2.410}$$

The first integral (without the vorticity strength) is:

$$I1 = \frac{1}{2\pi} \int_0^{l_j} \ln(r) ds = -\frac{1}{2\pi} \int_{r_j}^{r_{ij+1}} \ln(r) \frac{r}{(x^* - s)} dr \tag{2.411}$$

$$= -\frac{1}{2\pi} \int_{r_{ij}}^{r_{ij+1}} \ln(r) \frac{r}{\sqrt{r^2 - y^{*2}}} dr. \tag{2.412}$$

We now integrate by parts where $u = \ln r$ and $dv = r dr / \sqrt{r^2 - y^{*2}}$ and

so $du = dr/r$ and $v = \sqrt{r^2 - y^{*2}}$. So the integral becomes:

$$= -\frac{1}{2\pi}\left[\ln(r)\sqrt{r^2 - y^{*2}}\Big|_{r_{ij}}^{r_{ij+1}} - \int_{r_{ij}}^{r_{ij+1}} \frac{\sqrt{r^2 - y^{*2}}}{r} dr\right] \tag{2.413}$$

$$= -\frac{1}{2\pi}\left[\sqrt{r_{ij+1}^2 - y^{*2}} \ln r_{ij+1} - \sqrt{r_{ij}^2 - y^{*2}} \ln r_{ij} - \int_{r_{ij}}^{r_{ij+1}} \frac{\sqrt{r^2 - y^{*2}}}{r} dr\right] \tag{2.414}$$

$$= -\frac{1}{2\pi}\left[(x^* - l_j) \ln r_{ij+1} - x^* \ln r_{ij} - \int_{r_{ij}}^{r_{ij+1}} \frac{\sqrt{r^2 - y^{*2}}}{r} dr\right], \tag{2.415}$$

where the first two terms were simplified based on the geometry in Fig. 2.62. The rest of the integral we evaluate with the change of variables $u^2 = r^2 - y^{*2}$ where $udu = rdr$:

$$-\int_{r_{ij}}^{r_{ij+1}} \frac{\sqrt{r^2 - y^{*2}}}{r} dr \tag{2.416}$$

$$= -\int_{x^*}^{x^*-l_j} \frac{u^2}{u^2 + y^{*2}} du \tag{2.417}$$

$$= \int_{x^*-l_j}^{x^*} \frac{u^2}{u^2 + y^{*2}} du \tag{2.418}$$

$$= \left[u - y^* \tan^{-1}\left(\frac{u}{y^*}\right)\right]_{x^*-l_j}^{x^*} \tag{2.419}$$

$$= l_j - y^*\left(\tan^{-1}\left(\frac{x^*}{y^*}\right) - \tan^{-1}\left(\frac{x^* - l_j}{y^*}\right)\right) \tag{2.420}$$

$$= l_j - y^*\beta_{ij}. \tag{2.421}$$

Plugging this back in results in the final evaluation of the first integral:

$$I1 = -\frac{1}{2\pi}\left[(x^* - l_j) \ln r_{ij+1} - x^* \ln r_{ij} + l_j - y^*\beta_{ij}\right] \tag{2.422}$$

$$= \frac{1}{2\pi}\left[x^* \ln r_{ij} - (x^* - l_j) \ln r_{ij+1} + y^*\beta_{ij} - l_j\right]. \tag{2.423}$$

We now take on the second integral in Eq. 2.408 (without the vorticity constants).

$$I2 = \frac{1}{2\pi l_j} \int_0^{l_j} s \ln(r) ds. \tag{2.424}$$

We solve for s using the geometric relationships (Fig. 2.62) $s = x^* -$

$\sqrt{r^2 - y^{*2}}$:

$$I2 = \frac{1}{2\pi l_j} \int_0^{l_j} \left(x^* - \sqrt{r^2 - y^{*2}} \right) \ln(r) ds \tag{2.425}$$

$$= \frac{x^*}{2\pi l_j} \int_0^{l_j} \ln(r) ds - \frac{1}{2\pi l_j} \int_0^{l_j} \sqrt{r^2 - y^{*2}} \ln(r) ds \tag{2.426}$$

$$= \frac{x^*}{l_j} I1 - \frac{1}{2\pi l_j} \int_0^{l_j} \sqrt{r^2 - y^{*2}} \ln(r) ds. \tag{2.427}$$

The second term we convert using Eq. 2.410 and $\sqrt{r^2 - y^{*2}} = (x^* - s)$:

$$= \frac{x^*}{l_j} I1 + \frac{1}{2\pi l_j} \int_{r_{ij}}^{r_{ij+1}} (x^* - s) \ln(r) \frac{r}{(x^* - s)} dr \tag{2.428}$$

$$= \frac{x^*}{l_j} I1 + \frac{1}{2\pi l_j} \int_{r_{ij}}^{r_{ij+1}} r \ln(r) dr \tag{2.429}$$

$$= \frac{x^*}{l_j} I1 + \frac{1}{2\pi l_j} \left[\frac{r^2}{2} \left(\ln r - \frac{1}{2} \right) \right]_{r_{ij}}^{r_{ij+1}} \tag{2.430}$$

$$= \frac{x^*}{l_j} I1 + \frac{1}{2\pi l_j} \left[\frac{r_{ij+1}^2}{2} \left(\ln r_{ij+1} - \frac{1}{2} \right) - \frac{r_{ij}^2}{2} \left(\ln r_{ij} - \frac{1}{2} \right) \right]. \tag{2.431}$$

Putting the pieces together we finally have an expression for the stream function produced by this panel of linear vortices:

$$\psi_{vij} = I1_{ij} \gamma_j + I2_{ij} (\gamma_{j+1} - \gamma_j) \tag{2.432}$$

$$= (I1_{ij} - I2_{ij}) \gamma_j + I2_{ij} \gamma_{j+1}, \tag{2.433}$$

where

$$I1_{ij} = \frac{1}{2\pi} \left[x_{ij}^* \ln r_{ij} - (x_{ij}^* - l_j) \ln r_{ij+1} + y_{ij}^* \beta_{ij} - l_j \right] \tag{2.434}$$

$$I2_{ij} = \frac{x_{ij}^*}{l_j} I1 + \frac{1}{4\pi l_j} \left[r_{i,j+1}^2 \left(\ln r_{i,j+1} - \frac{1}{2} \right) - r_{ij}^2 \left(\ln r_{ij} - \frac{1}{2} \right) \right]. \tag{2.435}$$

We must be careful when the evaluation point lies on the panel ($i = j$ or $i = j + 1$). In these cases the argument to the log function will be zero. However, whenever the argument to the log is zero, the term multiplying that log would also be zero, so each term remains well-defined, and the stream function is always bounded.

The only new terms that we have, compared to the last section, are x^* and y^*. We can easily compute the distances in the global coordinate system:

$$x_{ij} = x_i - x_j \tag{2.436}$$

$$y_{ij} = y_i - y_j, \tag{2.437}$$

which we then rotate to our panel coordinate system:

$$x^*_{ij} = x_{ij} \cos\theta_j + y_{ij} \sin\theta_j \tag{2.438}$$

$$y^*_{ij} = -x_{ij} \sin\theta_j + y_{ij} \cos\theta_j. \tag{2.439}$$

When reusing the prior equations for the other terms, we should keep in mind that point i now refers to a panel endpoint and not a panel center.

Special treatment is needed at the trailing edge. Most airfoils have a gap at the trailing edge, and XFOIL uses a trailing-edge panel with sources and vortices across that gap. This is needed to prevent flow into the trailing-edge gap and to enable smooth streamlines toward the trailing edge. For simplicity in our present discussion, we'll restrict our attention to sharp airfoils. In this case we have a redundant equation (sinces nodes 1 and nodes $N+1$ are identical). That $N+1$ equation is replaced by an extrapolation, using the three points closest to the trailing edge. This extrapolation uses the difference in γ between the upper and lower surfaces, and assumes that the middle difference is the average of the differences to either end (TODO: figure):

$$\frac{(\gamma_{N+1} - \gamma_1) + (\gamma_{N-1} - \gamma_3)}{2} = \gamma_N - \gamma_2. \tag{2.440}$$

Or in other words:

$$\gamma_1 - 2\gamma_2 + \gamma_3 - \gamma_{N-1} + 2\gamma_N - \gamma_{N+1} = 0. \tag{2.441}$$

We also have to modify our calculation of logarithms for the coincident points (in a similar manner to where the evaluation point lies on the panel).

With our stream functions defined, we can now define our boundary condition. We would like the outer boundary of the airfoil to be a streamline, and thus by definition the stream function must be a constant (but yet unknown) value ψ_0 at each node on the airfoil surface. We now have $N+2$ unknowns for N panels: $N+1$ unknowns for the values of γ defined at the panel endpoints, and ψ_0. The stream function condition applied at each node provides $N+1$ equations and our final equation is the Kutta condition. In the prior section we set the tangential velocities as equal at the trailing edge panels (or rather as equal and opposite given our sign convention on the tangential direction). In this case we set the vortex strengths as equal and opposite, which would produce the same desired condition on the tangential velocities:

$$\gamma_1 = -\gamma_{N+1}. \tag{2.442}$$

The total stream function at node i is the sum of the freestream, the contribution from the vortices on each panel (Eq. 2.433):

$$\psi_0 = \psi_{\infty_i} + \sum_{j=1}^{N} (I1_{ij} - I2_{ij})\gamma_j + I2_{ij}\gamma_{j+1}. \tag{2.443}$$

This is a linear equation of our unknowns of the form:

$$\psi_0 + A_{ij}\gamma_j = \psi_{\infty_i}, \tag{2.444}$$

where

$$A_{ij} = \begin{cases} -I1_{i,1} + I2_{i,1} & \text{if } j = 1 \\ -I2_{i,N+1} & \text{if } j = N+1 \\ -I1_{i,j} + I2_{i,j} - I2_{i,j-1} & \text{otherwise} \end{cases}. \tag{2.445}$$

We can now assemble the stream function condition and the Kutta condition in a single matrix. Note that we replaced the $N+1$ row with the extrapolation for a sharp trailing edge, and then appended the row for the Kutta condition.

$$\begin{bmatrix} A_{1,1} & & \cdots & & A_{1,N+1} & 1 \\ \vdots & & \vdots & & \vdots & \vdots \\ A_{N,1} & & \cdots & & A_{N,N+1} & 1 \\ 1 & -2 \quad 1 & 0 \cdots 0 & -1 \quad 2 & -1 & 0 \\ 1 & 0 \quad 0 & 0 \cdots 0 & 0 \quad 0 & 1 & 0 \end{bmatrix} \begin{bmatrix} \gamma_1 \\ \vdots \\ \gamma_{N+1} \\ \psi_0 \end{bmatrix} = \begin{bmatrix} \psi_{\infty_1} \\ \vdots \\ \psi_{\infty_N} \\ 0 \\ 0 \end{bmatrix}. \tag{2.446}$$

For convenience we will refer to this augmented matrix as $\tilde{A}$ and thus, the entire matrix problem can be expressed as:

$$\tilde{A}x = b. \tag{2.447}$$

Often, one wants to evaluate at multiple angles of attack and this can be done efficiently by separating out the angle of attack dependence. The only place the angle of attack appears is in the freestream contributions (Eq. 2.406), which can be expressed as:

$$\psi_{\infty_i} = k_{1i}\cos\alpha + k_{2i}\sin\alpha, \tag{2.448}$$

where $k_1 = V_\infty y_i$ and $k_2 = -V_\infty x_i$. Or in other words:

$$\tilde{A}x = b_1\cos\alpha + b_2\sin\alpha, \tag{2.449}$$

where b_1 is the right-hand side of Eq. 2.446 using only the k_1 terms (and similarly for b_2). The solution is:

$$x = \tilde{A}^{-1}b_1\cos\alpha + \tilde{A}^{-1}b_2\sin\alpha. \tag{2.450}$$

We see that the first linear solve is exactly the original problem but with $\alpha = 0$ whereas the second linear solve is the original problem with $\alpha = \pi/2$. Thus, rather than executing a new linear solve for every angle of attack, we can instead precompute two linear solves then obtain solutions at other angles of attack through inexpensive weighted vector sum:

$$x = \tilde{A}^{-1}b\big|_{\alpha=0} \cos\alpha + \tilde{A}^{-1}b\big|_{\alpha=\pi/2} \sin\alpha. \tag{2.451}$$

We now have a solution for γ, and fortunately obtaining the tangential velocity is far easier in this case than the last section. Previously, we derived the tangential velocity across a panel of constant vorticity (see u_v^* in **??**). Just above the panel the tangential velocity is $\gamma/2$ and just below it is $-\gamma/2$ and so the discontinuous jump in tangential velocity across the panel is γ. These relationship holds generally, across any vortex sheet. Consider the infinite vortex sheet shown and the contour shown in **??**. If we compute the contour integral for circulation (Eq. 2.75) and equate that the circulation contained in the contour (where γ is the strength per unit length) we have:

$$\Gamma = V_{tu}l - V_{tl}l = \gamma l \tag{2.452}$$

or in other words the vorticity γ is equivalent to the jump in tangential velocity across the sheet.

$$\gamma = \Delta V_t \tag{2.453}$$

In more general cases, like in our panel where we have linearly varying vorticity, γ represents the local jump in tangential velocity.

Lamb observes that for an enclosed solid boundary (e.g., $\partial\phi/\partial n = 0$ everywhere on the boundary), if there are no singularities inside the boundary, then the velocity must be zero everywhere in the interior (otherwise continuity would be violated since there is no flow across the boundary).[10] If the internal velocity is zero, our external tangential velocity is then precisely γ.

10. Lamb, *Hydrodyamics*, 1945.

$$V_{ti} = \gamma_i \tag{2.454}$$

We also already know that the normal velocity is zero so we can directly compute the pressure coefficient (Eq. 2.28) at each node:

$$C_p(x_i, y_i) = 1 - \left(\frac{\gamma_i}{V_\infty}\right)^2 \tag{2.455}$$

We can easily integrate the linear variation in circulation along each panel to obtain the total circulation:

$$\Gamma = \sum_{i=1}^{N} \frac{1}{2}(\gamma_i + \gamma_{i+1})l_i, \tag{2.456}$$

from which we can obtain the lift coefficient as before.

Pitching moment is a little more work because if the vorticity is linear then the pressure varies quadratically (Eq. 2.455). In the prior section we found that normal force contribution of panel i is (see Eq. 2.383 before we make the assumption that C_p is constant over the panel):

$$c_{n\,i} = -\frac{1}{c}\int_{\text{panel}} C_p dx \tag{2.457}$$

and the axial force contribution is:

$$c_{a\,i} = \frac{1}{c}\int_{\text{panel}} C_p \frac{dy}{dx} dx \tag{2.458}$$

It we use the relationships $dx = ds\cos\theta$ and $dy = ds\sin\theta$, so that we can change the expressions to integrals along the panel, then the force coefficient contributions become:

$$c_{n\,i} = -\frac{\cos\theta_i}{c}\int_0^{l_i} C_p ds \tag{2.459}$$

$$c_{a\,i} = \frac{\sin\theta_i}{c}\int_0^{l_i} C_p ds \tag{2.460}$$

In both cases we need to integrate the pressure coefficient along a given panel:

$$\int_0^{l_i} C_p ds = \int_0^{l_i}\left[1 - \frac{1}{V_\infty^2}\left(\gamma_i + (\gamma_{i+1} - \gamma_i)\frac{s}{l_i}\right)^2\right] ds \tag{2.461}$$

$$= l_i - \frac{1}{V_\infty^2}\int_0^{l_i}\left(\gamma_i^2 + 2\gamma_i(\gamma_{i+1} - \gamma_i)\frac{s}{l_i} + (\gamma_{i+1} - \gamma_i)^2\frac{s^2}{l_i^2}\right) ds \tag{2.462}$$

$$= l_i - \frac{1}{V_\infty^2}\left(\gamma_i^2 l_i + \gamma_i(\gamma_{i+1} - \gamma_i)l_i + (\gamma_{i+1} - \gamma_i)^2\frac{l_i}{3}\right) \tag{2.463}$$

$$= l_i\left[1 - \frac{1}{V_\infty^2}\left(\gamma_i\gamma_{i+1} + \frac{(\gamma_{i+1} - \gamma_i)^2}{3}\right)\right] \tag{2.464}$$

We can now use the same equations in the prior section to compute pitching moment (Eqs. 2.388 and 2.389).

Example 2.15 Simple airfoil verification.

We'll again use a simple airfoil in order to check your implementation of this linear vortex method. We need more points than the diamond airfoil for the extrapolation condition. And since we've restricted ourselves to sharp airfoils we need to ensure the first and last point are the same. We use the an angle of attack of 5° with $V_\infty = 1$ for the following airfoil coordinates:

x	y
1.0	0
0.6	-0.02
0.3	-0.03
0	0
0.3	0.07
0.6	0.04
1.0	0

Below we list various intermediate values to facilitate checking your implementation:

$$\beta = \begin{bmatrix} 3.14159 & -0.00712746 & -0.0428309 & -0.0996687 & 0.0 & 0.0 \\ 3.14159 & 3.14159 & -0.066642 & -0.258136 & -1.27934 & -1.52084 \\ -0.00950994 & 3.14159 & 3.14159 & -1.47113 & -1.34156 & -0.186401 \\ -0.033321 & -0.0663477 & 3.14159 & 3.14159 & -0.162664 & -0.0665682 \\ -0.191788 & -1.27934 & -1.34156 & 3.14159 & 3.14159 & 0.0 \\ -1.47113 & -1.34156 & -0.162664 & -0.166237 & 3.14159 & 3.14159 \\ 3.14159 & -0.00712746 & -0.0428309 & -0.0996687 & 0.0 & 3.14159 \end{bmatrix} \tag{2.465}$$

$$r = \begin{bmatrix} 0.0 & 0.4005 & 0.700643 & 1.0 & 0.703491 & 0.401995 & 0.0 \\ 0.4005 & 0.0 & 0.300167 & 0.600333 & 0.313209 & 0.06 & 0.4005 \\ 0.700643 & 0.300167 & 0.0 & 0.301496 & 0.1 & 0.308058 & 0.700643 \\ 1.0 & 0.600333 & 0.301496 & 0.0 & 0.308058 & 0.601332 & 1.0 \\ 0.703491 & 0.313209 & 0.1 & 0.308058 & 0.0 & 0.301496 & 0.703491 \\ 0.401995 & 0.06 & 0.308058 & 0.601332 & 0.301496 & 0.0 & 0.401995 \\ 0.0 & 0.4005 & 0.700643 & 1.0 & 0.703491 & 0.401995 & 0.0 \end{bmatrix} \tag{2.466}$$

$$x^* = \begin{bmatrix} -0.0 & -0.400444 & -0.693541 & 0.973841 & 0.703491 & 0.401995 \\ 0.4005 & -0.0 & -0.297516 & 0.57976 & 0.307466 & 0.00597022 \\ 0.700625 & 0.300167 & 0.0 & 0.285335 & 0.00995037 & -0.291546 \\ 0.998752 & 0.599001 & 0.301496 & 0.0 & -0.291546 & -0.593042 \\ 0.695631 & 0.296835 & 0.00995037 & 0.308058 & 0.0 & -0.301496 \\ 0.397503 & -0.00199889 & -0.291546 & 0.593394 & 0.301496 & 0.0 \\ -0.0 & -0.400444 & -0.693541 & 0.973841 & 0.703491 & 0.401995 \end{bmatrix} \tag{2.467}$$

$$y^* = \begin{bmatrix} 0.0 & -0.00666297 & -0.0995037 & -0.22723 & 0.0 & 0.0 \\ 0.0 & 0.0 & -0.0398015 & -0.155815 & -0.0597022 & -0.0597022 \\ -0.00499376 & 0.0 & -0.0 & -0.0973841 & -0.0995037 & -0.0995037 \\ -0.0499376 & -0.0399778 & 0.0 & 0.0 & -0.0995037 & -0.0995037 \\ -0.104869 & -0.0999445 & -0.0995037 & 0.0 & 0.0 & 0.0 \\ -0.0599251 & -0.0599667 & -0.0995037 & -0.0973841 & 0.0 & 0.0 \\ 0.0 & -0.00666297 & -0.0995037 & -0.22723 & 0.0 & 0.0 \end{bmatrix} \tag{2.468}$$

$$I1 = \begin{bmatrix} -0.122068 & -0.0291163 & -0.00803766 & -0.0081575 & -0.0290569 & -0.122285 \\ -0.122068 & -0.105264 & -0.0392263 & -0.0395114 & -0.0899628 & -0.109876 \\ -0.0459208 & -0.105264 & -0.105518 & -0.0890045 & -0.085021 & -0.0456607 \\ -0.0148913 & -0.0389715 & -0.105518 & -0.106759 & -0.0387783 & -0.01492 \\ -0.0449497 & -0.0834872 & -0.085021 & -0.106759 & -0.105518 & -0.0458238 \\ -0.108706 & -0.0906997 & -0.0387783 & -0.0400367 & -0.105518 & -0.122285 \\ -0.122068 & -0.0291163 & -0.00803766 & -0.0081575 & -0.0290569 & -0.122285 \end{bmatrix} \tag{2.469}$$

$$I2 = \begin{bmatrix} -0.0450985 & -0.0123545 & -0.00260197 & -0.00551122 & -0.0167431 & -0.0771374 \\ -0.0769692 & -0.0406887 & -0.0168839 & -0.0223939 & -0.0518879 & -0.0442013 \\ -0.0273579 & -0.0645752 & -0.0407629 & -0.0497845 & -0.0374261 & -0.0185315 \\ -0.0101331 & -0.0221861 & -0.0647552 & -0.0411223 & -0.0167471 & -0.00477029 \\ -0.0266961 & -0.0467953 & -0.0374261 & -0.0656368 & -0.0407629 & -0.0184998 \\ -0.0649471 & -0.0384371 & -0.0167471 & -0.0228024 & -0.0647552 & -0.0451476 \\ -0.0450985 & -0.0123545 & -0.00260197 & -0.00551122 & -0.0167431 & -0.0771374 \end{bmatrix} \tag{2.470}$$

$$A = \begin{bmatrix} 0.0769692 & 0.0618602 & 0.0177902 & 0.00524826 & 0.017825 & 0.0618907 & 0.0771374 & 1.0 \\ 0.0450985 & 0.141544 & 0.063031 & 0.0340014 & 0.0604688 & 0.117563 & 0.0442013 & 1.0 \\ 0.0185629 & 0.0680466 & 0.12933 & 0.079983 & 0.0973794 & 0.0645553 & 0.0185315 & 1.0 \\ 0.00475824 & 0.0269185 & 0.062949 & 0.130392 & 0.0631535 & 0.0268968 & 0.00477029 & 1.0 \\ 0.0182536 & 0.0633879 & 0.0943902 & 0.0785483 & 0.130392 & 0.0680869 & 0.0184998 & 1.0 \\ 0.0437594 & 0.11721 & 0.0604683 & 0.0339814 & 0.0635653 & 0.141893 & 0.0451476 & 1.0 \\ 1.0 & -2.0 & 1.0 & 0.0 & -1.0 & 2.0 & -1.0 & 0.0 \\ 1.0 & 0.0 & 0.0 & 0.0 & 0.0 & 0.0 & 1.0 & 0.0 \end{bmatrix} \tag{2.471}$$

$$b = \left[-0.087156, -0.072217, -0.056033, 0.0, 0.043587, -0.012446, 0.0, 0.0\right]^T \tag{2.472}$$

$$x = \left[-0.713200, -0.947055, -1.198137, 0.629998, 1.517047, 1.123737, 0.713200, -0.107272\right]^T \tag{2.473}$$

$$C_p = \left[0.491346, 0.103087, -0.435532, 0.603103, -1.301433, -0.262786, 0.491346\right]^T \tag{2.474}$$

$$c_l \text{ (Kutta-Joukowski)} = 0.7159 \tag{2.475}$$

$$c_l \text{ (integration)} = 0.500 \tag{2.476}$$

$$c_{m_{qc}} = -0.0460. \tag{2.477}$$

Example 2.16 Convergence in number of panels.

We again consider the NACA 2412, but this time look at convergence in terms of the number of panels. We start with 8 panels and increase the number of panels all the way up to 1024 (though we only plot up to 512 for clarity). We use the XFOIL approach of this section, and the Hess-Smith approach of the prior section. For both approaches we discretize the airfoil once with linear spacing along x, and again with cosine spacing (see Section 2.8.3). The

convergence in lift coefficient (using the Kutta-Joukowski formula) with number of panels is shown in Fig. 2.70 on a semilog scale.

All converge towards the same value, but some converge much more quickly than others. The XFOIL results converge faster than the Hess-Smith results. That is expected as XFOIL uses linear distributions for the singularities, whereas the Hess-Smith method only uses constant distributions. For the XFOIL approach, cosine spacing converges much faster than linear spacing. For the Hess-Smith approach, cosine spacing doesn't seem to provide any advantage. The former converges from above, while the latter from below, but both with similar convergence rates.

Arbitrarily choosing 0.2% accuracy as our benchmark, we would require the following number of panels: 38 for XFOIL cosine spacing, 170 for XFOIL linear spacing, 200 for Hess-Smith cosine spacing, and 228 for Hess-Smith linear spacing.

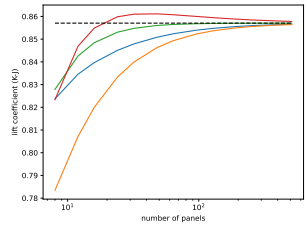

Fig. 2.70 Convergence of lift coefficient with number of panels using both linear and cosine spacing. The dashed line shows the value all the curves asymptote towards.

Viscous Flow

3

In the last chapter we saw that panel methods are an effective technique for irrotational flows, a reasonable assumption for attached, low speed flows, outside the boundary layer. To extend the utility of the methods we turn our attention to numerical methods for resolving boundary layers and computing drag.

By the end of this chapter you should be able to:

1. TODO

3.1 Boundary Layer Fundamentals

Recall the discussion on shear stress and the no slip condition discussed in Section 1.3. The shear stress is proportional to the velocity gradients (Eq. 1.10). Because the velocity is zero at a solid wall, near the wall the velocity gradients will be large, and thus the shear stresses will be large. For a streamlined body, only this near-wall region has large enough velocity gradients to be significantly affected by viscosity — a region we call the *boundary layer*. It is called the boundary layer because it only occurs near the boundary of the solid object, and is generally small relative to the size of the body.

Within the boundary layer viscous effects must be included. Outside of the boundary layer, assuming the flow is not separated, we can treat the flow as inviscid. This behavior allows us to re-use the inviscid flow behavior studied in the previous chapter, with some modifications confined to a small region. To be clear, the behavior is continuous and there is no actual clear line that divides viscous behavior from inviscid. Still, it will be useful to define a boundary layer "height", and we will discuss a few definitions for boundary layer size in this chapter.

For blunt bodies, or streamlined bodies at high angles of attack (which act like a blunt body), flow separation occurs and a wake develops. Once flow separation occurs there is no longer a reasonably defined boundary layer and viscous behavior extends across a large

region comparable to the body size. We can no longer "correct" inviscid flow solutions as the viscous effects are widespread.

Figure 3.1 depicts many of the features seen in a boundary layer and viscous flows in general. For now we will just run through a quick overview, and subsequently will discuss these features in more detail. Starting from a stagnation point the boundary layer begins as laminar. Over some region the boundary layer instabilities become significant and the boundary layer transitions to a turbulent boundary layer. Eventually, the boundary layer will separate from the body and leave behind a wake. Ideally, for a streamlined body, this separation occurs right at the trailing edge of the body. From this figure we see two mechanism for drag. The first, is drag from the shear stresses acting over the body. We call this *skin-friction drag*. The second, is the momentum deficit caused by the wake and depicted on the right of Fig. 3.1. This deficit leads to a lower pressure on the aft end of the body, and we call this *pressure drag*. Pressure drag is primarily affected by the shape of the body. Note that while separation was shown as occurring after turbulent flow in Fig. 3.1, separation can sometimes occur in the laminar region.

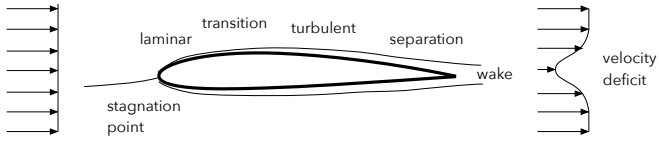

Fig. 3.1 Depiction of salient features for viscous flow around a body.

The word *laminar* suggests multiple laminae, or layers. Conceptually, it is meant to describe flow behavior that acts like multiple distinct layers passing over each other (i.e., slow layers near the wall and faster layers away from the wall). In laminar flow there is mixing across the layers, but it not readily visible as the mixing primarily occurs at molecular scales. In contrast a *turbulent* flow has unsteady mixing across multiple scales (small to large). Because the mixing occurs on larger scales the flow is affected across a larger region and thus the boundary layer height is larger as compared to laminar flow (see Fig. 3.2). Also because a turbulent boundary creates more mixing, the velocity gradient is larger at the wall, and thus the shear stress at the wall is also larger (see again Fig. 3.2).

The shear stress at the wall is given by:

$$\tau_w = \mu \left.\frac{\partial u}{\partial y}\right|_{y=0} \tag{3.1}$$

Because we are often interested in normalized values, we normalize

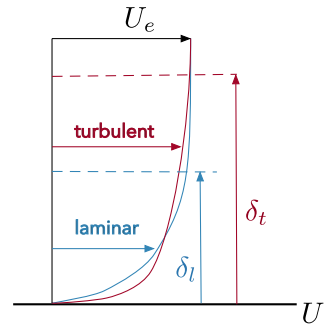

Fig. 3.2 An overlaid laminar and turbulent boundary layer.

this shear stress and call it the *skin friction coefficient*:

$$c_f = \frac{\tau_w}{\frac{1}{2}\rho V_e^2} \tag{3.2}$$

where V_e is called the *edge velocity*, or the velocity just outside of the boundary layer in the inviscid region. Note that the edge velocity, unlike freestream velocity, is a local quantity. It changes as the inviscid flow accelerates and decelerates around the body.

Transition refers to the change from a laminar boundary layer to a turbulent one. We often think of transition occurring at a specific point, but it really occurs over a region. The mechanism of transition is the growth of instabilities in the boundary layer. (TODO: figure) For low Reynolds number instabilities are damped (the viscous forces are high relative to inertial) and the flow remains laminar. For high Reynolds numbers the instabilities are amplified causing the large-scale mixing of turbulent flow. For a flat plate, transition occurs at a Reynolds number of approximately: $Re = 2 \times 10^5$–3×10^6. As the flow progresses over a solid surface, the length of the boundary layer becomes longer, and thus the local Reynolds number grows, eventually leading to transition.

Several factors influence transition. The freestream conditions are a significant factor. If the incoming flow is already highly turbulent, then transition will occur more quickly. Pressure gradients are a major factor. Even a very small adverse gradient can cause transition. The surface roughness of the body is another major factor. A rougher surface will amplify instabilities and lead to earlier transition. As discussed in the paragraphs following Ex. 1.3, sometimes roughness elements are intentionally added over a wing to trigger turbulent flow. Heat transfer is a less common, but potentially important factor. Cooling can be used to stabilize a boundary layer.* Suction and blowing is an active strategy that is sometimes used to delay boundary layer transition. A device is oriented normal to a wall, sucking in the slow moving air particles near the wall. This results in a more stable boundary layer. (TODO: show the math). Blowing injects momentum in the streamwise direction stabilizing the boundary layer.

*We'll discuss why cooling stabilizes in Section 3.5, after we've developed some boundary layer theory.

Separation refers to the flow detaching from the surface and creating a wake. The process is depicted in Fig. 3.3. Recall the discussion surrounding Fig. 1.8 regarding an adverse pressure gradient. In an adverse pressure gradient, the fluid near the wall slows down until eventually the velocity gradient is zero (vertical), the flow separates, and after that point the flow near the wall may be reversed in the eddies of the resultant wake. Because the velocity gradient is zero at the point of separation, the shear stress is also zero (Eq. 3.1). Checking

for zero shear stress is one way to detect separation numerically. This fact also explains why one should avoid creating stagnation points in an adverse pressure gradient. Slowing the velocity to zero means the flow is guaranteed to separate. A common engineering solution is to use a fairing to avoid the stagnation.

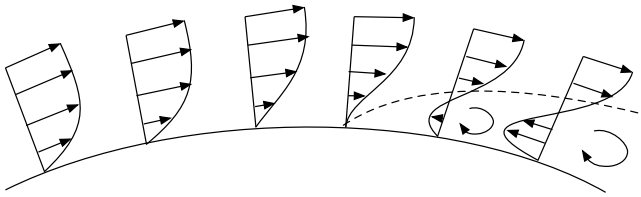

Fig. 3.3 Fluid near the wall slows down until eventually it separates.

Separation generally leads to a massive increase in drag, and a significant drop in lift. Once separation occurs, the flow may reattach, especially if it occurs early on the body. When this occurs, the separation and reattachment points envelope a recirculating region known as a *separation bubble* (and because this has to occur early on the body to provide a chance to reattach, it usually separates in the laminar region, becomes turbulent then reattaches, and is called a laminar separation bubble).

As shown in Fig. 3.2, a turbulent boundary layer has higher velocities closer to the surface, and is thus more resistant to separation. This creates a common design tradeoff where turbulent flow may be desirable in delaying pressure drag increases, but at a cost of higher skin friction drag. A classic example of using this tradeoff beneficially is in the design of a golf ball. From Fig. 1.8 we note the large drop in drag for a cylinder, which occurs after the transition to turbulence. This is because the turbulent boundary layer separates further back over the sphere, resulting in a smaller wake, and less pressure drag. For higher Reynolds numbers, the skin friction drag grows and so the curve starts to rise again.

For a streamlined body the pressure drag is (hopefully) significantly smaller than the skin friction drag, and so more substantial laminar flow may be desirable. However, a 100% laminar flow airfoil is not very useful. For a laminar body to not separate it would have to be made very thin and be restricted to a narrow range of small lift coefficients. So although laminar flow is desirable to a point, we still want the airfoil to transition to turbulent flow at some point, so that it is more robust against separation across various conditions. Even if separation does not occur, the presence of viscosity can significantly alter the pressure distribution (or equivalently can be thought of as altering the effective

shape of the body). We will revisit this idea again later in this chapter.

While the discussion of this section focused on drag, as that is the primary effect of viscosity, it also affects the lift. Notably the lift curve slope is often slightly reduced by the presence of viscosity. And, once separated, a precipitous drop in lift occurs, which is known as *stall* (see Fig. 3.4).

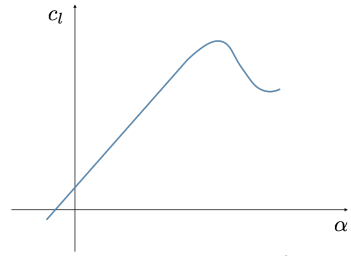

Fig. 3.4 Viscosity causes a reduction in lift curve slope and flow separation causes stall. (TODO: add a dashed line for inviscid slope)

3.2 Boundary Layer Equations

In this section we derive a simplified version of the Navier Stokes equations that is applicable within the boundary layer. We start with the steady, compressible, 2D Navier Stokes equations (neglecting the normal shear stresses τ_{xx} and τ_{yy}, which are typically insignificant).

$$\begin{aligned} \frac{\partial(\rho u)}{\partial x} + \frac{\partial(\rho v)}{\partial y} &= 0 \\ \rho\left(u\frac{\partial u}{\partial x} + v\frac{\partial u}{\partial y}\right) &= -\frac{\partial p}{\partial x} + \frac{\partial}{\partial y}\left[\mu\left(\frac{\partial u}{\partial y} + \frac{\partial v}{\partial x}\right)\right] \\ \rho\left(u\frac{\partial v}{\partial x} + v\frac{\partial v}{\partial y}\right) &= -\frac{\partial p}{\partial y} + \frac{\partial}{\partial x}\left[\mu\left(\frac{\partial u}{\partial y} + \frac{\partial v}{\partial x}\right)\right] \end{aligned} \tag{3.3}$$

In the boundary layer, we use the coordinate direction x to follow the surface that the boundary layer is developing on, and y as a direction normal to the local surface (Fig. 3.5). Our first assumption is that we can still use the Cartesian form of our governing equations shown above, but with our boundary layer definition of x and y, which are not actually Cartesian. This assumes that the boundary layer height is very small relative to the local radius of curvature, a reasonable assumption for most streamlined shapes (similar like the locally flat assumption of the ground we might use when predicting local behavior, even though the Earth surface is curved). A centrifugal pressure gradient term can be added if the curvature is significant, but for our purposes we will assume that it is not.

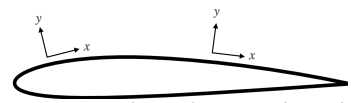

Fig. 3.5 Local coordinates in boundary layer that follow the profile of the blade.

Within the boundary layer we anticipate that some of the terms are much smaller than others, and thus can be neglected to give us a simplified set of equations appropriate for analysis only within the boundary layer. We derive this simplified set of equations by examining the order of magnitude of each term. We assume that the boundary layer height (δ) is much smaller than the distance the boundary layer covers (L). Those lengths also provide appropriate length scales for y and x respectively. We know that the horizontal velocity is V_e just outside the boundary layer, by definition, and zero at the surface, so a typical order of magnitude for the horizontal velocity is V_e. Then, from

an order-of-magnitude analysis using the continuity equation above (ignoring the minor changes in density), we know that the two terms must balance each other so we expect that:

$$\frac{V_e}{L} \propto \frac{v}{\delta} \tag{3.4}$$

Or, in other words:

$$v \propto \frac{\delta}{L} V_e \tag{3.5}$$

This provides us with a scale for the vertical velocities in the boundary layer, which we see will be much smaller than the horizontal velocities.

Examining the first and second terms of the x momentum equation, with an order of magnitude analysis, we expect that:

$$\rho u \frac{\partial u}{\partial x} \propto \frac{\rho V_e^2}{L} \tag{3.6}$$

and

$$\rho v \frac{\partial u}{\partial y} \propto \rho \frac{\delta}{L} V_e \frac{V_e}{\delta} \propto \frac{\rho V_e^2}{L} \tag{3.7}$$

Thus, we see that both of these inertial terms are of similar magnitudes.

Pressure just outside the boundary layer is proportional to the dynamic pressure of the edge velocity, so we assume that

$$\frac{\partial p}{\partial x} \propto \frac{\rho V_e^2}{L}, \tag{3.8}$$

which is also of the same magnitude.

The viscous terms are:

$$\frac{\partial}{\partial y}\left[\mu \frac{\partial u}{\partial y}\right] \propto \mu \frac{V_e}{\delta^2} \tag{3.9}$$

and

$$\frac{\partial}{\partial y}\left[\mu \frac{\partial v}{\partial x}\right] \propto \mu \frac{V_e}{L^2} \tag{3.10}$$

Comparing these two terms we see that the first is much larger than the second, and so the second term can be neglected within the boundary layer.

We know that we cannot neglect both viscous terms as compared to our inertial terms, otherwise this wouldn't be much of a boundary layer, so that means that those two terms must be of similar magnitudes:

$$\frac{\rho V_e^2}{L} \propto \mu \frac{V_e}{\delta^2} \tag{3.11}$$

or

$$\mu \propto \frac{\rho V_e \delta^2}{L} \tag{3.12}$$

We can express this in terms of a Reynolds number for the flow just outside the boundary layer:

$$\frac{\delta}{L} = \frac{1}{\sqrt{Re_L}} \tag{3.13}$$

where $Re_L = \rho V_e L/\mu$ In other words, are assumption that δ is small compared to L is analogous to assuming that the Reynolds number is large.

We now apply the same analysis to the y momentum equation. The order of magnitude analysis results in:

$$\rho u \frac{\partial v}{\partial x} \propto \frac{\rho V_e^2 \delta}{L^2} \tag{3.14}$$

$$\rho v \frac{\partial v}{\partial y} \propto \frac{\rho V_e^2 \delta}{L^2} \tag{3.15}$$

$$\frac{\partial p}{\partial y} \propto \frac{\rho V_e^2}{\delta} \tag{3.16}$$

$$\frac{\partial}{\partial x}\left[\mu \frac{\partial u}{\partial y}\right] \propto \frac{\rho V_e^2 \delta}{L^2} \tag{3.17}$$

$$\frac{\partial}{\partial x}\left[\mu \frac{\partial v}{\partial x}\right] \propto \frac{\rho V_e^2 \delta^3}{L^4} \tag{3.18}$$

If we factor out $\rho V_e^2/L$ from each term, for easier comparison, we see that the first, second, and fourth terms are of magnitude δ/L whereas the pressure term is of magnitude $1/(\delta/L)$, and the last is $(\delta/L)^3$. In other words, the pressure term is much larger than all the other terms and so we can neglect all others except pressure.

Dropping all of the small terms (one viscous term in x momentum, and all but the pressure term in the y momentum) results in the *boundary layer equations*:

$$\begin{aligned} \frac{\partial(\rho u)}{\partial x} + \frac{\partial(\rho v)}{\partial y} &= 0 \\ \rho\left(u\frac{\partial u}{\partial x} + v\frac{\partial u}{\partial y}\right) &= -\frac{\partial p}{\partial x} + \frac{\partial}{\partial y}\left(\mu\frac{\partial u}{\partial y}\right) \\ \frac{\partial p}{\partial y} &= 0 \end{aligned} \tag{3.19}$$

The last equation says that pressure is independent of y. In other words, at a given x location, the pressure at the surface of the object will be the same as the pressure at the edge of the boundary layer. This is quite fortunate as it means the pressure field we find from an inviscid solution is the same pressure felt directly by the body without modification by the boundary layer (as long as we account for the effective shape changes caused by the boundary layer—a topic discussed later). While the boundary layer equations are an approximation of the full Navier Stokes equations, experimental data supports this conclusion. If pressure is not dependent on y then it is only a function of x and the partial derivative becomes a total derivative:

$$\frac{\partial p}{\partial x} \rightarrow \frac{dp}{dx} \tag{3.20}$$

Furthermore, since the pressure just outside the boundary layer, is the same all the way through the boundary layer (not a function of y), then we can compute dp/dx just outside the boundary layer. If just outside the boundary layer, then we can assume the flow is inviscid and use Euler's equation. We use the subscript e to refer to "edge" properties, or in other words the inviscid solution just outside the boundary layer. Euler's equation gives:

$$\frac{dp}{dx} = -\rho V_e \frac{dV_e}{dx} \tag{3.21}$$

We substitute the above into the boundary layer equations.

$$\begin{aligned} &\frac{\partial(\rho u)}{\partial x} + \frac{\partial(\rho v)}{\partial y} = 0 \\ &\rho\left(u\frac{\partial u}{\partial x} + v\frac{\partial u}{\partial y}\right) = \rho V_e \frac{dV_e}{dx} + \frac{\partial}{\partial y}\left(\mu\frac{\partial u}{\partial y}\right) \end{aligned} \tag{3.22}$$

If will also make the assumption of incompressibility then we can pull density out of the first equation, and viscosity can come out of the derivative (normally it is a function of temperature, but if the flow is incompressible then temperature is constant).

$$\begin{aligned} &\frac{\partial u}{\partial x} + \frac{\partial v}{\partial y} = 0 \\ &u\frac{\partial u}{\partial x} + v\frac{\partial u}{\partial y} = V_e \frac{dV_e}{dx} + \nu\frac{\partial^2 u}{\partial y^2} \end{aligned} \tag{3.23}$$

Keep in mind, that V_e is not an unknown, but rather an input from the outer inviscid solution.

This set of equations is still nonlinear, but it is easier to solve than the original Navier Stokes equations. The Navier Stokes are an *elliptic* PDE because it contains second derivatives in both x and y. Physically, an elliptic PDE requires defining boundary conditions in all directions. The boundary layer equations are a *parabolic* PDE because second derivatives only appear in one variable, y. Parabolic PDEs do not require boundary conditions in all directions, but instead can use a "time" marching approach (like the wave equation). That means we just need to specify conditions on one end (i.e., upstream), and then we can march the solution downstream.

Even though the equations are simpler, few analytic solutions exist. We will explore one of these, but for the most part these analytic solutions are of less interest as their pertain to simplified geometries and flow conditions. Typically we are interested in arbitrary geometries and so will use numerical solutions to solve for boundary layers. These methods are useful as long as the boundary layers remain attached, and do not have excessive curvature.

3.2.1 Displacement and Momentum Thickness

While we have talked about the "height" of the boundary layer, it is not clear how we should quantify this, and in fact multiple approaches exist. The two most important ones are the displacement thickness and the momentum thickness. The displacement thickness is the distance we would need to displace the wall so that an exterior inviscid flow (i.e., at V_e) would have the same mass flow rate as that actual flow. For example, the left side of Fig. 3.6 shows a boundary layer, and the mass flow deficit is the area colored in red. On the right side of figure we have an inviscid flow with the body displaced just enough so that the red area is equal to corresponding area on the left. From the above definition, δ^* is the height of the red rectangle on the right.

The mass flow rate on the left is:

$$\dot{m} = \int_0^h \rho u dy \tag{3.24}$$

and on the right the mass flow rate is (we keep the first term as an integral for convenience in the rest of the derivation):

$$\int_0^h \rho_e V_e dy - \rho_e V_e \delta^* \tag{3.25}$$

We now equate these two mass flow rates:

$$\int_0^h \rho u dy = \int_0^h \rho_e V_e dy - \rho_e V_e \delta^* \tag{3.26}$$

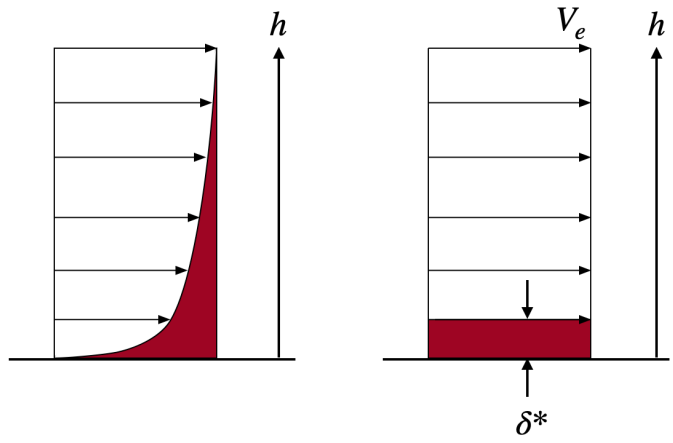

Fig. 3.6 A depiction of displacement thickness, where the actual flow is on the left, and the idealized displacement thickness is shown on the right.

Rearraning:

$$\rho_e V_e \delta^* = \int_0^h (\rho_e V_e - \rho u) dy \tag{3.27}$$

Then solving for δ^* gives:

$$\delta^* = \int_0^h \left(1 - \frac{\rho u}{\rho_e V_e}\right) dy \tag{3.28}$$

As $y \to h$ the term $\rho u \to \rho_e V_e$ and so the integrand approaches zero. Thus, we can extend the integration limits without changing the result. By convention, since the end limit h is not precise, the integration is extended to infinity.

$$\delta^* = \int_0^\infty \left(1 - \frac{\rho u}{\rho_e V_e}\right) dy \tag{3.29}$$

If incompressible, then the densities cancel out.

One physical meaning of the displacement thickness is that it tells us how much larger we should to make the body in the inviscid flow simulation to simulate the presence of the boundary layer (Fig. 3.7). The actual viscous flow experiences a decrease in mass flow because of the boundary layer, which could be treated as an inviscid flow around a larger body (larger by the displacement thickness).

Thus, one approach to account for the boundary layer is to first solve the inviscid flow (e.g., panel method) with the original body to get V_e, then solve the boundary layer equations to get δ^*, next modify the body shape using the displacement thickness, and repeat the process as needed. The main difficulty with this approach is that it requires modifying the geometry and repaneling the geometry, which can be challenging and computationally expensive.

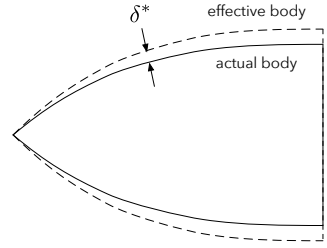

Fig. 3.7 The displacement thickness provides an "effective" shape for the body in a viscous flow.

An easier, and more common approach, is to keep the geometry as is but modify the boundary condition using the *transpiration velocity*. For the original inviscid flow solution the surface boundary condition is the no flow through condition $V_n = 0$. However, with a boundary layer we are actually solving the inviscid solution outside of the boundary layer, and at the edge of the boundary layer the normal velocity is not necessarily zero. Thus, if can find an expression for V_n we can use our original geometry but modify the boundary condition.

To find an appropriate value for V_n, we first apply the continuity equation in the boundary layer:

$$\frac{\partial(\rho u)}{\partial x} + \frac{\partial(\rho v)}{\partial y} = 0 \tag{3.30}$$

and in the external flow:

$$\frac{\partial(\rho_e V_e)}{\partial x} + \frac{\partial(\rho_e V_n)}{\partial y} = 0 \tag{3.31}$$

where V_n is the normal velocity We subtract the second equation from the first, and integrate across the boundary layer.

$$\int_0^h \frac{\partial}{\partial x}(\rho_e V_e - \rho u)dy = \int_0^h \frac{\partial}{\partial y}(\rho v - \rho_e V_n)dy \tag{3.32}$$

The order of differentiating and integrating can be swapped for the first term, and in the second term the integral and differentiation cancel out.

$$\frac{\partial}{\partial x}\left[\rho_e V_e \left(\int_0^h \left(1 - \frac{\rho u}{\rho V_e}\right) dy\right)\right] = [\rho v - \rho_e V_e]_0^h \tag{3.33}$$

$$= (\rho_e V_n - \rho_e V_n) - (0 - \rho_e V_n) \tag{3.34}$$

$$= \rho_e V_n \tag{3.35}$$

The term in parenthesis on the left is the displacement thickness. Thus, we have our new boundary condition:

$$V_n = \frac{1}{\rho_e}\frac{d}{dx}(\rho_e V_e \delta^*) \tag{3.36}$$

For incompressible flow this simplifes to:

$$V_n = \frac{d}{dx}(V_e \delta^*) \tag{3.37}$$

The alternate procedure then is to analyze the geometry using an inviscid analysis to obtain V_e, then solve the boundary layer equations

to obtain δ^*, next reanalyze the inviscid analysis using the modified boundary condition (with fixed geometry/paneling), and repeat as needed. Rather than a fixed point iteration, a more effective approach is to solve the equations in a coupled manner using Newton's method.

An alternative measure of boundary layer height is the momentum thickness, which we call θ. This is the distance we would need to displace the wall so that an exterior inviscid flow (i.e., at V_e) would have the same momentum flow rate as that actual flow.

On the left of Fig. 3.8 the true momentum flow rate is:

$$\int_0^h \rho u^2 dy \tag{3.38}$$

On the right side the momentum flow of this hypothetical scenario is:

$$\dot{m} V_e - \rho_e V_e^2 \theta \tag{3.39}$$

where the mass flow rate is reduced because of the displacement as shown in Eq. 3.24. Inserting that equation gives the following for the

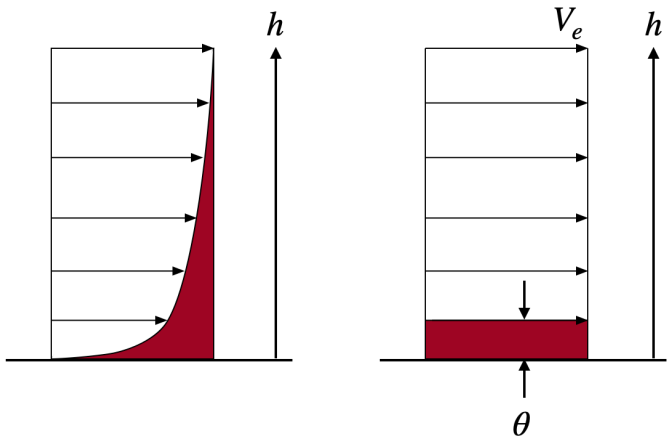

Fig. 3.8 A depiction of momentum thickness, where the actual flow is on the left, and the idealized momentum thickness is shown on the right.

right hand side:

$$\int_0^h \rho u V_e dy - \rho_e V_e^2 \theta \tag{3.40}$$

Equating the two momentum flow rates gives:

$$\int_0^h \rho u^2 dy = \int_0^h \rho u V_e dy - \rho_e V_e^2 \theta \tag{3.41}$$

Rearranging

$$\rho_e V_e^2 \theta = \int_0^h (\rho u V_e - \rho u^2) dy \tag{3.42}$$

then solving for θ and again extending the upper limit to infinity gives:

$$\theta = \int_0^\infty \frac{\rho u}{\rho_e V_e}\left(1 - \frac{u}{V_e}\right) dy \tag{3.43}$$

The primary usefulness of the momentum thickness is that it is a measure of momentum deficit, and thus is directly related to drag. For example, the skin friction drag on a flat plate is proportional to the momentum thickness at the end of the plate:

$$D' = \rho V_e^2 \theta_L \tag{3.44}$$

where θ_L indicates the momentum thickness at $x = L$.

3.2.2 Laminar Flat Plate: Blasius Solution

There are a few analytic solutions to the boundary layer equations, and one that is particularly useful is the Blasius solution. It is a solution to laminar, incompressible, boundary layers over a flat plate with no pressure gradient. In this text we are less interested in analytic solutions to simple geometries and more interested in numerical solutions around arbitrary shapes so we will skip the derivation.

The results are:

$$\delta^* = \frac{1.72x}{\sqrt{Re_x}} \tag{3.45}$$

$$\theta = \frac{0.664x}{\sqrt{Re_x}} \tag{3.46}$$

where

$$Re_x = \frac{\rho V x}{\mu} \tag{3.47}$$

is the local Reynolds number.

The local skin friction coefficient is:

$$c_f = \frac{\tau}{q_\infty} = \frac{0.664}{\sqrt{Re_x}} \tag{3.48}$$

and the total skin friction coefficient, integrated across the plate, is:

$$C_f = \frac{1}{q_\infty L}\int_0^L \tau dx = \frac{1}{L}\int_0^L c_f dx = \frac{1.328}{\sqrt{Re_L}} \tag{3.49}$$

Notice the $1/\sqrt{x}$ behavior of the skin friction coefficient, suggesting that most of the skin friction drag occurs near the leading edge (at least within the laminar portion of the boundary layer).

The boundary layer equations can be solved for compressible laminar boundary layers also, but the result is a set of coupled ODEs that requires a numerical solution.

3.2.3 Turbulent Flat Plate: Schlichting

There is no analytic solution to turbulent boundary layers, so instead we rely on empirical fits. There are many such fits, one popular one was developed by Schlichting for turbulent incompressible boundary layers on flat plates without a pressure gradient.

$$\delta^* = \frac{0.046x}{Re_x^{0.2}} \tag{3.50}$$

$$\theta = \frac{0.036x}{Re_x^{0.2}} \tag{3.51}$$

$$c_f = \frac{0.0592}{Re_x^{0.2}} \tag{3.52}$$

$$C_f = \frac{0.074}{Re_L^{0.2}} \tag{3.53}$$

Notice that, as expected, the boundary layer height and skin friction increases faster with x for a turbulent boundary layer as opposed to laminar.

3.2.4 Momentum Integral Equation

Exact solutions of the boundary layer equations are difficult to impossible in general cases. One of the main quantities we are interested in, with regards to a boundary layer analysis, is drag. An integral approach allows us to approximate the skin friction drag in a boundary layer. Just like differential and integral forms of the governing equation are both useful, we will derive an integral form of the mass and momentum equations within the boundary layer.

We consider a general case, and only at the end simplify for incompressible flow. Consider a control volume as shown in Fig. 3.9 for a small slice of the boundary layer. The control volume has a small width $\Delta x \to 0$, and it extends until the boundary layer reaches the edge velocity (or using standard boundary layer notation as $y/\delta \to \infty$). We will apply a mass and momentum balance to this control volume.

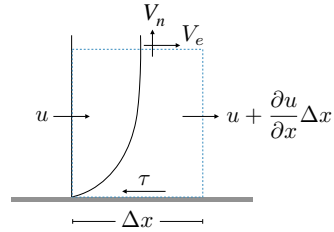

Fig. 3.9 A control volume within a boundary layer.

Steady mass balance:

The standard equation for a steady mass balance is:

$$\int \rho \vec{V} \cdot d\vec{A} = 0 \tag{3.54}$$

There is a boundary layer profile coming in on the left, and a different one leaving on the right, and there is also potentially some vertical

velocity V_n of unknown magnitude and sign leaving through the top of the control volume as noted on the figure.

$$-\int_0^h \rho u dy + \int_0^h \left(\rho u + \frac{\partial(\rho u)}{\partial x}\Delta x\right) dy + \rho_e V_n \Delta x = 0 \tag{3.55}$$

The first integral cancels with part of the second integral, and then Δx cancels out of the remaining terms leaving:

$$\int_0^h \frac{\partial(\rho u)}{\partial x} dy + \rho_e V_n = 0 \tag{3.56}$$

Thus, we can solve for the unknown vertical velocity at the edge of the boundary layer.

$$V_n = -\frac{1}{\rho_e}\int_0^h \frac{\partial(\rho u)}{\partial x} dy \tag{3.57}$$

Steady momentum balance in the x-direction:

The general form for a steady momentum balance in the x-direction is:

$$\int \rho V_x(\vec{V}\cdot d\vec{A}) = -\int p d\vec{A}_x + F_x \tag{3.58}$$

Applying to our situation yields:

$$\begin{aligned} -\int_0^h \rho u^2 dy + \int_0^h \left(\rho u^2 + \frac{\partial(\rho u^2)}{\partial x}\Delta x\right) dy + V_e \rho_e V_n \Delta x = \\ \int_0^h p dy - \int_0^h \left(p + \frac{\partial p}{\partial x}\Delta x\right) dy - \tau \Delta x \end{aligned} \tag{3.59}$$

Most of the terms are straightforward. The mass flow rate out of the top is the same, but is multiplied by its x-component of velocity V_e. The pressure on the top surface is unknown, but because it is a vertical face it does not contribute any force in the x-direction. The shear stress creates a force on the fluid in the negative x-direction.

We can cancel terms just like in the mass balance:

$$\int_0^h \frac{\partial(\rho u^2)}{\partial x} dy + V_e \rho_e V_n = -\int_0^h \frac{\partial p}{\partial x} dy - \tau \tag{3.60}$$

Solving for τ and substituting in V_n from the mass balance (Eq. 3.57) gives the following expression for the shear stress:

$$\tau = -\int_0^h \frac{\partial p}{\partial x} dy - \int_0^h \frac{\partial(\rho u^2)}{\partial x} dy + V_e \int_0^h \frac{\partial(\rho u)}{\partial x} dy \tag{3.61}$$

Euler (outside boundary layer)

We can remove the pressure by using the 1D Euler momentum equation in differential form. Because we are considering the flow outside of the boundary layer, the flow is inviscid and so the Euler equation applies:

$$dp = -\rho V dV \tag{3.62}$$

Thus,

$$\frac{dp_e}{dx} = -\rho_e V_e \frac{dV_e}{dx} \tag{3.63}$$

The pressure derivative in Eq. 3.61 is actual a total derivative (and not a partial derivative) because according to the boundary layer approximation ($dp/dy = 0$) so p is only a function of x. Also the value of p is constant across the boundary layer (thus $p(x) = p_e(x)$. Thus, we can substitute this equation directly in.

Simplifying

Substituting this result back into Eq. 3.61 yields

$$\tau = \int_0^h \rho_e V_e \frac{dV_e}{dx} dy - \int_0^h \frac{\partial(\rho u^2)}{\partial x} dy + V_e \int_0^h \frac{\partial(\rho u)}{\partial x} dy \tag{3.64}$$

We can swap out the last term by using the chain rule:

$$\frac{\partial(\rho u V_e)}{\partial x} = \rho u \frac{\partial V_e}{\partial x} + V_e \frac{\partial(\rho u)}{\partial x} \tag{3.65}$$

Rearranging:

$$V_e \frac{\partial(\rho u)}{\partial x} = \frac{\partial(\rho u V_e)}{\partial x} - \rho u \frac{\partial V_e}{\partial x} \tag{3.66}$$

Substituting this result into Eq. 3.64 (and noting that V_e does not vary with y by definition and so the derivative is a total derivative) yields:

$$\tau = \int_0^h \rho_e V_e \frac{dV_e}{dx} dy - \int_0^h \frac{\partial(\rho u^2)}{\partial x} dy + \int_0^h \left(\frac{\partial(\rho u V_e)}{\partial x} - \rho u \frac{dV_e}{dx} \right) dy \tag{3.67}$$

We now collect like terms

$$\tau = \int_0^h (\rho_e V_e - \rho u) \frac{dV_e}{dx} dy + \int_0^h \frac{\partial(\rho u (V_e - u))}{\partial x} dy \tag{3.68}$$

In the first integral we note that dV_e/dx is independent of y and can thus be pulled out of the integral. We then multiply and divide that term by

$\rho_e V_e$. For the second integral, we reverse the order of integration and differentiation, and multiply and divide that term by $\rho_e V_e^2$

$$\tau = \frac{dV_e}{dx}\rho_e V_e \int_0^h \left(1 - \frac{\rho u}{\rho_e V_e}\right) dy + \frac{\partial}{\partial x}\left(\rho_e V_e^2 \int_0^h \frac{\rho u}{\rho_e V_e}\left(1 - \frac{u}{V_e}\right) dy\right) \tag{3.69}$$

We see that the first integral is the definition of the displacement thickness δ^*, and the second integral is the definition of the momentum thickness θ.

$$\tau = \frac{dV_e}{dx}\rho_e V_e \delta^* + \frac{\partial}{\partial x}\left(\rho_e V_e^2 \theta\right) \tag{3.70}$$

Expanding the second derivative and noting the the partial derivative is a total derivative since all of the quantities do not change in y results in:

$$\tau = \frac{dV_e}{dx}\rho_e V_e \delta^* + \rho_e V_e^2 \frac{d\theta}{dx} + 2\rho_e V_e \frac{dV_e}{dx}\theta + \frac{d\rho_e}{dx} V_e^2 \theta \tag{3.71}$$

Dividing by $\rho_e V_e^2$ and collecting like terms gives:

$$\frac{\tau}{\rho_e V_e^2} = \frac{dV_e}{dx}\frac{1}{V_e}(\delta^* + 2\theta) + \frac{d\theta}{dx} + \frac{d\rho_e}{dx}\frac{1}{\rho_e}\theta \tag{3.72}$$

We now multiply the first term by $1/2$ on the top and bottom and use the definition of the local skin friction coefficient. For the second term we factor out θ and define a new variable called the shape factor: $H = \delta^*/\theta$. The variable H is related to the "health" of the boundary layer (with smaller H as healthier). A flat plate, for example, has a value of $H < 2.59$ for a favorable pressure gradient, and $H > 2.59$ for an adverse one. As H exceeds approximately 2.2 a laminar boundary layer will typically transition, whereas a turbulent boundary layer will typically separate.

$$\frac{1}{2}c_f = \frac{dV_e}{dx}\frac{\theta}{V_e}(H + 2) + \frac{d\theta}{dx} + \frac{d\rho_e}{dx}\frac{1}{\rho_e}\theta \tag{3.73}$$

Finally, we would like to relate the derivative of density to the derivative of velocity. If we assume that the flow outside the boundary layer is isentropic (an assumption that is consistent with the irrotationality assumption), that we can use the isentropic relationship

$$\frac{p}{\rho^\gamma} = \text{constant} \tag{3.74}$$

Taking derivatives yields:

$$\frac{dp}{dx} = \frac{\gamma p}{\rho}\frac{d\rho}{dx} \tag{3.75}$$

Using the definition of the speed of sound gives

$$\frac{dp}{dx} = a^2 \frac{d\rho}{dx} \tag{3.76}$$

We again, make use of Euler's equation (since the flow can be assumed inviscid outside of the boundary layer), to relate pressure to velocity:

$$\frac{dp}{dx} = a^2 \frac{d\rho}{dx} = -\rho V \frac{dV}{dx} \tag{3.77}$$

Thus,

$$\frac{d\rho_e}{dx} = -\rho_e M_e^2 \frac{1}{V_e} \frac{dV_e}{dx} \tag{3.78}$$

We now substitute this expression into Eq. 3.73

$$\frac{1}{2} c_f = \frac{dV_e}{dx} \frac{\theta}{V_e} (H+2) + \frac{d\theta}{dx} + -M_e^2 \frac{1}{V_e} \frac{dV_e}{dx} \theta \tag{3.79}$$

We can now combine like terms yielding the final result:

$$\frac{1}{2} c_f = \frac{d\theta}{dx} + \frac{dV_e}{dx} \frac{\theta}{V_e} \left(H + 2 - M_e^2 \right) \tag{3.80}$$

This is the Von Kármán Momentum Integral Equation. We've been able to express the mass and momentum balance in a compact equation relating the important quantities in the boundary layer. If the flow is incompressible then that means $M_e \to 0$ and we have the incompressible form:

$$\frac{1}{2} c_f = \frac{d\theta}{dx} + \frac{dV_e}{dx} \frac{\theta}{V_e} (H+2) \tag{3.81}$$

This equation contains too many unknowns to solve by itself (θ, H, c_f), but can be solved in connection with empirical relationships for laminar or turbulent boundary layers.

3.3 Thwaites' Method: Numerical Solution of Laminar Incompressible Boundary Layers

Consider a generic boundary layer as shown in Fig. 3.10. We typically draw it with the axes the other way, so that the boundary layer is vertical, but drawing it this way is more natural to look at the slope and curvature.

At the wall ($y = 0$) we know that $u = 0$ and $v = 0$. The only relevant velocity scale is V_e and a natural length scale is the momentum thickness θ. Thus, at the wall we expect that:

$$\left(\frac{\partial u}{\partial y} \right)_w \propto \frac{V_e}{\theta} \tag{3.82}$$

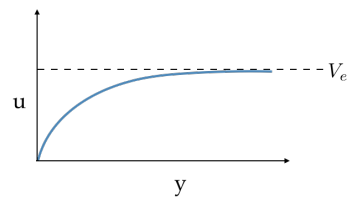

Fig. 3.10 A depiction of the boundary layer (rotated from our typical perspective).

Thwaites postulated that for a laminar boundary layer the proportionality is linear, so we can write this as an equality by multiplying by some unknown scalar l.

$$\left(\frac{\partial u}{\partial y}\right)_w = \frac{V_e}{\theta} l \tag{3.83}$$

Similarly, we expect the curvature to follow the form:

$$\left(\frac{\partial u^2}{\partial y^2}\right)_w \propto -\frac{V_e}{\theta^2} \tag{3.84}$$

Again, the assumption is that we can multiply by a unknown scalar (λ) to form an equality:

$$\left(\frac{\partial u^2}{\partial y^2}\right)_w = -\frac{V_e}{\theta^2}\lambda \tag{3.85}$$

In the above we have assumed negative curvature (which is indicative of a healthy boundary layer), but the sign of λ will allow the curvature to change.

We use our boundary layer momentum equation (Eq. 3.23):

$$u\frac{\partial u}{\partial x} + v\frac{\partial u}{\partial y} = V_e\frac{dV_e}{dx} + \nu\frac{\partial^2 u}{\partial y^2} \tag{3.86}$$

and substitute in values at the wall.

$$0 = V_e\frac{dV_e}{dx} - \nu\frac{V_e}{\theta^2}\lambda \tag{3.87}$$

From the above we find that:

$$\lambda = \frac{\theta^2}{\nu}\frac{dV_e}{dx} \tag{3.88}$$

Recall the momentum integral equation:

$$\frac{c_f}{2} = \frac{d\theta}{dx} + \frac{dV_e}{dx}\frac{\theta}{V_e}(H+2) \tag{3.89}$$

Let us relate c_f to the velocity gradient at the wall so we can make use of Eq. 3.83.

$$\frac{c_f}{2} = \frac{\tau_w}{\rho V_e^2} = \frac{1}{\rho V_e^2}\mu\left.\frac{\partial u}{\partial y}\right|_w = \frac{\nu}{V_e^2}\frac{V_e}{\theta} l = \frac{\nu l}{\theta V_e} \tag{3.90}$$

Substitution this into the momentum integral equation, and solving Eq. 3.88 for $\frac{dV_e}{dx}$ and substituting that in as well gives:

$$\frac{\nu l}{\theta V_e} = \frac{d\theta}{dx} + \frac{\lambda\nu}{\theta^2}\frac{\theta}{V_e}(H+2) \tag{3.91}$$

We move the unknown terms l, λ to one side:

$$\frac{V_e}{\nu}\theta\frac{d\theta}{dx} = l - \lambda(H+2) \tag{3.92}$$

Thwaites found that plotting the left hand side (which is nondimensional) for numerous exact solutions of the boundary layer equations resulted in a remarkably good linear relationship.

$$\frac{V_e}{\nu}\theta\frac{d\theta}{dx} = 0.225 - 3\lambda \tag{3.93}$$

That form suggests that both H and l are functions of only λ. The above equations is an ODE that we can use to solve for θ.

$$\frac{d\theta}{dx} = 0.225\frac{\nu}{V_e\theta} - 3\lambda\frac{\nu}{V_e\theta} \tag{3.94}$$

Finally, substituting in Eq. 3.88 gives the ODE:

$$\boxed{\frac{d\theta}{dx} = \frac{0.225\nu}{V_e\theta} - \frac{3\theta}{V_e}\frac{dV_e}{dx}} \tag{3.95}$$

With some additional algebraic manipulations we can solve this ODE analytically, however the results requires an integral that typically still requires a numerical solution. Thus, it is generally easiest just to numerically solve the ODE using the above expression.

We now need expressions for l and H, which we showed should be functions only of λ. Notice from Eq. 3.88 that a positive value of λ corresponds to a favorable pressure gradient (and negative curvature in the boundary layer Eq. 3.85). The opposite is true for negative λ, thus we expect as λ becomes increasingly negative the boundary layer will transition (or possibly separate). Data fits for l and H come from Cebeci and Bradshaw [11]:

11. Cebeci and Bradshaw, *Physical and Computational Aspects of Convective Heat Transfer*, 1988.

$$\left.\begin{aligned} l &= 0.22 + 1.57\lambda - 1.8\lambda^2 \\ H &= 2.61 - 3.75\lambda - 5.24\lambda^2 \end{aligned}\right\} \text{ if } 0 \le \lambda \le 0.1 \tag{3.96}$$

$$\left.\begin{aligned} l &= 0.22 + 1.402\lambda + \frac{0.018\lambda}{0.107+\lambda} \\ H &= 2.088 + \frac{0.0731}{0.14+\lambda} \end{aligned}\right\} \text{ if } -0.1 < \lambda < 0 \tag{3.97}$$

If $\lambda \le -0.1$ then laminar separation is predicted. The data fits do not extend beyond $\lambda > 0.1$, but we can just use the value at $\lambda = 0.1$ for larger values of λ.

Once, we solve the ODE for θ we compute λ from Eq. 3.88, l and H from the above expressions, and δ^* from the definition of H ($H = \delta^*/\theta$). The skin friction coefficient we compute from Eq. 3.90:

$$c_f = \frac{2\nu l}{\theta V_e} \tag{3.98}$$

The only remaining piece needed to solve the ODE is an inital condition. For a flat plate the initial boundary layer height is zero. In the analytic form we can use that directly, but for the numerical solution starting from $\theta_0 = 0$ causes numerical problems as can be seen from Eq. 3.95. Instead we can start from small value like $x_0 = 10^{-6}$ and initialize θ_0 with the corresponding height from the Blasius solution:

$$\theta_0 = \frac{0.664 x_0}{\sqrt{Re_{x_0}}} \tag{3.99}$$

For an airfoil the boundary layer height is nonzero at the stagnation point (bottom half of Fig. 3.11). Moran derives an expression for the initial height at a stagnation point based on a Taylor series expansion of the edge velocity [9]. The result is:

$$\theta_0 = \left[\frac{0.075\nu}{(dV_e/dx)_0} \right]^{1/2} \tag{3.100}$$

9. Moran, *An Introduction to Theoretical and Computational Aerodynamics*, 1984.

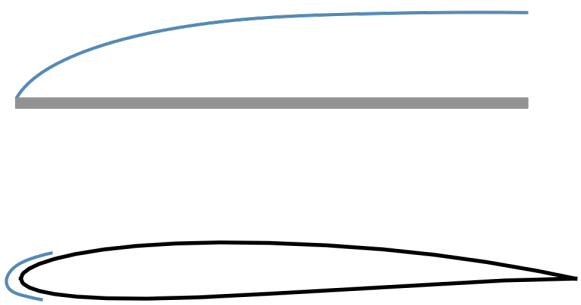

Fig. 3.11 Boundary layer height starts from zero for a flat plate, but has a nonzero height for an airfoil at the stagnation point.

The ODE should be terminated if there is laminar separation ($\lambda < -0.1$ as discussed above), or when transition is predicted (see Section 3.5.1).

Analytic Solution The above presentation focused on a numerical solution of the ODE, but it can also be solved analytically. The numerical solution is clearer, and more naturally leads to reusing similar methodology for the turbulent boundary layer solution (which must be solved numerically). However for hand calculations an analytic solution can be useful.

Starting with Eq. 3.95 moving one term to the other side and multiplying through by $2\theta V_e^6$ gives:

$$\frac{d\theta}{dx} + \frac{3\theta}{V_e}\frac{dV_e}{dx} = \frac{0.225\nu}{V_e\theta} \tag{3.101}$$

$$2\theta\frac{d\theta}{dx}V_e^6 + 6\theta^2 V_e^5\frac{dV_e}{dx} = 0.45\nu V_e^5 \tag{3.102}$$

$$\frac{d}{dx}(\theta^2 V_e^6) = 0.45\nu V_e^5 \tag{3.103}$$

Now we integrate from 0 the starting point of boundary layer to x_p the x point along the boundary layer we wish to evaluate at:

$$\int_0^{x_p}\frac{d}{dx}(\theta^2 V_e^6)dx = \int_0^{x_p} 0.45\nu V_e^5 dx \tag{3.104}$$

$$\theta^2 V_e^6\Big|_0^{x_p} = \int_0^{x_p} 0.45\nu V_e^5 dx \tag{3.105}$$

$$\theta(x_p)^2 = \frac{\theta_0^2 V_{e0}^6}{V_e(x_p)^6} + \frac{0.45\nu}{V_e(x_p)^6}\int_0^{x_p} V_e(x)^5 dx \tag{3.106}$$

This expression provides an integral-based solution to solve for the momentum thickness at any point, as an alternative from the ODE approach.

3.4 Head's Method: Numerical Solution of Turbulent Incompressible Boundary Layers

A corresponding approach for turbulent boundary layers is Head's method. There is an improved method called Green's method, that is particularly useful if rapid flow changes exist. Its numerical solution is not any more difficult, but the equations are quite a bit longer, so we will present Head's method for simplicity.

We start with the same figure we used in deriving the momentum integral equation Fig. 3.9, and the intermediate result relating the normal velocity the velocity gradient across the control volume (Eq. 3.57). In this case the flow is assumed to be incompressible and so the density is cancelled out. We also assume that this "entrainment velocity" is pulled into the control volume rather than using the default out direction and so the sign is reversed:

$$V_n = \int_0^{\delta}\frac{\partial u}{\partial x}dy \tag{3.107}$$

The integral extends out to some arbitrary distance δ. Head assumed that the normalized entrainment velocity, was self-similar with the

mean velocity profile, namely with H.

$$\frac{V_n}{V_e} = f(H) \tag{3.108}$$

Thus, for our boundary layer we have:

$$\frac{V_n}{V_e} = \frac{1}{V_e}\int_0^\delta \frac{\partial u}{\partial x} dy = f(H) \tag{3.109}$$

We now apply a series of algebraic manipulations:

$$\frac{\partial}{\partial x}\int_0^\delta u dy = V_e f(H) \tag{3.110}$$

$$\frac{\partial}{\partial x}\int_0^\delta (V_e - V_e + u) dy = V_e f(H) \tag{3.111}$$

$$\frac{\partial}{\partial x}\int_0^\delta V_e \left[1 - \left(1 - \frac{u}{V_e}\right)\right] dy = V_e f(H) \tag{3.112}$$

$$\frac{\partial}{\partial x}\left(V_e(\delta - \delta^*)\right) = V_e f(H) \tag{3.113}$$

We define the following new variable for convenience:

$$H_1 = \frac{\delta - \delta^*}{\theta} \tag{3.114}$$

The above equation then becomes:

$$\frac{d}{dx}(V_e \theta H_1) = V_e f(H) \tag{3.115}$$

From experimental measurements Head determined a relationship for $f(H)$ and between H_1 and H:

$$f(H) = 0.0306(H_1 - 3)^{-0.6169} \tag{3.116}$$

$$H_1 = \begin{cases} 0.8234(H - 1.1)^{-1.287} + 3.3 & H \leq 1.6 \\ 1.5501(H - 0.6778)^{-3.064} + 3.3 & H > 1.6 \end{cases} \tag{3.117}$$

To solve the ODE we need to expand Eq. 3.115:

$$\frac{dV_e}{dx}\theta H_1 + \frac{d\theta}{dx} V_e H_1 + \frac{dH_1}{dx} V_e \theta = V_e\, 0.0306(H_1 - 3)^{-0.6169} \tag{3.118}$$

Solving for dH_1/dx gives:

$$\frac{dH_1}{dx} = \frac{0.0306}{\theta}(H_1 - 3)^{-0.6169} - \frac{dV_e}{dx}\frac{H_1}{V_e} - \frac{d\theta}{dx}\frac{H_1}{\theta} \tag{3.119}$$

This equation is undefined if $H_1 < 3$ and so we need to protect against that. An H_1 value that low corresponds to a large H (separation) and so we simply set $dH_1/dx = 0$ if that occurs.

We also have the momentum integral equation, which we rearrange for $d\theta/dx$:

$$\frac{d\theta}{dx} = \frac{c_f}{2} - \frac{dV_e}{dx}\frac{\theta}{V_e}(H+2) \tag{3.120}$$

These two equations form a set of coupled linear ODEs where we solve for H_1 and θ simultaneously.

The remaining difficulties are that we have H_1 as a function of H, but need its inverse, and we have too many unknowns: θ, H_1 and c_f. The equation for H_1 (Eq. 3.117) can be easily inverted:

$$H = \begin{cases} 0.86(H_1 - 3.3)^{-0.777} + 1.1 & H_1 \geq 5.3 \\ 1.1538(H_1 - 3.3)^{-0.326} + 0.6778 & H_1 < 5.3 \end{cases} \tag{3.121}$$

These equations are undefined if $H_1 < 3.3$. As H_1 approaches 3.3 from above, the value of H approaches infinity (corresponding to separation). Thus, if $H_1 < 3.3$ we could simply return $H = 3.0$ (a typical large value for H corresponding to separation).

The skin friction coefficient can be estimated using the following semi-empirical formula:

$$c_f = 0.246 \times 10^{-0.678H} Re_\theta^{-0.268} \tag{3.122}$$

where

$$Re_\theta = \frac{V_e \theta}{\nu} \tag{3.123}$$

We now need two initial conditions. When the turbulent boundary layer is initiated from a laminar boundary layer on the same surface we assume continuity of the momentum thickness. In other words θ_0 is the final value of θ in the laminar section. After transition the value of H drops. As an initial value, we use the H value for a turbulent flat plate: $H = 1.28$ (see Eqs. 3.50 and 3.51). This value of H corresponds to a starting value of $H_1 = 10.6$ using Eq. 3.117.

Separation is predicted as H becomes large. The skin friction coefficient from the above formula goes to zero as H approaches infinity. Near separation the shape factor increases rapidly, so specifying a precise number makes little difference. A typical value is to assign $H = 3$ to correspond to separation, in which case the ODE should be terminated.

3.5 Transition Prediction Methods

Now that we know how to simulate a laminar boundary layer, and a turbulent boundary layer, we need to be able to predict when transition occurs. Before discussing a specific method, we discuss the mechanism of transition and some critical factors.

Transition is fundamentally caused by instability, on in other words the amplification of disturbances. At low Reynolds numbers, the viscous forces are large compared to inertial forces so disturbances that arise are damped. Thus, the flow can remain laminar. For large Reynolds numbers the viscous forces are comparatively small. In this case there is not enough damping in the system to prevent rapid growth in disturbances and so turbulent flow develops. As the Reynolds number in the boundary layer increases, from an increasing length that the boundary layer traverses, eventually the disturbances will grow and turbulence will develop. While we will often predict a point of transition we should keep in mind that there is no actual point, but rather a region over which the flow transitions from laminar behavior to turbulence.

Some of the most relevant factors that affect turbulence are freestream conditions, surface roughness, and pressure gradients. If the incoming air is already turbulent or is disturbed to a greater degree, transition will occur sooner. A rough surface introduces larger and more frequent disturbances in the flow leading to earlier transition. This affect is sometimes used intentionally in wind tunnels as discussed in Ex. 1.3. While favorable pressure gradients can stabilize a boundary layer, as discussed earlier in this chapter, even a slightly adverse pressure gradient can induce transition.

Two other factors that affect transition, but don't as often naturally are suction/blowing and heating/cooling. Sometimes a device is added within a wall to suck out the boundary layer, so new air can fill in and remain laminar longer. Or a device might cool the wall and stabilize the boundary layer longer. Such devices expend energy so one must be careful, say on a vehicle, that the device doesn't use more energy than it saves through the drag reduction. In other applications, like a quiet supersonic wind tunnel, the energy savings is not important, but keeping the boundary layer laminar is important so that disturbances (i.e., noise) from the turbulent boundary layers on the tunnel's walls don't affect the flow behavior on the test device.

It is not obvious why cooling should stabilize a boundary layer so we briefly discuss that here. If we apply the compressible boundary layer equations (Eq. 3.22) at the wall ($u = v = 0$), and assume no pressure

gradient to isolate the effect of heat transfer, we see that:

$$0 = \frac{\partial}{\partial y}\left(\mu \frac{\partial u}{\partial y}\right)_w \tag{3.124}$$

We now expand the derivative while carefully noting the difference between μ (mu) and u (note that we drop all of the w subscripts for simplicity, but all quantities should be evaluated at the wall).

$$\frac{\partial \mu}{\partial y}\frac{\partial u}{\partial y} + \mu \frac{\partial^2 u}{\partial y^2} = 0 \tag{3.125}$$

As briefly discussed in connection with Thwaite's method (Section 3.3) we would like the curvature to be negative for stability. More formally, stability theory suggests that a point of inflection is unstable at high Reynolds number, and since the curvature is negative as it approaches the edge velocity, it should be negative at the wall as well. Solving for the curvature:

$$\frac{\partial^2 \mu}{\partial y^2} = -\frac{1}{\mu}\frac{\partial \mu}{\partial y}\frac{\partial u}{\partial y} \tag{3.126}$$

Viscosity is positive, and the velocity gradient at the wall is positive, so to maintain negative curvature we require the viscosity gradient to be positive. Viscosity is a function of temperature so we can expand that derivative as:

$$\frac{\partial \mu}{\partial y} = \frac{\partial \mu}{\partial T}\frac{\partial T}{\partial y} \tag{3.127}$$

For a gas, $d\mu/dT$ is positive (opposite for a liquid) so for stability in the boundary layer we require the temperature gradient moving away form the wall to be positive. Thus, if we cool the wall we can create a stronger temperature gradient and delay transition.

3.5.1 Transition Prediction Methods

The e^n method is perhaps the best method for predicting transition, but is more complex than the methods discussed in this section. The H-Rx method developed by Wazzan [12] uses the e^n method (with $n = 9$) with a range of pressure gradients, surface heating, and suction. The results and then parametrized as a function of the shape factor. The result is a simple method that works well across a wide range of 2D (and axisymmetric) flows.

12. Wazzan et al., *The H-Rx method for predicting transition*, 1981.

The local Reynolds number is:

$$Re_x = \frac{V_e x}{\nu} \tag{3.128}$$

and transition is predicted if $2.1 < H < 2.8$ and

$$\log_{10}(Re_x) > -40.4557 + 64.8066H - 26.7538H^2 + 3.3819H^3 \quad (3.129)$$

This relationship is visualized in Fig. 3.12. We see that as H increases then the critical transition Reynolds number decreases (i.e., transition occurs sooner).

The type of transition captured by these methods is caused by Tollmien-Schlichting (TS) waves, and is only relevant for two-dimensional flows. Predicting transition in three dimensions is much more complicated and must consider crossflow instabilities and attachment line instabilities.

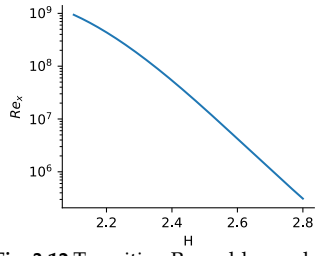

Fig. 3.12 Transition Reynolds number for the H-Rx method.

3.6 Drag Prediction

One of the main purposes of developing the boundary layer is to predict drag. Since we can compute c_f throughout the boundary layer, we can integrate that along the surface. However, that integration will only give us the skin friction drag (and not pressure drag). Instead, a particularly effective method is the Squire and Young formula.

$$c_d = \frac{2\theta_{TE}}{c}\left(\frac{V_{eTE}}{V_\infty}\right)^{\frac{H_{TE}+5}{2}} \quad (3.130)$$

where the subscript TE indicates the end of the boundary layer properties at the trailing edge. The formula must be applied over the upper and lower surfaces separately and added together. This formula gives total 2D viscous drag (sum of skin friction and pressure drag). If we wanted to separate out the two components we could integrate the skin friction drag as discussed above, then subtract that value from this total drag to get the pressure component.

Compaisons of this formula against against RANS CFD simulations for a variety of airfoils has suggested agreement in drag predictions within 2-3% (until stall is approached)[13]. This is remarkably good agreement for such a simple formula. Some comparisons from their paper are shown in Fig. 3.13.

13. Coder and Maughmer, *Numerical Validation of the Squire–Young Formula for Profile-Drag Prediction*, 2015.

3.7 Turbulence

To initiate a discussion on turbulence, consider the two jet flows shown in Fig. 3.14 and note the similarities and differences. One observation is that turbulent structures exist at multiple length scales, and that we notice smaller length scales at the higher Reynolds number. On the

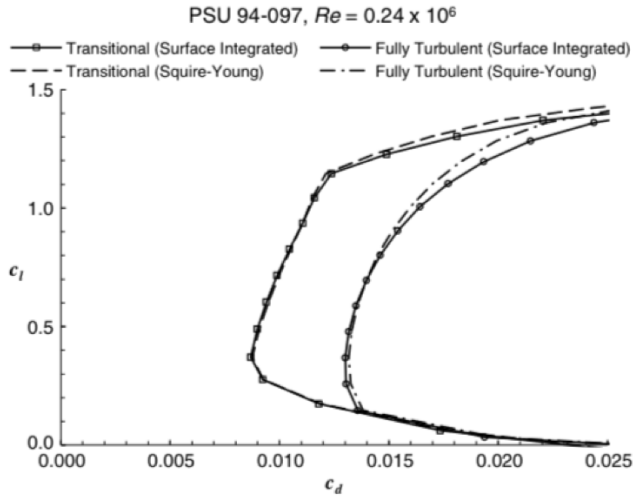

Fig. 3.13 Figure from Coder and Maughmer.[13]

left, we see larger turbulent structures, and on the right, with a higher Reynolds number, we see much smaller turbulent structures. Another observation is that the large-scale features (e.g., spreading angle) seem to be largely independent of the Reynolds number.

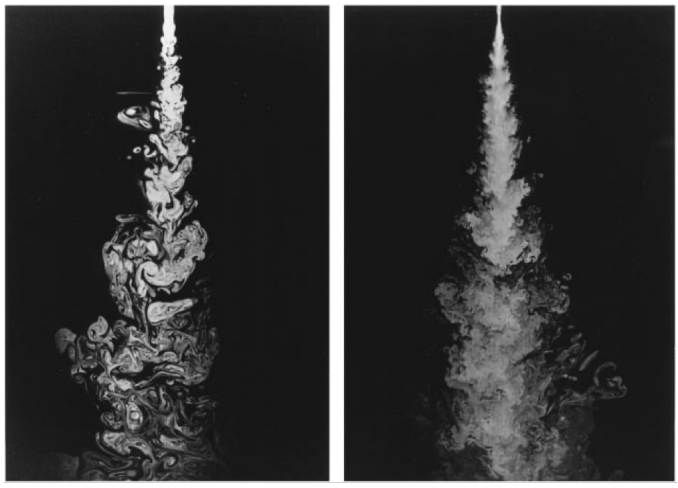

Re = 2,500 Re = 10,000

Fig. 3.14 The mixing transition in turbulent flows, Paul E. Dimotakis

These are general characteristics. Large-scale features are generally independent of Reynolds number, but the details of the turbulent structure are highly Reynolds number dependent, with smaller scales appearing as Reynolds number increases. This behavior creates the difficulty in simulating high Reynolds number flows—we have to resolve increasingly smaller and smaller scales.

3.7.1 Direct Numerical Simulation

In *direct numerical simulation* (DNS) we resolve all spatial and temporal scales of the flow (the smallest scales are known as the *Kolmogorov scale* as will be discussed later). Thus, we solve the Navier–Stokes equations without the need for any turbulence model. The cost of DNS scales with Re^3. Currently, this approach is only practical on very simple geometries with low Reynolds numbers (approximately $O(10^3)$).*

*This video shows a DNS simulation for a small portion of a turbulent boundary layer and gives some appreciation for the scales and complexity involved: https://youtu.be/4KeaAhVoPIw.

3.7.2 Reynolds Averaged Navier Stokes and Turbulence Models

Most aerodynamic flows of interest occur at much higher Reynolds numbers where DNS is not practical. Another approach to this turbulent problem is Reynolds-averaging, which leads to solving the *Reynolds-averaged Navier–Stokes* (RANS) equations. In a RANS simulation we do not resolve the instantaneous turbulent structures, but rather solve for a time-averaged solution (think about the result from time-averaging the flow behavior shown in Fig. 3.14). We are giving up some details of the solution, and thus may lose some accuracy depending on which engineering quantities are of interest, in exchange we enable high Reynolds number solutions.

Before deriving the RANS equations (or rather an example subset of them) we need to review the concept of an expected value, or average. The expected value of some random variable X will be denoted with the following bracket notation, and is given as:

$$\langle X \rangle = E[X] = \int_{-\infty}^{\infty} x p(x) dx \tag{3.131}$$

where $p(x)$ is a probability density function for x (e.g., a normal distribution). If X can only take on discrete quantities, then the expected value would be given by the sum:

$$\langle X \rangle = \sum_{i=1}^{\infty} x_i p_i \tag{3.132}$$

where p_i is the probability associated with event x_i.

In the *Reynolds decomposition* we split every flow variable into an average component and a fluctuating component:

$$u = \langle u \rangle + u' \tag{3.133}$$

Some important properties of expectation are shown below. Expectation is a linear operator and so commutes with other linear operators like addition:

$$\langle u + v \rangle = \langle u \rangle + \langle v \rangle \tag{3.134}$$

The average value of the fluctuations is zero by definition:

$$\langle u' \rangle = 0 \tag{3.135}$$

Differentiation is also a linear operator and so it commutes:

$$\left\langle \frac{\partial u}{\partial x} \right\rangle = \frac{\partial \langle u \rangle}{\partial x} \tag{3.136}$$

The expected value of a variable is a constant and so can be pulled out of another expectation:

$$\langle \langle u \rangle v \rangle = \langle u \rangle \langle v \rangle = 0 \tag{3.137}$$

Before working out an example set of RANS equations, one quantity we will need is the expectation of the product of two random variables. We can work that out using the rules we've already established:

$$\langle uv \rangle = \langle (\langle u \rangle + u')(\langle v \rangle + v') \rangle \tag{3.138}$$

$$= \langle \langle u \rangle \langle v \rangle \rangle + \langle u' \langle v \rangle \rangle + \langle \langle u \rangle v' \rangle + \langle u'v' \rangle \tag{3.139}$$

$$= \langle u \rangle \langle v \rangle + \langle u'v' \rangle \tag{3.140}$$

Note that even though the average of u' and the average of v' are both zero, the average of their product is not necessarily zero.

We now examine the 2D incompressible Navier-Stokes equations, with Reynolds-averaging. The standard mass and momentum equations (x-direction only for brevity) are shown below.

$$\frac{\partial u}{\partial x} + \frac{\partial v}{\partial y} = 0 \tag{3.141}$$

$$\frac{\partial u}{\partial t} + u\frac{\partial u}{\partial x} + v\frac{\partial u}{\partial y} = -\frac{1}{\rho}\frac{\partial p}{\partial x} + \nu\left(\frac{\partial^2 u}{\partial x^2} + \frac{\partial^2 u}{\partial y^2}\right) \tag{3.142}$$

If we follow the same procedure shown above, introducing Reynolds-averaging, and simplifying, we obtain the following equations:

$$\frac{\partial \langle u \rangle}{\partial x} + \frac{\partial \langle v \rangle}{\partial y} = 0 \tag{3.143}$$

$$\frac{\partial \langle u \rangle}{\partial t} + \langle u \rangle \frac{\partial \langle u \rangle}{\partial x} + \langle v \rangle \frac{\partial \langle u \rangle}{\partial y} = -\frac{1}{\rho}\frac{\partial \langle p \rangle}{\partial x} + \nu\left(\frac{\partial^2 \langle u \rangle}{\partial x^2} + \frac{\partial^2 \langle u \rangle}{\partial y^2}\right) - \left(\frac{\partial}{\partial x}\langle u'u' \rangle + \frac{\partial}{\partial y}\langle u'v' \rangle\right) \tag{3.144}$$

Notice, that the equations appear almost identical to the original equations when we replace the instantaneous quantity (e.g., u) with

a time-averaged quantity (e.g., $\langle u \rangle$). However, an extra term has been introduced as highlighted in the equation above.

Multiplying the entire equation by ρ (and considering all three dimensions) we have extra terms of the form:

$$\rho \langle u_i' u_j' \rangle \tag{3.145}$$

This quantity is called the *Reynolds stress tensor* (RST) because it has units of stress and appears in the equation in a similar way as the standard stress tensor. The problem, is that we have introduced additional unknowns that we don't have equations for, in other words, we have a closure problem. This is where *turbulence models* come in, as a way to model these additional terms.

Before discussing some turbulence models, we explore the turbulent kinetic energy (TKE) equation, which will lend some insight into the behavior of turbulence. This equation is formed by taking this new mean momentum equation, subtracting it from the original momentum equation, then multiplying by the velocity u_j. The result is:

$$\begin{aligned} \underbrace{\frac{\partial k}{\partial t} + \langle u_i \rangle \frac{\partial k}{\partial x_i}}_{Dk/Dt} + \underbrace{\frac{\partial}{\partial x_i}\left(\frac{1}{2}\langle u_i' u_j' u_j' \rangle + \frac{1}{\rho}\langle u_i' p' \rangle - 2\nu \langle u_j' s_{ij}' \rangle\right)}_{\nabla \cdot T \text{ transport}} \\ = \underbrace{-\langle u_i' u_j' \rangle \frac{\partial \langle u_j \rangle}{\partial x_i}}_{\text{P: production}} - \underbrace{2\nu \langle s_{ij}' s_{ij}' \rangle}_{\epsilon \text{ : dissapation}} \end{aligned} \tag{3.146}$$

The quantity k is the kinetic energy of turbulence:

$$k = \frac{1}{2}\langle u_i' u_i' \rangle = \frac{1}{2}\left(u'^2 + v'^2 + w'^2\right) \tag{3.147}$$

It is proportional to the trace of the RST ($2\rho k$), and is one of the most important parameters in turbulence. Often it is reported as a nondimensional value called the *turbulence intensity*, which is the root-mean-squared of the velocity fluctuations normalized by the magnitude of the mean velocity.

$$I = \frac{\sqrt{\frac{2}{3}k}}{\|\langle u_i \rangle\|} = \frac{\sqrt{\frac{1}{3}\left(u'^2 + v'^2 + w'^2\right)}}{\sqrt{\langle u \rangle^2 + \langle v \rangle^2 + \langle w \rangle^2}} \tag{3.148}$$

The quantity s_{ij}' is the symmetric part of the stress tensor (using fluctuating components):

$$s_{ij}' = \frac{1}{2}\left(\frac{\partial u_i'}{\partial x_j} + \frac{\partial u_j'}{\partial x_i}\right) \tag{3.149}$$

Equation 3.146 has labels below various terms. The first term is the total change in kinetic energy. Energy is produced at large scales from the mean flow field (u_j). This productive term is usually positive. The transport term is a divergence moving energy from the large scales to smaller scales. The dissipation term is always negative and shows that energy is dissipated by viscosity at the small scales where the gradients in s'_{ij} are large. The dissipation term, ε is also used to define the Kolmogorov scale, addressing how small of scales to we need to resolve in a turbulent simulation. The overall equation shows how turbulent kinetic energy flows through a fluid in an energy cascade. It is generated at large scales, transported to smaller and smaller scales, and dissipated at the smallest scales where viscosity dominates.

We now briefly introduce a few turbulence models. Recall that we need a model for the RST:

$$\rho\langle u'_i u'_j\rangle \tag{3.150}$$

Boussinesq proposed a relationship with the mean flow, in what is known as the *Boussinesq hypothesis*. The idea is to mimic the regular stress tensor (Eq. 1.132), but replace the viscosity with a new term called the *eddy viscosity* (μ_t). Note that the negative is added to cancel the negative that appears in Eq. 3.144, and make it of the same form as the stress tensor.

$$-\rho\langle u'_i u'_j\rangle = \mu_t\left(\frac{\partial\langle u_i\rangle}{\partial x_j}+\frac{\partial\langle u_j\rangle}{\partial x_i}-\frac{2}{3}\left(\frac{\partial\langle u_k\rangle}{\partial x_k}\right)\delta_{ij}\right) \tag{3.151}$$

However, this cannot be a suitable model as it has zero trace, and recall that the trace of the RST is $2\rho k$. We then add a diagonal term to produce the appropriate trace, where C is a yet unknown constant:

$$-\rho\langle u'_i u'_j\rangle = \mu_t\left(\frac{\partial\langle u_i\rangle}{\partial x_j}+\frac{\partial\langle u_j\rangle}{\partial x_i}-\frac{2}{3}\left(\frac{\partial\langle u_k\rangle}{\partial x_k}\right)\delta_{ij}\right)+C\delta_{ij} \tag{3.152}$$

Taking the trace of both sides yields: $-2\rho k = 3C$ or $C = -2/3\rho k$. Thus, we have a model for the RST (rearranged in a more standard form):

$$-\rho\langle u'_i u'_j\rangle = \mu_t\left(\frac{\partial\langle u_i\rangle}{\partial x_j}+\frac{\partial\langle u_j\rangle}{\partial x_i}-\frac{2}{3}\left(\frac{\partial\langle u_k\rangle}{\partial x_k}\right)\delta_{ij}\right)-\frac{2}{3}\rho k\delta_{ij} \tag{3.153}$$

Note the similarities to the stress tensor in Eq. 1.132 (and Eq. 1.113 with pressure included), repeated below:

$$\sigma_{ij} = \mu\left(\frac{\partial u_i}{\partial x_j}+\frac{\partial u_j}{\partial x_i}-\frac{2}{3}\left(\frac{\partial u_k}{\partial x_k}\right)\delta_{ij}\right)-p\delta_{ij} \tag{3.154}$$

This a commonly used model, although its accuracy has been shown to be poor in some scenarios. And, although we now have a model for the RST, we still have an unknown, the eddy viscosity, and so need yet another model.

Various turbulence models are used to fill this gap. We won't go into detail, but rather provide a high-level overview of some of the main ones. Perhaps the most commonly used turbulence model for CFD is the k–ϵ model. This model uses the TKE equation (Eq. 3.146), for k, the turbulent kinetic energy and an empirical PDE for ϵ (the dissipation term). The eddy viscosity is then related as:

$$\mu_t = C\rho\frac{k^2}{\epsilon} \tag{3.155}$$

where C is one of five adjustable constants used in the model.

The k–ω model is similarly based on 2 PDEs, where $\omega = \epsilon/k$. This model typically performs better in the near-wall region, in areas with large streamwise pressure gradients (although k–ϵ typically performs better when separation occurs), or for compressible flows.

The Spalart-Allmaras turbulence model is a popular one-equation model. It was designed specifically for aerospace applications with wall-bounded flows. It has been shown to work particularly well for boundary layers with adverse pressure gradients but still attached or only mildly separated. It is not a good general model, and can produce large errors for other scenarios like free shear flows, jet flows, etc.

The RST model does not use the Bousennisq hypothesis, but rather has a separate model for each term in the RST. This is the most computationally intensive of these models.

One final comment on the RANS equations is on its suitability in two-dimensions. If we refer back to the vorticty equation (Eq. 1.149) we note that the vortex stretching term is only nonzero in 3D. Vortex stretching is a critical mechanism in turbulence to transfer turbulent energy across the various scales. In other words, turbulence is fundamentally a three-dimensional phenomenon. While 2D RANS is often used, for example in airfoil simulations, and can be a useful approach, there is good reason to be even more skeptical of turbulence models in two-dimensional flows.

3.8 Turbulent Boundary Layers

We now take a closer look at the behavior within a boundary layer. Laminar boundary layers are straightforward. They are geometrically similar and the profile is known from the Blasius solution. For turbulent

boundary layers, no matter how we nondimensionalize, we cannot collapse the profiles onto a single curve. This is because the layers closer to the surface act on very different length scales than layers further away. Instead, we will think of a turbulent boundary layer as being composed of separate inner and outer layers. Figure 3.15 is a classic figure demonstrating different behavior in separate regions.

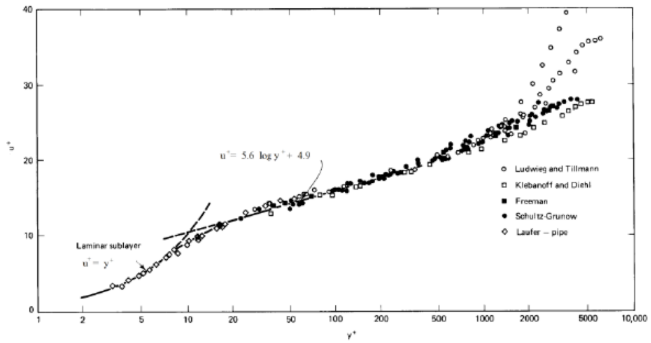

Fig. 3.15 Nondimensional velocity versus nondimensional distance from wall showing different behavior in different sublayers with a turbulent boundary layer. Figure from Clauser.[14]

14. Clauser, *The Turbulent Boundary Layer*, 1956.

Near the wall, viscosity is the most important parameter governing the fluid behavior. In this region the Reynolds stresses are negligible. At the wall the velocity fluctuations must be zero, so the Reynolds stresses are zero at the wall. Figure 3.16 depicts the viscous stresses and Reynolds stresses within a turbulent boundary layer, where we see that viscous stresses dominate in the near-wall region.

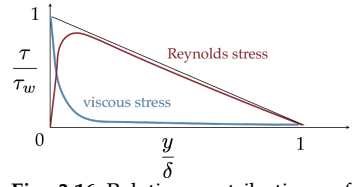

Fig. 3.16 Relative contributions of stresses within a turbulent boundary layer.

The relevant parameters near the wall are thus the viscosity (ν), density (ρ), and the shear stress at the wall (τ_w). From those quantities we can form a velocity and length scale to use in nondimensionalization. The velocity scale is called the *friction velocity*:

$$u_\tau = \sqrt{\frac{\tau_w}{\rho}} \tag{3.156}$$

and the viscous length scale is:

$$\delta_v = \frac{\nu}{u_\tau} \tag{3.157}$$

The nondimensional distance from the wall is then:

$$y^+ = \frac{y}{\delta_v} = \frac{u_\tau y}{\nu} \tag{3.158}$$

This quantity is called the *y plus* value. It is a nondimensional distance, but from the above equation can also be thought of as a Reynolds

number using the relevant near-wall velocity scale. The fractional contributions of the stresses are shown again in Fig. 3.17, this time as a function of y^+.

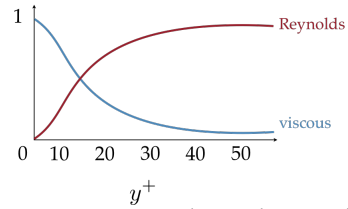

Fig. 3.17 Fractional contribution of stresses as a function of y^+ in a turbulent boundary layer.

In general, we expect the mean velocity gradient to be a function of the distance from the wall, with both the viscous length scale, and the boundary layer height as relevant length scales: However, as we've argued, for the inner portion of the boundary layer the flow behavior is independent of the outer portion of the boundary layer (i.e., independent of V_e and δ). In fact, the behavior doesn't depend on whether it is a boundary layer or any other wall shear layer (e.g., an internal flow). We then expect the mean velocity gradient to be given by

$$\frac{d\langle U\rangle}{dy} = \frac{u_\tau}{y} f\left(\frac{y}{\delta_v}\right) \tag{3.159}$$

where f is some yet unknown function with the constants u_τ/y factored out of the function so that the remaining function is nondimensional (i.e., potentially universal). We define the nondimensional velocity profile as:

$$u^+ = \frac{u}{u_\tau} \tag{3.160}$$

Then the above expression reduces to the following nondimensional relationship:

$$\begin{aligned} \frac{d\langle U\rangle}{dy} &= \frac{u_\tau}{y} f\left(\frac{y}{\delta_v}\right) \\ \frac{du^+}{dy^+} &= \frac{1}{y^+} f(y^+) \end{aligned} \tag{3.161}$$

Or in other words, u^+ can only depend on y^+ in this inner layer ($u^+ = f(y^+)$). This prediction of universal behavior with the inner layer of turbulent boundary layer is called the *law of the wall*. The inner portion of a turbulent boundary layer comprises about 10–20% of the full boundary layer height.

Within the inner layer, two sublayers are identified. The first is the *viscous sublayer* also called the *laminar inner sublayer*. This layer extends from the wall to approximately $y^+ = 5$. In this region viscosity dominates and so little mixing occurs, which is way it is referred to as a laminar inner sublayer. Near the wall, the wall shear stress dominates the behavior:

$$\tau_w = \mu \frac{\partial u}{\partial y} \tag{3.162}$$

If we rearrange, and integrate, assuming the shear stress and viscosity

don't change appreciably in this small region then:

$$u = \frac{\tau_w}{\mu} y = \frac{u_\tau^2 \rho}{\mu} y \tag{3.163}$$

where we introduced the friction velocity in the last step. We now nondimensionalize by dividing the velocity by the friction velocity:

$$u^+ = \frac{u}{u_\tau} = \frac{\rho u_\tau u}{\mu} = y^+ \tag{3.164}$$

The resulting prediction is linear behavior in the viscous sublayer.

Further away we expect an intermediate region where viscosity has little effect, but where the external flow also has little effect. In this region we expect the mean rate of strain to be constant. In other words, we expect the nondimensional function that defines the mean velocity gradient, $f(y^+)$ to be constant. This is typically written as follows:

$$f(y^+) = \frac{1}{\kappa} \tag{3.165}$$

where κ is the von Karman constant. From Eq. 3.161 we then get:

$$\frac{du^+}{dy^+} = \frac{1}{y^+} \frac{1}{\kappa} \tag{3.166}$$

We integrate this expression to obtain:

$$u^+ = \frac{1}{\kappa} \ln y^+ + C \tag{3.167}$$

This is called the *log law*. Typical values for the two constants, obtaining from experiments on a smooth wall, are: $\kappa = 0.41$ (when using a natural log) and $C = 5$.

Figure 3.18 shows both the inner layer and the log law on a semilog scale. The inner layer applies up to about $y^+ = 5$ and the low law starts at about $y^+ = 30$. In between we have a buffer region where neither law applies. If we refer back to Fig. 3.15 we see that the log law eventually breaks down. In this outer layer there is no universal behavior, and this outer layer comprises about 80% of the boundary layer. it appears as a small region only because it is a log scale on that axis (note how it extends from about $y^+ = 1000$–5000 for that case, which is 80% of the total height.).

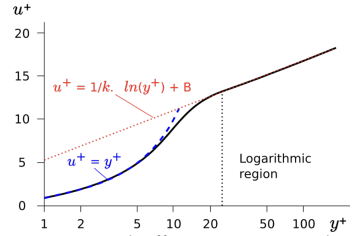

Fig. 3.18 A buffer region exists between the inner sublayer and the log law.

3.9 Large Eddy Simulation

Finally, we give a brief introduction to large eddy simulation (LES). This technique has a fidelity between DNS and RANS. The concept is

motivated by the turbulent boundary layer behavior we just saw. The method explicitly solves large-scale features (e.g., large eddies), but uses a subgrid-scale model rather than trying to resolve all the small scales like DNS does. From the above discussion we expect that we can do a reasonable job at modeling the small scales in a universal way. The larger scales have non-universal behavior, contain the most energy, and are strongly affected by geometry, so we explicitly solve for these. This technique could also be thought of as a low-pass filter (i.e., we ignore the high frequency, small scale, behavior).

Finite Wing

4

A basic wing is just a loft between two or more airfoils (Fig. 4.1). We've learned some techniques to compute forces and moments on an airfoil and would now like to understand how that relates to computing forces and moments on wings.

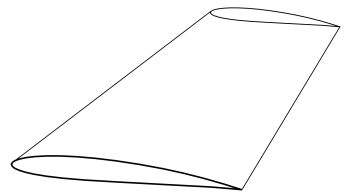

Fig. 4.1 A basic wing is just a loft between two airfoils.

4.1 Geometry

Before diving into the physics, let us get a few terms out of the way as it relates to geometry. The wingspan, or *span*, is a planar projection of the lateral extent of the wing and is denoted as b (Fig. 4.2). In other words, a vertical winglet will increase the length of the wing, but it does not increase span. This quantity is usually unambiguous, but for flexible wings we may need to specify the loading conditions at which the span is measured (e.g., span at 1g).

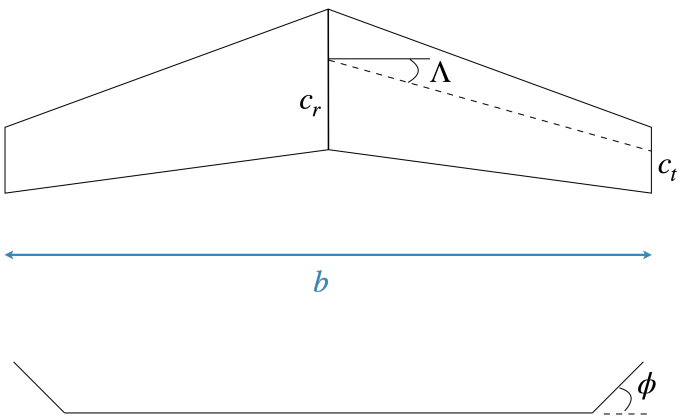

Fig. 4.2 Some nomenclature for a basic wing. Top view (top) and side view (bottom).

The wing area, or just *area*, S, is another important quantity though it can have many definitions (wetted area, projected area, gross area, etc.). Typically, we are interested in a reference area, and we note this explicitly as S_{ref}. The reference area is a flat projected area that scales with the wing, but is primarily used for normalization purposes. A typical reference area uses a trapezoidal shape whether or not the actual

wing is trapezoidal (see Fig. 4.3).

Sweep, Λ, is a shear angle that is usually measured at the quarter-chord line, though sometimes at the leading edge. Sweep need not be constant along the wing, and instead may be a distribution. *Dihedral*, ϕ, is a rotation angle that also need not be constant along the wing and can be a distribution. Both can be seen in Fig. 4.2.

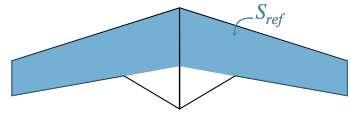

Fig. 4.3 Trapezoidal reference area.

Chord, c, is rarely constant, though in simple cases it may follow a linear distribution where one only needs to know the root chord c_r and the tip chord c_t (Fig. 4.2). Another common wing design uses multiple linear segments. In the general case, the chord is a curve. *Twist* (Fig. 4.4), θ, is similarly often defined as piecewise linear, though can be a general curved shape. Twist is usually measured about the quarter chord.

The nondimensional quantity, *aspect ratio*, is given by:

$$AR = \frac{b^2}{S_{\text{ref}}} \tag{4.1}$$

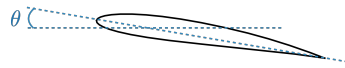

Fig. 4.4 Definition of twist.

A high aspect ratio wing and a low aspect wing are contrasted in Fig. 4.5. Another nondimensional quantity that is sometimes used is the taper ratio:

$$\lambda = \frac{c_t}{c_r} \tag{4.2}$$

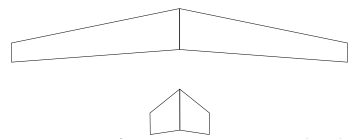

Fig. 4.5 High aspect ratio wing (top), and low aspect ratio wing (bottom).

This quantity is less direct for curved shapes, but can still apply to the trapezoidal reference area to give a qualitative understanding of the shape. A taper ratio of 1 would correspond to a constant chord wing, whereas a taper ratio of 0.1 would be higher tapered. Modern transport aircraft typically have a taper ratio of around 0.2.

The mean geometric chord is simply:

$$\bar{c} = \frac{S_{\text{ref}}}{b} \tag{4.3}$$

though this quantity isn't used very much. More relevant is the mean aerodynamic chord, which is a chord-weighted average chord. This quantity is used in stability and control calculations, to normalize pitching moment and to compute static margin, and is also typically used as the length scale in Reynolds number calculations.

$$c_{mac} = \frac{2}{S}\int_0^{b/2} c^2 dy \tag{4.4}$$

where

$$S = 2\int_0^{b/2} c\, dy \tag{4.5}$$

For a linearly tapered wing this integral evaluates to:

$$c_{mac} = \frac{2}{3}\left(c_r + c_t - \frac{c_r c_t}{c_r + c_t}\right) \tag{4.6}$$

4.2 Downwash

The flow behavior over a wing has some fundamental differences as compared to airfoils, also called infinite wings. A finite wing has a three-dimensional flow field, with a *crossflow* component of velocity perpendicular to the airfoils. In other words, a wing doesn't solely act like a series of airfoils stacked together.

A unique feature of lifting wings is that they produce a *wake vortex* as seen in Fig. 4.6. A common explanation for the vortex is that a lifting wing has higher pressure on the bottom surface as compared to the top, and so fluid will circulate around the tips as shown in Fig. 4.7. The resulting vortex is often called a tip vortex. This is a helpful conceptualization, but is a somewhat misleading explanation. It seems to suggest that a box wing (Fig. 4.8), which does not have a "tip", would not produce a vortex. It also leads to some erroneous conclusions about the benefits of winglets.

As we will see more clearly later on, these wake vortices produce *downwash*, or downward moving air, behind the wing. Downwash can be viewed more fundamentally as a consequence of Newton's third law. If a body is producing lift, colloquially we might say that means that the air is pushing the body up. Thus, by Newton's third law, the body must be pushing the air downward. Thus, any three-dimensional lifting body will leave behind a wake of downward moving air. The lift is not (and cannot) be generated uniformly along the wing. The lift must go to zero somewhere on the wing (e.g., at a wing tip where a pressure difference cannot be sustained between the upper and lower surfaces), or on a closed wing, like the box wing, the force would have to be reduced on one side to produce a net lift. In any case, variations in the lift distribution are directly related to the vorticity, and the vorticity will "roll-up" towards the center of vorticity forming a vortex, or in some cases, multiple vortices. Another way to think of vortex formation is that the downward moving air will be next to a region of still air, and that velocity gradient (which is vorticity) will induce a rotation. A more complete picture of the downwash and wake vortices can be seen in Fig. 4.9.

A major consequence of this downwash, is that energy is left behind in the wake. Or in other words, the wing produces drag. This type of drag is called *induced drag* or sometimes *vortex drag*. To completely eliminate induced drag, we would have to eliminate the downwash. In other words, if flying into still air, any disturbances made by the aircraft would need to be cancelled out, so the air behind the aircraft would also be still. But, if there is no downwash left behind, then from the above

Fig. 4.6 Picture of aircraft flying through colored smoke to visualize the wake vortex. Picture from NASA, public domain.

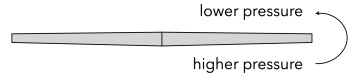

Fig. 4.7 Common explanation for tip vortex that is helpful but incomplete.

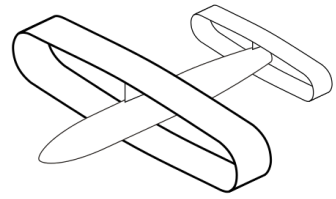

Fig. 4.8 Box or annual wing. Image from Steelpillow, Wikimedia, CC BY-SA 3.0.

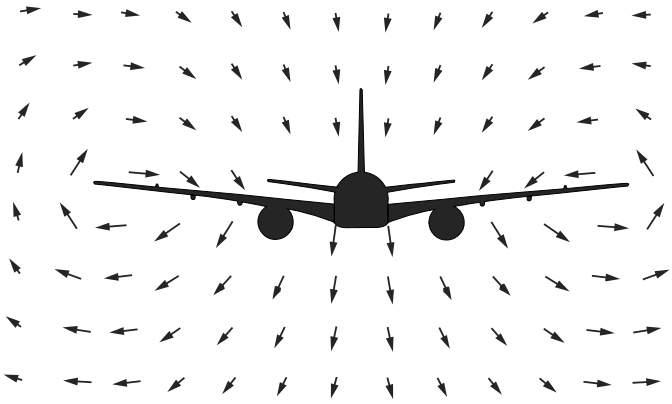

Fig. 4.9 Induced velocity from a lifting body showing the region of downwash, and circulation from the wake vortices.

arguments there would be no lift. Thus, any lifting body must always have induced drag. Although we cannot eliminate induced drag, there are things we can do to reduce it as will be discussed later.

As a side note, we can see from Fig. 4.9 that although the wake vortices induced downwash on the wing, to the sides of the wing they induced upwash, or a region of rising air. This behavior provides the motivation for formation flight. A second aircraft, or bird, positioned behind and to the side of a lead aircraft (Fig. 4.10) can fly in a region of rising air and thus reduce the energy required to maintain their lift.

The presence of downwash also changes our effective angle of attack. As depicted in Fig. 4.11, without downwash the angle of attack is the angle between the freestream velocity and the local chord line. However, the presence of downwash alters the relative incoming

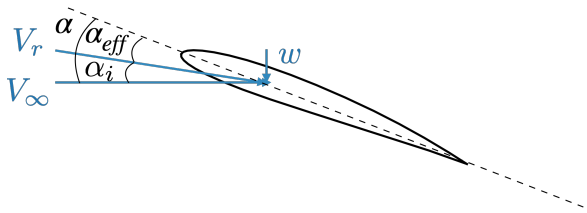

Fig. 4.11 Induced angle of attack.

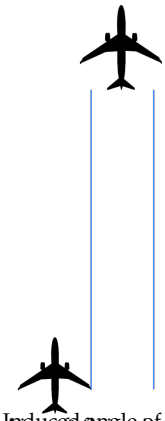

Fig. 4.10 Aircraft flying in formation can reduce their induced drag.

velocity V_r. The effective angle of attack, α_{eff}, is reduced by the *induced angle of attack*, α_i:

$$\alpha_{eff} = \alpha - \alpha_i \tag{4.7}$$

4.3 Vortex Filaments

We continue with the assumptions of incompressible and irrotational flow, and thus are still governed by Laplace's equation (potential flow).

But in this case the singularities we use are line vortices. A cross section of a line vortex is just the point vortex we've seen before (Fig. 5.2). Or in other words, the line vortex is like the point vortex but extruded out of the plane. The circulation of the vortex is defined by the right hand rule, the fingers curl around in the direction of induced velocity and the thumb points along the line defining the direction of circulation.

An infinite vortex behaves just like the point vortex we studied in Chapter 2. In other words, the velocity has a magnitude:

$$|V| = \frac{\Gamma}{2\pi r} \tag{4.8}$$

and is a tangential direction given by the right hand rule. We can now have line vortices of any length, not just infinite. Another special case, is a semi-infinite vortex where the vortex extends to infinity in one direction only. If measuring the velocity in the plane where the vortex filament ends, its magnitude is given by:

$$|V| = \frac{\Gamma}{4\pi r}\,. \tag{4.9}$$

Not surprisingly, the induced velocity has half the magnitude of an infinite vortex.

For an arbitrary vortex line segment, referred to as a *vortex filament*, we need to use the *Biot-Savart Law*. This law comes from magnetostatics and describes the magnetic field induced by a constant electric current. The same equation is used in aerodynamic applications to compute the velocity induced by a filament of constant vorticity.*

We can derive Biot-Savart's Law as follows. First, we assume an incompressible flow:

$$\nabla \cdot \vec{V} = 0 \tag{4.10}$$

We now define

$$\vec{V} = \nabla \times \vec{A} \tag{4.11}$$

where $\vec{A}$ is an arbitrary vector since, $\nabla \cdot \nabla \times \vec{A} = 0$ for any $\vec{A}$ (a vector identity). The vorticity is given by the curl of the velocity:

$$\vec{\omega} = \nabla \times \vec{V} = \nabla \times (\nabla \times \vec{A}) = \nabla(\nabla \cdot \vec{A}) - \nabla^2 \vec{A} \tag{4.12}$$

Since, $\vec{A}$ is arbitrary, we choose it to be divergence free (i.e., $\nabla \cdot \vec{A} = 0$). The above equation then reduces to:

$$\vec{\omega} = -\nabla^2 \vec{A} \tag{4.13}$$

We recognize this equation as Poisson's equation, which has a known solution:

$$\vec{A}(\vec{q}) = \frac{1}{4\pi} \int \frac{\vec{\omega}(\vec{s})}{|\vec{q} - \vec{s}|} d^3 s \tag{4.14}$$

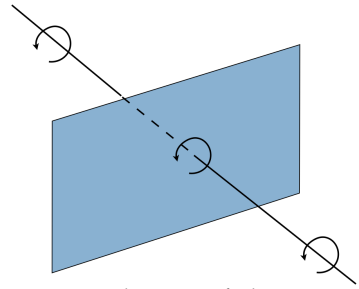

Fig. 4.12 A depiction of a line vortex. In a plane perpendicular to the line vortex the behavior is exactly that of a point vortex.

*The connection to electromagnetic induction is the reason that vortex drag is referred to as induced drag.

where q is the field location, and s is the location of the vorticity. In our case, we need the curl of this quantity (see Eq. 4.11). We can show that[†]

[†]This is straightforward to show for Cartesian coordinates.

$$\nabla \times \frac{\vec{\omega}(\vec{s})}{|\vec{q}-\vec{s}|} = \frac{\vec{\omega} \times (\vec{q}-\vec{s})}{|\vec{q}-\vec{s}|^3} \tag{4.15}$$

Thus:

$$\vec{V}(\vec{q}) = \frac{1}{4\pi} \int \frac{\vec{\omega} \times (\vec{q}-\vec{s})}{|\vec{q}-\vec{s}|^3} d^3s \tag{4.16}$$

Finally, we use a line vortex (infinitely thin) so the volume integral reduces to a line integral, where the circulation is constant along the filament $\omega d^3s = \Gamma d\vec{l}$. We also define $\vec{r} = \vec{q} - \vec{s}$ for simplicity. In other words, $\vec{r}$ is the distance from the integration point on the filament to the evaluation point in the field where velocity is computed.

$$\vec{V} = \frac{\Gamma}{4\pi} \int \frac{d\vec{l} \times \vec{r}}{|r|^3} \tag{4.17}$$

Note that this is a path integral, so the vortex filament can take any arbitrary curved shape. The direction $\vec{l}$ points in the direction of positive circulation.

Often, we will use vortex filaments that are straight line segments. Let's apply the Biot-Savart law to a straight line segment as shown in Fig. 4.13. The segment $d\vec{l}$ is a distance r away from a point we want to evaluate the induced velocity at. The distance h is the perpendicular distance from the vortex to the point. For the moment we won't worry about directions, for a simple filament it is obvious from the geometry, but later we will be more rigorous about directions. The magnitude of the cross product is:

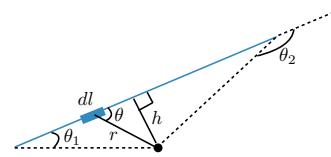

Fig. 4.13 A vortex filament and a point where the induced velocity is computed at.

$$d\vec{l} \times \vec{r} = dl\, r \sin\theta \tag{4.18}$$

From the geometry we see that

$$\sin\theta = \frac{h}{r} \tag{4.19}$$

$$\tan\theta = \frac{h}{l_h - l} \tag{4.20}$$

where l_h is the point on the vortex filament that intersects with h (a constant value), and l is a variable that moves along the filament. We use the first expression to solve for r and the second to solve for dl:

$$r = \frac{h}{\sin\theta} \tag{4.21}$$

$$dl = \frac{h}{\sin^2\theta} d\theta \tag{4.22}$$

Making these substitutions into Eq. 4.17 yields:

$$|\vec{V}| = \frac{\Gamma}{4\pi}\int_{\theta_1}^{\theta_2}\frac{\sin\theta}{h}d\theta \tag{4.23}$$

The distance h is a constant so it can be pulled out of the integral leaving us with a simple analytic expression for the magnitude of the induced velocity from the vortex segment:

$$V_\theta = \frac{\Gamma}{4\pi h}(\cos\theta_1 - \cos\theta_2) \tag{4.24}$$

Notice, that this expression returns the expected velocity magnitude for an infinite vortex (Eq. 4.8) and semi-infinite vortex (Eq. 4.9) when using $\theta_1 = 0, \theta_2 = \pi$ for the former case, and $\theta_1 = 0, \theta_2 = \pi/2$ for the latter.

To better understand how we can use vortex filaments for modeling purposes, let's consider a control volume that surrounds a vortex filament as shown in Fig. 4.14. You can imagine this control volume as a piece of paper that we wrap around the filament, without touching the filament. Let's now use Stoke's theorem (Eq. 1.59) on this control volume, with the velocity vector as the vector of interest:

$$\int_A \left(\nabla\times\vec{V}\right)\cdot d\vec{A} = \oint_C \vec{V}\cdot d\vec{\ell} \tag{4.25}$$

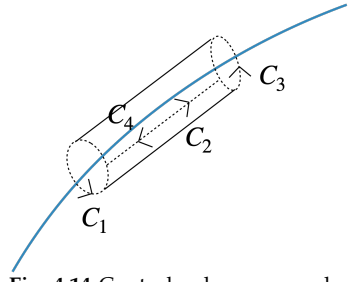

Fig. 4.14 Control volume around a vortex filament.

The quantity $\nabla\times\vec{V}$ we recognize as vorticity, and the left-hand-side as the definition of circulation (Eq. 2.75). We will use a closed-path contour starting from C_1 (around the circle), across the end of the "folded paper" (C_2), around the other circular end C_3, and back along the seam C_4 to close the path. The area enclosed by this contour does not having any vorticity crossing it. All of the vorticity is contained in the filament, and the filament does not cross the area enclosed by this contour (again imagine the area as that of a paper wrapped around the filament). Thus, the left hand side of the above integral is zero, there is no vorticity flux through the area. The contour integral around the full path must then also be zero. We break up that integral into four parts.

$$\int_{C_1}\vec{V}\cdot d\vec{\ell} + \int_{C_2}\vec{V}\cdot d\vec{\ell} + \int_{C_3}\vec{V}\cdot d\vec{\ell} + \int_{C_4}\vec{V}\cdot d\vec{\ell} = 0\,. \tag{4.26}$$

The integral along C_2 and C_4 are along the same segment, just in opposite directions, so they will cancel out. The integrals around the ends, we can see as the definition of circulation and each will contain the circulation of the filament (see Eq. 2.75 and **??**). The two contours traverse in opposite directions, and so will have opposite signs.

$$\Gamma_1 - \Gamma_3 = 0 \tag{4.27}$$

From the above expression, we see that $\Gamma_1 = \Gamma_3$. Or in other words, *the circulation along a vortex filament must be constant*. The corollary is a filament cannot just suddenly end in the fluid, otherwise, the contour integral on one end would be zero and the above equation would not be satisfied. We can still use arbitrary vortex filaments, but we have to connect them to other filaments. The segments must form a closed path, or extend to infinity. Collectively these conditions are known as *Helmholtz's vortex theorems*.

With those requirements in mind, a simple model of a wing might look like that shown in Fig. 4.15. The bound vortex stays fixed in the wing, and from a side view, looks the same as the circulation generated from an airfoil. The new addition for a wing is the trailing vortices. The trailing vortices look like a reasonable first model for a wake vortex (Fig. 4.6). Because, the vortices cannot end in the fluid, they are closed with a starting vortex (or more typically we just extend the trailing vortices to infinity). The starting vortex is physically observable when impulsively accelerating a wing. Notice that the strength and direction of the vortices must stay constant around the loop. Based on the drawn direction of circulation, we see that the vortices all generate downwash on the inside of the rectangle formed by the vortex filament path. Thus, this model is a first step toward modeling the downwash, that is a consequence of any three-dimensional lifting body, as discussed at the beginning of this chapter. We typically omit the

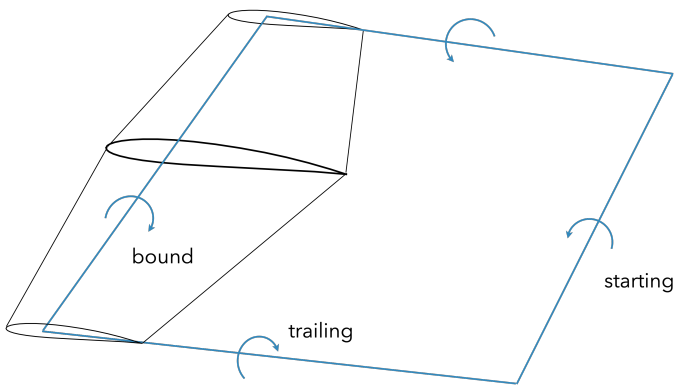

Fig. 4.15 A closed path vortex filament from a wing.

starting vortex, extending the trailing vortices to infinity, and call the resulting configuration a *horseshoe vortex* because of the horseshoe-like shape. From Eq. 4.24 we can compute the predicted downwash w at any location along the wing, based on the trailing vortices. Note that the bound vortex does not contribute any downwash at the quarter-

chord (with the bound vortex placed at the quarter-chord), since the distance from the center of the singularity is zero. The contributions from the two trailing vortices are shown in Fig. 4.16. While we do get downwash across the wing, the model is over simplified. The circulation distribution is modeled as constant along the wing with only one horseshoe vortex, and we know that the circulation must go to zero at the tips. Furthermore, this model predicts infinite downwash at the tip, an unphysical result (in fact, downwash at the tip generally isn't even large for a real wing). So a single horseshoe vortex is clearly insufficient to model a lifting wing, but it provides a starting point for improved models, two of which we will study in this chapter.

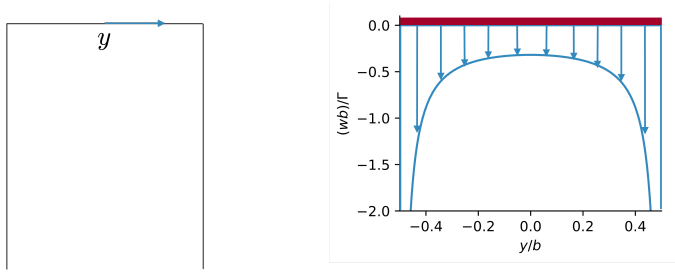

Fig. 4.16 The downwash induced at the wing from a single horseshoe vortex model. Left is a top view showing the horseshoe vortex, and the right figure is a back view showing the resultant downwash distribution.

4.4 Lifting Line Theory

If one horseshoe vortex is too crude to represent a wing, perhaps we can obtain a reasonable model by using multiple horseshoe vortices. A depiction of three horseshoe vortices, and the resulting lift distribution is shown in Fig. 4.17. The lift distribution is blocky, but is a better

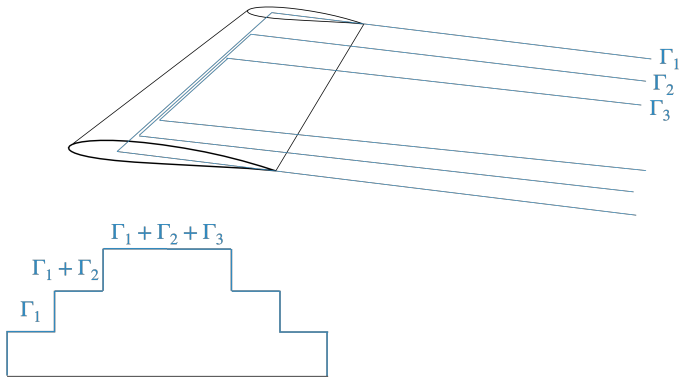

Fig. 4.17 A blocky but more realistic representation of the lift distribution as compared to a single horsesehoe vortex.

representation than the constant lift distribution produced by one

horseshoe. Notice that each additional horseshoe vortex adds an incremental circulation ($\Delta\Gamma$) to the overall circulation. In lifting line theory we extend this idea with an infinite number of horseshoe vortices, each contributing an infinitesimal change $d\Gamma$. Because we have an infinite number of vortices, it is more helpful to think of a continuously varying vorticity distribution, γ, where the vorticity is the derivative of the circulation along the *lifting line* (the line along which vorticity is distributed).

$$\gamma = \frac{d\Gamma}{dy} \tag{4.28}$$

We no longer have horseshoe vortices, but rather a vortex sheet of continuous varying vorticity. That continuously varying vorticity allows us to produce any arbitrary, smooth lift distribution.

We would like to compute the velocity induced by a vortex sheet along the lifting line. Consider Fig. 4.18, where the vorticity (γ) varies along the lifting line (as a function of a dummy variable y'), and we wish to compute the infinitesimal vertical velocity (dw) induced at some other location y. The lift distribution is increased by some $d\Gamma$ at this position, and so the corresponding strength of the trailing vortex at this particular position is: $d\Gamma = \frac{d\Gamma}{dy}dy = \gamma dy$. Each trailing vortex is a semi-infinite vortex, inducing a velocity at position y of (see Eq. 4.9):

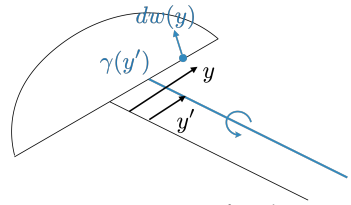

Fig. 4.18 Integration of trailing vortices along the lifting line.

$$dw(y) = -\frac{\gamma(y')dy'}{4\pi(y - y')} \tag{4.29}$$

The negative sign is needed because the circulation is decreasing with y on this side of the wing ($\gamma = d\Gamma/dy < 0$), and with a positive $(y - y')$, the resulting induced velocity is up (positive). Integrating across the lifting line gives:

$$w(y) = -\frac{1}{4\pi}\int_{-b/2}^{b/2} \frac{\gamma(y')dy'}{(y - y')} \tag{4.30}$$

From Fig. 4.11 we see that the induced angle of attack is given by (with the negative sign needed because we defined the induced velocity as positive up in the above equation):

$$\alpha_i = \tan^{-1}\left(\frac{-w}{V_\infty}\right) = \tan^{-1}\left(\frac{1}{4\pi V_\infty}\int_{-b/2}^{b/2} \frac{\gamma(y')dy'}{(y - y')}\right) \tag{4.31}$$

We can relate the lift coefficient to circulation through the Kutta-Joukowsi formula (Eq. 2.172), and the definition of the lift coefficient (eqn:lift2d):

$$L' = \rho V_\infty \Gamma = c_l \frac{1}{2}\rho V_\infty^2 c \Rightarrow c_l = \frac{2\Gamma}{V_\infty c} \tag{4.32}$$

Using the effective angle of attack from Eq. 4.7 in place of the angle of attack in Eq. 1.21, we relate the induced angle of attack to the lift coefficient across the linear portion:

$$c_l = m(\alpha - \alpha_0 - \alpha_i) \tag{4.33}$$

Putting those pieces together gives:

$$\frac{2\Gamma(y)}{V(y)c(y)} = m(y)\left(\alpha(y) - \alpha_0(y) - \tan^{-1}\left(\frac{1}{4\pi V(y)}\int_{-b/2}^{b/2}\frac{\gamma(y')dy'}{(y-y')}\right)\right) \tag{4.34}$$

This equation is known as the *fundamental equation of lifting line theory*. Given a known inflow speed, chord, and airfoil distribution, this equation, in principle, allows us to solve for the resulting lift distribution. The unknowns Γ and γ are not independent; recall that $\gamma = d\Gamma/dy$.

4.4.1 Elliptic Lift Distribution

Before looking at solving for a general situation, we start with a given solution: an elliptic lift distribution (Fig. 4.19). As we will see, an elliptic lift distribution is an efficient design from an induced drag point of view. An elliptic lift distribution is what it sounds like, the distribution of lift follows an elliptic shape:

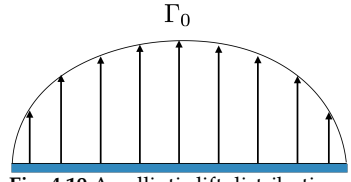

Fig. 4.19 An elliptic lift distribution.

$$\Gamma(y) = \Gamma_0\sqrt{1 - \left(\frac{y}{b/2}\right)^2} \tag{4.35}$$

where Γ_0 is the max circulation at the middle of the wing. The above is actually the circulation distribution, but the lift distribution is just a scalar multiple of this from the Kutta-Joukowski theorem:

$$L'(y) = \rho_\infty V_\infty \Gamma_0\sqrt{1 - \left(\frac{y}{b/2}\right)^2} \tag{4.36}$$

As one would expect, an elliptic lift distribution integrates nicely:

$$L = \int_{b/2}^{b/2} L'dy = \rho_\infty V_\infty \Gamma_0 b\frac{\pi}{4} \tag{4.37}$$

We equate this quantity to the lift from the definition of the lift coefficient:

$$L = C_L\frac{1}{2}\rho V_\infty^2 S \tag{4.38}$$

This allows us to relate the quantity Γ_0 to known properties of the wing:

$$\Gamma_0 = \frac{2V_\infty S C_L}{b\pi} \tag{4.39}$$

We will need the vorticity distribution to use in the fundamental lifting line equation:

$$\gamma(y') = \frac{d\Gamma}{dy}(y') = -\Gamma_0 \frac{4y}{b^2} \frac{1}{\sqrt{1-(2y/b)^2}} \tag{4.40}$$

We will now use the same type of cosine transformation we used in thin airfoil theory (Eq. 2.246), except we want the integrate from -1 to 1 (wingtip to wingtip), rather than from 0 to 1 (leading edge to trailing edge of airfoil):

$$y = \frac{b}{2}\cos\theta \text{ where } \theta = [\pi, 0] \tag{4.41}$$

Plugging the above vorticity distribution into Eq. 4.30, and using the cosine transformation gives the following equation for the induced velocity:

$$w(\theta) = -\frac{\Gamma_0}{2\pi b}\int_\pi^0 \frac{\cos\theta'}{\cos\theta - \cos\theta'} d\theta' \tag{4.42}$$

This is the same integral we saw in deriving thin airfoil theory (Eq. 2.250). Our integral corresponds directly to the $n = 1$ case (Eq. 2.252). Thus, the induced velocity distribution evaluates to:

$$w(\theta) = -\frac{\Gamma_0}{2b} \tag{4.43}$$

From this equation we see that the downwash (down because of the negative sign), is constant along the wing. In other words, *an elliptic lift distribution produces constant downwash*. This will be an important point later, but for now we note that this is a very different distribution than predicted by the overly simplified single horseshoe vortex (Fig. 4.16).

We already related our peak circulation, Γ_0, to known wing quantities (Eq. 4.39), so we plug those into this expression for downwash:

$$w = -\frac{\Gamma_0}{2b} = -\frac{V_\infty C_L}{AR\pi} \tag{4.44}$$

We then use the definition of the induced angle of attack to obtain:

$$\tan\alpha_i = \frac{-w}{V_\infty} = \frac{C_L}{\pi AR} \tag{4.45}$$

With the induced angle of attack defined in terms of known aircraft quantities (for an elliptic lift distribution), we can relate this angle to the lift and induced drag as seen in Fig. 4.20. We see that

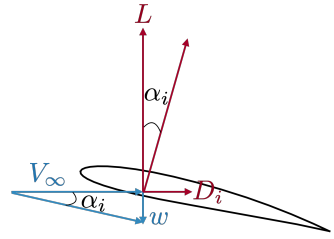

Fig. 4.20 Relationship between induced angle of attack and the lift and induced drag vectors.

$$\tan \alpha_i = \frac{D_i}{L} \tag{4.46}$$

or rearranging, and normalizing:

$$C_{Di} = C_L \tan \alpha_i \tag{4.47}$$

If we substitute the expression for an elliptic lift distribution (Eq. 4.45) we now have an equation for the induced drag produced by an elliptic lift distribution:

$$C_{Di} = \frac{C_L^2}{\pi AR} \tag{4.48}$$

where AR is defined using the reference area. To obtain an expression for induced drag, we multiply both sides by the dynamic pressure:

$$C_{Di}\frac{1}{2}\rho V_\infty^2 S = \frac{C_L^2}{\pi AR}\frac{1}{2}\rho V_\infty^2 S \tag{4.49}$$

Then expand the lift coefficient in terms of lift:

$$D_i = \frac{LC_L}{\pi AR} = \frac{L^2}{q_\infty S \pi AR} \tag{4.50}$$

The final result is:

$$D_i = \frac{L^2}{q_\infty \pi b^2} \tag{4.51}$$

While we assumed we have an elliptic lift distribution, we have not discussed how to produce such a distribution. To better understand this we use the fundamental lifting line equation (Eq. 4.34). For an elliptic lift distribution we've shown that the downwash, and thus the induced angle of attack is constant along the wing. Thus, the $\tan^{-1}$ term is a constant. The circulation term $\Gamma(y)$ is elliptic, and so if we move everything else to the right-hand side, those terms must also form an elliptic distribution. Because the induced angle of attack is constant, and if we assume that the inflow velocity, $V(y)$, is constant along the wing (as would be typical) then the remaining terms:

$$m(y)c(y)(\alpha(y) - \alpha_0(y)) \tag{4.52}$$

must form an elliptic distribution. To simplify, let's assume that we use the same airfoil throughout the wing (though not necessarily the same size airfoil). In that case, the lift curve slope (m) and the zero-lift angle of attack (α_0) would be constant along the wing. We would then need the produce $c(y)\alpha(y)$ to be elliptic. One way to achieve this is to use a wing with no twist, then $\alpha(y)$ is constant, and so the chord distribution

Fig. 4.21 The Supermarine Spitfire is a well-known example of an aircraft with an elliptic wing. Image from Adrian Pingstone, Wikimedia, public domain.

of the wing must be elliptic. This approach was perhaps most famously employed with the Spitfire (Fig. 4.21), a British WWII-era aircraft. If all we need is $c(y)\alpha(y)$ to be elliptic, that means we can produce an elliptic lift distribution with *any* arbitrary chord distribution, by appropriately twisting the wing (and thus changing $\alpha(y)$). Manufacturing an elliptic shape is more expensive, and unnecessary, so such an approach is rarely used anymore. Of course, not just any chord distribution is desirable. There are structural implications, and small chords will lead to premature stall.

4.4.2 Method of Restricted Variations

One simple way to show that the elliptic lift distribution is the minimum induced drag solution (for a fixed span and lift), is the *method of restricted variations*. In this method we consider some arbitrary lift distribution and we add differential amounts of lift at arbitrary locations (Fig. 4.22), subject to some constraints. For example, if we want to minimize induced drag, then we need the differential of induced drag to be zero. From the Kutta-Joukowski theorem the indued drag is given by:

$$D_i = \rho w \Gamma \tag{4.53}$$

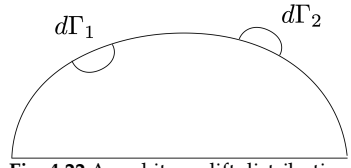

Fig. 4.22 An arbitrary lift distribution from which we add or subtract differential amounts of lift at arbitray locations.

where w is the downwash. Thus, if we add some small amount of circulation at two arbitrary locations, to maintain a minimum in induced drag we require (for an incompressible flow):

$$\delta D_i = 0 \Rightarrow w_1 \delta\Gamma_1 + w_2 \delta\Gamma_2 = 0 \tag{4.54}$$

Furthermore, we want to add these arbitrary circulations such that the lift is constant:

$$\delta L = 0 \Rightarrow \delta\Gamma_1 + \delta\Gamma_2 = 0 \tag{4.55}$$

If we combine these two equations we see that $w_1 = w_2$, but since 1 and 2 are arbitrary locations along the wing, this means that for minimum induced drag, with a fixed lift, the downwash must be constant along the wing. We already saw that an elliptic lift distribution produces constant downwash. Thus, *an elliptic lift distribution is the minimum induced drag solution for a fixed lift and span*.

This simple method can be used to produce various formulas. One example, is adding a root bending moment constraint as was shown by R. T. Jones. Such a constraint is interesting, but not usually useful as a structural constraint as it ignores thickness, and can be misleading for nonplanar wings. One minor variation is to consider minimum induced drag for a nonplanar wing. Figure 4.23 for example shows

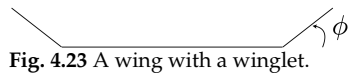

Fig. 4.23 A wing with a winglet.

a wing with a winglet. More generally, we allow to dihedral angle to vary continuously along the wing. In this case, the induced drag equation looks the same except we use the normalwash since "down" is not particularly relevant for a nonplanar wing. The normalwash is the induced velocity normal to the section of the wing. For minimum induced drag we need

$$\delta D_i = 0 \Rightarrow V_{n1}\delta\Gamma_1 + V_{n2}\delta\Gamma_2 = 0 \tag{4.56}$$

The lift equation looks similar, but we need to take only the vertical component of the circulation, which contributes to lift.

$$\delta L = 0 \Rightarrow \delta\Gamma_1 \cos\phi_1 + \delta\Gamma_2 \cos\phi_2 = 0 \tag{4.57}$$

Combing these two equations leads to the insight that the normalwash (V_n), in the farfield, should be proportional to the local dihedral angle:

$$V_n = w_0 \cos\phi \tag{4.58}$$

where w_0 is some constant.

This formula dispels another common misconception associated with winglets. A back view of a wing with a vertical winglet is depicted in Fig. 4.24. We see that the wake vortex, which induces a downwash on the wing, induces a sidewash on the winglet. We then consider a top view of the winglet, showing the airfoil in Fig. 4.25, with the wing-induced sidewash coming from right to left. Vectorially combining this velocity with the freestream results in the relative velocity V_r. From the Kutta-Jouwkoski theorem this inflow would produce a force at a right angle as depicted by the arrow emanating from the airfoil. Thus, we see that the airfoil produces a component of thrust, and is sometimes given as an explanation for why winglets are beneficial.

However, from our above derivation, we can see that this would not be an optimal winglet. The dihedral angle is 90° and so an optimally loaded winglet should be produce a net zero normalwash. Such a scenario is depicted in Fig. 4.26 where the winglet is loaded such that the normalwash of the winglet on itself, exactly cancels the normalwash induced by the wing on the winglet. Thus, no net thrust is produced. While this may seem to have eliminated any benefit, we have not considered the induced velocity of the winglet on the wing. In this scenario, the vortices generated by the winglet would produce an upwash on the main wing (near the tip), thus reducing the induced drag of the wing.

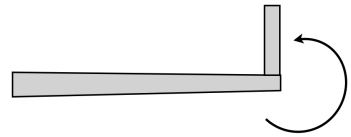

Fig. 4.24 Back view of wing with winglet.

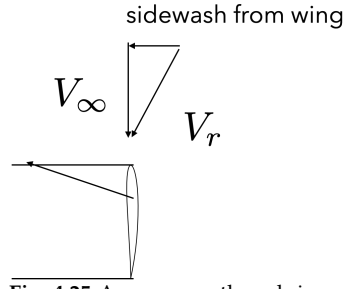

Fig. 4.25 A common, though incorrect explanation for the benefits of winglets.

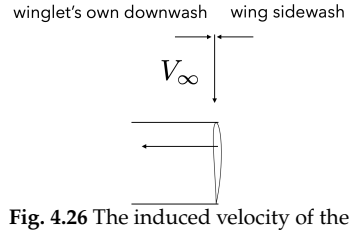

Fig. 4.26 The induced velocity of the wing on winglet cancels the induced velocity of the winglet on itself.

4.4.3 Contribution of the Bound Vortex

In lifting line theory we considered only trailing vortices in our integral. In doing so we obtained the result that the downwash, normalized by the freestream, at the wing should be $-\frac{C_L}{\pi AR}$. More generally, the induced velocity from these trailing vortices is depicted both in front of and downstream of the wing with the red curve shown in Fig. 4.27. As we go far upstream the trailing vortices have no effect, and far downstream they behave like an infinite vortex and so the induced velocity is twice as large. We now consider the bound vortex. The bound vortex may not induce a velocity on itself, but it certainly affects the wing. Far upstream and downstream the bound vortex will not induce any velocity. As we approach the bound vortex, for a straight wing, it will act like a point vortex, inducing very high velocities as we approach the lifting line as depicted with the blue line. The total induced velocity, trailing plus bound, is depicted in green. This is what the actual induced velocity distribution looks like, but this is problematic because the downwash at the wing is clearly not $-\frac{C_L}{\pi AR}$, which was the basis of our induced drag derivation. That result seems to only be applicable if we ignore the bound vortex, which does not seem justifiable.

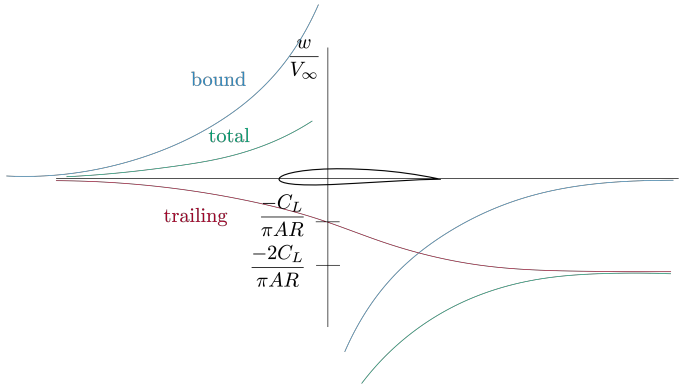

Fig. 4.27 Induced velocity from trailing and bound vortices (both separately and combined).

It turns out that we can ignore the influence of the bound vortex, but only when computing drag. In the real wing, the vorticity is not all concentrated along a line, but rather the vorticity is distributed. We could depicted that with a large number of discrete vortices as seen in Fig. 4.28. Let's now consider an arbitrary pair of these vortices, one with circulation Γ_1 and the other with circulation Γ_2 (Fig. 4.29). The first vortex induced a velocity on the second vortex, in the downward

Fig. 4.28 Bound vorticity distributed along the wing.

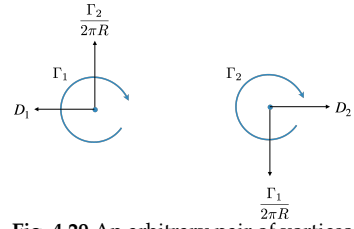

Fig. 4.29 An arbitrary pair of vortices and their mutually induced velocities.

direction with magnitude

$$|w_2| = \frac{\Gamma_1}{2\pi R} \tag{4.59}$$

where R is the distance between them. Conversely, the second induces an upward velocity on the first:

$$|w_1| = \frac{\Gamma_2}{2\pi R} \tag{4.60}$$

From the Kutta-Joukowski theorem the induced drag experienced on the first vortex, from the induced velocity is:

$$D_{i1} = -\rho w_1 \Gamma_1 = -\rho \frac{\Gamma_1 \Gamma_2}{2\pi R} \tag{4.61}$$

where the negative sign came from the right hand rule. Conversely, the induced drag experienced by the second vortex is:

$$D_{i2} = \rho w_2 \Gamma_2 = \rho \frac{\Gamma_1 \Gamma_2}{2\pi R} \tag{4.62}$$

The total induced drag of the pair of vortices ($D_{i1} + D_{i2}$) is 0. Because we chose any two arbitrary vortices, this is a general result: *the total induced drag of the bound vortices always cancels*. This is true for any orientation and in three-dimensions, as long as they are bound vortices (i.e., perpindicular to the freestream velocity). This result demonstrates why the lifting line concept works and why the induced drag formulas are correct, even though we have ignored the influence of the bound vortices.

4.4.4 Lift Curve Slope Reduction

Before considering a more general case, it is also worth noting that the presence of downwash affects the lift curve slope. If we had an infinite wing, with a constant airfoil, the lift coefficient would be given by:

$$C_L = m(a - \alpha_0) \tag{4.63}$$

where m is the lift curve slope, which we saw is theoretically equal to 2π for a thin airfoil (Eq. 2.288). For a finite wing we need to include the induced angle of attack:

$$C_L = m(a - \alpha_0 - \alpha_i) \tag{4.64}$$

In the case, of an elliptic lift distribution (Eq. 4.45) this expression becomes:

$$C_L = m\left(a - \alpha_0 - \tan^{-1}\left(\frac{C_L}{\pi AR}\right)\right) \tag{4.65}$$

If we assume that the induced angle of attack is small then:

$$C_L \approx m\left(a - \alpha_0 - \frac{C_L}{\pi AR}\right) \tag{4.66}$$

We now take derivatives of both sides with respect to α:

$$\frac{dC_L}{d\alpha} = m\left(1 - \frac{dC_L}{d\alpha}\frac{1}{\pi AR}\right) \tag{4.67}$$

Solving for the lift curve slope gives:

$$C_{L,\alpha} = \frac{m}{1 + \frac{m}{\pi AR}} \tag{4.68}$$

This equation shows that if the wing had an infinite aspect ratio, then our lift curve slope would be the same as that of the airfoil, as expected. However, the presence of downwash reduces the lift curve slope of the wing. As an example, for an aspect ratio of 8, the predicted lift curve slope from the above formula would be 1.6π instead of 2π. Note that the above formula is just an approximation that assumes constant airfoils, an elliptic lift distribution, and a small induced angle of attack. Still it is a reasonable first estimate and more importantly illustrates the general behavior of a reduced lift curve slope for a finite wing.

4.4.5 General Lift Distribution

To motivate a general case, let's consider again an elliptic lift distribution:

$$\Gamma(y) = \Gamma_0\sqrt{1 - \left(\frac{y}{b/2}\right)^2} \tag{4.69}$$

but use the coordinate transformation from Eq. 4.41:

$$\Gamma(\theta) = \Gamma_0\sqrt{1 - \cos^2\theta} = \Gamma_0 \sin\theta \tag{4.70}$$

Like we did in thin airfoil theory for a cambered airfoil (Section 2.9.5), we will represent the general case with a Fourier sine series:

$$\Gamma(\theta) = 2bV_\infty \sum_{n=1}^{N} A_n \sin(n\theta) \tag{4.71}$$

The choice of constant $2bV_\infty$ is arbitrary, though we would like to choose it so that the coefficients A_n are nondimensional.

We plug the above into the fundamental lifting line equation (Eq. 4.34).

$$\alpha(\theta) - \alpha_0(\theta) = \frac{2b}{\pi c(\theta)} \sum_{n=1}^{N} A_n \sin(n\theta) + \sum_{n=1}^{N} nA_n \frac{\sin(n\theta)}{\sin\theta} \tag{4.72}$$

In the above we made use of a small angle approximation

$$\alpha_i = \tan^{-1}\left(\frac{-w}{V_\infty}\right) \approx \frac{-w}{V_\infty} \tag{4.73}$$

There are N unknowns, where N depends on how many terms we wish to include in the Fourier series, so we need N equations. This is done through a *collocation* method. This means that we choose N points along the span and apply the above equation at each of the N points, resulting in N equations and N unknowns that we can solve for simultaneously as a linear system of equations. For symmetric loadings, which is common, all the even coefficients of the series ($A_2, A_4, \ldots$) are zero so we need not include them as unknowns. Asymmetric loadings are used as well, for example, to simulate a wing with aileron deflection.

Because of the orthogonality of the Fourier terms the integral for lift simplifies to:

$$C_L = A_1 \pi AR \tag{4.74}$$

The induced drag equation becomes:

$$C_{Di} = \frac{C_L^2}{\pi AR} \sum_{n=1}^{N} n \left(\frac{A_n}{A_1}\right)^2 \tag{4.75}$$

Even though the lift coefficient only depends on one coefficient, unlike thin airfoil theory, you can't compute A_1 independently. As we saw above with the collocation method, all of the coefficients must be computed simultaneously. Thus, accuracy improves as you include more coefficients in the Fourier series even if we only were interested in lift.

For convenience, the coefficient terms in induced drag are wrapped up into a single constant called the *inviscid span efficiency*:

$$e_{inv} = \left(\sum_{n=1}^{N} n \left(\frac{A_n}{A_1}\right)^2\right)^{-1} \tag{4.76}$$

Then, the induced drag coefficient formula simplifies to:

$$C_{Di} = \frac{C_L^2}{\pi AR e_{inv}} \tag{4.77}$$

or in dimensional terms:

$$D_i = \frac{L^2}{q \pi b^2 e_{inv}} \tag{4.78}$$

If we compare Eq. 4.77 with Eq. 4.48 we see that for an elliptic lift distribution $e_{inv} = 1$. Thus, the inviscid span efficiency could be considered a measure of how close the lift distribution is to elliptic. All planar distributions will have $e_{inv} \leq 1$, so as we saw previously, the elliptic lift distribution is the minimum induced drag solution assuming a planar lift distribution and a fixed span. A nonplanar lift distribution (e.g., adding winglets) can increase the inviscid span efficiency above 1.

Various extensions to lifting line theory have been developed over the years, often referred to as a nonlinear lifting line theory. We do not describe those in more detail here, though they can be quite useful, but rather describe an alternative approach that is perhaps more commonly used in the next section.

4.5 Vortex Lattice Method

The panel methods of Chapter 2 can be extended into three dimensions (with some additional considerations), but we will instead consider a simpler, and widely-used method, for early stage design of three dimensional lifting surfaces (e.g., wings, tails). The vortex lattice method (VLM) is essentially an extension of thin airfoil theory into three dimensions, or it could also be thought of as a simplified implementation of a 3D panel code.

In this method, a lifting surface is divided into panels, and each panel has a horseshoe vortex as shown in Fig. 4.30. The trailing vortices extends into the $+x$ direction of the body axes.

A VLM uses the thin airfoil assumption so that lifting surfaces are flat (not curved), and changes in twist are handled in the boundary condition and not the geometry. A wing may be represented with multiple flat surfaces, for example a wing and winglets. Curved surfaces require a more general 3D panel method.

A VLM can have both spanwise and chordwise panels. If only spanwise panels are used, it is called a *Weissinger* formulation. This simplification is appropriate for high aspect ratio wings where resolving the chordwise pressure distribution is less significant in obtaining an accurate lift distribution.

Because the vortex filaments automatically satisfy the governing equations, the only remaining conditions to satisfy are flow tangency and the Kutta condition. The flow tangency condition (or no-flow-through condition) will be applied at select control points. Because each horseshoe vortex has a constant (as yet unknown) strength, we can only have one control point per panel, thus maintaining an equal

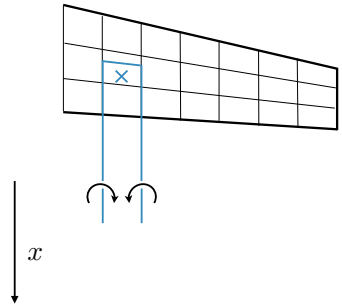

Fig. 4.30 An example paneling on a lifting surface. A horseshoe vortex is depicted on one panel, and each panel will have its own horseshoe vortex. The x denotes the control point for the given panel.

number of unknowns and equations. The control point was denoted as an x in Fig. 4.30.

A vortex lattice method uses what is called a lumped vortex method, this means that distributed vorticity along each panel is all lumped into one vortex as shown in Fig. 2.56. Even with multiple chordwise panels, this approach is still used, just with the vorticity lumped into separate vortices for each chordwise panel. Back in **??** we already considered this exact scenario and determined from thin airfoil theory that the vorticity should be placed at the quarter chord, and the control point at the three-quarters-chord. The placing of the vortex at the quarter chord could also be motivated by the fact that it is the location of the aerodynamic center according to thin airfoil theory as seen previously in Section 2.9.7. Also note that in using the lift result from thin airfoil theory we have implicitly imposed the Kutta condition already. Thus, all that remains is satisfying flow tangency at the control points.

4.5.1 Aerodynamic Influence Coefficients (AIC)

As noted, the control point on each panel is at the section's three-quarters-chord point. There is one control point for each panel. The boundary condition is flow tangency:

$$V_n|_{cp} = 0 \tag{4.79}$$

where the cp subscript denotes a control point, and the boundary condition is applied at each control point separately. The velocity can be broken up into four terms: the freestream velocity, velocity from rigid-body rotation, self-induced velocity from the vortices, and other external velocity sources such as upstream wakes or gusts. The freestream velocity is defined as the negative of the translational motion of the vehicle (thus it is constant for the entire aircraft, unlike gusts which may vary along the aircraft and are lumped in $\vec{V}_{other}$). The flow tangency boundary condition is thus:

$$\left[(\vec{V}_\infty - \vec{\Omega} \times \vec{r}_b + \vec{V}_{ind} + \vec{V}_{other}) \cdot \hat{n}\right]_{cp} = 0 \tag{4.80}$$

where $\vec{r}_b$ is a vector from the aircraft center of gravity to a point of interest. We will move the induced term to one side, and all other terms to the other side (where the cp subscript is dropped for simplicity in notation):

$$\vec{V}_{ind} \cdot \hat{n} = -(\vec{V}_\infty - \vec{\Omega} \times \vec{r} + \vec{V}_{other}) \cdot \hat{n} \tag{4.81}$$

To keep the notation simple we will denote the velocity on the right-hand side as $\vec{V}_{ext}$ (external velocity).

$$\vec{V}_{ind} \cdot \hat{n} = -\vec{V}_{ext} \cdot \hat{n} \tag{4.82}$$

In general the rotational velocity, self-induced velocity, and other velocity sources like gusts all vary along the aircraft, and so this boundary condition will be applied separately at each control point i.

$$\vec{V}_{ind,i} \cdot \hat{n}_i = -\vec{V}_{ext,i} \cdot \hat{n}_i \tag{4.83}$$

External Velocities

Angle of attack and sideslip angle are defined in the standard way (Fig. 4.31). In this case, the the freestream velocity vector in the body axes is:

$$\vec{V}_\infty = V_\infty \begin{bmatrix} \cos\alpha \cos\beta \\ -\sin\beta \\ \sin\alpha \cos\beta \end{bmatrix} \tag{4.84}$$

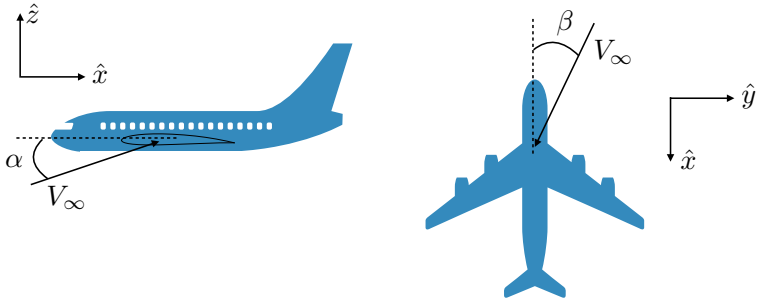

Fig. 4.31 Angle of attack and sideslip shown in body axes.

The rotational velocity is defined about the center of gravity and is simply:

$$\Omega = \begin{bmatrix} \Omega_x \\ \Omega_y \\ \Omega_z \end{bmatrix} \tag{4.85}$$

The radial vector used in determining rotational velocities is the distance from the aircraft center of gravity to the control point of interest:

$$\vec{r}_i = \vec{r}_{cp,i} - \vec{r}_{cg} \tag{4.86}$$

If we only have one chordwise panel, or even if we have a few, it generally doesn't make sense to use camber in defining the normal direction. Furthermore, camber was implicitly accounted for in the use of positioning the bound vortex and control point (recall that the derivation assumed parabolic camber of any arbitrary magnitude). The normal vector is a function of the local twist and dihedral as shown in Fig. 4.32. Twist cannot be lumped with angle of attack for nonplanar wings. To illustrate why, imagine the twist on a winglet (sometimes

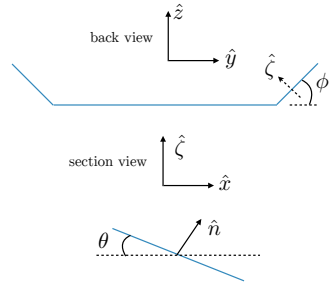

Fig. 4.32 Angles and coordinate systems used to determine normal vector to each panel. Top figure shows dihedral, while the bottom shows twist.

called the cant angle), it moves the surface in a very different way than changing the angle of attack of the entire aircraft.

From Fig. 4.32 we can resolve $\hat{\zeta}$ and $\hat{n}$ into components as follows:

$$\hat{\zeta} = -\sin\phi\hat{y} + \cos\phi\hat{z} \tag{4.87}$$

$$\hat{n} = \sin\theta\hat{x} + \cos\theta\hat{\zeta} \tag{4.88}$$

Substituting Eq. 4.87 into Eq. 4.88 yields:

$$\hat{n} = \begin{bmatrix} \sin\theta \\ -\cos\theta\sin\phi \\ \cos\theta\cos\phi \end{bmatrix} \tag{4.89}$$

Using the panel discretization where y and z define the corner points of the horseshoe vortices (Fig. 4.33):

$$\sin\phi_i = \frac{z_{i+1} - z_i}{\sqrt{(y_{i+1} - y_i)^2 + (z_{i+1} - z_i)^2}} \tag{4.90}$$

$$\cos\phi_i = \frac{y_{i+1} - y_i}{\sqrt{(y_{i+1} - y_i)^2 + (z_{i+1} - z_i)^2}} \tag{4.91}$$

Induced Velocities

From the Biot-Savart law (Eq. 4.17) the induced velocity from all of the vortex filaments at control point i is:

$$\vec{V}_{ind,i} = \sum_j \frac{\Gamma_j}{4\pi} \int_j \frac{d\vec{l}_j \times \vec{r}_{ij}}{|r_{ij}|^3} \tag{4.92}$$

where r_{ij} is the distance from a point on the line vortex j to control point i. We can reexpress this sum by separating out the geometric terms from the circulation:

$$\vec{V}_{ind,i} = \sum_j \hat{V}_{ij}\Gamma_j \tag{4.93}$$

where $\hat{V}$ is the induced velocity at the control point, for unit circulation. Thus, the boundary condition at the ith control point (Eq. 4.83) becomes:

$$\sum_j \Gamma_j \hat{V}_{ij} \cdot \hat{n}_i = -\vec{V}_{ext,i} \cdot \hat{n}_i \tag{4.94}$$

Each control point is one equation, and putting them all together forms a linear system of equations:

$$[AIC]\Gamma = b \tag{4.95}$$

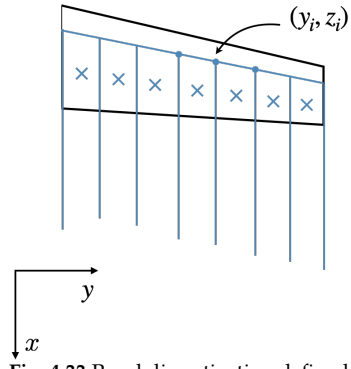

Fig. 4.33 Panel discretization defined by the corner points.

where

$$b_i = -\vec{V}_{ext,i} \cdot \hat{n}_i \tag{4.96}$$

and the aerodynamic influence coefficient matrix is given by:

$$AIC_{ij} = \hat{V}_{ij} \cdot \hat{n}_i \tag{4.97}$$

The main challenge then is to determine $\hat{V}_{ij}$

We use the velocity induced by a vortex segment (Eq. 4.24) to compute the induced velocity from a horseshoe vortex, which is comprised of three segments. This time we will need to be more careful with directions. First, we convert this expression in terms of vectors so that we can use it more generally in a computational implementation. Second, the angles θ are less convenient to work with, we would prefer to use vectors instead. We define the quantities $\vec{r}_0$, $\vec{r}_1$ and $\vec{r}_2$ as shown in Fig. 4.34. Vector $\vec{r}_0$ starts at one end of the vortex filament and ends at the other end of the filament pointing in the direction of positive circulation according to the right hand rule. Vector $\vec{r}_1$ points from the start of the filament to the point of interest, and vector $\vec{r}_2$ points from the end of the filament to the point of interest.

We use the definition of the dot product to obtain the angles.

$$\vec{r}_0 \cdot \vec{r}_1 = |\vec{r}_0||\vec{r}_1| \cos\theta_1 \Rightarrow \cos\theta_1 = \frac{\vec{r}_0 \cdot \vec{r}_1}{|\vec{r}_0||\vec{r}_1|} \tag{4.98}$$

$$\vec{r}_0 \cdot \vec{r}_2 = |\vec{r}_0||\vec{r}_2| \cos\theta_2 \Rightarrow \cos\theta_2 = \frac{\vec{r}_0 \cdot \vec{r}_2}{|\vec{r}_0||\vec{r}_2|} \tag{4.99}$$

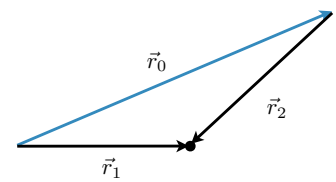

Fig. 4.34 Definitions for vectors used in horseshoe vortex derivation.

The distance h is just $r_1 \sin\theta_1$, but again we want to eliminate the explicit dependence on angles. Using the definition of the cross product:

$$|\vec{r}_0 \times \vec{r}_1| = |\vec{r}_0||\vec{r}_1| \sin\theta_1 \tag{4.100}$$

Thus,

$$h = |\vec{r}_1| \frac{|\vec{r}_0 \times \vec{r}_1|}{|\vec{r}_0||\vec{r}_1|} = \frac{|\vec{r}_0 \times \vec{r}_1|}{|\vec{r}_0|} \tag{4.101}$$

Finally, we need to determine the direction of V_θ. We have defined $\vec{r}_0$ to correspond to the direction of the circulation $\vec{\Gamma}$. Thus, the direction is a unit vector in the direction of $\vec{r}_0 \times \vec{r}_1$. In other words,

$$\vec{V}_\theta = V_\theta \frac{\vec{r}_0 \times \vec{r}_1}{|\vec{r}_0 \times \vec{r}_1|} \tag{4.102}$$

Putting all of these pieces together yields:

$$\begin{aligned} \vec{V}_\theta &= \frac{\Gamma|\vec{r}_0|}{4\pi|\vec{r}_0 \times \vec{r}_1|} \frac{\vec{r}_0 \times \vec{r}_1}{|\vec{r}_0 \times \vec{r}_1|} \left(\frac{\vec{r}_0 \cdot \vec{r}_1}{|\vec{r}_0||\vec{r}_1|} - \frac{\vec{r}_0 \cdot \vec{r}_2}{|\vec{r}_0||\vec{r}_2|} \right) \\ &= \frac{\Gamma}{4\pi} \frac{\vec{r}_0 \times \vec{r}_1}{|\vec{r}_0 \times \vec{r}_1|^2} \left(\frac{\vec{r}_0 \cdot \vec{r}_1}{|\vec{r}_1|} - \frac{\vec{r}_0 \cdot \vec{r}_2}{|\vec{r}_2|} \right) \end{aligned} \tag{4.103}$$

To simplify further we can express $\vec{r}_0$ in terms of $\vec{r}_1$ and $\vec{r}_2$:

$$\vec{r}_0 = \vec{r}_1 - \vec{r}_2 \tag{4.104}$$

Making this substitution yields:

$$= \frac{\Gamma}{4\pi} \frac{\vec{r}_1 \times \vec{r}_2}{|\vec{r}_1 \times \vec{r}_2|^2} \left(\frac{|\vec{r}_1|^2 - \vec{r}_2 \cdot \vec{r}_1}{|\vec{r}_1|} - \frac{\vec{r}_1 \cdot \vec{r}_2 - |\vec{r}_2|^2}{|\vec{r}_2|} \right) \tag{4.105}$$

We can expand the cross product in the denominator:

$$\begin{aligned} |\vec{r}_1 \times \vec{r}_2|^2 &= (\vec{r}_1 \times \vec{r}_2) \cdot (\vec{r}_1 \times \vec{r}_2) \\ &= (\vec{r}_1 \cdot \vec{r}_1)(\vec{r}_2 \cdot \vec{r}_2) - (\vec{r}_2 \cdot \vec{r}_1)(\vec{r}_1 \cdot \vec{r}_2) \\ &= |\vec{r}_1|^2 |\vec{r}_2|^2 - (\vec{r}_1 \cdot \vec{r}_2)^2 \end{aligned} \tag{4.106}$$

Let's also simplify the expression in parenthesis from Eq. 4.105. We will factor out a common term:

$$\begin{aligned} \left(\frac{|\vec{r}_1|^2 - \vec{r}_2 \cdot \vec{r}_1}{|\vec{r}_1|} - \frac{\vec{r}_1 \cdot \vec{r}_2 - |\vec{r}_2|^2}{|\vec{r}_2|} \right) &= \left(|\vec{r}_1| - \frac{\vec{r}_1 \cdot \vec{r}_2}{|\vec{r}_1|} - \frac{\vec{r}_1 \cdot \vec{r}_2}{|\vec{r}_2|} + |\vec{r}_2| \right) \\ &= \left(\frac{|\vec{r}_1||\vec{r}_2|}{|\vec{r}_2|} - \frac{\vec{r}_1 \cdot \vec{r}_2}{|\vec{r}_1|} - \frac{\vec{r}_1 \cdot \vec{r}_2}{|\vec{r}_2|} + \frac{|\vec{r}_1||\vec{r}_2|}{|\vec{r}_1|} \right) \\ &= (|\vec{r}_1||\vec{r}_2| - \vec{r}_1 \cdot \vec{r}_2) \left(\frac{1}{|\vec{r}_2|} + \frac{1}{|\vec{r}_1|} \right) \end{aligned} \tag{4.107}$$

If we substitute Eq. 4.106 and Eq. 4.107 into Eq. 4.105 we get

$$\vec{V}_\theta = \frac{\Gamma}{4\pi} \frac{\vec{r}_1 \times \vec{r}_2}{(|\vec{r}_1|^2 |\vec{r}_2|^2 - (\vec{r}_1 \cdot \vec{r}_2)^2)} (|\vec{r}_1||\vec{r}_2| - \vec{r}_1 \cdot \vec{r}_2) \left(\frac{1}{|\vec{r}_2|} + \frac{1}{|\vec{r}_1|} \right) \tag{4.108}$$

We can now factor the term in the denominator

$$|\vec{r}_1|^2 |\vec{r}_2|^2 - (\vec{r}_1 \cdot \vec{r}_2)^2 = \left[|\vec{r}_1||\vec{r}_2| + (\vec{r}_1 \cdot \vec{r}_2) \right] \left[|\vec{r}_1||\vec{r}_2| - (\vec{r}_1 \cdot \vec{r}_2) \right] \tag{4.109}$$

which partially cancels with one of the terms in the numerator. The result is an expression for the induced velocity from one vortex filament in terms of only the two vectors $\vec{r}_1$ and $\vec{r}_2$.

$$\vec{V}_\theta = \frac{\Gamma}{4\pi} \frac{\vec{r}_1 \times \vec{r}_2}{(|\vec{r}_1||\vec{r}_2| + \vec{r}_1 \cdot \vec{r}_2)} \left(\frac{1}{|\vec{r}_1|} + \frac{1}{|\vec{r}_2|} \right) \tag{4.110}$$

Now we apply this formula to the horseshoe vortex shown in Fig. 4.35. For the two bound vortices we need to allow some of the vector magnitudes to extend to infinity to represent the semi-infinite vortices.

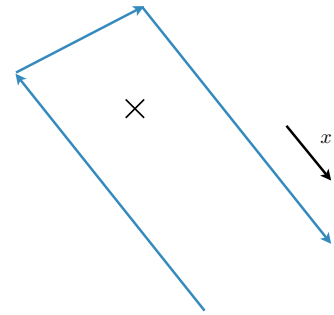

Fig. 4.35 A horseshoe vortex.

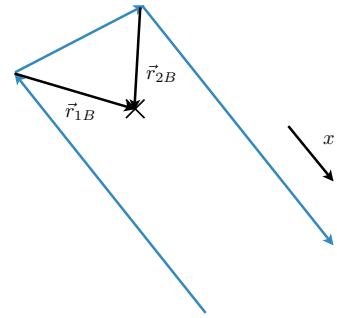

Fig. 4.36 Contribution of bound vortex induced velocity at the control point.

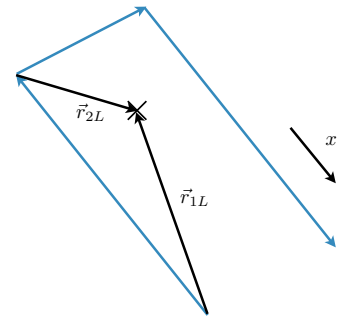

Fig. 4.37 Contributions from the left semi-infinite vortex.

The bound vortex uses all the terms of the formula. We use subscript B to denote the vectors shown in Fig. 4.36.

$$\vec{V}_{\theta B} = \frac{\Gamma}{4\pi} \frac{\vec{r}_{1B} \times \vec{r}_{2B}}{(|\vec{r}_{1B}||\vec{r}_{2B}| + \vec{r}_{1B} \cdot \vec{r}_{2B})} \left(\frac{1}{|\vec{r_{1B}}|} + \frac{1}{|\vec{r_{2B}}|} \right) \tag{4.111}$$

For the left vortex (Fig. 4.37) we can see that as the end of the vortex goes to infinity:

$$|\vec{r}_{1L}| \to \infty \tag{4.112}$$

$$\frac{\vec{r}_{1L}}{|\vec{r}_{1L}|} = -\hat{x} \tag{4.113}$$

If we divide the top and bottom of Eq. 4.110 by $|\vec{r}_1|$ and let $|\vec{r}_1| \to \infty$ the expression simplifies (where we use L to denote the left vortex):

$$\vec{V}_{\theta L} = \frac{\Gamma}{4\pi} \frac{-\hat{x} \times \vec{r}_{2L}}{(|\vec{r}_{2L}| - \hat{x} \cdot \vec{r}_{2L})} \left(\frac{1}{|\vec{r_{2L}}|} \right) \tag{4.114}$$

But note that $\vec{r}_{2L} = \vec{r}_{1B}$, so we can rewrite this contribution as:

$$\vec{V}_{\theta L} = \frac{\Gamma}{4\pi} \frac{\vec{r}_{1B} \times \hat{x}}{(|\vec{r}_{1B}| - \vec{r}_{1B} \cdot \hat{x})} \left(\frac{1}{|\vec{r_{1B}}|} \right) \tag{4.115}$$

For the right vortex (Fig. 4.38) we see that as the vortex goes off to infinity:

$$|\vec{r}_{2R}| \to \infty \tag{4.116}$$

$$\frac{\vec{r}_{2R}}{|\vec{r}_{2R}|} = -\hat{x} \tag{4.117}$$

If we divide the top and bottom of Eq. 4.110 by $|\vec{r}_2|$ and let $|\vec{r}_2| \to \infty$ the expression simplifies (where we use R to denote the right vortex):

$$\vec{V}_{\theta R} = \frac{\Gamma}{4\pi} \frac{\vec{r}_{1R} \times -\hat{x}}{(|\vec{r}_{1R}| + \vec{r}_{1R} \cdot -\hat{x})} \left(\frac{1}{|\vec{r_{1R}}|} \right) \tag{4.118}$$

But note that $\vec{r}_{1R} = \vec{r}_{2B}$, so we can rewrite this contribution as:

$$\vec{V}_{\theta R} = -\frac{\Gamma}{4\pi} \frac{\vec{r}_{2B} \times \hat{x}}{(|\vec{r}_{2B}| - \vec{r}_{2B} \cdot \hat{x})} \left(\frac{1}{|\vec{r_{2B}}|} \right) \tag{4.119}$$

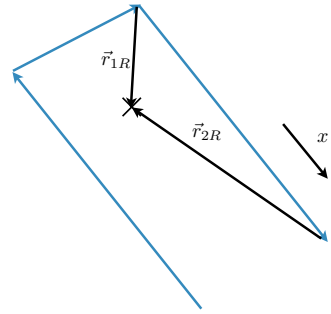

Fig. 4.38 Contributions from the right semi-infinite vortex.

Putting it all together (and dropping the B subscript): the total induced velocity at some point r measured relative to the bound vortex corners as seen in Fig. 4.36 is:

$$\vec{V} = \frac{\Gamma}{4\pi} \left[\frac{\vec{r}_1 \times \vec{r}_2}{(|\vec{r}_1||\vec{r}_2| + \vec{r}_1 \cdot \vec{r}_2)} \left(\frac{1}{|\vec{r}_1|} + \frac{1}{|\vec{r}_2|} \right) + \frac{\vec{r}_1 \times \hat{x}}{(|\vec{r}_1| - \vec{r}_1 \cdot \hat{x})} \frac{1}{|\vec{r}_1|} - \frac{\vec{r}_2 \times \hat{x}}{(|\vec{r}_2| - \vec{r}_2 \cdot \hat{x})} \frac{1}{|\vec{r}_2|} \right] \tag{4.120}$$

Finally, we want the velocity for unit circulation and so

$$\hat{V}_{ij} = \frac{1}{4\pi}\left[\frac{\vec{r}_1 \times \vec{r}_2}{(|\vec{r}_1||\vec{r}_2| + \vec{r}_1 \cdot \vec{r}_2)}\left(\frac{1}{|\vec{r}_1|} + \frac{1}{|\vec{r}_2|}\right) + \frac{\vec{r}_1 \times \hat{x}}{(|\vec{r}_1| - r_{1x})}\frac{1}{|\vec{r}_1|} - \frac{\vec{r}_2 \times \hat{x}}{(|\vec{r}_2| - r_{2x})}\frac{1}{|\vec{r}_2|}\right] \tag{4.121}$$

where each vector points from the corner of the horseshoe vortex at position j to control point i (Fig. 4.39):

$$\vec{r}_1 = \vec{r}_{CPi} - \vec{r}_j \tag{4.122}$$

$$\vec{r}_2 = \vec{r}_{CPi} - \vec{r}_{j+1} \tag{4.123}$$

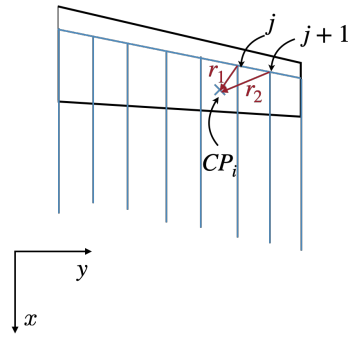

Fig. 4.39 Depiction of two vectors used in computing influence of bound vortex j at control point i.

Symmetry

If the aircraft is symmetric then it is more efficient to only solve for the circulation on half of the aircraft. This reduces the size of the linear system in half. Solving a dense linear system is approximately an $O(n^3)$ operation, and the linear system solve is the main computational cost of the VLM, so if taking advantage of symmetry is possible it is generally worth doing so. This is straightforward in constructing the AIC matrix. The only change is that for each control point we need to add the influence of horseshoe vortex i as well as the influence from its mirror image $-i$. The vector $\vec{r}_{-i}$ is identical to $\vec{r}_i$ except that the sign of the y component is flipped (assuming symmetry about the x-z plane).

4.5.2 Near-Field Forces and Moments

Forces and moments can be computed in the near field using the Kutta-Joukowski theorem:

$$\vec{F}'_i = \rho \vec{V}_i \times \vec{\Gamma}_i \tag{4.124}$$

First, we must compute the local velocity vector at each bound vortex. Like the boundary condition, this requires a sum of the the freestream velocity (translation), rotation, induced velocity, and other external velocities.

$$\vec{V} = \vec{V}_\infty - \vec{\Omega} \times \vec{r}_b + \vec{V}_{ind} + \vec{V}_{other} \tag{4.125}$$

This time the induced velocity is not computed at the control points, but rather at the center of the bound vortex. We can reuse Eq. 4.121, but evaluated at the center of each bound vortex. This eliminates the first term (when evaluating the influence of the panel on itself) because

the bound vortex does not induce any velocity on itself. The velocity induced at the center of vortex i is:

$$\vec{V}_{ind,i} = \sum \Gamma_j \bar{V}_{ij} \tag{4.126}$$

The induced velocity per unit circulation, $\bar{V}_{ij}$, is computed using Eq. 4.121, but with the following vectors.

$$\vec{r}_1 = \vec{r}_{i,mid} - \vec{r}_j \tag{4.127}$$

$$\vec{r}_2 = \vec{r}_{i,mid} - \vec{r}_{j+1} \tag{4.128}$$

where $\vec{r}_{i,mid} = (\vec{r}_i + \vec{r}_{i+1})/2$.

Using the Kutta-Joukowski theorem, where the force is constant across a panel, results in a force for each panel of:

$$\vec{F}_i = \rho \vec{V}_i \times \vec{\Gamma}_i \Delta s_i \tag{4.129}$$

where the direction of Γ is defined by

$$\vec{\Gamma}_i \Delta s_i = \Gamma_i (\vec{r}_{i+1} - \vec{r}_i) \tag{4.130}$$

The total forces are then

$$\vec{F} = \sum_i \vec{F}_i \tag{4.131}$$

$$= \sum_i \rho \Gamma_i \left(\sum_j (\Gamma_j \hat{V}_{ij}) + \vec{V}_\infty - \vec{\Omega} \times \vec{r}_i + \vec{V}_{other,i} \right) \times (\vec{r}_{i+1} - \vec{r}_i) \tag{4.132}$$

The total moments are given by:

$$\vec{M} = \sum_i \vec{r}_{m,i} \times \vec{F}_i \tag{4.133}$$

where $\vec{r}_{m,i}$ is the vector originating from some specified reference point (often the aircraft c.g.) and ending at the location of force F_i (i.e., $\vec{r}_{m,i} = \vec{r}_{i,mid} - \vec{r}_{cg}$).

These forces and moments are in the body coordinate system. However, as aerodynamicists, we generally care about forces in the wind axes (oriented with the freestream) because that is the coordinate system where lift and drag are defined. The rotation from body axes to wind axes is accomplished by the following rotations:

$$\begin{bmatrix} D \\ Y \\ L \end{bmatrix} = \begin{bmatrix} \cos\beta & -\sin\beta & 0 \\ \sin\beta & \cos\beta & 0 \\ 0 & 0 & 1 \end{bmatrix} \begin{bmatrix} \cos\alpha & 0 & \sin\alpha \\ 0 & 1 & 0 \\ -\sin\alpha & 0 & \cos\alpha \end{bmatrix} \begin{bmatrix} F_x \\ F_y \\ F_z \end{bmatrix} \tag{4.134}$$

We rotate moments similarly (although for dynamics leaving them in the body-coordinate system in generally preferred).

4.5.3 Simpler Alternative to Estimating Forces/Moments

The above procedure for computing the forces/moments is a bit complex for a first implementation and not necessary most of the time. For many simulations there is no sideslip, rotation, or gusts. Furthermore, if we neglect the impact of self-induction on the forces/moments we can simplify the calculations greatly. Most scenarios are symmetric, and thus the side force, rolling moment, and yawing moment calculations are unnecessary as they will end up at zero. This impact of induction on lift is almost always negligibly small, and consequently the impact on pitching moments is too. Drag is of course, a different story as it occurs because of the induced velocities, but this is most accurately computed with a far-field method anyway (discussed in following section).

In other words, we assume that the total velocity vector is:

$$\vec{V} = \begin{bmatrix} V_\infty \cos\alpha \\ 0 \\ V_\infty \sin\alpha \end{bmatrix} \tag{4.135}$$

With this assumptions the lift across the wing can be computed as:

$$L = \rho V_\infty \sum_i \Gamma_i (y_{i+1} - y_i) \tag{4.136}$$

where the sum occurs across each panel. This can be derived from the above equations neglecting the induction terms, or directly from the Kutta-Joukowski theorem using a wind coordinate system. To see this, note that the trailing vortices are in the x-direction and so the x-component of velocity will not contribute any force, and the z-component will only create forces in the y direction, which must all cancel out for a symmetric case. The bound vortex can, in general, have all three components. The x component is the same as the trailing vortices and contributes nothing. The z component is the same (just reversed role for x and z). The only nonzero contributor is the y component of circulation. Thus, the lift from an individual panel is:

$$\rho V_\infty \Gamma_y \Delta s \tag{4.137}$$

However, from Fig. 4.40 we see that $\Gamma_y = \Gamma \cos\Lambda$ and the length $\Delta s = dy/\cos\Lambda$ thus the lift from an individual panel can be expressed as:

$$\rho V_\infty \Gamma \Delta y \tag{4.138}$$

This expression is equally valid for nonplanar wings.

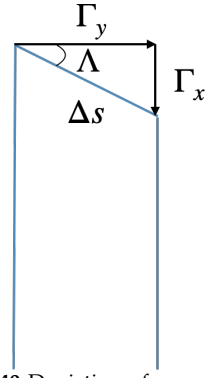

Fig. 4.40 Depiction of a vortex segment on a swept wing.

Similarly, the pitching moment is given by:

$$M = -\rho V_\infty \cos\alpha \sum_i r_{xi}\Gamma_i(y_{i+1} - y_i) \tag{4.139}$$

where r_x is the distance in the body frame from the point where the moment is computed about (usually the c.g.) to the middle of the quarter chord of each panel. Keep in mind that that this is the moment from the lift distribution and does not include any pitching moments generated by the airfoil shape. In other words, one generally needs to add the pitching moments contributed from the airfoils to obtain an accurate total pitching moment of the wing/aircraft.

Notice that the angle of attack appears because the lift is perpendicular to V_∞ (wind frame) but the distance r_x is measured in the body frame (see Fig. 4.41). This simplified approach leaves out one additional term, the contribution to the moment from $r_z F_x$. Effectively this is the contribution of drag to the pitching moment (though not exactly, because F_x and drag occur in different axes), but this term is almost always very small as drag is much smaller than lift and r_z is much smaller than r_x.

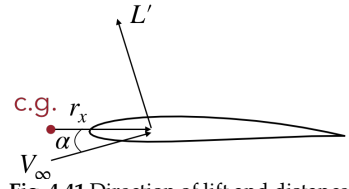

Fig. 4.41 Direction of lift and distance from c.g. to location lift is computed at.

4.5.4 Far-field Induced Drag

The induced drag can also be evaluated in the far-field using a Trefftz plane analysis with a drag-free wake. We leverage the concept discussed in Section 1.12 where forces can be determined from the velocity and pressure field on far away control surfaces. In the case of drag, for an incompressible flow, we only need to know the velocity field on a downstream plane, which is called the Trefftz plane. This procedure generally produces a more accurate estimate of induced drag.

The proper way to evaluate the drag is to evolve the wake downstream (this is called a force-free wake). Unfortunately, wake propagation is computationally intensive. A far-field analysis shows that a drag-free wake, even though the wake shape is nonphysical, produces the same induced drag as the actual force-free wake*. A drag-free wake (i.e., a wake that simply moves straight back in the freestream direction) is *much* simpler to compute. Using our wind coordinate system it means that the wake simply projects straight back in the $+x_w$ direction (which differs from the $+x_b$ direction we have been using, although the difference between these two is generally negligibly small for purposes of projecting the wake). The induced drag calculation then simply

*Not exactly. We do need to neglect a couple of terms, though a careful analysis of a variety of wing shapes shows those terms to be negligibly small, especially for the level of fidelity we are interested in with a VLM.

becomes a two-dimensional analysis computing the influence of the wake on itself.

A farfield analysis shows that the induced drag is (a general result, not specific to VLM):

$$D_i = \int \frac{\rho}{2} V_n \Gamma ds \tag{4.140}$$

where the integral is performed across the wake trace, Γ is the circulation shed at the trailing edge of the aircraft, equivalent to the potential jump across the wake, and V_n is the normlwash (induced velocity normal to the wake). For the VLM case, we have discretized spanwise panels and so the induced drag becomes a summation:

$$D_i = \frac{\rho}{2} \sum_i V_{ni} \Gamma_i \Delta s_i \tag{4.141}$$

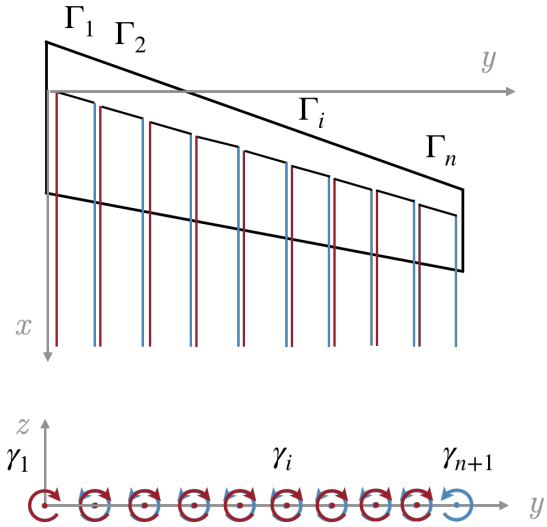

Fig. 4.42 Wake trace from horseshoe vortices in farfield. Only half of wing is shown, but the below assumes we are modeling the full wing.

Each panel sheds two vortices of opposite signs, that overlap with the neighboring vortices as shown in Fig. 4.42. These vortex strengths partially cancel. If Γ_i defines the circulation of each horseshoe vortex, and γ_i is the net circulation of each point vortex in the far-field, then:

$$\gamma_i = \begin{cases} -\Gamma_1 & \text{for } i = 1 \\ \Gamma_{i-1} - \Gamma_i & \text{for } i = 2 \ldots n \\ \Gamma_n & \text{for } i = n+1 \end{cases} \tag{4.142}$$

Figure 4.43 diagrams the analysis we need to perform. A given point vortex j induces a velocity on the center of panel i. The center

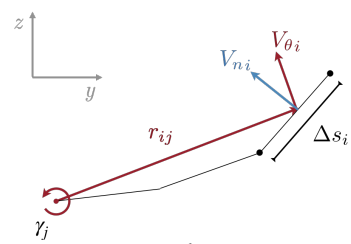

Fig. 4.43 Diagram for computing induced velocities in farfield.

point of panel i is the projection of the control points, or if not given we will assume linear spacing:

$$\bar{y}_i = \frac{1}{2}(y_{i+1} + y_i) \tag{4.143}$$

$$\bar{z}_i = \frac{1}{2}(z_{i+1} + z_i) \tag{4.144}$$

$$\tag{4.145}$$

Each point vortex γ_j induces a tangential velocity given by:

$$\vec{V}_{\theta,ij} = \frac{\vec{\gamma}_j \times \hat{r}_{ij}}{2\pi|r_{ij}|} = \frac{\vec{\gamma}_j \times \vec{r_{ij}}}{2\pi|r_{ij}|^2} \tag{4.146}$$

The induced velocity V_θ is always perpendicular to r_{ij}, but we want the component of velocity that is normal to panel i (the negative sign exists because downwash is positive in the induced drag calculation):

$$V_{nij} = -\vec{V}_{\theta,ij} \cdot \hat{n}_i \tag{4.147}$$

$$\tag{4.148}$$

and

$$V_{ni} = \sum_j V_{nij} \tag{4.149}$$

The induced drag is thus:

$$D_i = \frac{\rho}{2} \sum_i \sum_j \Gamma_i V_{nij} \Delta s_i \tag{4.150}$$

$$= \frac{\rho}{2} \sum_i \sum_j \Gamma_i \left(-\frac{\vec{\gamma}_j \times \vec{r_{ij}}}{2\pi|r_{ij}|^2} \right) \cdot \hat{n}_i \Delta s_i \tag{4.151}$$

The circulation is always aligned with the x-axis because it is a drag-free wake, and thus r is always in the $y-z$ plane. Calculating this explicitly:

$$\vec{\gamma}_j = \gamma_j \hat{x} \tag{4.152}$$

$$\vec{r}_{ij} = (\bar{y}_i - y_j)\hat{y} + (\bar{z}_i - z_j)\hat{z} \tag{4.153}$$

$$\vec{\gamma}_j \times \vec{r_{ij}} = \gamma_j(\bar{y}_i - y_j)\hat{z} - \gamma_j(\bar{z}_i - z_j)\hat{y} \tag{4.154}$$

$$\hat{n}_i = -\sin\phi_i \hat{y} + \cos\phi_i \hat{z} \tag{4.155}$$

$$\hat{n}_i \Delta s_i = -(z_{i+1} - z_i)\hat{y} + (y_{i+1} - y_i)\hat{z} \tag{4.156}$$

$$(\vec{\gamma}_j \times \vec{r_{ij}}) \cdot (\hat{n}_i \Delta s_i) = \gamma_j(\bar{z}_i - z_j)(z_{i+1} - z_i) + \gamma_j(\bar{y}_i - y_j)(y_{i+1} - y_i) \tag{4.157}$$

$$V_{nij}\Delta s_i = \frac{-\gamma_j(\bar{z}_i - z_j)(z_{i+1} - z_i) - \gamma_j(\bar{y}_i - y_j)(y_{i+1} - y_i)}{2\pi[(\bar{y}_i - y_j)^2 + (\bar{z}_i - z_j)^2]} \tag{4.158}$$

The result is that the induced drag is given by:

$$D_i = \frac{\rho}{4\pi} \sum_{i=1}^{n} \sum_{j=1}^{n+1} \Gamma_i \gamma_j k_{ij} \tag{4.159}$$

where

$$k_{ij} = \frac{(y_j - \bar{y}_i)(y_{i+1} - y_i) + (z_j - \bar{z}_i)(z_{i+1} - z_i)}{(y_j - \bar{y}_i)^2 + (z_j - \bar{z}_i)^2} \tag{4.160}$$

The sum over i occurs across each control point, whereas the sum over j occurs over each vortex at the edges of the panels.

Symmetry

If the wing and circulation distribution is symmetric, and we model only half of the wing, then the induced drag only requires a sum on half of the wing (multiplied by 2):

$$D_i = \rho_\infty \sum_{i=1}^{N} V_{n\,i} \Gamma_i \Delta s_i \tag{4.161}$$

If we sum only over half of the wing we have to modify the calculation of Γ_1 since the circulation in the middle of the wing exactly cancels with the other side (see Fig. 4.42).

$$\gamma_i = \begin{cases} 0 & \text{for } i = 1 \\ \Gamma_{i-1} - \Gamma_i & \text{for } i = 2 \ldots n \\ \Gamma_n & \text{for } i = n+1 \end{cases} \tag{4.162}$$

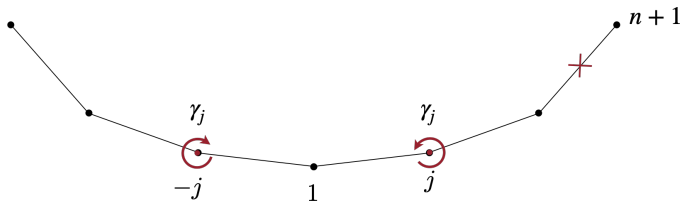

Fig. 4.44 Induced velocity in the farfield for a symmetric configuration.

Also, when calculating the induced velocity at panel i we should add not only the contribution from γ_j on the same side of the wing, but the contribution from γ_j on the opposite side of the wing as depicted in Fig. 4.44. The resulting induced drag is:

$$D_i = \frac{\rho}{2\pi} \sum_{i=1}^{n} \sum_{j=1}^{n+1} \Gamma_i \gamma_j (k_{i,j} - k_{i,-j}) \tag{4.163}$$

where

$$k_{i,\pm j} = \frac{(\pm y_j - \bar{y}_i)(y_{i+1} - y_i) + (z_j - \bar{z}_i)(z_{i+1} - z_i)}{(\pm y_j - \bar{y}_i)^2 + (z_j - \bar{z}_i)^2} \tag{4.164}$$

5 3D Potential Flow

5.1 3D Singularties

This section follows essentially the same procedures as in Section 2.4 so we move through the derivations a bit more rapidly this time. In this section we derive three-dimensional singularities. The 3D Laplace's equation is as follows for Cartesian coordinates:

$$\frac{\partial^2\phi}{\partial x^2} + \frac{\partial^2\phi}{\partial y^2} + \frac{\partial^2\phi}{\partial z^2} = 0, \tag{5.1}$$

and for spherical coordinates:

$$\frac{\partial^2\phi}{\partial r^2} + \frac{2}{r}\frac{\partial\phi}{\partial r} + \frac{1}{r^2\sin\theta}\frac{\partial}{\partial\theta}\left(\sin\theta\frac{\partial\phi}{\partial\theta}\right) + \frac{1}{r^2\sin\theta}\frac{\partial^2\phi}{\partial\psi^2} = 0 \tag{5.2}$$

where ψ is the azimuthal angle and θ is the polar angle (Fig. 5.1).

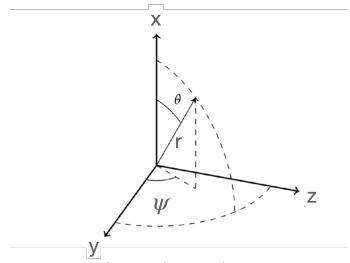

Fig. 5.1 Spherical coordinate system.

5.1.1 Uniform Flow

For uniform flow we can again set each term in Laplace's equation to zero separately leading to the general solution:

$$\phi = k_1 x + k_2 y + k_3 z \tag{5.3}$$

where k_i are any constants. These constants represent the x, y, z components of a freestream velocity:

$$\phi(x, y, z) = u_\infty x + v_\infty y + w_\infty z \tag{5.4}$$

5.1.2 Source

We again assume a purely radial solution: $\phi = R(r)$, which leads to:

$$R'' + \frac{2}{r}R' = 0 \tag{5.5}$$

Rearranging then integrating (where C is an arbitrary constant) gives:

$$\frac{R''}{R'} = -\frac{2}{r} \tag{5.6}$$

$$\ln R' = -2\ln r + \ln C \tag{5.7}$$

$$\ln R' = \ln \frac{C}{r^2} \tag{5.8}$$

$$R' = \frac{C}{r^2} \tag{5.9}$$

$$R = -\frac{C}{r} \tag{5.10}$$

We choose the constant $C = \Lambda/4\pi$ where the normalizing constant is chosen so that the volumetric flow rate is Λ as we will see shortly.

$$\phi(r) = -\frac{\Lambda}{4\pi r} \tag{5.11}$$

The gradient in spherical coordinates is:

$$\vec{\nabla}\phi = \frac{\partial\phi}{\partial r}\hat{r} + \frac{1}{r}\frac{\partial\phi}{\partial\theta}\hat{\theta} + \frac{1}{r\sin\theta}\frac{\partial\phi}{\partial\psi}\hat{\psi} \tag{5.12}$$

So, again the velocity is purely radial:

$$V_r = \frac{\Lambda}{4\pi r^2} \tag{5.13}$$

$$V_\theta = 0 \tag{5.14}$$

$$V_\psi = 0 \tag{5.15}$$

The volumetric flux through a sphere surrounding the source is:

$$\int_A \vec{V}\cdot d\vec{A} = \int_{\theta=0}^{\pi}\int_{\psi=0}^{2\pi} \frac{\Lambda}{4\pi r^2}\hat{r}\cdot(r^2 d\psi \sin\theta d\theta)\hat{r} \tag{5.16}$$

$$= \int_{\theta=0}^{\pi}\int_{\psi=0}^{2\pi} \frac{\Lambda}{4\pi} d\psi \sin\theta d\theta \tag{5.17}$$

$$= \int_0^{\pi} \frac{\Lambda}{2}\sin\theta d\theta \tag{5.18}$$

$$= \Lambda \tag{5.19}$$

as expected.

5.1.3 Vortex

There is no analogue to a point vortex in 3D, althogh we can create a line vortex. If we assume a purely azimuthal solution ($\phi = P(\psi)$)

then we get $P'' = 0$ with the solution $\phi = k\psi$ for any constant k. This is exactly the same solution as the point vortex solution in 2D, except because we are three-dimensions the flow would rotate about the entire x axis of Fig. 5.1.

In other words, a line vortex looks like an extruded point vortex as shown in Fig. 5.2. As a general solution, the line need not be straight. Line vortices will be important in modeling wings (Chapter 4) and so we defer further discussion until then.

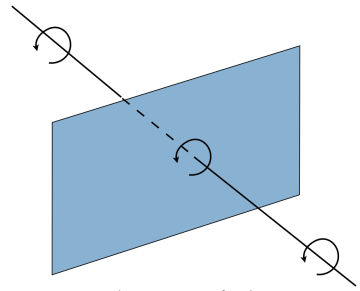

Fig. 5.2 A depiction of a line vortex. In a plane perpendicular to the line vortex the behavior is exactly that of a point vortex.

5.1.4 Doublet

We now consider a solution of the form $\phi = R(r)T(\theta)$ and thus assume azimuthal symmetry.

$$R''T + \frac{2}{r}R'T + \frac{1}{r^2 \sin\theta}\frac{\partial}{\partial\theta}(\sin\theta RT') = 0 \tag{5.20}$$

$$R''T + \frac{2}{r}R'T + \frac{1}{r^2 \sin\theta}(\cos\theta RT' + \sin\theta RT'') = 0 \tag{5.21}$$

$$R''T + \frac{2}{r}R'T + \frac{RT'}{r^2\tan\theta} + \frac{RT''}{r^2} = 0 \tag{5.22}$$

$$r^2\frac{R''}{R} + 2r\frac{R'}{R} + \frac{T'}{T\tan\theta} + \frac{T''}{T} = 0 \tag{5.23}$$

Separating out the radial and polar parts:

$$r^2\frac{R''}{R} + 2r\frac{R'}{R} = m \tag{5.24}$$

$$\frac{T'}{T\tan\theta} + \frac{T''}{T} = -m \tag{5.25}$$

The radial equation is again a Cauchy-Euler equation with known solutions r^k:

$$r^2k(k-1)r^{k-2} + 2rkr^{k-1} - mr^k = 0 \tag{5.26}$$

$$k(k-1) + 2k - m = 0 \tag{5.27}$$

$$k^2 + k - m = 0 \tag{5.28}$$

Recall that m was an arbitrary constant, so to make the solution clearer we choose to define the constant as $m = n(n+1)$ we then have:

$$k(k+1) = n(n+1) \tag{5.29}$$

The solutions are then: $k = n$ and $k = -(n+1)$. Thus:

$$R(r) = Ar^n + \frac{B}{r^{n+1}} \tag{5.30}$$

As we did in the 2D case we set $A = 0$ since the potential must remain bounded as $r \to \infty$.

The polar equation is:

$$T'' + T' \frac{1}{\tan\theta} + n(n+1)T = 0 \tag{5.31}$$

This second order ODE is known as the Legendre equation and its solutions are Legendre polynomials:

$$T(\theta) = P_n(\cos\theta) \tag{5.32}$$

where P_n is the n^{th} Legendre polynomial.

The total solution is then:

$$\phi = \frac{B}{r^{n+1}} P_n(\cos\theta) \tag{5.33}$$

For aerodynamics are only interested in the lowest order solution $n = 1$:

$$\phi = \frac{B}{r^2}\cos\theta \tag{5.34}$$

$$\phi = \frac{B}{r^3} x \tag{5.35}$$

We again normalize the constant by 4π:

$$\phi(r,\theta) = \frac{\mu\cos\theta}{4\pi r^2} = \frac{\mu x}{4\pi r^3} \tag{5.36}$$

This defines a doublet of strength μ oriented in the $-x$ direction. Using the gradient (Eq. 5.12) we compute the velocity components:

$$V_r = -\frac{\mu\cos\theta}{2\pi r^3} \tag{5.37}$$

$$V_\theta = -\frac{\mu\sin\theta}{4\pi r^3} \tag{5.38}$$

$$V_\psi = 0 \tag{5.39}$$

5.2 Green's Identities

In Chapter 2 we suggested that we could obtain potential flow solutions over any flow field by some appropriate combination of sources, vortices, and doublets. We will now prove this mathematically through repeated use of the divergence theorem (Eq. 1.60). If we apply the divergence

theorem to $\nabla\phi$ we get:

$$\int_{\forall} \nabla \cdot \nabla\phi d\forall = \int_S \nabla\phi \cdot \hat{n} dA \tag{5.40}$$

$$\int_{\forall} \nabla^2\phi d\forall = \int_S \frac{\partial\phi}{\partial n} dA. \tag{5.41}$$

If Laplace's equation is satisfied everywhere in the domain, then that means that the normal velocity must be zero on all the boundaries. We motivated this from a no flow through condition, but now see further mathematical justification.

We now apply the divergence theorem to $\psi\nabla\phi$ where ψ and ϕ are both scalar functions:

$$\int_{\forall} \nabla \cdot (\psi\nabla\phi) d\forall = \int_S (\psi\nabla\phi) \cdot \hat{n} dA \tag{5.42}$$

$$\int_{\forall} \nabla\psi \cdot \nabla\phi + \psi\nabla^2\phi d\forall = \int_S (\psi\nabla\phi) \cdot \hat{n} dA \tag{5.43}$$

We repeat the same procedure but with the function $\phi\nabla\psi$:

$$\int_{\forall} \nabla \cdot (\phi\nabla\psi) d\forall = \int_S (\phi\nabla\psi) \cdot \hat{n} dA \tag{5.44}$$

$$\int_{\forall} \nabla\phi \cdot \nabla\psi + \phi\nabla^2\psi d\forall = \int_S (\phi\nabla\psi) \cdot \hat{n} dA \tag{5.45}$$

We now subtract these two equations:*

$$\int_{\forall} (\psi\nabla^2\phi - \phi\nabla^2\psi) d\forall = \int_S (\psi\nabla\phi - \phi\nabla\psi) \cdot \hat{n} dA \tag{5.46}$$

*Equation 5.43 is known as Green's first identity, and Eq. 5.46 is Green's second identity.

Let's now set ψ as the most basic solution to Laplace's equation, namely a source (Eq. 5.11), and we assume that ϕ is another solution to Laplace's equation, though its form is yet unknown. We'll set the source at unit strength, and allow the source to be centered at an arbitrary location $\vec{r}_0$:

$$\psi = -\frac{1}{4\pi} \frac{1}{|\vec{r} - \vec{r}_0|} \tag{5.47}$$

Plugging that into the above equation gives (noting that $\nabla^2\phi = 0$ everywhere in the domain):

$$\int_{\forall} \phi\nabla^2 \left(\frac{1}{4\pi} \frac{1}{|\vec{r} - \vec{r}_0|} \right) d\forall = \frac{1}{4\pi} \int_S \left[-\left(\frac{1}{|\vec{r} - \vec{r}_0|} \right) \nabla\phi + \phi\nabla \left(\frac{1}{|\vec{r} - \vec{r}_0|} \right) \right] \cdot \hat{n} dA \tag{5.48}$$

For the left-side integral, the Laplacian operator on the source term is zero everywhere except at $\vec{r} = \vec{r}_0$, and so ϕ evaluated at $\vec{r}_0$ is the only

portion of ϕ that remains and it comes out of the integral. We also know that the magnitude of that integral is 1 (see Eq. 5.19), and so we are left with:[†]

[†]This equation is Green's third identity.

$$\phi(\vec{r}_0) = \frac{1}{4\pi} \int_S \left(\phi \frac{\partial}{\partial n} \left(\frac{1}{|\vec{r} - \vec{r}_0|} \right) - \frac{1}{|\vec{r} - \vec{r}_0|} \frac{\partial \phi}{\partial n} \right) dA \tag{5.49}$$

Let's first examine the second term. We interpreted $-1/(4\pi|\vec{r} - \vec{r}_)|)$ as a unit source at $\vec{r}_0$ that we evaluate at some location $\vec{r}$. But the two terms in the absolute value can be swapped with no change in the result, given the equivalent interpretation of a unit source located at r (on the boundary) evaluated at some location $\vec{r}_0$ in the domain. Thus, we can see that this last term can be interpreted as the contribution from a distribution of sources on the boundary with strength per unit area of $\partial\phi/\partial n$.

For the second term we recall that $d/dx(1/r) = -x/r^3$. So examining Eq. 5.36 as a doublet oriented in the $-x$ direction, and using the same swap of $\vec{r}$ and $\vec{r}_0$, we can see that this term can be interpreted as the contribution from a distribution of doublets on the boundary, oriented in the normal direction, with a strength per unit area of ϕ. Thus, for any potential flow we can represent the solution at all entire points $\vec{r}_0$ by summing up the contribution of source and normally-oriented doublet distributions on the boundary whose strengths per unit area are $\partial\phi/\partial n$ and ϕ respectively.

5.3 3D Distributions

5.4 3D Panel Code

Compressible Flow

6

Potential flow has been a useful assumption allowing us to solve for aerodynamic flowfields around low-speed objects. The inclusion of a boundary layer model addressed a major limitation of the viscous (non-irrotational) behavior near the body. In this section we discuss fundamentals of compressible flow. We then relax the incompressibility assumption to extend potential flow to some compressible flow regimes. We will see that we can extend the methodologies we have been using to compressible flow fields if we can add a restriction on small disturbances (thin bodies, small angles of attack). Finally, we discuss shock wave and expansion theory, which are exact solutions as an alternative to the simplifications introduced for compressible potential flow.

6.1 Compressible Flow Fundamentals

We begin with a review of thermodyamics and some key concepts related to compressible flow.

6.1.1 Mach Cone

As an initial motivation to compressibility, consider a one-dimensional disturbance in a pipe. Imagine a small transmitter that makes a periodic beeping noise. In the top of Fig. 6.1 we see sound waves moving, at the speed of sound (a), in both directions. Now imagine a freestream flow in the pipe, moving left to right, at a speed less than the speed of sound. This scenario is depicted in the middle pane of Fig. 6.1. The sound waves moving to the left of the transmitter now move at the reduced speed $a - V$, relative to an inertial frame, whereas the sound waves on the right move faster at the speed $V + a$. From the figure we see that the frequency is also changed with the background moving air so that the waves are compressed to the left, and expanded to the right. If we now increase the freestream speed so that V is greater than the speed of sound, we have the scenario on the bottom of Fig. 6.1. The sound waves emitted to the right move even faster at the speed $V + a$. However, the sound waves that were emitted to the left, are

completely overwhelmed by the high speed flow, and actually move to the right at the speed $V - a$. Thus, no sound waves are transmitted upstream. In other words, if you were standing in the pipe upstream of the transmitter, you could walk all the way up to it and not hear it at all. *In supersonic flow disturbances cannot flow upstream.*

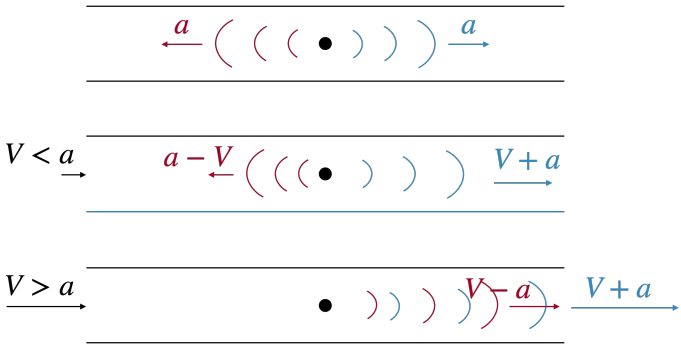

Fig. 6.1 A one-dimensional flow example with a sound wave emitter and varying freestream speeds in a pipe.

Let's now consider a similar scenario in three dimensions. In the stationary case, not drawn, spherical sound waves radiate out in all directions. Now imagine that the transmitter is moving at a subsonic speed ($M < 1$), or equivalently is stationary in a subsonic freestream. This is depicted on the left of Fig. 6.2. The scenario is similar to that

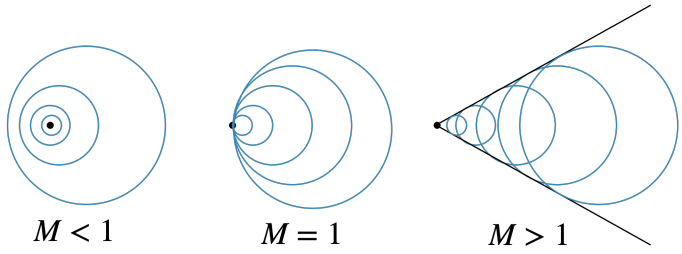

Fig. 6.2 A three-dimensional flow example with a sound wave emitter and varying freestream speeds.

of the one-dimensional case with subsonic inflow. The sound waves are compressed in the front, and expand in the back. As we increase in speed, we reach the limiting case ($M = 1$), where no sound waves are omitted forward, instead they pile up in a vertical front. The case on the right shows the scenario where the transmitter moves faster than the speed of sound ($M > 1$). In this case, all the sound waves travel to the right, like that they do in the 1D case, except that they form a *Mach cone*.

Another way to think about this shape, is that as each spherical sound wave is emitted, the transmitter flys faster than that wave, thus moving outside of it, before emitting the next wave. Instead of piling

up vertically, the sound waves pile up along the Mach cone. As the Mach number increases the Mach cone tilts flatter. Isolating one sound wave in Fig. 6.3 we can see that the angle if related by:

$$\sin \mu = \frac{a}{V} = \frac{1}{M} \tag{6.1}$$

Therefore the *Mach angle* is given by:

$$\mu = \sin^{-1}\left(\frac{1}{M}\right) \tag{6.2}$$

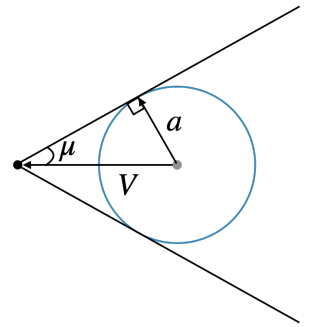

Fig. 6.3 Mach cone and one sound wave depicted.

Like the 1D case, the implication is that outside of the Mach cone you could not hear the transmitter. Notice that if you are above (or below) the transmitter, there are regions you could be where the transmitter would fly past you but you still would not have heard it yet.

For an aircraft the scenario is similar, except that the pressure waves are continuous, and they are not infinitesimally weak disturbances (which is what sound waves are). Instead, we get shock waves, which will be discussed later in this chapter. But for now we note that a Mach cone is an infinitesimally weak shock wave and represents the limiting case.

6.1.2 Ideal Gas

In fluids we are primarily interested in *intensive* properties. Intensive properties are not dependent on the size of the system, and instead are properties defined at a point. Some intensive variables, like pressure, temperature, and density, that we are already familiar with, do not have an extensive counterpart (extensive variables depend on the size of the system). Other intensive variables that do have an extensive counterpart are often referred to as *specific* quantities, and are defined per unit mass. For example, *specific volume*, v, is the volume per unit mass, or the inverse of density:

$$v = \frac{1}{\rho} \tag{6.3}$$

Specific internal energy, e, is the internal energy per unit mass, and specific entropy, s, is the entropy per unit mass. Specific enthalpy, h, is the enthalpy per unit mass and is defined as:

$$h = e + pv \tag{6.4}$$

Conceptually, you could think of enthalpy as a combination of internal energy plus work, where the work is that required to reach the given

pressure and volume. Note that even though we have used the term "work", enthalpy, like all of these other parameters, is a *state variable*, meaning that it is path independent and only depends on the current state. The variables pressure, temperature, and density that we are already familiar with are also state variables.

Thermodynamic state variables are related through an *equation of state*. Any two intensive thermodynamic quantities completely define the state. In other words, a third variable would not be independent but rather would depend on the first two. We can write any intensive property as a function of any two other intensive properties. For example:

$$e = e(s, T) \tag{6.5}$$

$$T = T(s, v) \tag{6.6}$$

$$p = p(h, T) \tag{6.7}$$

The most common equation of state is the *ideal gas law*:

$$p = p(\rho, T) = \rho R T \tag{6.8}$$

where R is the *specific gas constant*. For air, that is not chemically reacting, its value is:

$$R = 286.9 \frac{\mathrm{J}}{\mathrm{kg} \cdot \mathrm{K}} \tag{6.9}$$

An ideal gas assumes that the intermolecular forces between the gas molecules are negligible. In contrast, a *real gas* accounts for intermolecular forces. Intermolecular forces become significant if the air is at a very high pressure and a low temperature, a scenario which rarely applies in the field of aerodynamics. Sometimes vibration, dissociation, and ionization that occurs at the high temperatures of reentry vehicles are called real-gas effects, but this is a misnomer. These behaviors are not caused by intermolecular forces, but rather by chemical reactions and other high temperature effects that we shall discuss shortly.

The most general case of ideal gases occurs with chemically reacting mixtures of ideal gases. In this case chemical reactions occur, but intermolecular forces are still negligible. Air becomes a chemically reacting mixture of ideal gases above approximately 2500 K.

If there are no chemical reactions, then for an ideal gas the internal energy only depends on temperature. The proof is a bit lengthy, but traverses some concepts we need anyway.

We start with the first law of thermodynamics, which can be expressed as:

$$de = \delta q + \delta w \tag{6.10}$$

This equation states that the change in the internal energy of an isolated system is equal to the energy applied as heat (q) and as work on the surroundings (w). We use the differential de because internal energy is a state variable, whereas the changes in work and heat and noted by δ since they are, in general, path dependent. For a *reversible* process (e.g., inviscid), the work done by a fluid on a system is:

$$\delta w = -pdv \tag{6.11}$$

The second law of thermodynamics can be expressed as:

$$ds \geq \frac{\delta q}{T} \tag{6.12}$$

where s is the entropy, and T is the temperature. In an idealized process, where the heat transfer is reversible, then the expression is an equality and we place these last two equations in the first law of thermodynamics to obtain:

$$de = Tds - pdv \tag{6.13}$$

or

$$Tds = de + pdv \tag{6.14}$$

which is known as *Gibbs equation*. This is an expression of the first and second law of thermodynamics for a reversible process, or as a way to relate thermodynamic variables at a given state. We can also write this equation in terms of enthalpy by taking derivatives of its definition (Eq. 6.4) and substituting in the Gibbs equation:

$$Tds = dh - vdp \tag{6.15}$$

Or we can express in terms of the *Gibbs free energy*: $g = h - Ts$. Substituting this into Gibbs equation gives:

$$dg = vdp - sdT \tag{6.16}$$

To prove that internal energy for an ideal gas depends only on temperature, let us first assume the general case, where internal energy depends on two variables: $e = e(P, T)$. The total differential is given by:

$$de = \left(\frac{\partial e}{\partial p}\right)_T dp + \left(\frac{\partial e}{\partial T}\right)_p dT \tag{6.17}$$

We want to derive the conditions where the dependence on pressure drops out, and the internal energy thus only depends on temperature. In other words, to show under what conditions:

$$\left(\frac{\partial e}{\partial p}\right)_T = 0 \tag{6.18}$$

We can rewrite the Gibbs equation (Eq. 6.14) in terms of these derivatives:

$$\left(\frac{\partial e}{\partial p}\right)_T = T\left(\frac{\partial s}{\partial p}\right)_T - p\left(\frac{\partial v}{\partial p}\right)_T \tag{6.19}$$

If we compare one of the forms of Gibbs equation (Eq. 6.16) with a differential for $g(p, T)$:

$$dg = \left(\frac{\partial g}{\partial p}\right)_T dp + \left(\frac{\partial g}{\partial T}\right)_p dT \tag{6.20}$$

we see that:

$$v = \left(\frac{\partial g}{\partial p}\right)_T \tag{6.21}$$

and

$$s = -\left(\frac{\partial g}{\partial T}\right)_p \tag{6.22}$$

The second partial derivatives shown below must also be equal:

$$\frac{\partial^2 g}{\partial p \partial T} = \frac{\partial^2 g}{\partial T \partial p} \tag{6.23}$$

Applying that in this case gives:

$$\left(\frac{\partial v}{\partial T}\right)_p = -\left(\frac{\partial s}{\partial p}\right)_T \tag{6.24}$$

This is one of the *Maxwell relations*. We can derive other such identities in a similar way using different forms of the Gibbs equation, comparing the differentials, and equating second derivatives. For our present purposes this is the only identity we need. We substitute this into Eq. 6.19 to obtain:

$$\left(\frac{\partial e}{\partial p}\right)_T = -T\left(\frac{\partial v}{\partial T}\right)_p - p\left(\frac{\partial v}{\partial p}\right)_T \tag{6.25}$$

We now have a relationship between internal energy and the specific volume. The right side vanishes for a constant density fluid. But it also vanishes for an ideal gas ($v = \frac{RT}{p}$):

$$\left(\frac{\partial e}{\partial p}\right)_T = -T\frac{R}{p} + p\frac{R}{Tp^2} = 0 \tag{6.26}$$

Actually, it vanishes any fluid where $v = f(T/p)$. Thus, the left side of Eq. 6.17 vanishes and so $e = e(T)$ only. From the definition of enthalpy,

we can show that for an ideal gas the enthalpy also only depends on temperature.

$$h = e + pv \tag{6.27}$$
$$= e + RT \tag{6.28}$$
$$= e(T) + RT \tag{6.29}$$
$$\Rightarrow h = h(T) \tag{6.30}$$

We call this a *thermally perfect gas*.

6.1.3 Heat Capacity

A thermally perfect gas has implications on its heat capacity. The specific heat capacity is heat capacity per unit mass, where heat capacity refers to the amount of heat required to produce a unit change in temperature. For a gas, heat capacity differs significantly if the heating occurs in a fixed container (constant volume), or in the atmosphere where it can expand (constant pressure). These two quantities are called the specific heat capacity at constant volume and constant pressure respectively. Mathematically they are defined as:

$$c_v \equiv \left(\frac{\partial e}{\partial T}\right)_v \tag{6.31}$$
$$c_p \equiv \left(\frac{\partial h}{\partial T}\right)_p \tag{6.32}$$

For a thermally perfect gas, both e and h are functions only of temperature and so these become simple differentials.

$$c_v \equiv \left(\frac{de}{dT}\right)_v \tag{6.33}$$
$$c_p \equiv \left(\frac{dh}{dT}\right)_p \tag{6.34}$$

For a *calorically perfect gas*, the specific heats are also independent of temperature, and are thus considered constants.

$$e = c_v T \tag{6.35}$$
$$h = c_p T \tag{6.36}$$

For both of these latter two cases, the specific heats are related to the specific gas constant as follows. From the definitions of the specific heat capacities:

$$c_p - c_v = \frac{d}{dT}(h - e) \tag{6.37}$$

We then use the definition of enthalpy (Eq. 6.4):

$$c_p - c_v = \frac{d}{dT}(pv) \tag{6.38}$$

Now, the ideal gas law (Eq. 6.8):

$$c_p - c_v = \frac{d}{dT}(RT) = R \tag{6.39}$$

Thus,

$$c_p - c_v = R \tag{6.40}$$

Another key parameter is the ratio of specific heats:

$$\gamma = \frac{c_p}{c_v} \tag{6.41}$$

Using this equation and Eq. 6.40 we can show that:

$$c_p = \frac{\gamma}{\gamma - 1} R \tag{6.42}$$

$$c_v = \frac{1}{\gamma - 1} R \tag{6.43}$$

Thus, any two of these constants defines the gas.

To better understand the different conditions separating calorically perfect, thermally perfect, a chemically reacting mixture of ideal gases, and real gases, we consider the nature of the diatomic molecules that make up air (Fig. 6.4). In classical statistical mechanics the internal energy of a molecule is given by:

$$e = \frac{1}{2} nRT \tag{6.44}$$

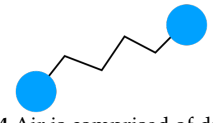

Fig. 6.4 Air is comprised of diatomic molecules.

where n is the number of degrees of freedom. Or in terms of the specific heat capacity at constant volume:

$$c_v = \frac{\partial e}{\partial T} = \frac{1}{2} nR \tag{6.45}$$

For most aerodynamic scenarios the temperature is such that the translational and rotational degrees of freedom are active. There are three translational modes, and while there are also three rotational modes, in practice only two are realized. That is because of the nature of a diatomic molecule where the moment of inertia about the internuclear axis (line joining the two atoms), is negligibly small compared to the

moments of inertia about the other two axes (not only because of the shape but also because almost all the mass of an atom is concentrated at its center). Thus, it would take an inordinately high temperature to reach this last rotational energy state. Thus, for most aerodynamic scenarios these five modes are activated, and the specific heats can be considered constant (i.e., calorically perfect):

$$c_v = \frac{5}{2}R \tag{6.46}$$

$$c_p = \frac{7}{2}R \tag{6.47}$$

$$\gamma = \frac{7}{5} = 1.4 \tag{6.48}$$

For everything in this book we will assume a calorically perfect gas.

If temperature increases beyond approximately 700 K (e.g., at higher Mach numbers), then the vibration mode is activated, which is an exchange of potential and kinetic energy along the internuclear axis. In this case, the specific heats can no longer be considered constant, but rather are a function of temperature (i.e., thermally perfect).

If temperature increases even further, beyond approximately 2500K for air, then chemical reactions begin (i.e., a chemically reacting mixture of ideal gases). Now the specific heats are a function of temperature and pressure.

To reach the "real" gas state (i.e., not an ideal gas), we would need to go the other way and decrease temperature, while simultaneously increasing pressure tremendously (say above 1,000 atm).

6.1.4 Isentropic Relations

An isentropoic flow is both adiabatic (no heat or mass transfer) and is reversible. In this case:

$$\frac{Ds}{Dt} = 0\,, \tag{6.49}$$

which means that the total derivative of the entropy is zero. In other words, the entropy is constant for a given fluid particle. If steady, then the entropy is constant along a streamline, and any many aerodynamic flows the freestream is uniform and so the entropy is then constant everywhere.

We use Gibbs equation (Eq. 6.14), rewritten as follows:

$$ds = \frac{de}{T} + \frac{p}{T}dv \tag{6.50}$$

Using the definition of the heat capacity at constant volume for a calorically perfect gas (Eq. 6.35) for the de term, and the ideal gas equation of state for the second term (Eq. 6.8) yields:

$$ds = c_v \frac{dT}{T} + R\frac{dv}{v} \tag{6.51}$$

If calorically perfect then c_v is constant with temperature and we can integrate both sides:

$$s_2 - s_1 = c_v \ln\left(\frac{T_2}{T_1}\right) + R\ln\left(\frac{v_2}{v_1}\right) \tag{6.52}$$

For an isentropic process $s_2 - s_1 = 0$ and thus we have:

$$\frac{c_v}{R}\ln\left(\frac{T_2}{T_1}\right) = -\ln\left(\frac{v_2}{v_1}\right) \tag{6.53}$$

Using the properties of a logarithm, we can rewrite both terms as:

$$\begin{aligned} \ln\left(\frac{T_2}{T_1}\right)^{\frac{c_v}{R}} &= \ln\left(\frac{v_1}{v_2}\right) \\ &= \ln\left(\frac{\rho_2}{\rho_1}\right) \end{aligned} \tag{6.54}$$

Using Eq. 6.43 and taking the exponential of both sides gives:

$$\left(\frac{T_2}{T_1}\right)^{\frac{1}{\gamma-1}} = \left(\frac{\rho_2}{\rho_1}\right) \tag{6.55}$$

Similarly, we can use Gibbs equation in terms of the enthalpy (Eq. 6.15):

$$ds = \frac{dh}{T} - v\frac{dp}{T} \tag{6.56}$$

Use the definition of the coefficient of specific heat at constant pressure, for a thermally perfect gas (Eq. 6.36), and the ideal gas law (Eq. 6.8):

$$ds = c_p \frac{dT}{T} - R\frac{dp}{p} \tag{6.57}$$

We integrate both sides and use the isentropic assumption:

$$0 = c_p \ln\left(\frac{T_2}{T_1}\right) - R\ln\left(\frac{p_2}{p_1}\right) \tag{6.58}$$

Use the logarithm properties and Eq. 6.42 gives:

$$\ln\left(\frac{T_2}{T_1}\right)^{\frac{\gamma}{\gamma-1}} = \ln\left(\frac{p_2}{p_1}\right) \tag{6.59}$$

Taking the exponential of both sides results in:

$$\left(\frac{T_2}{T_1}\right)^{\frac{\gamma}{\gamma-1}} = \left(\frac{p_2}{p_1}\right) \tag{6.60}$$

Comparing this equation with Eq. 6.55 we have the *isentropic relations* for a calorically perfect gas:

$$\frac{p_2}{p_1} = \left(\frac{\rho_2}{\rho_1}\right)^{\gamma} = \left(\frac{T_2}{T_1}\right)^{\frac{\gamma}{\gamma-1}} \tag{6.61}$$

6.1.5 Energy Equation

For incompressible flows we only needed a mass and momentum equation. Those balance laws provide 4 equations for the 4 independent variables (pressure and the three components of velocity). For compressible flows we have added another variable, ρ, and so need another equation. The internal energy and temperature are not new variables but rather are state variables defined through an equation of state (Section 6.1.2) and heat capacity equations (Section 6.1.3).

Following the same pattern as shown previously in Eq. 1.82 we can form an energy balance equation:

$$\frac{\partial}{\partial t}\int_{\forall} \rho e d\forall + \int_S \rho e(\vec{V}\cdot d\vec{A}) = \dot{W}_{in} + \dot{Q}_{in} \tag{6.62}$$

where $e = e + \frac{V^2}{2}$ is the total specific energy (specific internal energy plus specific kinetic energy), and the last two terms are the net work and heat into the system. This is a form of the first law of thermodynamics (Eq. 6.10).

Work on the fluid comes from pressure and shear stresses acting on the exterior control surface. As it is not used in this chapter will not expand on the viscous component of the work term:

$$\dot{W} = -\int_S p(\vec{V}\cdot d\vec{A}) + W_{\text{viscous}} \tag{6.63}$$

There may be other sources of work internal to the control volume, for example from a shaft, which would need to be explicitly added just like internal forces.

For heat there is a volumetric heating term and a viscous term. Again, we will not expand on the viscous term in this introduction:

$$\dot{Q} = \int_{\forall} \rho \dot{q} d\forall + Q_{\text{viscous}} \tag{6.64}$$

where $\dot{q}$ is the rate of heat addition per unit mass.

If we plug this into the above energy equation it becomes:

$$\frac{\partial}{\partial t}\int_{\forall}\rho\epsilon d\forall + \int_{S}\rho h_T(\vec{V}\cdot d\vec{A}) = \int_{\forall}\rho\dot{q}d\forall + W_{\text{viscous}} + Q_{\text{viscous}} \tag{6.65}$$

where $h_T = h + \frac{V^2}{2}$ is the total enthalpy.

Commuting differentiation and integration, and using the divergence theorem results in:

$$\int_{\forall}\frac{\partial\rho\epsilon}{\partial t}d\forall + \int_{\forall}\nabla\cdot(\rho h_T\vec{V})d\forall = \int_{\forall}\rho\dot{q}d\forall + \text{ viscous terms} \tag{6.66}$$

We now put everything into one integral, and as before because this equation must apply to any control volume in the fluid the integrand must be zero everywhere. This gives the differential form, where we have used an inviscid assumption:

$$\frac{\partial\rho\epsilon}{\partial t} + \nabla\cdot(\rho h_T\vec{V}) = \rho\dot{q} \tag{6.67}$$

Extra work terms, like shaft work can still be explicit added to this equation.

The first term we can express in terms of total enthalpy:

$$\begin{aligned}\rho\epsilon &= \rho e + \rho\frac{V^2}{2}\\ &= \rho e + \rho\frac{V^2}{2} + \rho\frac{p}{\rho} - p\\ &= \rho e + \rho\frac{V^2}{2} + \rho p\nu - p\\ &= \rho h + \rho\frac{V^2}{2} - p\\ &= \rho h_T - p\end{aligned} \tag{6.68}$$

Substituting into the energy equation gives:

$$\frac{\partial\rho h_T}{\partial t} + \nabla\cdot(\rho h_T\vec{V}) = \frac{\partial p}{\partial t} + \rho\dot{q} \tag{6.69}$$

To make this equation more useful we expand the derivatives:

$$h_T\frac{\partial\rho}{\partial t} + \rho\frac{\partial h_T}{\partial t} + h_T\nabla\cdot(\rho\vec{V}) + \nabla h_T\cdot\rho\vec{V} = \frac{\partial p}{\partial t} + \rho\dot{q} \tag{6.70}$$

The first and third terms go to zero from the continuity equation (Eq. 1.88).

$$\rho \frac{\partial h_T}{\partial t} + \nabla h_T \cdot \rho \vec{V} = \frac{\partial p}{\partial t} + \rho \dot{q} \tag{6.71}$$

If steady and adiabatic, good assumptions for much of aerodynamics, the equations simplifies considerably to:

$$\nabla h_T \cdot \rho \vec{V} \tag{6.72}$$

In words, this equation means that total enthalpy is constant along a streamline. This result is a much simpler form of the energy equation:

$$h_{T1} = h_{T2} \tag{6.73}$$

or

$$h_1 + \frac{V_1^2}{2} = h_2 + \frac{V_2^2}{2} \tag{6.74}$$

This is a form of Bernoulli's equation, but for a compressible flow. It comes with all of the same limitations (except incompressibility): steady, along a streamline, no work or heat transfer, inviscid. The freestream for many compressible flow scenarios comes from a reservoir of constant total enthalpy, and in those cases the total enthalpy is constant everywhere. The simplicity of this equation makes it highly useful for many compressible flows.

Because we have assumed adiabatic and invscid, the flow is isentropic. Using Eq. 6.56 for constant entropy we see that:

$$dh = v dp \tag{6.75}$$

If we now invoke an incompressibility assumption we can integrate both sides to get:

$$h_2 - h_1 = \frac{1}{\rho}(p_2 - p_1) \tag{6.76}$$

Substituting this into Eq. 6.74, and multiplying through by ρ gives the classic Bernoulli equation:

$$p_1 + \frac{1}{2}\rho V_1^2 = p_2 + \frac{1}{2}\rho V_2^2 \tag{6.77}$$

or

$$p_{T1} = p_{T2} \tag{6.78}$$

where p_T is the total pressure. Note that this makes use of the incompressible definition of total pressure, a definition that is not applicable for a compressible flow. We will learn what total pressure looks like for a compressible flow later in this chapter.

6.1.6 Speed of Sound

A sound wave is an infinitesimally weak pressure wave. That means that the flow properties may change, isentropically, by some differential amount across a sound wave as pictured in Fig. 6.5 We will denote a as the speed of sound, or in other words the speed that a sound wave moves in the fluid.

We now consider a small control volume whose sides are parallel to the sound wave. Thus, the fluid enters one side of the control volume, and exits on the other side of the sound wave. Applying a mass balance across the sound wave yields:

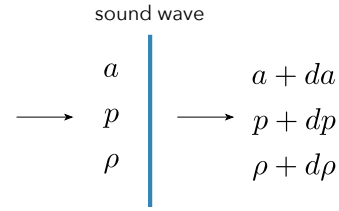

Fig. 6.5 A sound wave, or infinitely weak disturbance, across which the fluid properties change by some differential amount.

$$\rho a A = (\rho + d\rho)(a + da)A \tag{6.79}$$

where A is some arbitrary cross-sectional size based on the control volume size. Cancelling out the area term, expanding the products on the right hand side, and removing the product of differential terms that goes to zero in the limit, gives:

$$\rho a = \rho a + a d\rho + \rho da \tag{6.80}$$

$$\Rightarrow da = -\frac{a}{\rho} d\rho \tag{6.81}$$

Next, we apply a momentum balance across the sound wave. Because a sound wave is an isentropic disturbance there are no viscous terms.

$$pA + \rho a^2 A = (p + dp)A + (\rho + d\rho)(a + da)^2 A \tag{6.82}$$

$$0 = dp + 2\rho a da + a^2 d\rho \tag{6.83}$$

We substitute in the results from Eq. 6.81

$$0 = dp - 2a^2 d\rho + a^2 d\rho \tag{6.84}$$

$$\Rightarrow dp = a^2 d\rho \tag{6.85}$$

The result is:

$$a = \sqrt{\left(\frac{\partial p}{\partial \rho}\right)_s} \tag{6.86}$$

The subscript s denotes that this is the partial derivative at constant entropy (i.e., an isentropic process). From Eq. 6.61 we see that for a calorically perfect isentropic process we can write:

$$\frac{p}{\rho^\gamma} = \text{constant} \tag{6.87}$$

Taking derivatives and substituting into the speed of sound gives:

$$a = \sqrt{\frac{\gamma p}{\rho}} \tag{6.88}$$

For an ideal gas, which is applicable since we already made a more restrictive calorically perfect assumption, we have the following expression for the speed of sound:

$$a = \sqrt{\gamma RT} \tag{6.89}$$

Thus, we see that for a calorically perfect gas, the speed of sound is only a function of temperature.

We can reexpress dynamic pressure:

$$\begin{aligned} q &= \frac{1}{2}\rho V^2 \\ &= \frac{1}{2}\rho M^2 a^2 \\ &= \frac{1}{2}\rho M^2 \frac{\gamma p}{\rho} \\ &= \frac{\gamma}{2} p M^2 \end{aligned} \tag{6.90}$$

This latter form is typically a more convenient representation of dynamic pressure for compressible flows:

$$q = \frac{\gamma}{2} p M^2 \tag{6.91}$$

6.1.7 Total (Stagnation) Quantities

Stagnation pressure, or *total pressure*, is the equivalent pressure we would obtain if we took a point in the fluid and isentropically slowed it to stagnation. Note that total pressure is a property of the fluid at every point. It is well defined at every point in the fluid whether or not the point in question is at a stagnation point or whether or not the flow is isentropic.

Using a form of the energy equation appropriate for an isentropic process

$$h_1 + \frac{V_1}{2} = h_2 + \frac{V_2}{2} \tag{6.92}$$

For a calorically perfect gas we can substitute in Eq. 6.36:

$$c_p T_1 + \frac{V_1}{2} = c_p T_2 + \frac{V_2}{2} \tag{6.93}$$

Now let's consider condition 1 our hypothetical stagnation condition, and condition 2 the flow conditions at an arbitrary point in the fluid:

$$c_p T_T = c_p T + \frac{V}{2} \tag{6.94}$$

where T_T is called the *total temperature*. Rearranging and using the relationship between c_p and the other gas constants Eq. 6.42 as well as the equation for the speed of sound (Eq. 6.89):

$$\frac{T_T}{T} = 1 + \frac{(\gamma - 1)}{2} M^2 \tag{6.95}$$

Using the isentropic relations (Eq. 6.61) then gives us expressions for *total pressure* and *total density*:

$$\frac{p_T}{p} = \left(1 + \frac{\gamma - 1}{2} M^2\right)^{\gamma/(\gamma-1)} \tag{6.96}$$

$$\frac{\rho_T}{\rho} = \left(1 + \frac{\gamma - 1}{2} M^2\right)^{1/(\gamma-1)} \tag{6.97}$$

Note that the compressible definition for total pressure (Eq. 6.96) is very different then the incompressible counterpart ($p_T = p + \frac{1}{2}\rho V^2$)

6.1.8 Viscosity

Classical thermodynamics does not provide an expression for viscosity in terms of other thermodynamic variables. Instead we rely on kinetic theory and experiments. For a gas, a commonly-used model is called *Sutherland's Law*:

$$\mu(T) = \mu_{ref} \left(\frac{T}{T_{ref}}\right)^{3/2} \frac{T_{ref} + S}{T + S} \tag{6.98}$$

where

$$\mu_{ref} = 1.716 \times 10^{-5} \text{ kg/(m·s)} \tag{6.99}$$

$$T_{ref} = 273.15 \text{ K} \tag{6.100}$$

$$S = 110.4 \text{ K} \tag{6.101}$$

Note that the viscosity is only a function of temperature.

6.2 Full Potential Equation

We continue with the same assumption of irrotational flow:

$$\nabla \times \vec{V} = 0 \tag{6.102}$$

but now allow the fluid to be compressible. Irrotational flow can still be a useful approximation for some compressible flows. Shock waves are an irreversible process and so are not irrotational, but potential flow theory can permit infinitely weak shocks (isentropic Mach waves).

If compressible, the continuity equation becomes:

$$\nabla \cdot (\rho \vec{V}) = 0 \tag{6.103}$$

and the momentum equation, if invsicid as is necessary for irrotational flow, is:

$$\rho \vec{V} \cdot \nabla \vec{V} = -\nabla p \tag{6.104}$$

Using a vector identity we can expand the left-hand side as follows, and cross out the second term because of the irrotationality assumption.

$$\rho \left(\frac{1}{2} \nabla (\vec{V} \cdot \vec{V}) - \vec{V} \times \cancel{(\nabla \times \vec{V})} \right) = -\nabla p \tag{6.105}$$

Because we have assumed irrotational flow, there is no viscosity and no heat transfer, and the energy equation reduces to the isentropic relation (Eq. 6.61):

$$\frac{p}{\rho^\gamma} = k \tag{6.106}$$

where k is a constant. We take derivatives of the isentropic relationship and insert in the definition of the speed of sound (Eq. 6.88):

$$\nabla p = k\gamma \rho^{\gamma-1} \nabla \rho \tag{6.107}$$

$$= \gamma \frac{p}{\rho} \nabla \rho \tag{6.108}$$

$$= a^2 \nabla \rho \tag{6.109}$$

We substitute this result into the momentum equation:

$$\rho \frac{1}{2} \nabla (\vec{V} \cdot \vec{V}) = -a^2 \nabla \rho \,, \tag{6.110}$$

and divide by ρ on both sides:

$$\frac{1}{2} \nabla (\vec{V} \cdot \vec{V}) = -a^2 \frac{\nabla \rho}{\rho} \,. \tag{6.111}$$

Next, we take the dot product with velocity on both sides of the equation.

$$\vec{V} \cdot \left(\frac{1}{2} \nabla (\vec{V} \cdot \vec{V}) \right) = -a^2 \vec{V} \cdot \frac{\nabla \rho}{\rho} \tag{6.112}$$

If we expand the continuity equation via the chain rule:

$$\begin{aligned} \nabla \rho \cdot \vec{V} + \rho (\nabla \cdot \vec{V}) &= 0 \\ \vec{V} \cdot \nabla \rho &= -\rho (\nabla \cdot \vec{V}) \end{aligned} \tag{6.113}$$

we see that we can substitute this term into the right side of the momentum equation:

$$\vec{V} \cdot \left(\frac{1}{2} \nabla (\vec{V} \cdot \vec{V}) \right) = a^2 \nabla \cdot \vec{V} \tag{6.114}$$

Rearranging gives:

$$a^2 \nabla \cdot \vec{V} - \frac{1}{2} \vec{V} \cdot \nabla (\vec{V} \cdot \vec{V}) = 0 \tag{6.115}$$

Finally, we make the substitution $\vec{V} = \nabla \phi$ for the potential function.

$$\nabla^2 \phi - \frac{1}{a(\phi)^2} \left(\frac{1}{2} \nabla \phi \cdot \nabla (\nabla \phi \cdot \nabla \phi) \right) = 0 \tag{6.116}$$

This equation is called the (steady) *full potential equation*. It isn't used directly very much anymore as modern numerical methods for solving the Euler equations are just as easy to work with and don't carry the limitations of isentropic or irrotational flow. However, this equation does form the basis of various small disturbance theories as we will see in this chapter. Note that for an incompressible flow the speed of sound is infinite ($a \to \infty$) and the above expression reduces to Laplace's equation as expected:

$$\nabla^2 \phi = 0 \tag{6.117}$$

Actually, we haven't fully expressed the equation. We wrote that the speed of sound a is a function of ϕ but did not explicitly show this. It makes the above expression less clear, but below we show how this can be done. For a steady, adiabatic compressible flow we shows that total enthalpy is conserved along a streamline (Eq. 6.92). If we have a constant freestream, as is almost always the case for potential flow, then the upstream enthalpy is the same for every streamline and so we can say that the total enthalpy is constant everywhere. The assumptions of steady flow and constant total enthalpy are not actually necessary to derive the full potential equations. There is an unsteady version, but

the derivation is quite a bit longer and not needed for our purposes. If total enthalpy is constant we can write:

$$h + \frac{V^2}{2} = \text{const} \tag{6.118}$$

$$c_p T + \frac{1}{2}(\vec{V} \cdot \vec{V}) = \text{const} \tag{6.119}$$

$$\frac{\gamma R}{\gamma - 1} T + \frac{1}{2}(\vec{V} \cdot \vec{V}) = \text{const} \tag{6.120}$$

$$\frac{a^2}{\gamma - 1} + \frac{1}{2}(\vec{V} \cdot \vec{V}) = \text{const} \tag{6.121}$$

$$\tag{6.122}$$

where c_p is specific heat at constant pressure, and we have assumed a calorically perfect gas (Eq. 6.36), and used Eqs. 6.42 and 6.89. We now apply this equation at two points, the freesteam and an arbitrary point in the fluid.

$$\frac{a^2}{\gamma - 1} + \frac{1}{2}(\vec{V} \cdot \vec{V}) = \frac{a_\infty^2}{\gamma - 1} + \frac{1}{2} V_\infty^2 \tag{6.123}$$

or rearranging:

$$a^2 = a_\infty^2 - \frac{\gamma - 1}{2}(V_\infty^2 - \vec{V} \cdot \vec{V}) \tag{6.124}$$

Or in terms of the potential function.

$$a^2 = a_\infty^2 - \frac{\gamma - 1}{2}(V_\infty^2 - \nabla\phi \cdot \nabla\phi) \tag{6.125}$$

This equations gives the desired relationship, $a(\phi)$, and thus we see that the full potential equation only depends on one unknown: ϕ.

6.3 Small Disturbance Equations

In the remainder of this chapter we will need to make use of partial derivatives many times. In order to simplify notation we will often use the following:

$$\phi_x \equiv \frac{\partial \phi}{\partial x} \tag{6.126}$$

$$\phi_{xx} \equiv \frac{\partial^2 \phi}{\partial x^2} \tag{6.127}$$

$$\tag{6.128}$$

We now will introduce the small disturbance equations. We align our axis with the freestream, and assume that a body in the flow creates

only small disturbances relative to freestream values.

$$\phi = V_\infty x + \hat{\phi} \tag{6.129}$$

where $\hat{\phi}$ is a small disturbance in ϕ. In terms of velocities this means that:

$$\begin{aligned} u &= V_\infty + \hat{u} \\ v &= \hat{v} \\ w &= \hat{w} \end{aligned} \tag{6.130}$$

where $\hat{u}, \hat{v}, \hat{w}$ are disturbance velocities.

We start with the velocity from the full potential equation (Eq. 6.115) and introduce the perturbation velocities. It will be easier to do this one term at a time, where again we will use the subscripts to denote partial derivatives. We will also temporarily drop the hats for convenience

$$\nabla \cdot \vec{V} = u_x + v_y + w_z \tag{6.131}$$

$$\vec{V} \cdot \vec{V} = V_\infty^2 + 2V_\infty u + u^2 + v^2 + w^2 \tag{6.132}$$

$$\nabla(\vec{V} \cdot \vec{V}) = \begin{bmatrix} 2V_\infty u_x + 2uu_x + 2vv_x + 2ww_x \\ 2V_\infty u_y + 2uu_y + 2vv_y + 2ww_y \\ 2V_\infty u_z + 2uu_z + 2vv_z + 2ww_z \end{bmatrix} \tag{6.133}$$

$$\begin{aligned} \frac{1}{2}\vec{V} \cdot \nabla(\vec{V} \cdot \vec{V}) = (V_\infty + u)(V_\infty u_x + uu_x + vv_x + ww_x) + \\ v(V_\infty u_y + uu_y + vv_y + ww_y) + \\ w(V_\infty u_z + uu_z + vv_z + ww_z) \end{aligned} \tag{6.134}$$

We also need to substitute the perturbation into the definition of the speed of sound (Eq. 6.124):

$$a^2 = a_\infty^2 - \frac{\gamma - 1}{2}(V_\infty^2 - V_\infty^2 + 2V_\infty u + u^2 + v^2 + w^2) \tag{6.135}$$

$$= a_\infty^2 - \frac{\gamma - 1}{2}(2V_\infty u + u^2 + v^2 + w^2) \tag{6.136}$$

$$\tag{6.137}$$

Because u, v, w are all small, their products are even smaller and do we can drop these terms. The derivatives of u, v, w may not necessarily be small, and so we cannot drop products of derivatives times the velocities yet.

$$\begin{aligned} \frac{1}{2}\vec{V} \cdot \nabla(\vec{V} \cdot \vec{V}) \approx V_\infty^2 u_x + V_\infty uu_x + V_\infty vv_x + V_\infty ww_x \\ + V_\infty uu_x + V_\infty vu_y + V_\infty wu_z \end{aligned} \tag{6.138}$$

and

$$a^2 \approx a_\infty^2 - (\gamma - 1)V_\infty u \tag{6.139}$$

Substituting all of this into the full potential equations (Eq. 6.116) gives:

$$(a_\infty^2 - (\gamma-1)V_\infty u)(u_x + v_y + w_z) - V_\infty^2 u_x - V_\infty(2uu_x + vv_x + ww_x + vu_y + wu_z) = 0 \tag{6.140}$$

Collecting like terms yields:

$$(a_\infty^2 - (\gamma - 1)V_\infty u - V_\infty^2 - 2V_\infty u)u_x + a_\infty^2(v_y + w_z) - (\gamma - 1)V_\infty u(v_y + w_z) - V_\infty(vv_x + ww_x + vu_y + wu_z) = 0 \tag{6.141}$$

We now simplify and divide through by a_∞^2.

$$\left(1 - M_\infty^2 - (\gamma + 1)M_\infty^2 \frac{u}{V_\infty}\right) u_x + v_y + w_z - (\gamma - 1)M_\infty^2 \frac{u}{V_\infty}(v_y + w_z) - M_\infty^2 \frac{1}{V_\infty}(vv_x + ww_x + vu_y + wu_z) = 0 \tag{6.142}$$

Now we can see that every term has a velocity derivative term, and so those terms that are also multiplied by an additional perturbation velocity (u, v, w) will be much smaller. However, there is one term we cannot drop. We see that when the Mach number is close to 1 then the term $1 - M_\infty^2$ is small and so the remaining term in those parenthesis will be significant and can't be dropped. On the other hand, all the terms from uv_y onward are small for all Mach numbers and so we can drop them.

$$\left(1 - M_\infty^2 - (\gamma + 1)M_\infty^2 \frac{u}{V_\infty}\right) u_x + v_y + w_z = 0 \tag{6.143}$$

We can now write this in terms of the potential.

$$\left(1 - M_\infty^2 - (\gamma + 1)M_\infty^2 \frac{\hat{\phi}_x}{V_\infty}\right) \hat{\phi}_{xx} + \hat{\phi}_{yy} + \hat{\phi}_{zz} = 0 \tag{6.144}$$

This equation is called the *transonic small disturbance equation* (TSD). As discussed, the ϕ_x term is small unless the Mach number is close to one (hence the transonic in the name), but for Mach numbers not close to one we will be able to drop the term.

In a similar process we can compute the pressure coefficient for small disturbances in a compressible flow. We cannot use the simplified C_p calculation in terms of velocities as that used Bernoulli's equation

and does not apply for compressible flow. Instead, we go back to the original definition.

$$C_p = \frac{p - p_\infty}{\frac{1}{2}\rho_\infty V_\infty^2} \tag{6.145}$$

For compressible flows it is more convenient to use a different form of the dynamic pressure in terms of the Mach number (Eq. 6.91).Substituting this into the definition of the pressure coefficient gives:

$$C_p = \left(\frac{p}{p_\infty} - 1\right)\frac{2}{\gamma M_\infty^2} \tag{6.146}$$

Now we need to go back to our energy equation (Eq. 6.119), which we apply between an arbitrary location and at freestream.

$$c_p T + \frac{1}{2}\vec{V}\cdot\vec{V} = c_p T_\infty + \frac{V_\infty^2}{2} \tag{6.147}$$

Solving for T/T_∞:

$$\frac{T}{T_\infty} = 1 + \frac{1}{2T_\infty c_p}\left(V_\infty^2 - \vec{V}\cdot\vec{V}\right) \tag{6.148}$$

Using the definition $c_p = \gamma R/(\gamma - 1)$ and substituting in the speed of sound ($a^2 = \gamma RT$) gives:

$$\frac{T}{T_\infty} = 1 + \frac{\gamma - 1}{2a_\infty^2}\left(V_\infty^2 - \vec{V}\cdot\vec{V}\right) \tag{6.149}$$

Now we make use of the isentropic relationships between pressure and tempreature (Eq. 6.61): Applying to the above equation and substituting into the pressure coefficient gives:

$$C_p = \left[\left(1 + \frac{(\gamma - 1)}{2a_\infty^2}\left(V_\infty^2 - \vec{V}\cdot\vec{V}\right)\right)^{\gamma/(\gamma-1)} - 1\right]\frac{2}{\gamma M_\infty^2} \tag{6.150}$$

So far, everything is exact, but now we can introduce the small perturbation assumption:

$$V_\infty^2 - \vec{V}\cdot\vec{V} = V_\infty^2 - (V_\infty^2 + 2V_\infty\hat{u} + \hat{u}^2 + \hat{v}^2 + \hat{w}^2) \tag{6.151}$$

$$= -(2V_\infty\hat{u} + \hat{u}^2 + \hat{v}^2 + \hat{w}^2) \tag{6.152}$$

Substituting that into the pressure coefficient gives:

$$C_p \approx \left[\left(1 - \frac{(\gamma - 1)}{2a_\infty^2}(2V_\infty\hat{u} + \hat{u}^2 + \hat{v}^2 + \hat{w}^2)\right)^{\gamma/(\gamma-1)} - 1\right]\frac{2}{\gamma M_\infty^2} \tag{6.153}$$

Now, we make use of the binomial approximation, which is:

$$(1+x)^{\alpha} \approx 1 + \alpha x + \frac{1}{2}\alpha(\alpha-1)x^2 + \ldots \tag{6.154}$$

This equation can be found from a Taylor's series and applies when x is small relative to 1. In our case the 'x' term contains only perturbation velocities and so is small by definition.

$$\begin{aligned} C_p \approx \Bigg[& 1 - \frac{\gamma}{(\gamma-1)} \frac{(\gamma-1)}{2a_\infty^2}(2V_\infty \hat{u} + \hat{u}^2 + \hat{v}^2 + \hat{w}^2) \\ & + \frac{1}{2}\frac{\gamma}{(\gamma-1)}\frac{1}{(\gamma-1)}\frac{(\gamma-1)^2}{4a_\infty^4}(2V_\infty \hat{u} + \hat{u}^2 + \hat{v}^2 + \hat{w}^2)^2 - 1 \Bigg] \frac{2}{\gamma M_\infty^2} \end{aligned} \tag{6.155}$$

We will retain up to second-order terms:

$$\begin{aligned} C_p &\approx \left[-\frac{\gamma}{2a_\infty^2}(2V_\infty \hat{u} + \hat{u}^2 + \hat{v}^2 + \hat{w}^2) + \frac{1}{2}\frac{\gamma}{a_\infty^4} V_\infty^2 \hat{u}^2 \right] \frac{2}{\gamma M_\infty^2} \\ &= -2\frac{\hat{u}}{V_\infty} - \left(\frac{\hat{u}^2 + \hat{v}^2 + \hat{w}^2}{V_\infty^2} \right) + M_\infty^2 \left(\frac{\hat{u}}{V_\infty} \right)^2 \end{aligned} \tag{6.156}$$

Rearranging like terms gives our final result:

$$C_p = -\left[\frac{2\hat{u}}{V_\infty} + (1 - M_\infty^2)\left(\frac{\hat{u}}{V_\infty}\right)^2 + \left(\frac{\hat{v}}{V_\infty}\right)^2 + \left(\frac{\hat{w}}{V_\infty}\right)^2 \right] \tag{6.157}$$

Like the full potential equation, the TSD equation is by itself no longer of much interest (though it was of significant interest historically). Instead, we will look at the subsonic and supersonic cases separately where the Mach number is away from one and the ϕ_x term can be dropped. Some useful insights and formulas will result for these two cases.

6.4 Subsonic Small Disturbance

If the Mach number is less than approximately 0.8, and only small disturbances are introduced in the flow field, then the TSD equation (Eq. 6.144) can be reduced to:

$$\left(1 - M_\infty^2\right)\hat{\phi}_{xx} + \hat{\phi}_{yy} + \hat{\phi}_{zz} = 0 \tag{6.158}$$

The boundary conditions for inviscid flow are flow tangency, where we use the function $f(x)$ to represent the shape of the body:

$$\frac{df}{dx} = \frac{\hat{v}}{V_\infty + \hat{u}} \approx \frac{\hat{v}}{V_\infty} \tag{6.159}$$

or

$$V_\infty \frac{df}{dx} = \hat{v} = \hat{\phi}_y \tag{6.160}$$

If we drop all second order terms from the small disturbance pressure coefficient equation (Eq. 6.157) we have:

$$C_p = -\frac{2\hat{u}}{V_\infty} = -\frac{2}{V_\infty}\hat{\phi}_x \tag{6.161}$$

We repeat those three equations, without the hat to simplify the notation, and we write out the partial derivatives to make the following derivation clearer.

$$\left(1 - M_\infty^2\right)\frac{\partial^2\phi}{\partial x^2} + \frac{\partial^2\phi}{\partial y^2} + \frac{\partial^2\phi}{\partial z^2} = 0 \tag{6.162}$$

$$V_\infty \frac{df}{dx} = \frac{\partial\phi}{\partial y} \tag{6.163}$$

$$C_p = -\frac{2}{V_\infty}\frac{\partial\phi}{\partial x} \tag{6.164}$$

The first equation is almost Laplace's equation, but not quite. Perhaps with a change of variables we can transform it to Laplace's equation. We introduce the following change of variables, where A, β and C are constants (we use β as this will be an important constant, and β is conventionally used for this purpose). We scale the potential, and shape by some unknown constant. We choose x as the one variable that doesn't scale (this is general as all other scaling is relative to this). Recall that the the body is aligned in the x direction, so we scale the other coordinate directions by some other unknown constant $(1/\beta)$.

$$\phi = A\bar{\phi} \tag{6.165}$$

$$x = \bar{x} \tag{6.166}$$

$$y = \frac{1}{\beta}\bar{y} \tag{6.167}$$

$$z = \frac{1}{\beta}\bar{z} \tag{6.168}$$

$$f = C\bar{f} \tag{6.169}$$

As an example, using the chain rule, and the above change of variables, gives the following for the derivative with respect to y:

$$\frac{\partial\phi}{\partial y} = \frac{\partial\phi}{\partial\bar{y}}\frac{d\bar{y}}{dy} = \frac{\partial\phi}{\partial\bar{y}}\beta = \frac{\partial\bar{\phi}}{\partial\bar{y}}A\beta \tag{6.170}$$

Similarly, the the second derivative of y we get:

$$\frac{\partial^2 \phi}{\partial y^2} = \frac{\partial}{\partial y}\left(A\beta \frac{\partial \bar{\phi}}{\partial \bar{y}}\right) = A\beta \frac{\partial}{\partial \bar{y}}\left(\frac{\partial \bar{\phi}}{\partial y}\right) = A\beta \frac{\partial}{\partial \bar{y}}\left(\frac{\partial \bar{\phi}}{\partial \bar{y}}\frac{d\bar{y}}{dy}\right) = A\beta^2 \frac{\partial^2 \bar{\phi}}{\partial \bar{y}^2} \tag{6.171}$$

If we make the change of variable substitutions into the governing equation we get:

$$\left(1 - M_\infty^2\right) \cancel{A}\bar{\phi}_{\bar{x}\bar{x}} + \cancel{A}\beta^2 \bar{\phi}_{\bar{y}\bar{y}} + \cancel{A}\beta^2 \bar{\phi}_{\bar{z}\bar{z}} = 0 \tag{6.172}$$

If we choose to define β as:

$$\beta = \sqrt{1 - M_\infty^2} \tag{6.173}$$

then we get

$$\bar{\phi}_{\bar{x}\bar{x}} + \bar{\phi}_{\bar{y}\bar{y}} + \bar{\phi}_{\bar{z}\bar{z}} = 0 \tag{6.174}$$

which is Laplace's equation! This means that through a change of coordinates we can continue to use Laplace's equation for compressible potential flow as long as the disturbances are small and the Mach number is not too close to 1.

Next, let's check how this impacts our boundary condition. The change of coordinates gives:

$$V_\infty C \frac{d\bar{f}}{d\bar{x}} = A\beta \frac{\partial \bar{\phi}}{\partial \bar{y}} \tag{6.175}$$

Ideally, we don't want to modify the geometry when using the coordinate transformation so we would like $C = 1$ (Eq. 6.169), and we would like the ratio above $C/(A\beta)$ to also equal 1 so that we don't have to stretch the geometry when applying the boundary condition. If $C = 1$ that means we require $A = 1/\beta$. By choosing that set of constants we can use the original body shape without modification.

Finally, we need to check how our coordinate transformation impacts the computation of C_p.

$$C_p = -\frac{2}{V_\infty} A \frac{\partial \bar{\phi}}{\partial \bar{x}} \tag{6.176}$$

or since $A = 1/\beta$

$$C_p = -\frac{2}{V_\infty} \frac{\partial \bar{\phi}}{\partial \bar{x}} \frac{1}{\beta} \tag{6.177}$$

The result of the coordinate system change is:

$$\frac{\partial^2 \bar{\phi}}{\partial \bar{x}^2} + \frac{\partial^2 \bar{\phi}}{\partial \bar{y}^2} + \frac{\partial^2 \bar{\phi}}{\partial \bar{z}^2} = 0 \tag{6.178}$$

$$V_\infty \frac{d\bar{f}}{d\bar{x}} = \frac{\partial \bar{\phi}}{\partial \bar{y}} \tag{6.179}$$

$$C_p = -\frac{2}{V_\infty} \frac{\partial \bar{\phi}}{\partial \bar{x}} \frac{1}{\sqrt{1 - M_\infty^2}} \tag{6.180}$$

If we compare this set of equations to those in the original coordinate system (Eq. 6.162) we see that we successful transformed the governing equation to Laplace's equation, the boundary condition is unchanged, and the resulting C_p needs to be divided by β.

In other words, if we use the exact same process we used for solving Laplace's equation in incompressible flow (e.g., a panel method) all we need to do is multiply our resulting C_p by a correction factor:

$$C_p = \frac{C_{p_0}}{\sqrt{1 - M_\infty^2}} \tag{6.181}$$

where C_{p_0} is the pressure coefficient we would compute in the incompressible flow. This is called the *Prandtl-Glauert correction* or PG correction for short.

Furthermore, because the lift coefficient, moment coefficient, and lift curve slope are just integrals of pressure the same correction applies. For example:

$$c_l = \frac{c_{l0}}{\sqrt{1 - M_\infty^2}} \tag{6.182}$$

Note that the effect is that as the Mach number is increased, the lift and moment coefficients are increased as well.

One unnecessary limitation in the above derivation is that we only retained the linear terms in the small disturbance pressure coefficient equation (Eq. 6.157). Retaining additional terms and following a similar process gives the *Karman-Tsien* correction, which is not much more complicated but produces more accurate results.

$$C_p = \left[\frac{\beta}{C_{p_0}} + \frac{M_\infty^2}{2(1+\beta)} \right]^{-1} \tag{6.183}$$

Again, remember the main limitation (besides those of potential flow) is the assumption of small disturbances. Most of the time aerodynamic bodies are designed to only introduce small disturbances, indeed

this is what we imply we say a vehicle has an aerodynamic shape. However, as the Mach number is increased geometries need to become increasingly thin to prevent shock waves and large disturbances. Thus, these correction methods work reasonably well for moderate Mach numbers (near 0.5), but may be quite inaccurate as we approach Mach 0.7–0.8 and above depending on the geometry.

6.5 Supersonic Thin Airfoil Theory

Starting from the TSD equation (Eq. 6.144), we can also drop the higher order term if the Mach number is approximately above 1.2. The resulting equation is

$$-\beta^2\hat{\phi}_{xx} + \hat{\phi}_{yy} + \hat{\phi}_{zz} = 0 \tag{6.184}$$

where

$$\beta = \sqrt{M_\infty^2 - 1} \tag{6.185}$$

Note that we changed the definition of β for the supersonic case. This is no longer an elliptic PDE but rather is a hyperbolic one. Like the integral boundary layer equations, that means that the information flow is directional. Disturbances cannot go upstream, as is physically consistent with the behavior of supersonic flow (information travels with the speed of sound).

In this section we will focus on airfoils (i.e., 2D):

$$-\beta^2\hat{\phi}_{xx} + \hat{\phi}_{yy} = 0 \tag{6.186}$$

This equation has the exact same form as the one-dimensional wave equation, which has known solutions:

$$\hat{\phi} = F(x - \beta y) + G(x + \beta y) \tag{6.187}$$

where F and G are arbitrary functions.

A visualization of the flow behavior is shown in Fig. 6.6. The lines are often referred to as *characteristics*. Along a characteristic the flow properties are constant. Physically, they are Mach waves or infinitely weak (isentropic) shock waves. On the upper surface only the F function applies, while G applies on the lower surface (because Mach waves only travel downstream).

Recall that the boundary condition is approximately given as:

$$V_\infty \frac{dy}{dx} = \frac{d\hat{\phi}}{dy} \tag{6.188}$$

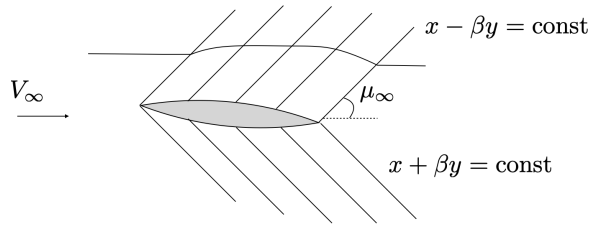

Fig. 6.6 Characteristic lines in a small disturbance supersonic flow field.

Applying this on the upper surface, and using thin-airfoil theory assumptions, as is consistent with small disturbances, yields:

$$V_\infty \left(\frac{dy}{dx}\right)_u = \left(\frac{d\hat{\phi}}{dy}\right)_{y=0^+} = -\beta F'(x) \tag{6.189}$$

If we solve this for F' we have:

$$F'(x) = -\frac{V_\infty}{\beta}\left(\frac{dy}{dx}\right)_u \tag{6.190}$$

Recall that the pressure coefficient (dropping higher order terms) is given by (Eq. 6.161):

$$C_p = -\frac{2}{V_\infty}\left(\frac{\partial \hat{\phi}}{\partial x}\right)_{y=0} \tag{6.191}$$

Evaluating on the upper surface gives:

$$C_p = -\frac{2}{V_\infty} F'(x) \tag{6.192}$$

Using the expression for F' above:

$$C_p = \frac{2}{\beta}\frac{dy}{dx} \tag{6.193}$$

The derivative dy/dx is the local slope of the airfoil, which we call θ, and β was defined previously:

$$C_p = \frac{2\theta}{\sqrt{M_\infty^2 - 1}} \tag{6.194}$$

This expression gives us a quick and easy way to estimate the pressure distribution on a supersonic airfoil with small disturbances. All that is needed is to know the airfoil shape (from which we get the slope θ) and the freestream Mach number. If we followed the same procedure for the lower surface we would get the same expression. Except that on the lower surface the direction of positive θ is opposite (or in other words a surface that inclines into the freestream is a positive theta).

As we did before with airfoils, we will separate the geometric description into a thickness distribution, a camber distribution, and an angle of attack. Specifically, we define the upper and lower surfaces as a superposition of camber and thickness distribution as follows:

$$y_u(x) = y_c(x) + \frac{1}{2}y_t(x) \tag{6.195}$$

$$y_l(x) = y_c(x) - \frac{1}{2}y_t(x) \tag{6.196}$$

Using the formula for the local pressure coefficient:

$$C_{p_u} = \frac{2}{\sqrt{M_\infty^2 - 1}}\left(-\alpha + \frac{dy_u}{dx}\right) \tag{6.197}$$

$$C_{p_l} = \frac{2}{\sqrt{M_\infty^2 - 1}}\left(\alpha - \frac{dy_l}{dx}\right) \tag{6.198}$$

The negative sign results from the way that θ is defined. Substituting in the camber and thickness distributions:

$$C_{p_u} = \frac{2}{\sqrt{M_\infty^2 - 1}}\left(-\alpha + \frac{dy_c}{dx} + \frac{1}{2}\frac{dy_t}{dx}\right) \tag{6.199}$$

$$C_{p_l} = \frac{2}{\sqrt{M_\infty^2 - 1}}\left(\alpha - \frac{dy_c}{dx} + \frac{1}{2}\frac{dy_t}{dx}\right) \tag{6.200}$$

The definition of the (inviscid) normal force coefficient is:

$$c_n = \frac{1}{c}\int_0^c (C_{p_l} - C_{p_u})dx \tag{6.201}$$

Substituting in the result from above gives:

$$c_n = \frac{2}{\sqrt{M_\infty^2 - 1}}\frac{1}{c}\int_0^c (2\alpha - 2\frac{dy_c}{dx})dx \tag{6.202}$$

$$= \frac{2}{\sqrt{M_\infty^2 - 1}}\frac{1}{c}\left(2\alpha\int_0^c dx - 2\int_0^c \frac{dy_c}{dx}dx\right) \tag{6.203}$$

$$= \frac{2}{\sqrt{M_\infty^2 - 1}}\frac{1}{c}\left(2\alpha c - 2\ y_c|_0^c\right) \tag{6.204}$$

$$= \frac{4\alpha}{\sqrt{M_\infty^2 - 1}} \tag{6.205}$$

The definition of the (inviscid) axial force coefficient is:

$$c_a = \frac{1}{c}\int_0^c \left(C_{p_u}\frac{dy_u}{dx} - C_{p_l}\frac{dy_l}{dx}\right)dx \tag{6.206}$$

Substituting in:

$$c_a = \frac{1}{c}\int_0^c \left(\frac{2}{\sqrt{M_\infty^2 - 1}} \left(-\alpha + \frac{dy_c}{dx} + \frac{1}{2}\frac{dy_t}{dx} \right) \left(\frac{dy_c}{dx} + \frac{1}{2}\frac{dy_t}{dx} \right) - \frac{2}{\sqrt{M_\infty^2 - 1}} \left(\alpha - \frac{dy_c}{dx} + \frac{1}{2}\frac{dy_t}{dx} \right) \left(\frac{dy_c}{dx} - \frac{1}{2}\frac{dy_t}{dx} \right) \right) dx \tag{6.207}$$

Several terms appear in both expressions and so cancel out. Removing those terms leaves us with:

$$c_a = \frac{2}{\sqrt{M_\infty^2 - 1}} \frac{1}{c} \int_0^c \left(-2\alpha \frac{dy_c}{dx} + 2\left(\frac{dy_c}{dx} \right)^2 + \frac{1}{2}\left(\frac{dy_t}{dx} \right)^2 \right) dx \tag{6.208}$$

For the first term under the integral, α is a constant and can be taken out. We already saw that

$$\int_0^c \frac{dy_c}{dx} dx = 0 \tag{6.209}$$

and so that whole term is zero. We are left with:

$$c_a = \frac{4}{\sqrt{M_\infty^2 - 1}} \left(\overline{\left(\frac{dy_c}{dx} \right)^2} + \frac{1}{4} \overline{\left(\frac{dy_t}{dx} \right)^2} \right) \tag{6.210}$$

where we define

$$\overline{\zeta} = \frac{1}{c}\int_0^c \zeta(x) dx \tag{6.211}$$

as a shorthand for convenience.

Finally, lift and drag are related to the normal and axial forces as follows:

$$c_l = c_n \cos\alpha - c_a \sin\alpha \tag{6.212}$$

$$c_d = c_n \sin\alpha + c_a \cos\alpha \tag{6.213}$$

Using a small angle approximation, consistent with thin airfoil theory, yields:

$$c_l \approx c_n - c_a \alpha \tag{6.214}$$

$$c_d \approx c_n \alpha + c_a \tag{6.215}$$

Conventionally, the $c_a \alpha$ term is neglected in the lift coefficient because it is of *much* smaller magnitude than c_n (c_a is small and α is small so

their product is very small). However, in the drag calculation both $c_n\alpha$ and c_a are of similar magnitude.

$$c_l \approx c_n \tag{6.216}$$
$$c_d \approx c_n\alpha + c_a \tag{6.217}$$

Thus:

$$\begin{aligned} c_l &= \frac{4\alpha}{\sqrt{M_\infty^2 - 1}} \\ c_d &= \frac{4}{\sqrt{M_\infty^2 - 1}}\left(\alpha^2 + \overline{\left(\frac{dy_c}{dx}\right)^2} + \frac{1}{4}\overline{\left(\frac{dy_t}{dx}\right)^2}\right) \end{aligned} \tag{6.218}$$

The (inviscid) pitching moment coefficient is:

$$c_{mle} = \frac{1}{c^2}\int_0^c \left(\left(C_{p_u} - C_{p_l}\right)x + C_{p_u}\frac{dy_u}{dx}y_u - C_{p_l}\frac{dy_l}{dx}y_l\right)dx \tag{6.219}$$

Making substitutions:

$$\begin{aligned} c_{mle} = \frac{1}{c^2}\frac{2}{\sqrt{M_\infty^2 - 1}}\int_0^c \Bigg[\left(-2\alpha + 2\frac{dy_c}{dx}\right)x + \left(-\alpha + \frac{dy_c}{dx} + \frac{1}{2}\frac{dy_t}{dx}\right)\left(\frac{dy_c}{dx} + \frac{1}{2}\frac{dy_t}{dx}\right)(y_c + y_t) - \\ \left(\alpha - \frac{dy_c}{dx} + \frac{1}{2}\frac{dy_t}{dx}\right)\left(\frac{dy_c}{dx} - \frac{1}{2}\frac{dy_t}{dx}\right)(y_c - y_t)\Bigg]dx \end{aligned} \tag{6.220}$$

Removing terms that cancel:

$$\begin{aligned} c_{mle} = \frac{1}{c^2}\frac{2}{\sqrt{M_\infty^2 - 1}}\int_0^c \Bigg[-2\alpha x + 2\frac{dy_c}{dx}x + y_c\left(-2\alpha\frac{dy_c}{dx} + 2\frac{dy_c}{dx}^2 + \frac{1}{2}\frac{dy_t}{dx}^2\right) + \\ y_t\left(-\alpha\frac{dy_t}{dx} + 2\frac{dy_c}{dx}\frac{dy_t}{dx}\right)\Bigg]dx \end{aligned} \tag{6.221}$$

Neglecting all second order terms:

$$c_{mle} \approx \frac{1}{c^2}\frac{2}{\sqrt{M_\infty^2 - 1}}\int_0^c \left[-2\alpha x + 2\frac{dy_c}{dx}x\right]dx \tag{6.222}$$
$$= \frac{1}{c^2}\frac{2}{\sqrt{M_\infty^2 - 1}}\left[-2\alpha\frac{c^2}{2} + \int_0^c 2\frac{dy_c}{dx}x\,dx\right] \tag{6.223}$$

The second term we can integrate by parts:

$$c_{mle} = \frac{1}{c^2}\frac{2}{\sqrt{M_\infty^2 - 1}}\left[-\alpha c^2 + 2(xy_c)_0^c - \int_0^c y_c\,dx\right] \tag{6.224}$$

The second term is zero, leading to

$$c_{mle} = -\frac{2}{\sqrt{M_\infty^2 - 1}}\left[\alpha + \frac{1}{c^2}\int_0^c y_c dx\right] \tag{6.225}$$

Substituting in the definition of the chord-averaged variable.

$$c_{mle} = -\frac{2}{\sqrt{M_\infty^2 - 1}}\left[\alpha + \frac{\overline{y_c}}{c}\right] \tag{6.226}$$

The aerodynamic center can be computing by noting the the moment at any other location can be found as:

$$M'(x) = M'_{le} + L'x \tag{6.227}$$

$$c_m(x) = c_{mle} + c_l\frac{x}{c} \tag{6.228}$$

The definition of the aerodynamic center is the location where $dc_m/d\alpha = 0$ or in other words, the pitching moment is independent of angle of attack.

$$\frac{dc_{mac}}{d\alpha} = \frac{dc_{mle}}{d\alpha} + \frac{dc_l}{d\alpha}\frac{x_{ac}}{c} = 0 \tag{6.229}$$

$$\Rightarrow \frac{x_{ac}}{c} = \frac{-dc_{mle}/d\alpha}{dc_l/d\alpha} \tag{6.230}$$

Using the results from the above equations gives:

$$\frac{x_{ac}}{c} = \frac{2/\beta}{4/\beta} = \frac{1}{2} \tag{6.231}$$

Thus, in supersonic thin airfoil theory the aerodynamic center is at the half chord, not the quarter chord as in subsonic thin airfoil theory.

Example 6.1 Diamond airfoil

As an example consider the diamond airfoil shown in Fig. 6.7. There is no camber, but the thickness over the first half of the airfoil is given by:

$$y_t = 2x\tan\theta \tag{6.232}$$

and for the latter half is:

$$y_t = 2(c - x)\tan\theta \tag{6.233}$$

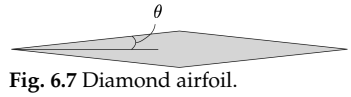

Fig. 6.7 Diamond airfoil.

If we evaluate the thickness term that appears in the integral:

$$\frac{1}{4}\overline{\left(\frac{dy_t}{dx}\right)^2} = \frac{1}{4c}\int_0^c \left(\frac{dy_t}{dx}\right)^2 dx \tag{6.234}$$

$$= \frac{1}{4c}\left[\int_0^{c/2}\left(\frac{dy_t}{dx}\right)^2 dx + \int_{c/2}^c \left(\frac{dy_t}{dx}\right)^2 dx\right] \tag{6.235}$$

$$= \frac{1}{4c}\left[4\tan^2\theta\frac{c}{2} + 4\tan^2\theta\frac{c}{2}\right] = \tan^2\theta = \left(\frac{t}{c}\right)^2 \tag{6.236}$$

The resulting drag coefficient estimate for the diamond airfoil is thus:

$$c_d = \frac{4}{\sqrt{M_\infty^2 - 1}} \left(\alpha^2 + \left(\frac{t}{c} \right)^2 \right) \tag{6.237}$$

Shock-expansion theory, discussed in the next section, is more accurate as it does not rely on the small disturbance assumptions and is well suited for numerical simulations. Although these simple methods are less exact, they give rise to analytic expressions that allow for back-of-the-envelope estimation and provide insight into the main factors that affect supersonic airfoils.

6.6 Shock Waves

Normal shock waves are perpendicular to the flow direction, whereas oblique shock waves occur at an angle relative to the flow. It is convenient to conceptually differentiate between normal shock waves and oblique shock waves, although theoretically we could treat every shock wave as a normal shock wave with an appropriate change of reference. The physics does not change between the two types, it is just a convenient construct to align with flow directions.

6.6.1 Normal Shock Waves

We determined the speed of sound by placing a control volume around a sound wave, which is an infinitely weak, isentropic, pressure wave (Section 6.1.6). To analyze shock waves, we use a similar process. However, a shock wave is not isentropic, and fluid properties change by a finite, discontinuous amount. Shock waves are not actually discontinuities, but are extremely thin regions (typically on the order of microns) across which fluid properties change rapidly. From the macro fluid level they appear discontinuous and are generally treated as such.

Consider the shock wave and control volume shown in Fig. 6.8. A mass, momentum, and energy balance yields:

$$\rho_1 u_1 = \rho_2 u_2 \tag{6.238}$$

$$p_1 + \rho_1 u_1^2 = p_2 + \rho_2 u_2^2 \tag{6.239}$$

$$h_1 + \frac{u_1^2}{2} = h_2 + \frac{u_2^2}{2} \tag{6.240}$$

In the latter two equations we have assumed that the flow is inviscid at the boundaries of the control volume. The shock wave itself is highly

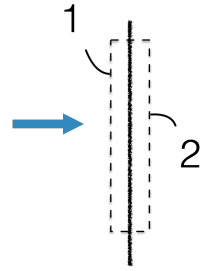

Fig. 6.8 Control volume around a shock wave.

viscous, but that viscous behavior is confined to the interior of the control volume. We make the control volume just large enough so that the boundaries are outside the large velocity gradients that occur within the shock wave.

If we assume a calorically perfect gas we can add the ideal gas equation of state and the simple relationship for specific heats:

$$p = \rho RT \tag{6.241}$$

$$h = c_p T \tag{6.242}$$

We now have five equations and five unknowns that we can solve algebraically. In the more general case, where specific heats vary with temperature and potentially pressure, these equations can still be solved but a numerical solution may be necessary.

Solving for the five unknowns results in the following shock jump equations:

$$\frac{u_2}{u_1} = \frac{\rho_1}{\rho_2} = \frac{2 + (\gamma - 1)M_1^2}{(\gamma + 1)M_1^2} \tag{6.243}$$

$$\frac{p_2}{p_1} = 1 + \frac{2\gamma}{\gamma + 1}(M_1^2 - 1) \tag{6.244}$$

$$\frac{T_2}{T_1} = \frac{h_2}{h_1} = \frac{p_2}{p_1}\frac{\rho_1}{\rho_2} \tag{6.245}$$

These ratios are plotted as a function of Mach number in Fig. 6.9.

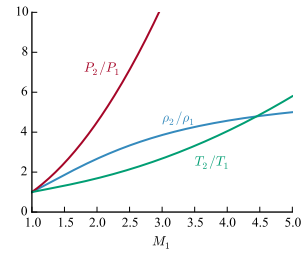

Fig. 6.9 Shock jump relationships.

From the derivation we can also show that the upstream Mach number is always supersonic and the downstream Mach number is always subsonic (with the speeds measured relative to the shock wave). The downstream Mach number is as follows:

$$M_2 = \sqrt{\frac{2 + (\gamma - 1)M_1^2}{2\gamma M_1^2 - (\gamma - 1)}} \tag{6.246}$$

and is plotted in Fig. 6.10: The downstream Mach number asymptotes to:

$$\lim_{M_1 \to \infty} M_2 = \sqrt{\frac{\gamma - 1}{2\gamma}} \approx .378 \tag{6.247}$$

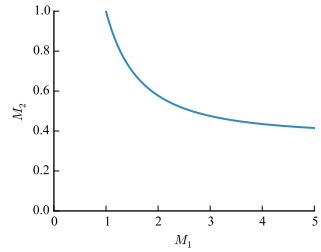

Fig. 6.10 Mach number downstream of a normal shockwave.

This is not to say that the downstream speed asymptotes, indeed the temperature keeps rising with increasing Mach number as shown in Fig. 6.9, and so the speed of sound and thus the actually speed must keep rising as well.

A shock wave, while viscous, is still adiabatic and so the total temperature is preserved:

$$T_{T1} = T_{T2} \tag{6.248}$$

Total pressure will not be constant, however, because of viscosity. We use the total pressure definition (Eq. 6.96) separately for the upstream and downstream properties.

$$\frac{p_{T1}}{p_1} = \left(1 + \frac{\gamma - 1}{2} M_1^2\right)^{\gamma/(\gamma-1)} \tag{6.249}$$

$$\frac{p_{T2}}{p_2} = \left(1 + \frac{\gamma - 1}{2} M_2^2\right)^{\gamma/(\gamma-1)} \tag{6.250}$$

We now divide the two equations by each other:

$$\frac{p_{T2}}{p_{T1}} = \frac{p_2}{p_1} \frac{\left(1 + \frac{\gamma-1}{2} M_2^2\right)^{\gamma/(\gamma-1)}}{\left(1 + \frac{\gamma-1}{2} M_1^2\right)^{\gamma/(\gamma-1)}} \tag{6.251}$$

We now substitute in Eq. 6.244 and Eq. 6.246:

$$\frac{p_{T2}}{p_{T1}} = \left(1 + \frac{2\gamma}{\gamma+1}(M_1^2 - 1)\right) \frac{\left(1 + \frac{\gamma-1}{2}\left(\frac{2+(\gamma-1)M_1^2}{2\gamma M_1^2 - (\gamma-1)}\right)\right)^{\gamma/(\gamma-1)}}{\left(1 + \frac{\gamma-1}{2} M_1^2\right)^{\gamma/(\gamma-1)}} \tag{6.252}$$

After some simplification we arrive at the, still rather lengthy, equation for the total pressure drop across a normal shock wave:

$$\frac{p_{T2}}{p_{T1}} = \left(\frac{\gamma+1}{2\gamma M_1^2 - (\gamma-1)}\right)^{\frac{1}{\gamma-1}} \left(\frac{(\gamma+1)M_1^2}{2 + (\gamma-1)M_1^2}\right)^{\frac{\gamma}{\gamma-1}} \tag{6.253}$$

This total pressure drop is plotted as a function of upstream Mach number in Fig. 6.11. Notice that the total pressure drop is relatively small for Mach numbers not much greater than one, but then starts to drop precipitously. This is why many proposed supersonic transports fly at Mach numbers that are only modestly above Mach 1. As the Mach number increases further the total pressure drop becomes very significant and thus the amount of energy burned increases rapidly with higher speeds. The relationship between Mach number and total pressure loss is not the same for an airplane, as the shock waves along an aircraft are not all normal shock waves. More general shock waves are discussed in the following section. However, the qualitative behavior is still relevant.

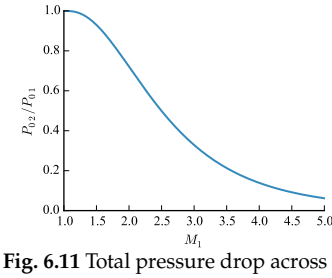

Fig. 6.11 Total pressure drop across a normal shockwave.

6.6.2 Oblique Shock Waves

An oblique shock wave forms at an angle between that of a normal shock wave (perpindicular) and that of a Mach wave (depicted with the angle μ in Fig. 6.2 and Eq. 6.2). Oblique waves are weaker than a normal shock wave, weaker in the sense that they produce less entropy or less total pressure loss, and thus less drag for a flight vehicle. A Mach wave is the limit of an infinitely weak oblique shock wave. Like a normal shock wave, an oblique shock wave is nonisentropic and behind the wave the pressure, density, and temperature all increase discretely. Unlike a normal shock wave, the Mach number behind an oblique shock wave may still be supersonic.

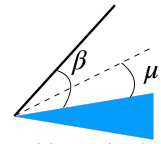

Fig. 6.12 An oblique shock wave angle (β) compared to a Mach wave angle (μ).

An oblique shock wave formed at an inside corner is depicted in Fig. 6.13. We call θ the turning angle, it is the angle change for the fluid flow. We call β the shock angle. It is the angle of the shock wave and produces the discrete change in direction for the flow, as well as the accompanying pressure, temperature, density increase.

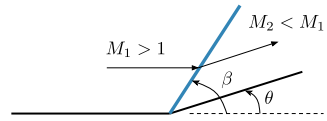

Fig. 6.13 An oblique shock wave.

Oblique shock waves are not really a special case, it is just a normal shock wave relative to the flow perpendicular to the wave (the tangential component of the flow is unaffected). However, it is convenient to rework the equations in a frame of reference relative to the incoming flow.

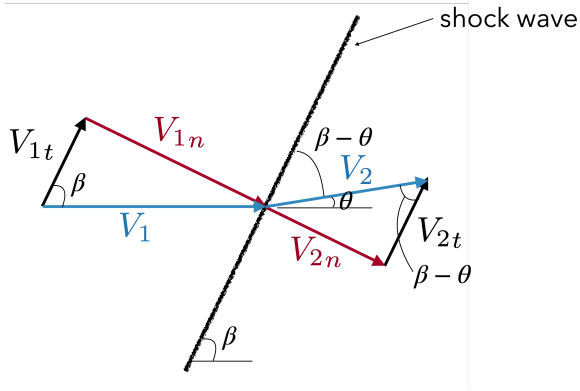

Fig. 6.14 Velocity components before and after an oblique shock wave.

Figure 6.14 depicts the velocity components upstream and downstream of an oblique shock. We have broken up the velocity vectors into components both normal to (subscript n) and tangential to (subscript t) the shock wave. The tangential component is unaffected, and the normal component follows the normal shock jump equations derived previously. From the previous discussion we now that the downstream normal component is always subsonic, however the downstream total

velocity vector may be, and often is, supersonic.

The incoming normal Mach number, as shown in Fig. 6.14, is:

$$M_{1n} = M_1 \sin\beta \tag{6.254}$$

and the exit Mach number is:

$$M_{2n} = M_2 \sin(\beta - \theta) \tag{6.255}$$

We can use the incoming normal Mach number in Eqs. 6.243 to 6.245 to compute the downstream pressure, density, and temperature (using M_{1n} in place of M_1 in the previous equations). However, this normal number depends on the shock angle β and that is not known beforehand. We only know the turning angle θ based on the problem geometry.

To relate these angles with known properties we refer back to Fig. 6.14 and note that:

$$\tan\beta = \frac{V_{1n}}{V_{1t}} \tag{6.256}$$

and

$$\tan(\beta - \theta) = \frac{V_{2n}}{V_{2t}} \tag{6.257}$$

We subtract these two equations, recalling that $V_{1t} = V_{2t}$ so:

$$\tan\beta - \tan(\beta - \theta) = \frac{V_{1n} - V_{2n}}{V_{1t}} \tag{6.258}$$

We expand the left hand side with a trig identity, and on the right hand side we divide top and bottom by V_{1n}.

$$\tan\beta - \frac{(\tan\beta - \tan\theta)}{1 + \tan\beta\tan\theta} = \frac{1 - \frac{V_{2n}}{V_{1n}}}{\frac{V_{1t}}{V_{1n}}} \tag{6.259}$$

On the left hand side we put the two terms on a common denominator, add, then simplify. On the right we use Eq. 6.243 to express the jump in velocity across the shock wave (nothing that we need to use the normal component of the upstream Mach number), and from Fig. 6.14 we see that the term in the denominator is just $1/\tan\beta$.

$$\frac{\tan^2\beta\tan\theta + \tan\theta}{1 + \tan\beta\tan\theta} = \tan\beta\left(1 - \frac{(2 + (\gamma - 1)M_{1_n}^2)}{(\gamma + 1)M_{1_n}^2}\right) \tag{6.260}$$

On the left we factor out $\tan\theta$ from the two terms in the numerator and use a trig identity on the remaining portion. On the right we expand with a common denominator and add the two terms.

$$\frac{\tan\theta(\sec^2\beta)}{1 + \tan\beta\tan\theta} = \tan\beta\left(\frac{2M_{1_n}^2 - 2}{(\gamma + 1)M_{1_n}^2}\right) \tag{6.261}$$

Using Eq. 6.254 we express M_{1n} in terms of the upstream Mach number. We move the sec^2 term to the denominator and expand $tan\beta$ to make the cancellations more obvious.

$$\frac{\tan\theta)}{\cos^2\beta(1+\tan\beta\tan\theta)} = \frac{\sin\beta}{\cos\beta}\left(\frac{2{M_1}^2\sin^2\beta-2}{(\gamma+1){M_1}^2\sin^2\beta}\right) \tag{6.262}$$

One the right side the $\sin\beta$ terms cancel. A $\cos\beta$ cancels across both sides. The remaining $\cos\beta$ term is distributed across the parenthetical term.

$$\frac{\tan\theta}{\cos\beta+\sin\beta\tan\theta)} = \left(\frac{2{M_1}^2\sin^2\beta-2}{(\gamma+1){M_1}^2\sin\beta}\right) \tag{6.263}$$

We now try to isolate θ by dividing both numerator and denominator of the left side term by $\tan\theta$.

$$\frac{1}{\left(\frac{\cos\beta}{\tan\theta}+\sin\beta\right)} = \left(\frac{2{M_1}^2\sin^2\beta-2}{(\gamma+1){M_1}^2\sin\beta}\right) \tag{6.264}$$

To isolate θ we invert both sides then subtract $\sin\beta$ from both sides.

$$\frac{\cos\beta}{\tan\theta} = \left(\frac{(\gamma+1){M_1}^2\sin\beta}{2{M_1}^2\sin^2\beta-2}\right) - \sin\beta \tag{6.265}$$

We now put the right hand side on a common denominator and add:

$$\frac{\cos\beta}{\tan\theta} = \left(\frac{(\gamma+1){M_1}^2\sin\beta-2{M_1}^2\sin^3\beta+2\sin\beta}{2{M_1}^2\sin^2\beta-2}\right) \tag{6.266}$$

On the right side we can factor a $\sin\beta$ term out of the numerator. Then we invert both sides and multiply by $\cos\beta$.

$$\tan\theta = \frac{\cos\beta}{\sin\beta}\left(\frac{2{M_1}^2\sin^2\beta-2}{(\gamma+1){M_1}^2-2{M_1}^2\sin^2\beta+2}\right) \tag{6.267}$$

We can simplify a bit more.

$$\tan\theta = \frac{1}{\tan\beta}\left(\frac{2({M_1}^2\sin^2\beta-1)}{(\gamma{M_1}^2+{M_1}^2(1-2\sin^2\beta)+2}\right) \tag{6.268}$$

Then using a trig identity on the denominator, leading to our final expression.

$$\tan\theta = \frac{2}{\tan\beta}\left(\frac{{M_1}^2\sin^2\beta-1}{{M_1}^2[\gamma+\cos(2\beta)]+2}\right) \tag{6.269}$$

We now have an explicit expression for θ in terms of β and M_1, although more typically what we want is β given M_1 and θ as inputs. In the latter case, this is still an implicit equation. Still the explicit form is convenient for creating graphs.

This oblique shock relationship is plotted in Fig. 6.15 for a few different incoming Mach numbers. Notice that for a given turning

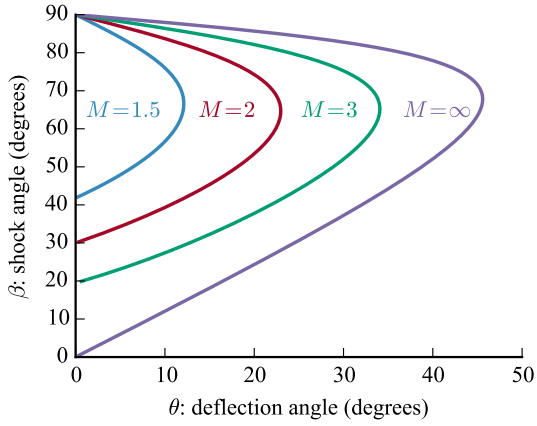

Fig. 6.15 Oblique shock relationship for different turning angles.

angle (θ) there are two solutions. These are called the *weak solution* and the *strong solution*. The weak solution typically occurs naturally. The strong solution may occur if downstream conditions require it—for example if we change the back pressure in an engine or wind tunnel. The limits of the weak and strong solution are Mach waves and normal shocks respectively, and occur at deflection angles of zero.

We also see that there is a maximum deflection angle, θ_{max} for a given Mach number. For the weak solution the downstream Mach number is supersonic, except for a small region of solutions near θ_{max}. For geometries that require a turning angle larger than this, an oblique shock will not occur, and instead a detached *bow shock* will form.

A bow shock is depicted in Fig. 6.16. As suggested by the numbered points, a bow shock passes through all points in the oblique shock relationships shown in Fig. 6.15. Point 1 corresponds to a normal shock. Point 2 is a strong oblique shock (with subsonic flow behind it). Point 3 is the dividing line between subsonic and supersonic downstream flow. Notice that this point occurs near to, but not at, θ_{max} Point 4 is a weak oblique shock. The shock angle is changing continuously through the bow shock, but asymptotes to that of a Mach wave (point 5). A blunt body will necessarily create a detached bow shock since a large turning angle is required.

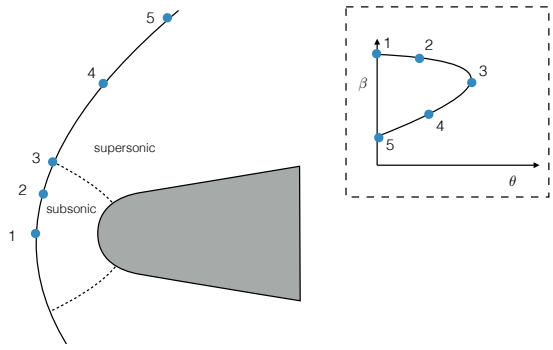

Fig. 6.16 A detatced bow shock wave.

6.7 Expansion Fans

An *expansion fan* also known as an expansion wave, or a Prandtl-Meyer expansion wave is essentially the opposite of an oblique shock. Through an expansion fan the Mach number increases, and pressure, density, and temperature all decrease. Whereas oblique shock waves occur on an inside corner, or more generally where the fluid turns in on itself, expansion fans occur on outside corners or where the fluid turns away from itself. Unlikely, a shock wave, an expansion fan occurs across a continuous region (the streamlines curve smoothly), and is isentropic. It is a continuous region consisting of an infinite number of Mach waves, each creating an infinitesimal isentropic change. The Mach waves starting at the incoming mach number:

$$\sin \mu_1 = \frac{1}{M_1} \tag{6.270}$$

and end at the exit Mach number:

$$\sin \mu_2 = \frac{1}{M_2} \tag{6.271}$$

This is depicted in Fig. 6.17.

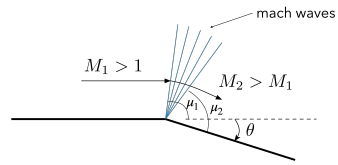

Fig. 6.17 An expansion fan.

15. Anderson, *Modern Compressible Flow: With Historical Perspective*, 2003.

The following derivation for analyzing an expansion fan is similar to that of Anderson.[15] Consider the flow through a Mach wave as exaggerated in Fig. 6.18. The turning angle is some infinitesimal amount $d\theta$ through which the velocity increases by some infinitesimal amount dV. We know that the change in velocity can only occur in a direction normal to the Mach wave (as it is the limit of an infinitely weak oblique shock wave). Thus, we can draw the velocity relationships as shown in Fig. 6.19. We can now relate the velocity vectors to the angles using the law of sines. The angles we can work out from the known information as shown in Fig. 6.20.

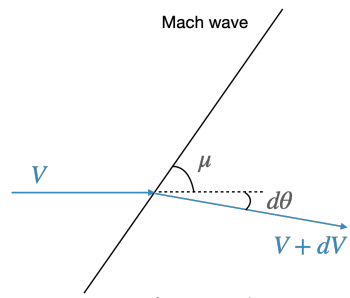

Fig. 6.18 Infinitesimal turning through a Mach wave.

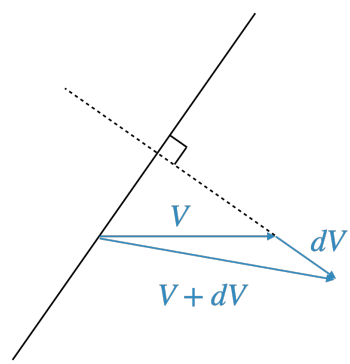

Fig. 6.19 The change in velocity occurs at a right angle to the Mach wave.

$$\frac{\sin\left(\frac{\pi}{2} + \mu\right)}{V + dV} = \frac{\sin\left(\frac{\pi}{2} - \mu - d\theta\right)}{V} \tag{6.272}$$

The trig expressions can be simplified as:

$$\frac{\cos\mu}{V+dV} = \frac{\cos(\mu+d\theta)}{V} \tag{6.273}$$

The right hand trig function we expand using the sum formula:

$$\frac{\cos\mu}{V+dV} = \frac{\cos\mu\cos d\theta - \sin\mu\sin d\theta}{V} \tag{6.274}$$

Since $d\theta$ is an infinitesimal amount, in the limit $\cos d\theta \to 1$ and $\sin d\theta \to d\theta$. The resulting equation is then:

$$\frac{\cos\mu}{V+dV} = \frac{\cos\mu - \sin\mu d\theta}{V} \tag{6.275}$$

We cross multiply:

$$\frac{\cos\mu}{\cos\mu - \sin(\mu)d\theta} = \frac{V+dV}{V} \tag{6.276}$$

Simplifying:

$$\frac{1}{1-\tan(\mu)d\theta} = 1 + \frac{dV}{V} \tag{6.277}$$

The left hand side we can expand using the series expansion:

$$\frac{1}{1-x} = 1 + x + x^2 + \ldots \text{ for } |x| < 1 \tag{6.278}$$

In our case, the x term is infinitesimally small so we can drop all higher order terms, which will be exact in the limit.

$$1 + \tan(\mu)d\theta = 1 + \frac{dV}{V} \tag{6.279}$$

We can cancel the ones, and since we know that $\sin\mu = 1/M$ (Eq. 6.2), we know that $\tan\mu = 1/\sqrt{M^2-1}$

$$\frac{1}{\sqrt{M^2-1}}d\theta = \frac{dV}{V} \tag{6.280}$$

Thus, we can relate the angle change to the velocity change as:

$$d\theta = \sqrt{M^2-1}\frac{dV}{V} \tag{6.281}$$

Now we wish to find the total angle change across a series of continuous Mach waves. In other words, we need to integrate both sides.

$$\int_{\theta_1}^{\theta_2} d\theta = \int_{M_1}^{M_2} \sqrt{M^2-1}\frac{dV}{V} \tag{6.282}$$

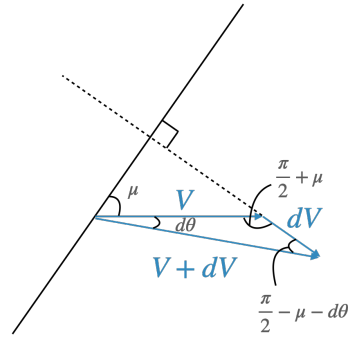

Fig. 6.20 Relevant angles to relate the velocity change and angle change.

The right integrand is in terms of V but we would like it to be in terms of the Mach number. We can expand derivatives of velocity in terms of Mach number ($V = Ma$):

$$dV = Mda + adM \tag{6.283}$$

Thus:

$$\frac{dV}{V} = M\frac{da}{V} + \frac{1}{M}dM \tag{6.284}$$

The speed of sound is given by (Eq. 6.89):

$$a = \sqrt{\gamma RT} \tag{6.285}$$

Rather than using the static fluid properties we could also express in terms of total conditions:

$$a_T = \sqrt{\gamma RT_T} \tag{6.286}$$

Dividing these two equations gives:

$$\frac{a_T}{a} = \sqrt{\frac{T_T}{T}} = \sqrt{1 + \frac{(\gamma - 1)}{2}M^2} \tag{6.287}$$

where the latter expression comes from the definition of total temperature (Eq. 6.95). We write this expression in terms of a:

$$a = a_T\left(1 + \frac{(\gamma - 1)}{2}M^2\right)^{-1/2} \tag{6.288}$$

Taking derivatives gives:

$$da = -a_T\frac{1}{2}\left(1 + \frac{(\gamma - 1)}{2}M^2\right)^{-3/2}\frac{(\gamma - 1)}{2}2MdM \tag{6.289}$$

$$= -a\frac{1}{2}\left(1 + \frac{(\gamma - 1)}{2}M^2\right)^{-1}(\gamma - 1)MdM \tag{6.290}$$

$$= -V\frac{\frac{(\gamma-1)}{2}}{1 + \frac{(\gamma-1)}{2}M^2}dM \tag{6.291}$$

Substituting this expression back into Eq. 6.284:

$$\frac{dV}{V} = \frac{\frac{-(\gamma-1)}{2}M}{1 + \frac{(\gamma-1)}{2}M^2}dM + \frac{1}{M}dM \tag{6.292}$$

$$= \frac{\frac{-(\gamma-1)}{2}M^2 + 1 + \frac{(\gamma-1)}{2}M^2}{M\left(1 + \frac{(\gamma-1)}{2}M^2\right)}dM \tag{6.293}$$

$$= \frac{1}{M\left(1 + \frac{(\gamma-1)}{2}M^2\right)}dM \tag{6.294}$$

We now have an expression in terms of Mach number that we can substitute into Eq. 6.282:

$$\Delta\theta = \int_{M_1}^{M_2} \frac{\sqrt{M^2-1}}{M\left(1+\frac{(\gamma-1)}{2}M^2\right)}dM \tag{6.295}$$

This expression can be analytically integrated, and as the result is somewhat long, we use the shorthand ν to represent the function.

$$\nu(M) = \sqrt{\frac{\gamma+1}{\gamma-1}}\tan^{-1}\sqrt{\frac{\gamma-1}{\gamma+1}(M^2-1)} - \tan^{-1}\sqrt{M^2-1} \tag{6.296}$$

Thus, the change in angle across the expansion fan is then computed as:

$$\Delta\theta = \nu(M_2) - \nu(M_1) \tag{6.297}$$

Propellers and Turbines

7

Both propellers and turbines use rotating blades but for different purposes. A propeller is designed to produce thrust and thus propel a vehicle, and in the process a torque is produced that opposes the blade motion and thus requires input power to maintain the rotation (top half of Fig. 7.1). A turbine is designed to produce a torque in the direction of blade motion and thus extract power from the moving fluid, and in the process a drag force is produced (bottom half of Fig. 7.1).

In Fig. 7.1 a streamtube passing through the rotor disk is also shown. A streamtube is a collection of streamlines. The propeller imparts momentum in the direction of the freestream and thus the streamtube area decreases (continuity equation). Conversely, the turbine extracts momentum leaving behind a wake of slower speeds and thus the streamtube area expands.

For conceptual design an effective method to analyze turbines and propellers is blade element momentum (BEM) theory. BEM theory is a combination of momentum balances and blade element (airfoil) analyses. The next two sections derive the theory from the perspective of a propeller and then from a perspective of a turbine. Both can be easily unified in a single derivation,[16] but when first learning the methods it is easier to comprehend when using the conventions of the application of interest. Reading only one of these sections is necessary. The two sections are written to stand alone, and because there is a lot of commonality between the two applications there is a lot of repeat material.

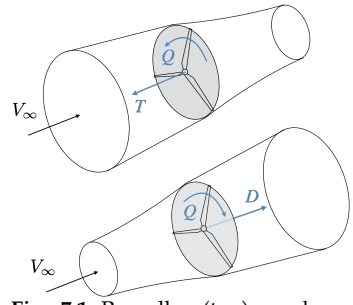

Fig. 7.1 Propeller (top) produces thrust and requires power (to overcome the resistive torque) to operate, whereas a turbine (bottom) produces torque and is accompanied by a resulting drag.

16. Ning, *Using Blade Element Momentum Methods with Gradient-Based Design Optimization*, 2021.

7.1 Blade Element Momentum Theory: Propellers

We will perform the derivation first from the perspective of a propeller and then from the perspective of a wind turbine. Note that we use the term propellers to generically refer to any turbomachine that adds momentum to the fluid.

7.1.1 Linear Momentum Balance

We will use a streamtube as our control volume, but rather than use one large streamtube across the entire rotor, we use an infinitesimally thin annulus streamtube at a given radial location of the rotor (Fig. 7.2). For convenience we define three stations as shown in the figure: upstream, at the rotor disk, and in the wake.

Figure 7.3 shows the control volume from a side view. First, we perform a mass balance. In the following derivation we neglect any variations in density. Compressibility, if necessary, is included in the blade element formulation.

$$\rho V_\infty A_\infty = \rho V_d A_d = \rho V_w A_w \tag{7.1}$$

Notice that as the velocity increases, the cross sectional area decreases.

Next, we apply an x-momentum balance across the entire control volume, where we take the positive direction for x as downwind:

$$\rho V_\infty(-V_\infty A_\infty) + \rho V_w(V_w A_w) = T \tag{7.2}$$

We make no assumption about the direction of the thrust, but rather let the equations determine the direction of thrust. The standard definition for thrust is the force opposite to V_∞. However, in the momentum balance we need to use the force the propeller exerts on the fluid, which is in the opposite direction, and is thus positive above. Combining these two expressions yields:

$$T = \rho A_d V_d(V_w - V_\infty) \tag{7.3}$$

It is not obvious that the pressure terms from the sides of the control volume cancel, but they do. We can come up with the same result more rigorously, with a cylindrical control volume that does not follow the streamlines, but the details are omitted here.

Let us now use a second control volume just across the disk. We will call the x location just upstream of the disk station 2, and just downstream will be called station 3. Performing a momentum balance yields (again neglecting any density changes across the disk):

$$\rho V_2(-V_2 A_2) + \rho V_3(V_3 A_3) = T + p_2 A_2 - p_3 A_3 \tag{7.4}$$

Because $A_2 = A_3 = A_d$ and the velocity must vary continuously through the disk ($V_2 = V_3$) the above expression simplifies to:

$$T = A_d(p_3 - p_2) \tag{7.5}$$

Combining the two expressions for thrust (Eqs. 7.3 and 7.5) yields:

$$\rho V_d(V_w - V_\infty) = (p_3 - p_2) \tag{7.6}$$

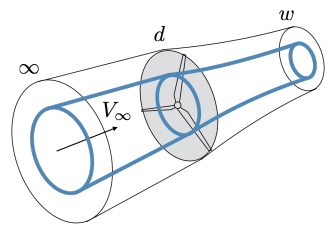

Fig. 7.2 The blue annulus streamtube is used as our control volume in the derivation of this section. The stations are denoted by ∞: far upstream, d: the rotor disk, and w in the far wake.

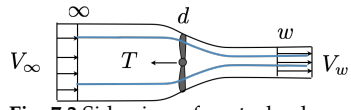

Fig. 7.3 Side view of control volume with resultant force T shown in typical thrust direction ($-x$ direction for our coordinate system).

To relate the pressure change from station 2 to 3, we use Bernoulli's equation (Eq. 6.77). We cannot apply Bernoulli's equation from station 2 to station 3 directly because work is done on the fluid between those stations. However, we can apply the equation upstream of the turbine and downstream of the turbine separately.

First, from station ∞ to station 2:

$$p_\infty + \frac{1}{2}\rho V_\infty^2 = p_2 + \frac{1}{2}\rho V_2^2 \tag{7.7}$$

then from station 3 to station w:

$$p_3 + \frac{1}{2}\rho V_3^2 = p_w + \frac{1}{2}\rho V_w^2 \tag{7.8}$$

If we subtract the two equations and simplify using $V_2 = V_3$, and assume our control volume is large enough so that $p_\infty = p_w$ we have

$$p_3 - p_2 = \frac{1}{2}\rho(V_w^2 - V_\infty^2) \tag{7.9}$$

This expression for the pressure drop is inserted into Eq. 7.6

$$\begin{aligned} \rho V_d(V_w - V_\infty) &= (p_3 - p_2) \\ \rho V_d(V_w - V_\infty) &= \frac{1}{2}\rho(V_w^2 - V_\infty^2) \\ V_d(V_w - V_\infty) &= \frac{1}{2}(V_w - V_\infty)(V_w + V_\infty) \\ V_d &= \frac{1}{2}(V_w + V_\infty) \end{aligned} \tag{7.10}$$

This yields the result that the velocity at the disk is half way between the upstream and downstream velocity. A similar relationship was derived for a lifting wing when we showed that the downwash at the wing is half of the downwash in the farfield.

With this relationship, we can generically relate the velocities at the 3 stations using the unknown induced velocity u (Fig. 7.4).

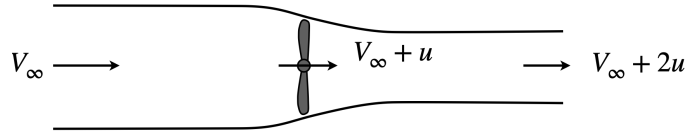

Fig. 7.4 Depiction of the induced velocity in at the rotor disk and in the farfield.

By convention one typically nondimensionalizes u as follows:

$$\begin{aligned} V_d &= V_\infty + u \\ &= V_\infty \left(1 + \frac{u}{V_\infty}\right) \\ &= V_\infty (1 + a) \end{aligned} \tag{7.11}$$

The quantity a is called the *axial induction factor*. Similarly, we can express the far-field velocity as:

$$V_w = V_\infty(1 + 2a) \tag{7.12}$$

With these definitions, we can express thrust in terms of the axial induction factor (using Eqs. 7.5, 7.6, 7.11, and 7.12):

$$\begin{aligned} T &= \rho A_d V_d (V_w - V_\infty) \\ &= \rho A_d V_\infty (1 + a)(V_\infty(1 + 2a) - V_\infty) \\ &= \rho A_d V_\infty^2 (1 + a)(2a) \end{aligned} \tag{7.13}$$

7.1.2 Extensions and Modifications to the Basic Methodology

The basic momentum theory ignores the hub and tip vortices that affect the induced velocity. Various correct methods exist; we use the simple analytical expression developed by Prandtl.[17]

17. Glauert, *Airplane Propellers*, 1935.

$$\begin{aligned} f_{tip} &= \frac{B}{2}\left(\frac{R - r}{r|\sin\phi|}\right) \\ F_{tip} &= \frac{2}{\pi}\arccos(\exp(-f_{tip})) \\ f_{hub} &= \frac{B}{2}\left(\frac{r - R_{hub}}{R_{hub}|\sin\phi|}\right) \\ F_{hub} &= \frac{2}{\pi}\arccos(\exp(-f_{hub})) \\ F &= F_{tip}F_{hub} \end{aligned} \tag{7.14}$$

The absolute value is necessary because our definition permits both positive and negative inflow angles. This hub/tip-loss factor (which is always between 0 and 1) is applied directly to the thrust.

$$T = 2a(1 + a)\rho A_d V_\infty^2 F \tag{7.15}$$

The tip loss function is visualized in Fig. 7.5

Another common modification is adjusting for high induction factors, but this is only applicable to turbines and is not discussed here.

We will use a disk area that is infinitesimally thin $A_d = 2\pi r$ so that we get a thrust per unit length. The final form for the thrust per unit length at a given radial section is then:

$$T' = 4a(1 + a)\rho V_\infty^2 \pi r F \tag{7.16}$$

If a is positive then the rotor is acting as a propeller, if negative it is acting as a turbine (and thus produces drag instead of thrust).

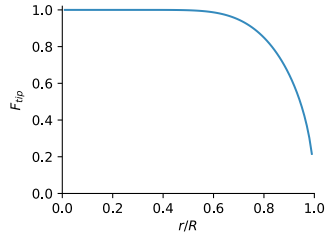

Fig. 7.5 Tip loss function, which goes to zero at the tip, to simulate a finite rotor.

7.1.3 Efficiency

For propellers, a quantity we often care about is the efficiency. So far we have been discussing the flow field from a frame fixed with the propeller (i.e., the left side of Fig. 7.6). In other words, in our frame of reference the propeller is not moving, freestream air is coming in at speed V_∞ and a wake is left behind at speed V_w. An understanding of efficiency is perhaps easier to see from a ground-fixed frame. To achieve that we simply vectorially subtract V_∞ from all the velocities (right side of Fig. 7.6). Now the propeller (i.e., with the aircraft) is moving with speed V_∞ into still air and leaving behind a wake with speed $V_w - V_\infty$.

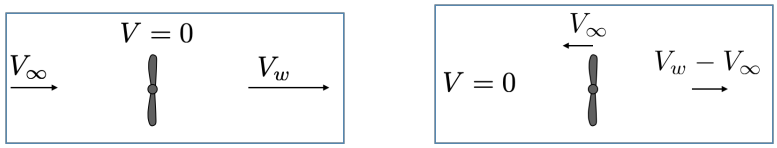

Fig. 7.6 Propeller shown in the frame of the propeller and in a ground-fixed frame.

The propulsive efficiency is given by the useful power out (TV_∞) divided by all the power put into the system (power out plus power left behind in the wake):

$$\eta = \frac{TV_\infty}{TV_\infty + \frac{1}{2}\dot{m}(V_w - V_\infty)^2} \tag{7.17}$$

If we plug in our expression for thrust (Eq. 7.16) and note that the mass flow rate is: $\dot{m} = \rho A_d V_d$ then this efficiency calculation can be simplified to:

$$\eta = \frac{2}{1 + \frac{V_w}{V_\infty}} \tag{7.18}$$

and our thrust in Eq. 7.13 can be written as:

$$T = \dot{m}(V_w - V_\infty) \tag{7.19}$$

What these equations tell us is that for maximum efficiency we would like $V_w = V_\infty$. In other words, we would like to leave no energy behind in the wake. However, that also means that the propeller produces zero thrust. Conversely, if we make V_w larger than we can increase our thrust, but at the expense of decreased efficiency. Another parameter we can change to increase thrust is to increase the mass flow rate $\dot{m}$, which generally means increasing the size of the propeller (A_d). Increasing propeller diameter allows us to increase propulsive thrust without sacrificing efficiency. Of course, increasing propeller diameter comes with its own tradeoffs specific to the application, but in general

leads to increased weight and noise. Additionally, increasing diameter may increase the tip Mach number, leading to shock waves, completely eliminating any efficiency gains.

7.1.4 Angular Momentum

Similar to the linear momentum case, where an induced velocity is produced in opposition to the force on the rotor, the rotation of the blades is accompanied by an induced swirl velocity in the opposite direction to that of the torque on the rotor. Unlike, the linear momentum case where the induced velocity change occurs across a large control volume, the rotational velocity change occurs only across the rotor disk. Conservation of momentum yields the same result as the linear case, where the induced velocity at the disk is halfway between its upstream and downstream values. In this case, upstream and downstream is just upstream and downstream of the rotor disk, instead of in the farfield. The induced rotational velocity is 0 upwind of the rotor, v in the plane of the rotor, and $2v$ downstream of the rotor (opposing the direction of the torque on the rotor). Just like before, we define a normalized version of this induced velocity, which we call the tangential induction factor: $a' = v/V_y$, where V_y is the tangential inflow velocity and in the absence of wind or other motion is just Ωr.

The angular momentum balance can be obtained by taking the position vector $\vec{r}$ crossed into the momentum equation. In this case we take r as the radial distance from the center of the turbine. We repeat the linear momentum equation from Eq. 1.99, except that we represent the pressure and shear terms generically as a sum of forces.

$$\frac{\partial}{\partial t}\int_{\forall} \rho \vec{V} d\forall + \int_A \rho \vec{V}\left(\vec{V}\cdot d\vec{A}\right) = \sum \vec{F} \tag{7.20}$$

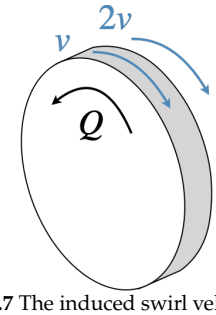

Fig. 7.7 The induced swirl velocity is in the direction opposite to that of the torque on the rotor.

Perform the cross product yields:

$$\frac{\partial}{\partial t}\int_{\forall} \rho(\vec{r}\times\vec{V}) d\forall + \int_A (\vec{r}\times\vec{V})\rho\left(\vec{V}\cdot d\vec{A}\right) = \sum \vec{r}\times\vec{F} \tag{7.21}$$

Although a rotating turbine is fundamentally unsteady, we are typically interested in time-averaged quantities (e.g., torque, thrust). Once time averaged, the time-dependent term goes to zero. Then, to express this equation more concisely we use the mass flow rate $\dot{m} = \rho\vec{V}\cdot d\vec{A}$, and recognize the right hand side as torque (Q):

$$\int_A \left(\vec{r}\times\vec{V}\right)\dot{m} = \sum \vec{Q} \tag{7.22}$$

We use a disk-shaped control volume that surrounds the rotor disk, and assume no axial component of velocity exists on the sides of the control volume. We are then interested in only the inflow and outflow velocity vectors into the control volume. Figure 7.8 uses an ground-centered inertial control volume, rather than a blade-centric control volume to show the velocity triangles. This is a somewhat unconventional frame of reference and orientation for a turbine/propeller, but is commonly used in turbomachinery analysis, and is convenient for this particular analysis. The figure illustrates the inflow and outflow on either side of the control volume, and notes the direction of blade rotation For a propeller the direction of torque opposes the rotation direction and so the induced velocity is in the direction of rotation as shown in the figure (opposite of the torque).

We define a positive torque as is conventional for propellers, which is that a positive torque opposes the direction of motion (i.e., torque is about our $-x$ axis and is thus negative in our chosen axes.) This means that the propeller must input power to overcome this resistive torque. Although that is a negative torque for our coordinate system, the momentum equations need the torque the rotor exerts on the fluid (not the torque the fluid exerts on rotor), and so we flip the sign again:

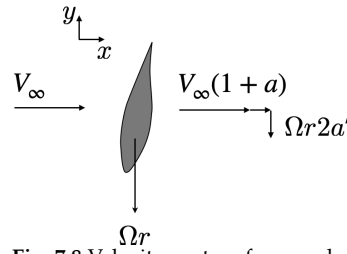

Fig. 7.8 Velocity vectors for angular momentum balance.

$$\begin{aligned} r\Omega r 2a'\dot{m} &= Q \\ \Omega r^2 2a'\dot{m} &= Q \end{aligned} \tag{7.23}$$

Using the results from the previous section:

$$\dot{m} = \rho V_d A_d = \rho V_\infty (1+a) A_d \tag{7.24}$$

adding the hub/tip loss factor, and using our infinitesimal annual ring area results in:

$$Q' = 4a'(1+a)\rho V_\infty \Omega r^2 \pi r F \tag{7.25}$$

For a turbine the sign of a' would reverse and consequently the sign for the torque and power would automatically switch as well.

7.1.5 Blade Element Theory

We have considered the momentum part of the theory, and now consider the blade element portion. Blade element is just another name for 2D airfoil theory. Consider the airfoil from a section of the blade shown in Fig. 7.9. The inflow plus induced velocities from the previous sections are shown resulting in the total inflow velocity vector W. The angle θ, from the plane of rotation to the airfoil chord line, is called the twist angle. The angle ϕ, from the plane of rotation to the inflow velocity

vector, is called in the inflow angle. The angle between the velocity vector and the chord line is the angle of attack:

$$\alpha = \theta - \phi \tag{7.26}$$

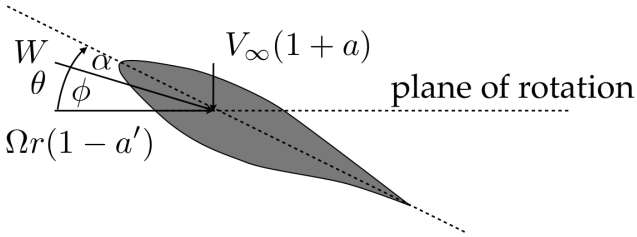

Fig. 7.9 Definition for positive twist and coordinate system for the blade element theory.

With a known angle of attack we can compute the sectional lift and drag coefficient from 2D airfoil data. The lift and drag coefficients may in general also be functions of the Reynolds number and Mach number.

$$\begin{aligned} c_l &= f_L(\alpha, Re, M) \\ c_d &= f_D(\alpha, Re, M) \end{aligned} \tag{7.27}$$

These lift and drag coefficients are generally computed from a spline so that the results vary smoothly. Because we do not know the induction factors yet we usually approximate the Reynolds number (and Mach number) using:

$$\begin{aligned} W_0 &= \sqrt{V_\infty^2 + (\Omega r)^2} \\ Re &= \frac{\rho W_0 c}{\mu} \end{aligned} \tag{7.28}$$

The impact of this approximation is usually negligible as Reynolds number changes occur across orders of magnitude. Instead of using Mach number as one of the inputs in the spline, we could just correct the lift coefficient with a Prandtl-Glauert rule:

$$c_l = \frac{c_{l0}}{\sqrt{1 - M^2}} \tag{7.29}$$

Using the Kutta-Joukowski theorem, the directions for the lift and drag coefficients, c_l and c_d are as shown in Fig. 7.10.

We need to resolve these forces into the normal and tangential directions as shown in the figure. These directions are consistent with the way we have defined thrust and torque in the momentum equations.

$$\begin{aligned} c_n &= c_l \cos\phi - c_d \sin\phi \\ c_t &= c_l \sin\phi + c_d \cos\phi \end{aligned} \tag{7.30}$$

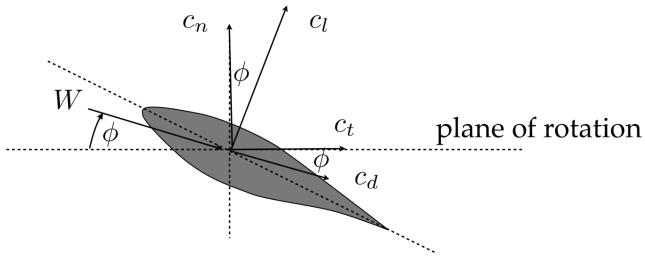

Fig. 7.10 Directions for the lift and drag forces from the Kutta Joukowski theorem.

To compute the total thrust and torque for this blade section we then multiply by the local dynamic pressure (not freestream, including induction) and the chord. This gives us the forces/moments per unit length for one blade, and so to get the forces for the entire rotor we need to multiply by the number of blades B:

$$\begin{aligned} T' &= BN' \\ T' &= Bc_n \frac{1}{2}\rho W^2 c \end{aligned} \tag{7.31}$$

$$\begin{aligned} Q' &= BrT' \\ Q' &= Brc_t \frac{1}{2}\rho W^2 c \end{aligned} \tag{7.32}$$

where

$$W = \sqrt{[V_\infty(1+a)]^2 + [\Omega r(1-a')]^2} \tag{7.33}$$

The above formulation is equally applicable to turbines, except that the positive direction of camber is usually flipped for turbine operation (imagine flipping the airfoil upside down). Regardless of the camber direction, any blade can operate as both a turbine or propeller with appropriate twist, but if we want an efficient turbine we would flip the camber. This is equivalent to modifying the airfoil functions as:

$$\begin{aligned} f_L &= -c_l(-\alpha, Re, M) \\ f_D &= c_d(-\alpha, Re, M) \end{aligned} \tag{7.34}$$

7.1.6 Blade Element Momentum

We can now combine the results from momentum theory and blade element theory. We first equate the linear momentum equations (thrust), and next the angular momentum equations (torque). Finally, we discuss the residual equation which determines whether or not we have consistency between the momentum and blade element theories.

We equate the thrust from momentum theory and blade element theory. Before doing so we define the nondimensional parameter:

$$\sigma' = \frac{Bc}{2\pi r} \tag{7.35}$$

which is called the local solidity. It is a measure of how much area the blades occupy relative to the disk area for a given radial station (hence local solidity and not total solidity). We now equate the two thrust equations:

$$\begin{aligned} 4a(1+a)\rho V_\infty^2 \pi r F &= B c_n \frac{1}{2}\rho W^2 c \\ 4a(1+a)F &= \sigma' c_n \left(\frac{W}{V_\infty}\right)^2 \end{aligned} \tag{7.36}$$

To simplify further we need to relate the inflow velocity to the induction factors. By referring to Fig. 7.11 we can come up with the following expressions:

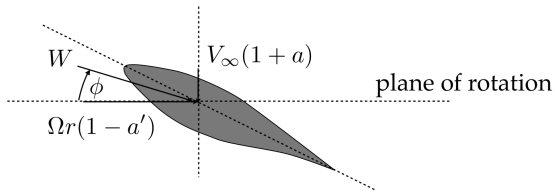

Fig. 7.11 Inflow angle and inflow velocities.

$$\sin\phi = \frac{V_\infty(1+a)}{W} \tag{7.37}$$

or

$$\cos\phi = \frac{\Omega r(1-a')}{W} \tag{7.38}$$

These can be rearranged as:

$$\frac{W}{V_\infty} = \frac{1+a}{\sin\phi} \tag{7.39}$$

or

$$\frac{W}{\Omega r} = \frac{1-a'}{\cos\phi} \tag{7.40}$$

We will use the first substitution for this thrust equation:

$$\begin{aligned} 4a(1+a)F &= \sigma' c_n \left(\frac{W}{V_\infty}\right)^2 \\ 4a(1+a)F &= \sigma' c_n \frac{(1+a)^2}{\sin^2\phi} \\ 4aF &= \sigma' c_n \frac{(1+a)}{\sin^2\phi} \end{aligned} \tag{7.41}$$

This equation can now be solved for a. After some algebraic manipulation the result is:

$$a = \frac{1}{\frac{4F\sin^2\phi}{\sigma' c_n} - 1} \tag{7.42}$$

We repeat a similar process for the torques. Equating the torques from momentum and blade element theories results in:

$$\begin{aligned} 4a'(1+a)\rho V_\infty \Omega r^2 \pi r F &= Brc_t \frac{1}{2}\rho W^2 c \\ 4a'(1+a)F &= \sigma' c_t \frac{W}{V_\infty}\frac{W}{\Omega r} \end{aligned} \tag{7.43}$$

We now substitute the relationships for W. This time we use one of each of the two equations:

$$\begin{aligned} 4a'(1+a)F &= \sigma' c_t \frac{(1+a)}{\sin\phi}\frac{(1-a')}{\cos\phi} \\ 4a'F &= \sigma' c_t \frac{1}{\sin\phi}\frac{(1-a')}{\cos\phi} \end{aligned} \tag{7.44}$$

We can now solve this for a':

$$a' = \frac{1}{\frac{4F\sin\phi\cos\phi}{\sigma' c_t} + 1} \tag{7.45}$$

The above equations allow us to compute the induction factors. However, we have to be careful as these calculations depend on ϕ and the angle of attack, which in turn depend on the induction factors (Fig. 7.9). Thus, we have a circular dependency and need to use an iterative method, or a root solver. Traditionally, this is done by considering a and a' as the unknowns and using the two equations above to form two residuals. However, we can greatly simplify the solution of these equations by considering ϕ and W as the unknowns [16,18]. The inflow velocity has no direct dependence in the BEM equations (other than in Reynolds number, which operates on a log scale and so the impact is negligible). This means that we can reduce the residuals to one equation, which is advantageous because one dimensional root finding problems can be solved with guaranteed convergence. The solution of the residual ensures compatibility between the blade element and momentum theories. From Fig. 7.11 we can write:

16. Ning, *Using Blade Element Momentum Methods with Gradient-Based Design Optimization*, 2021.

18. Ning, *A Simple Solution Method for the Blade Element Momentum Equations with Guaranteed Convergence*, 2014.

$$\tan\phi = \frac{V_\infty(1+a)}{\Omega r(1-a')} \tag{7.46}$$

This equation could be rearranged in many ways to form a residual equation, but as demonstrated in the above cited papers a numerically advantageous form is:

$$\mathcal{R}(\phi) = \frac{\sin\phi}{1+a} - \frac{V_\infty}{\Omega r}\frac{\cos\phi}{(1-a')} = 0 \tag{7.47}$$

In summary we define a residual function as follows:

$$\text{function } \mathcal{R}(\phi) \tag{7.48}$$

$$\alpha = \theta - \phi \tag{7.49}$$

$$c_l = f(\alpha, Re, M) \tag{7.50}$$

$$c_d = f(\alpha, Re, M) \tag{7.51}$$

$$c_n = c_l \cos\phi - c_d \sin\phi \tag{7.52}$$

$$c_t = c_l \sin\phi + c_d \cos\phi \tag{7.53}$$

$$a = \frac{\sigma' c_n}{4F \sin^2\phi - \sigma' c_n} \tag{7.54}$$

$$a' = \frac{\sigma' c_t}{4F \sin\phi \cos\phi + \sigma' c_t} \tag{7.55}$$

$$\text{return } \frac{\sin\phi}{1+a} - \frac{V_\infty}{\Omega r}\frac{\cos\phi}{(1-a')} \tag{7.56}$$

Generally, the solution will be in the bracket: $\phi = (0, \pi/2]$ (note the open bracket at zero). Thus, a method like Brent's method can be used to yield fast and robust convergence. If airfoil data has not been extended to such high angles, a smaller range may suffice.

This procedure yields a solution at one radial station of the blade (Fig. 7.12). Once we solve a section on the blade for the correct inflow angle ϕ^* we can recalculate the resulting loads and induction factors for that section:

$$c_n, c_t, a, a' = f(\phi^*) \tag{7.57}$$

We then compute the inflow velocity:

$$W^2 = (V_\infty(1+a))^2 + (\Omega r(1-a'))^2 \tag{7.58}$$

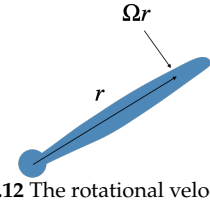

Fig. 7.12 The rotational velocity at a given radial station on the blade.

and the thrust and torque per unit length:

$$T' = Bc_n \frac{1}{2}\rho W^2 c \tag{7.59}$$

$$Q' = Brc_t \frac{1}{2}\rho W^2 c \tag{7.60}$$

We then need to repeat these procedure at multiple radial stations given by our chosen blade discretization. We then integrate across the blade to get total thrust and torque:

$$T = \int_{r_h}^{r_t} T' dr \tag{7.61}$$

$$Q = \int_{r_h}^{r_t} Q' dr \tag{7.62}$$

where r_h and r_t correspond to the hub and tip radius respectively. Right at the hub/tip the loads go to zero and so we need not compute at those points (indeed we cannot compute right at those points). Finally, from the torque we can compute the required power.

$$P = Q\Omega \tag{7.63}$$

While not necessary, it is often convenient to normalize using typical propeller conventions. The thrust, torque, and power coefficients are given by:

$$C_T = \frac{T}{\rho n^2 D^4} \tag{7.64}$$

$$C_Q = \frac{Q}{\rho n^2 D^5} \tag{7.65}$$

$$C_P = \frac{P}{\rho n^3 D^5} \tag{7.66}$$

where n is the number of revolutions per second:

$$n = \frac{\Omega}{2\pi} \tag{7.67}$$

and D is the diameter. The efficiency is given by:

$$\eta = \frac{P_{out}}{P_{in}} = \frac{TV_\infty}{Q\Omega} = \frac{C_T \rho n^2 D^4 V_\infty}{C_P \rho n^3 D^5} = J\frac{C_T}{C_P} \tag{7.68}$$

All of these outputs are functions of the advance ratio (another nondimensional parameter, recall discussion in Ex. 1.2):

$$J = \frac{V_\infty}{nD} \tag{7.69}$$

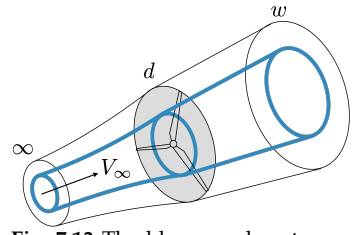

Fig. 7.13 The blue annulus streamtube is used as our control volume in the derivation of this section. The stations are denoted by ∞: far upstream, d: the rotor disk, and w in the far wake.

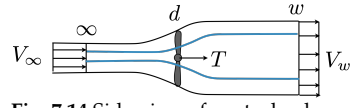

Fig. 7.14 Side view of control volume with resultant force T. Note that this is a drag force but is called thrust in the wind turbine community.

*Perhaps because it can be considered as a thrust force acting on the wind turbine tower, and that is generally the primary reason why this force is of interest in wind turbine applciations.

7.2 Blade Element Momentum Theory: Turbines

We now repeat the above derivations, but from the perspective of a turbine. This section will be briefer as we can reuse most of the same concepts, although there are a few unique considerations.

7.2.1 Linear Momentum Balance

We again use infinitesimally thin annulus streamtubes at each radial station along the rotor (Fig. 7.13), and adopt the same three stations: upstream, at the rotor disk, and in the wake.

Figure 7.14 shows the control volume from a side view. Note that the net force on the blade is actually a drag force, but in the wind

energy community it is referred to as a thrust* and so we will adopt that convention here. First, we perform a mass balance.

$$\rho V_\infty A_\infty = \rho V_d A_d = \rho V_w A_w \tag{7.70}$$

Notice that as the fluid slows down, the cross-sectional area increases.

Next, we apply an x-momentum balance across the entire control volume, where we take the positive direction for x as downwind:

$$\rho V_\infty(-V_\infty A_\infty) + \rho V_w(V_w A_w) = -T \tag{7.71}$$

The standard definition for thrust for a wind turbine is positive in the direction of V_∞. However, in the momentum balance we need to use the force the turbine exerts on the fluid, which is in the opposite direction, and is thus negative above. Combining these two expressions yields:

$$T = \rho A_d V_d(V_\infty - V_w) \tag{7.72}$$

It is not obvious that the pressure terms from the sides of the control volume cancel, but they do. We can come up with the same result more rigorously, with a cylindrical control volume that does not follow the streamlines, but the details are omitted here.

Let us now use a second control volume just across the disk. We will call the x location just upstream of the disk station 2, and just downstream will be called station 3. Performing a momentum balance yields :

$$\rho V_2(-V_2 A_2) + \rho V_3(V_3 A_3) = -T + p_2 A_2 - p_3 A_3 \tag{7.73}$$

Because $A_2 = A_3 = A_d$ and the velocity must vary continuously through the disk ($V_2 = V_3$) the above expression simplifies to:

$$T = A_d(p_2 - p_3) \tag{7.74}$$

Combining the two expressions for thrust (Eqs. 7.72 and 7.74) yields:

$$\rho V_d(V_\infty - V_w) = (p_2 - p_3) \tag{7.75}$$

To relate the pressure change from station 2 to 3, we use Bernoulli's equation (Eq. 6.77). We cannot apply Bernoulli's equation from station 2 to station 3 directly because work is done on the fluid between those stations. However, we can apply the equation upstream of the turbine and downstream of the turbine separately.

First, from station ∞ to station 2:

$$p_\infty + \frac{1}{2}\rho V_\infty^2 = p_2 + \frac{1}{2}\rho V_2^2 \tag{7.76}$$

then from station 3 to station w:

$$p_3 + \frac{1}{2}\rho V_3^2 = p_w + \frac{1}{2}\rho V_w^2 \tag{7.77}$$

If we subtract the two equations and simplify using $V_2 = V_3$, and assume our control volume is large enough so that $p_\infty = p_w$ we have

$$p_2 - p_3 = \frac{1}{2}\rho(V_\infty^2 - V_w^2) \tag{7.78}$$

This expression for the pressure drop is inserted into Eq. 7.75

$$\begin{aligned} \rho V_d(V_\infty - V_w) &= (p_2 - p_3) \\ \rho V_d(V_\infty - V_w) &= \frac{1}{2}\rho(V_\infty^2 - V_w^2) \\ V_d(V_\infty - V_w) &= \frac{1}{2}(V_\infty - V_w)(V_\infty + V_w) \\ V_d &= \frac{1}{2}(V_\infty + V_w) \end{aligned} \tag{7.79}$$

This yields the result that the velocity at the disk is half way between the upstream and downstream velocity. A similar relationship was derived for a lifting wing when we showed that the downwash at the wing is half of the downwash in the farfield.

With this relationship, we can generically relate the velocities at the 3 stations using the unknown induced velocity u (Fig. 7.15).

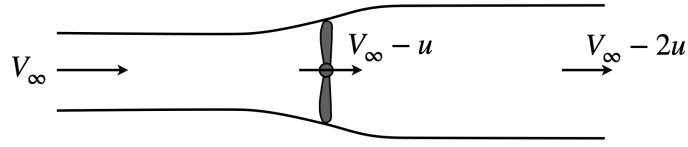

Fig. 7.15 Depiction of the induced velocity in at the rotor disk and in the farfield.

By convention one typically nondimensionalizes u as follows:

$$\begin{aligned} V_d &= V_\infty - u \\ &= V_\infty \left(1 - \frac{u}{V_\infty}\right) \\ &= V_\infty (1 - a) \end{aligned} \tag{7.80}$$

The quantity a is called the *axial induction factor*. Similarly, we can express the far-field velocity as:

$$V_w = V_\infty(1 - 2a) \tag{7.81}$$

With these definitions, we can express thrust in terms of the axial induction factor (using Eqs. 7.74, 7.75, 7.80, and 7.81):

$$\begin{aligned} T &= \rho A_d V_d (V_\infty - V_w) \\ &= \rho A_d V_\infty (1-a)(V_\infty - V_\infty(1-2a)) \\ &= \rho A_d V_\infty^2 (1-a)(2a) \end{aligned} \tag{7.82}$$

We then nondimensionalize this expression to form the thrust coefficient using turbine conventions. We use V_∞ as the reference velocity in the dynamic pressure, and the local annulus area as the reference area.

$$\begin{aligned} C_T &= \frac{T}{\frac{1}{2}\rho V_\infty^2 A_d} \\ &= 4a(1-a) \end{aligned} \tag{7.83}$$

One way to express the power is:

$$P = T V_d \tag{7.84}$$

Using Eqs. 7.80 and 7.82 we have:

$$P = \rho A_d V_\infty^3 (1-a)^2 2a \tag{7.85}$$

We normalize to compute the power coefficient:

$$\begin{aligned} C_P &= \frac{P}{\frac{1}{2}\rho V_\infty^3 A_d} \\ &= 4a(1-a)^2 \end{aligned} \tag{7.86}$$

To find the optimal induction for maximizing power we take derivatives of this expression with respect to a:

$$\begin{aligned} \frac{dC_P}{da} = 4a(2)(1-a)(-1) + 4(1-a)^2 &= 0 \\ -2a + (1-a) &= 0 \\ a^* &= 1/3 \end{aligned} \tag{7.87}$$

Thus, to maximize power, with no constraints, the optimal induction factor at each section is 1/3.[†] The corresponding maximum power coefficient is:

$$C_P(a = 1/3) = \frac{16}{27} \approx 0.59 \tag{7.88}$$

This is the maximum theoretical power coefficient for a turbine, and is known as the *Betz limit*.

[†] In practice there are many constraints, like thrust constraints, structural constraints, etc., and so the optimal induction is typically less than this value.

7.2.2 Extensions and Modifications to the Basic Methodology

The basic momentum theory ignores the hub and tip vortices that affect the induced velocity. Various correct methods exist; we use the simple analytical expression developed by Prandtl.[17]

17. Glauert, *Airplane Propellers*, 1935.

$$
\begin{aligned}
f_{tip} &= \frac{B}{2}\left(\frac{R-r}{r|\sin\phi|}\right) \\
F_{tip} &= \frac{2}{\pi}\arccos(\exp(-f_{tip})) \\
f_{hub} &= \frac{B}{2}\left(\frac{r-R_{hub}}{R_{hub}|\sin\phi|}\right) \\
F_{hub} &= \frac{2}{\pi}\arccos(\exp(-f_{hub})) \\
F &= F_{tip}F_{hub}
\end{aligned}
\tag{7.89}
$$

The absolute value is necessary because our definition permits both positive and negative inflow angles. This hub/tip-loss factor (which is always between 0 and 1) is applied directly to the thrust.

$$
C_T = 4a(1-a)F \tag{7.90}
$$

The tip loss function is visualized in Fig. 7.16

One unique consideration for turbines is dealing with high induction factors. The velocity in the wake from the momentum balance is shown in Eq. 7.81. If a increases above 0.5, then the equation predicts wake velocities that reverse direction. This reversal is non-physical, as the real flow entrains momentum in the wake through turbulence. Empirical data is needed to determine the behavior as a approaches 0.5 and beyond. Notional behavior of the thrust coefficient with large induction factors is seen in Fig. 7.17.

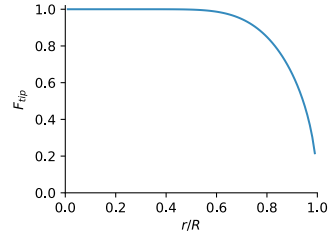

Fig. 7.16 Tip loss function, which goes to zero at the tip, to simulate a finite rotor.

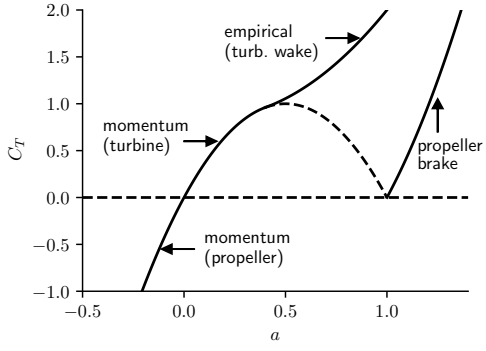

Fig. 7.17 Thrust coefficient as a function of axial induction factor

Various extension methods exist for the turbulent wake region. A common simple method is the quadratic fit from Glauert.[19] However, the Glauert correction does not maintain continuity when the tip/hub loss corrections are included. Buhl provided a small modification of Glauert's method to provide that continuity.[20] However, that modification leads to nonzero thrust loads when the tip correction is zero, which can be problematic for some optimization parameterizations. So we use a small modification of that approach.‡

$$C_T = \left(\frac{14}{9}a^2 - \frac{4}{9}a + \frac{8}{9}\right)F \quad \text{for } 0.4 \le a \le 1 \tag{7.91}$$

Additional considerations are needed for induction factors larger than 1, the propeller brake region. The current expression Eq. 7.83 predicts a change in sign in the thrust force for induction factors greater than 1. However, repeating the momentum balance shows that the force still acts as a drag device (i.e., thrust in the wind turbine convention).

$$C_T = -4a(1+a)F \quad \text{for } a \ge 1 \tag{7.92}$$

For this case the rotor behaves like a propeller (requiring power input) but with a large negative pitch so that the thrust is reversed allowing the rotor to act like an aerodynamic brake.

7.2.3 Angular Momentum

Similar to the linear momentum case, where an induced velocity is produced in opposition to the force on the rotor, the rotation of the blades is accompanied by an induced swirl velocity in the opposite direction to that of the torque on the rotor. Unlike, the linear momentum case where the induced velocity change occurs across a large control volume, the rotational velocity change occurs only across the rotor disk. Conservation of momentum yields the same result as the linear case, where the induced velocity at the disk is halfway between its upstream and downstream values. In this case, upstream and downstream is just upstream and downstream of the rotor disk, instead of in the farfield. The induced rotational velocity is 0 upwind of the rotor, v in the plane of the rotor, and $2v$ downstream of the rotor (opposing the direction of the torque on the rotor). Just like before, we define a normalized version of this induced velocity, which we call the tangential induction factor: $a' = v/V_y$, where V_y is the tangential inflow velocity and in the absence of wind or other motion is just Ωr.

The angular momentum balance can be obtained by taking the position vector $\vec{r}$ crossed into the momentum equation. In this case we

19. Glauert and Committee, *A General Theory of the Autogyro*, 1926.

20. Buhl Jr., *A New Empirical Relationship between Thrust Coefficient and Induction Factor for the Turbulent Windmill State*, 2005.

‡Pointed out in a personal communication from Kenneth Lønbæk.

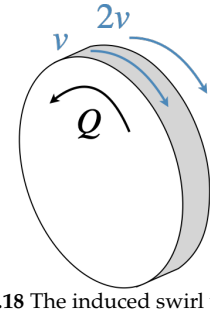

Fig. 7.18 The induced swirl velocity is in the direction opposite to that of the torque on the rotor.

take r as the radial distance from the center of the turbine. We repeat the linear momentum equation from Eq. 1.99, except that we represent the pressure and shear terms generically as a sum of forces.

$$\frac{\partial}{\partial t}\int_{\forall} \rho \vec{V} d\forall + \int_A \rho \vec{V}\left(\vec{V}\cdot d\vec{A}\right) = \sum \vec{F} \tag{7.93}$$

Perform the cross product yields:

$$\frac{\partial}{\partial t}\int_{\forall} \rho(\vec{r}\times\vec{V}) d\forall + \int_A (\vec{r}\times\vec{V})\rho\left(\vec{V}\cdot d\vec{A}\right) = \sum \vec{r}\times\vec{F} \tag{7.94}$$

Although a rotating turbine is fundamentally unsteady, we are typically interested in time-averaged quantities (e.g., torque, thrust). Once time averaged, the time-dependent term goes to zero. Then, to express this equation more concisely we use the mass flow rate $\dot{m} = \rho\vec{V}\cdot d\vec{A}$, and recognize the right hand side as torque (Q):

$$\int_A \left(\vec{r}\times\vec{V}\right)\dot{m} = \sum \vec{Q} \tag{7.95}$$

We use a disk-shaped control volume that surrounds the rotor disk, and assume no axial component of velocity exists on the sides of the control volume. We are then interested in only the inflow and outflow velocity vectors into the control volume. Figure 7.19 uses an ground-centered inertial control volume, rather than a blade-centric control volume to show the velocity triangles. This is a somewhat unconventional frame of reference and orientation for a turbine/propeller, but is commonly used in turbomachinery analysis, and is convenient for this particular analysis. The figure illustrates the inflow and outflow on either side of the control volume, and notes the direction of blade rotation. For a turbine the direction of torque is in the same direction as the rotation direction and so the induced velocity opposes the rotational direction as shown in the figure.

We define a positive torque as is conventional for turbines, which is that a positive torque is in the direction of motion (i.e., torque is about our $+x$ axis). The momentum equations need the torque the rotor exerts on the fluid (not the torque the fluid exerts on rotor), and so we flip the sign:

$$\begin{aligned} -r\Omega r 2a'\dot{m} &= -Q \\ \Omega r^2 2a'\dot{m} &= Q \end{aligned} \tag{7.96}$$

Using the results from the previous section:

$$\dot{m} = \rho V_d A_d = \rho V_\infty (1-a) A_d \tag{7.97}$$

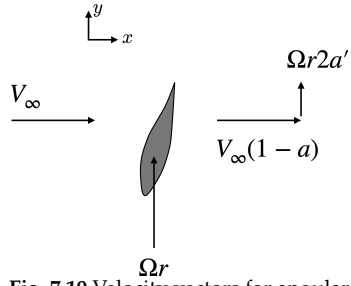

Fig. 7.19 Velocity vectors for angular momentum balance.

and adding the hub/tip loss factor results in:

$$Q' = \Omega r^2 2a' \rho V_\infty (1-a) A_d F \tag{7.98}$$

We normalize the torque in a similar way to thrust (but with an extra term for the radius):

$$\begin{aligned} C_Q &= \frac{Q'}{\frac{1}{2}\rho V_\infty^2 A_d r} \\ &= 4a'(1-a)\lambda_r F \end{aligned} \tag{7.99}$$

where

$$\lambda_r = \frac{\Omega r}{V_\infty} \tag{7.100}$$

is called the *local tip-speed ratio*.

7.2.4 Blade Element Theory

We have considered the momentum part of the theory, and now consider the blade element portion. Blade element is just another name for 2D airfoil theory. Consider the airfoil from a section of the blade shown in Fig. 7.20. The inflow plus induced velocities from the previous sections are shown resulting in the total inflow velocity vector W. The angle θ, from the plane of rotation to the airfoil chord line, is called the twist angle. The angle ϕ, from the plane of rotation to the inflow velocity vector, is called in the inflow angle. The angle between the velocity vector and the chord line is the angle of attack:

$$\alpha = \phi - \theta \tag{7.101}$$

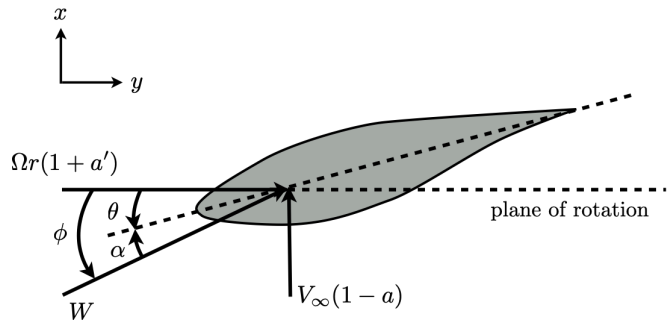

Fig. 7.20 Definition for positive twist and coordinate system for the blade element theory.

With a known angle of attack we can compute the sectional lift and drag coefficient from 2D airfoil data. The lift and drag coefficients may in general also be functions of the Reynolds number (for wind

turbines Mach numbers are generally low enough to be considered incompressible).

$$\begin{aligned} c_l &= f_L(\alpha, Re) \\ c_d &= f_D(\alpha, Re) \end{aligned} \tag{7.102}$$

These lift and drag coefficients are generally computed from a spline so that the results vary smoothly. Because we do not know the induction factors yet we usually approximate the Reynolds number using:

$$\begin{aligned} W_0 &= \sqrt{V_\infty^2 + (\Omega r)^2} \\ Re &= \frac{\rho W_0 c}{\mu} \end{aligned} \tag{7.103}$$

The impact of this approximation is usually negligible as Reynolds number changes occur across orders of magnitude.

Using the Kutta-Joukowski theorem, the directions for the lift and drag coefficients, c_l and c_d are as shown in Fig. 7.21.

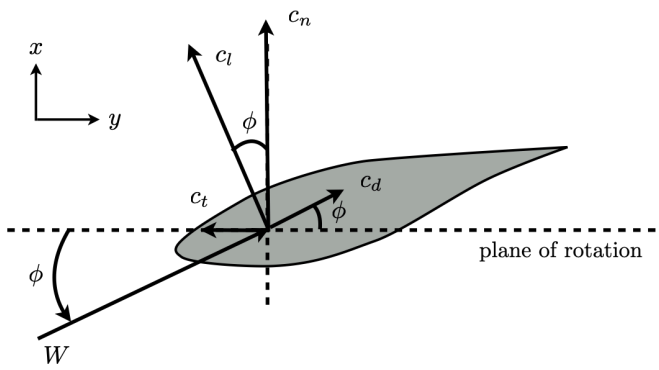

Fig. 7.21 Directions for the lift and drag forces from the Kutta Joukowski theorem.

We need to resolve these forces into the normal and tangential directions as shown in the figure. These directions are consistent with the way we have defined thrust and torque in the momentum equations.

$$\begin{aligned} c_n &= c_l \cos\phi + c_d \sin\phi \\ c_t &= c_l \sin\phi - c_d \cos\phi \end{aligned} \tag{7.104}$$

To compute the total thrust and torque for this blade section we then multiply by the local dynamic pressure (not freestream, including induction) and the chord. This gives us the forces/moments per unit length for one blade, and so to get the forces for the entire rotor we need to multiply by the number of blades B:

$$\begin{aligned} T' &= BN' \\ T' &= Bc_n \frac{1}{2}\rho W^2 c \end{aligned} \tag{7.105}$$

$$\begin{aligned} Q' &= BrT' \\ Q' &= Brc_t \frac{1}{2}\rho W^2 c \end{aligned} \tag{7.106}$$

where

$$W = \sqrt{[V_\infty(1-a)]^2 + [\Omega r(1+a')]^2} \tag{7.107}$$

If we use the same normalizations from the previous section we obtain:

$$C_T = c_n \sigma' \left(\frac{W}{V_\infty}\right)^2 \tag{7.108}$$

where

$$\sigma' = \frac{Bc}{2\pi r} \tag{7.109}$$

is called the *local solidity* and is a ratio of the area of the blades relative to the disk area, at a given radius.[§] Using Fig. 7.20 we can relate the velocities as:

[§]Total solidity, or sometimes just solidity, is the ratio of the total blade area relative to total disk area.

$$\sin\phi = \frac{V_\infty(1-a)}{W} \tag{7.110}$$

Thus, the local thrust coefficient from blade element theory is:

$$C_T = c_n \sigma' \left(\frac{(1-a)}{\sin\phi}\right)^2 \tag{7.111}$$

We repeat the same process for the torque coefficient. The velocities can be related using Eq. 7.110 or with

$$\cos\phi = \frac{\Omega r(1+a')}{W} \tag{7.112}$$

For the torque coefficient is will be convenient to use one of each substitution in place of W.

$$\begin{aligned} C_Q &= c_t \sigma' \left(\frac{W}{V_\infty}\right)^2 \\ &= c_t \sigma' \lambda_r \left(\frac{(1-a)(1+a')}{\sin\phi\cos\phi}\right) \end{aligned} \tag{7.113}$$

7.2.5 Blade Element Momentum

We can now combine the results from momentum theory and blade element theory. We first equate the linear momentum equations (thrust), and next the angular momentum equations (torque). Finally, we discuss the residual equation which determines whether or not we have consistency between the momentum and blade element theories.

We equate the thrust from momentum theory and blade element theory. In the wind turbine case, the thrust coefficient from momentum theory had three expressions. For $a < 0.4$ we have:

$$\begin{aligned} 4a(1-a)F &= c_n\sigma'\left(\frac{(1-a)}{\sin\phi}\right)^2 \\ 4aF &= c_n\sigma'\frac{(1-a)}{\sin^2\phi} \end{aligned} \tag{7.114}$$

It will be convenient to group some of these terms into a new nondimensional factor

$$\kappa = \frac{c_n\sigma'}{4F\sin^2\phi} \tag{7.115}$$

With that definition the solution for a is:

$$a = \frac{\kappa}{1+\kappa} \tag{7.116}$$

The criteria for this equation was expressed in terms of a, but this is not convenient as that is the quantity we are solving for. Instead, we will express the criteria in terms of κ. We require that

$$\begin{aligned} \frac{\kappa}{1+\kappa} &\le 0.4 \\ \kappa &\le 0.4(1+\kappa), \quad \text{(assuming } 1+\kappa > 0 \\ &\qquad \text{or in other words } \kappa > -1) \\ 0.6\kappa &\le 0.4 \\ \kappa &\le \frac{2}{3} \end{aligned} \tag{7.117}$$

Thus, this first cases applies if $-1 \le \kappa < 2/3$.

For the next case, $0.4 < a < 1$, we use the empirical momentum formula:

$$\left(\frac{14}{9}a^2 - \frac{4}{9}a + \frac{8}{9}\right)F = c_n\sigma'\left(\frac{1-a}{\sin\phi}\right)^2 \tag{7.118}$$

This yields a quadratic formula that can be solved for a. After simplification it yields (noting that only the negative sign in the quadratic formula is physically possible):

$$a = \frac{\gamma_1 - \sqrt{\gamma_2}}{\gamma_3} \tag{7.119}$$

where

$$\begin{aligned}\gamma_1 &= 2\kappa - \frac{1}{9}\\ \gamma_2 &= 2\kappa - \frac{1}{3}\\ \gamma_3 &= 2\kappa - \frac{7}{9}\end{aligned} \tag{7.120}$$

Using a similar process to express the criteria in terms of κ insteae of a, we can show that the equation applies when $\kappa > 2/3$ (and thus the denominator will never be zero).

The case for $a > 1$, the propeller break region, leads to a similar equation to the first case, but with a negative sign. The result is:

$$a = \frac{\kappa}{\kappa - 1} \tag{7.121}$$

If $a > 1$ then from Fig. 7.20 we see that the angle ϕ would need to change signs. Thus, this case only applies when $\phi < 0$. This case is exactly the same as the first momentum case, if we replace κ with $-\kappa$.

We can consolidate these three cases as shown in Algorithm 1. Note that $\kappa = -1$ is only physically consistent if $V_\infty = 0$.[16] For nonzero inflow, we know that κ cannot equal -1 so if any intermediate iterations produces κ = -1 we can simply return a nonzero residual and continue iterating.

16. Ning, *Using Blade Element Momentum Methods with Gradient-Based Design Optimization*, 2021.

Algorithm 1 Solve for the axial induced velocity.

if $\phi < 0$ **then**
  $\kappa = -\kappa$
end if

if $\kappa \leq 2/3$ **then**
  $a = \kappa/(1+\kappa)$ *if $\kappa = -1$ return any nonzero residual.*
else
  $a = (\gamma_1 - \sqrt{\gamma_2})/\gamma_3$
end if

We repeat a similar process for the torques, except in this case there iis only one equation. Equating the torque coefficients from momentum and blade element theories results in:

$$\begin{aligned}4a'(1-a)\lambda_r F &= c_t \sigma' \lambda_r \left(\frac{(1-a)(1+a')}{\sin\phi\cos\phi}\right)\\ 4a'F &= c_t\sigma'\left(\frac{(1+a')}{\sin\phi\cos\phi}\right)\end{aligned} \tag{7.122}$$

For convenience we define the nondimensional quantity:

$$\kappa' = \frac{c_t \sigma'}{4F \sin\phi \cos\phi} \tag{7.123}$$

We can now solve this for a':

$$a' = \frac{\kappa'}{1 - \kappa'} \tag{7.124}$$

The above equations allow us to compute the induction factors. However, we have to be careful as these calculations depend on ϕ and the angle of attack, which in turn depend on the induction factors (Fig. 7.20). Thus, we have a circular dependency and need to use an iterative method, or a root solver. Traditionally, this is done by considering a and a' as the unknowns and using the two equations above to form two residuals. However, we can greatly simplify the solution of these equations by considering ϕ and W as the unknowns.[16,18] The inflow velocity has no direct dependence in the BEM equations (other than in Reynolds number, which operates on a log scale and so the impact is negligible). This means that we can reduce the residuals to one equation, which is advantageous because one dimensional root finding problems can be solved with guaranteed convergence. The solution of the residual ensures compatibility between the blade element and momentum theories. From Fig. 7.20 we can write:

16. Ning, *Using Blade Element Momentum Methods with Gradient-Based Design Optimization*, 2021.

18. Ning, *A Simple Solution Method for the Blade Element Momentum Equations with Guaranteed Convergence*, 2014.

$$\tan\phi = \frac{V_\infty(1-a)}{\Omega r(1+a')} \tag{7.125}$$

$$= \frac{(1-a)}{\lambda_r(1+a')} \tag{7.126}$$

This equation could be rearranged in many ways to form a residual equation, but as demonstrated in the above cited papers a numerically advantageous form is:

$$\mathcal{R}(\phi) = \frac{\sin\phi}{1-a} - \frac{\cos\phi}{\lambda_r(1+a')} = 0 \tag{7.127}$$

In summary we define a residual function as follows:

$$\text{function } \mathcal{R}(\phi) \tag{7.128}$$
$$\alpha = \phi - \theta \tag{7.129}$$
$$c_l = f(\alpha, Re) \tag{7.130}$$
$$c_d = f(\alpha, Re) \tag{7.131}$$
$$c_n = c_l \cos\phi + c_d \sin\phi \tag{7.132}$$
$$c_t = c_l \sin\phi - c_d \cos\phi \tag{7.133}$$
$$\kappa = \frac{\sigma' c_n}{4F \sin^2\phi} \tag{7.134}$$
$$\text{Compute } a \text{ from Algorithm 1} \tag{7.135}$$
$$\kappa' = \frac{\sigma' c_t}{4F \sin\phi \cos\phi} \tag{7.136}$$
$$a' = \kappa'/(1 - \kappa') \tag{7.137}$$
$$\text{return } \frac{\sin\phi}{1 - a} - \frac{\cos\phi}{\lambda_r(1 + a')} \tag{7.138}$$

Generally, the solution will be in the bracket: $\phi = (0, \pi/2]$ (note the open bracket at zero). Thus, a method like Brent's method can be used to yield fast and robust convergence. If airfoil data has not been extended to such high angles, a smaller range may suffice.

This procedure yields a solution at one radial station of the blade (Fig. 7.22). Once we solve a section on the blade for the correct inflow angle ϕ^* we can recalculate the resulting loads and induction factors for that section:

$$c_n, c_t, a, a' = f(\phi^*) \tag{7.139}$$

We then compute the inflow velocity:

$$W^2 = (V_\infty(1 - a))^2 + (\Omega r(1 + a'))^2 \tag{7.140}$$

and the thrust and torque per unit length:

$$T' = Bc_n \frac{1}{2}\rho W^2 c \tag{7.141}$$
$$Q' = Brc_t \frac{1}{2}\rho W^2 c \tag{7.142}$$

We then need to repeat these procedure at multiple radial stations given by our chosen blade discretization. We then integrate across the

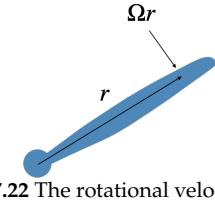

Fig. 7.22 The rotational velocity at a given radial station on the blade.

blade to get total thrust and torque:

$$T = \int_{r_h}^{r_t} T' dr \tag{7.143}$$

$$Q = \int_{r_h}^{r_t} Q' dr \tag{7.144}$$

where r_h and r_t correspond to the hub and tip radius respectively. Right at the hub/tip the loads go to zero and so we need not compute at those points (indeed we cannot compute right at those points). Finally, from the torque we can compute the required power.

$$P = Q\Omega \tag{7.145}$$

While not necessary, it is often convenient to normalize using typical turbine conventions. The thrust, torque, and power coefficients are given by:

$$C_T = \frac{T}{\frac{1}{2}\rho V_\infty^2 \pi R^2} \tag{7.146}$$

$$C_Q = \frac{Q}{\frac{1}{2}\rho V_\infty^2 \pi R^3} \tag{7.147}$$

$$C_P = \frac{P}{\frac{1}{2}\rho V_\infty^3 \pi R^2} \tag{7.148}$$

where R is the rotor radius. All of these outputs are functions of the tip-speed ratio

$$\lambda = \frac{\Omega R}{V_\infty} \tag{7.149}$$

7.3 Airfoil Data Corrections

The accuracy of the blade element methodology hinges on providing accurate airfoil data, namely the tables of lift and drag coefficients as functions of angle of attack (and potentially of Reynolds number and Mach number as well). Unfortunately, static airfoil tables, whether from experimental data or computational simulation, are rarely useful as is.

First, the airfoil forces, particularly the maximum lift, is significantly affected by rotation. Most airfoil data is based on non-rotating conditions. The Coriolis and centrifugal forces, generated from rotation, tend to delay stall and allow for higher lift coefficients. Rotation corrections are needed to account for this behavior.

Second, corrections for Reynolds number and/or Mach number may be needed. Ideally, airfoil coefficients are provided at multiple

Reynolds/Mach numbers. If so, we can interpolate directly on the data as Reynolds number and Mach number vary in the simulation. If such data is not available, corrections can account for modest variations. Mach number variation is rarely needed for wind turbines, or propellers designed for low-speed aircraft.

Third, the angle of attack range from most airfoil data sources is too limited. As compared to wings, the angle of attack along blades varies much more significantly. This is because rotation changes the local inflow speed, from small speeds near the hub to large speeds at the tip, and thus the local inflow angle varies considerably. Thus, we usually need to provide airfoil data across a larger range of angles of attack. For wind turbines, the incoming wind can change direction significantly, and startup and stopping introduces large changes in rotation speed that can be important loading conditions. All of these considerations lead to an even wider range of angles that need to be considered. Thus, for wind turbines in particular, we typically extrapolate the data across the full circle from $\alpha = -180°$ to $180°$. For propellers, the extrapolation can be much more modest and in some cases may not be needed at all depending on the conditions being analyzed (e.g., the range of advance ratios simulated).

If not extrapolated to large angles, we should reduce the solution range shown below Eq. 7.56 to not extend all the way to $\pi/2$. That is a wide enough value to bracket the solution without requiring any information, but a tighter bracket can work as well if we use information specific to our propeller. Knowing the twist angles, and provided angles of attack (assuming a solution exist within the range of provided data), we could provide a smaller upper bound on ϕ (Eq. 7.26).

7.3.1 Rotation Corrections

As discussed in Section 1.11.2, fluid moving in a rotating reference frame experiences additional apparent forces, namely a Coriolis force and a centrifugal force.* These forces are negligibly small for the flow around a rotor, except in the boundary layer or in areas of separation where the fluid is moving slowly.

The hub and tip vortices induce radial motion along the blade. The hub vortex induces flow towards the tip, and the tip vortex induces flow towards the hub, with the effects most pronounced near the ends. From Eq. 1.168 we can see the Coriolis force associated with these radial velocity components induces a force towards the trailing edge near the hub, and towards the leading edge near the tip (Fig. 7.23). These apparent forces act as a favorable and adverse pressure gradient

*Himmelskamp was the first to identify that the lift curves on sections of a rotating propeller blade differed significantly from the 2D wind tunnel data.[21] Although theoretical explanations did not come for some time after.

21. Himmelskamp, *Profile investigations on a rotating airscrew*, 1947.

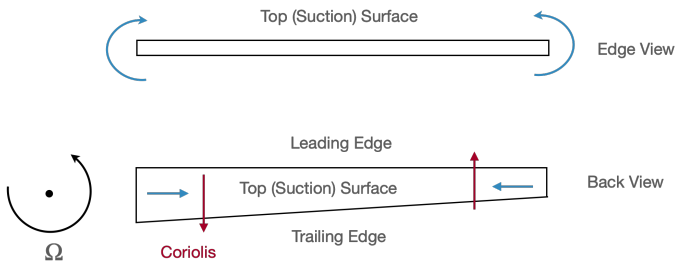

Fig. 7.23 Coriolis force generated from radial flow along blade.

respectively. Thus, near the hub, stall is delayed to higher lift coefficients because of the favorable pressure gradient. Conversely, near the tip, stall happens sooner than otherwise would occur on a non-rotating section.

In addition to the Coriolis force, there is a centrifugal force directed from hub to tip. This force accentuates the radial flow from the hub vortex, and somewhat counteracts the radial flow from tip vortex. Thus, we expect an even higher increase in maximum lift coefficients near the hub, and a more subdued impact on maximum lift decreases near the tip. Additionally, the radial flow from the centrifugal force extends the region of separation out further from the hub, an effect called *centrifugal pumping*. Thus, the effects of stall delay occur further out on the blade, although they are still most pronounced near the hub.

Many rotation corrections models exit. Sometimes these are called 3D corrections, as they correct 2D non-rotating data to account for the three-dimensional effects of radial flow. Although a basic motivation for the behavior was described above, the flow mechanisms are complex and still not fully understood. None of the models is considered highly generalizable, though many share similar features.

A common form is:

$$c_{l3D} = c_{l2D} + f_l\left(\frac{c}{R}, \frac{r}{R}, \lambda, \ldots\right)(c_{l_{pot}} - c_{l2D}) \tag{7.150}$$

where c_{l2D} is the provided non-rotating data, c_{l3D} is the rotationally-corrected data, $c_{l_{pot}}$ is the idealized potential flow solution (Eq. 2.287), and f_l is a function that differs between the methods. Note that although the theoretical lift curve slope is 2π (Eq. 2.288), and we can use that, it is usually preferable to use the lift curve slope from the actual data as determined by regression.

A similar expression is used for drag:

$$c_{d3D} = c_{d2D} + f_d\left(\frac{c}{R}, \frac{r}{R}, \lambda, \ldots\right)(c_{d0} - c_{d2D}) \tag{7.151}$$

where c_{d0} is the drag coefficient at zero degrees angle of attack. However, there is less agreement on rotation-based drag models. In fact, there is

not even agreement on whether the drag should increase or decrease (though most now predict an increase).

Many such models exist, only a few of which are highlighted below. One of the original models, is from Snell,[22,23] which identified the local solidity (c/r when stripping away constants) as a critical parameter in predicting the enhancement in lift coefficient near the hub. This model is simply:

$$f_l = 3.1\left(\frac{c}{r}\right)^2 \tag{7.152}$$

For lower tip-speed ratios this model can be improved with:[24]

$$f_l = 3.1\left(\frac{c}{r}\right)^2 \frac{\Omega r}{W} \tag{7.153}$$

where W is the local inflow velocity Eq. 7.33 or Eq. 7.107. If we ignore the smaller contribution from induction that the last term can be approximated as:

$$\frac{\Omega r}{W} \approx \frac{\lambda_r^2}{1+\lambda_r^2} \tag{7.154}$$

where λ_r is the local tip-speed ratio (Eq. 7.100). Note that the local tip-speed ratio is related to the tip-speed ratio Eq. 7.149 as:

$$\lambda_r = \frac{\lambda}{r/R} \tag{7.155}$$

This model does not have a corresponding drag formula.

Another popular model is from Du and Selig:[25]

$$f_l = \frac{1}{2\pi}\left[12.63(c/r)\left(\frac{a-(c/r)^{\frac{d}{\Lambda(r/R)}}}{b+(c/r)^{\frac{d}{2\Lambda(r/R)}}}\right)-1\right] \tag{7.156}$$

where a, b, and d are tunable parameters set to 1 by default, and Λ is a modified tip speed ratio:

$$\Lambda = \frac{\Omega R}{\sqrt{V_x^2+(\Omega R)^2}} = \frac{\lambda}{\sqrt{1+\lambda^2}} \tag{7.157}$$

Although a similar drag formula was proposed, it predicts a decrease in drag and is thus not often used.

Because these models are driven by the Coriolis force from the hub vortex, and the centrifugal pumping pushing the separation location further inboard, it should not be applied near the tip. For $r/R > 0.8$, no correction is applied (though the correction naturally drops off anyway with increasing radial location).

22. Snel, *Scaling laws for the boundary layer flow on rotating wind turbine blades*, 1991.

23. Snel et al., *Sectional prediction of lift coefficients on rotating wind turbine blades in stall*, 1994.

24. Lindenburg, *Investigation into Rotor Blade Aerodynamics: Analysis of the stationary measurements on the UAE phase-VI rotor in the NASA-Ames wind tunnel*, 2003.

25. Du and Selig, *A 3-D Stall-Delay Model for Horizontal Axis Wind Turbine Performance Prediction*, 1998.

Additionally, both of these methods will continue to provide enhanced lift coefficients at large angles of attack. In practice the correction should only be applied in full up to some maximum angle. After about 30 degrees the corrections is tapered off towards zero (e.g., until 50 degrees [24] or until 90 degrees[26]).

For drag, one approach is to use the simple result from Eggers [27] that relates the tangential force correction and the normal force correction as follows:

$$\Delta c_t = 0.12 \Delta c_n \tag{7.158}$$

where these terms refer to corrections in tangential and normal force respectively. We can relate these back to changes in lift and drag from the definitions of these coordinate systems Fig. 7.21

$$\Delta c_d = \Delta c_n \sin\phi - \Delta c_t \cos\phi \tag{7.159}$$

$$\Delta c_l = \Delta c_n \cos\phi + \Delta c_t \sin\phi \tag{7.160}$$

If we substitute Eq. 7.158 into the above two equations we have:

$$\Delta c_d = \Delta c_n \left(\sin\phi - 0.12\cos\phi\right) \tag{7.161}$$

$$\Delta c_l = \Delta c_n \left(\cos\phi + 0.12\sin\phi\right) \tag{7.162}$$

We now solve Eq. 7.162 for c_n and substitute it into Eq. 7.161 we have the relationship:

$$\Delta c_d = \Delta c_l \left(\frac{\sin\phi - 0.12\cos\phi}{\cos\phi + 0.12\sin\phi}\right) \tag{7.163}$$

With this technique we could then use any model for the lift correction, (i.e., Eq. 7.150 written in the form $c_{l3D} = c_{l2D} + \Delta c_l$) then compute a corresponding drag correction from Eq. 7.163 that we apply as follows:

$$c_{d3D} = c_{d2D} + \Delta c_d \tag{7.164}$$

Note that Eggers defines his own correction for the normal force although that isn't expounded on here.

While the above formulas were expressed in terms of the tip-speed ratio, the advance ratio (Eq. 7.69), used for propellers, is related to the tip speed ratio (Eq. 7.149) by:

$$\lambda = \pi / J \tag{7.165}$$

Rotation corrections can be done on the fly (i.e., computed at each iteration of the analysis), or they can be pre-computed and built into the airfoil polars that are fixed throughout the analysis. While on-the-fly is

24. Lindenburg, *Investigation into Rotor Blade Aerodynamics: Analysis of the stationary measurements on the UAE phase-VI rotor in the NASA-Ames wind tunnel*, 2003.

26. Laino et al., *Validation of the Aero-Dyn Subroutines Using NREL Unsteady Aerodynamics Experiment Data*, 2002.

27. Eggers Jr et al., *An Assessment of Approximate Modeling of Aerodynamic Loads on the uae Rotor*, 2003.

perhaps ideal, pre-computation is more common because the combined variation in airfoil data, post-stall behavior, rotation corrections, and extrapolation (discussed later in this section) can sometimes lead to unphysical results (e.g., abrupt changes, discontinuities, reversals, etc.). By pre-computing, all airfoil polars can be inspected and adjusted as needed.

The difficulty with pre-computing is that the corrections depend on the radial station (r), and so even in the case when a single airfoil is used for the entire blade, separate airfoil files should be created at each station. For wind turbines this is not so onerous as the airfoil typically varies across the blade anyway. However, sometimes the amount of effort is not justified for some blades where the rotational corrections are relatively modest, and the operating conditions explored are minimal and typical, so just one rotationally-corrected airfoil might be used for the whole blade. This can sometimes be justifiable as high angles of attack only occur near the root for normal operation, precisely where such corrections would be most needed.

7.3.2 Reynolds and Mach Number Corrections

Another correction that may be needed is for Reynolds number. If Reynolds number variation is significant, it is generally more accurate for the airfoil force coefficients to be provided at multiple Reynolds numbers (whether from computations or experiments). Then, the lift and drag at a given Reynolds number is computed through interpolation.

However, if such data is not available, an on-the-fly Reynolds number correction could be used instead. From Eq. 3.49 we have an analytic solution to the skin friction coefficient for laminar flow over a flat plate.

$$C_f = \frac{1.328}{\sqrt{Re_L}} \tag{7.166}$$

For a flat plate the skin friction coefficient is also the drag coefficient. For other shapes, the drag would still be (approximately) proportional to the skin friction coefficient. We represent this proportionality with some constant k:

$$c_d = \frac{k}{\sqrt{Re_L}} \tag{7.167}$$

If we know the drag at some Reynolds number, which we denote as condition 0, and wish to estimate the drag at some other Reynolds number (no subscript) we have the following ratio:

$$\frac{c_d}{c_{d0}} = \frac{\sqrt{Re_0}}{\sqrt{Re}} \tag{7.168}$$

A turbulent boundary layer is more likely and so we can repeat the same analysis with an empirical flat plate skin friction coefficient (Eq. 3.53). In this case:

$$\frac{c_d}{c_{d0}} = \left(\frac{Re_0}{Re}\right)^{0.2} \tag{7.169}$$

Both cases can be represented as:

$$c_d = c_{d0}\left(\frac{Re_0}{Re}\right)^{p} \tag{7.170}$$

where $p = 0.5$ for a purely laminar boundary layer, $p = 0.2$ for a turbulent boundary layer, or some other empirical value may be used based on additional data.

This equation provides a simple way to estimate the drag for modest changes in Reynolds number (at least within the same flow regime of laminar or turbulent), given the drag coefficient at some known Reynolds number (c_{d0}, Re_0). For modest changes in Reynolds number, lift typically shows little variation and so may be neglected within this approximation. While this method is not as accurate as providing data at multiple Reynolds number, it is straightforward to apply and may be sufficient in many cases.

For changes in Mach number similar approaches can be utilized. Ideally, data is provided at different Mach numbers. But, if not, the Prandtl-Glauert correction could be used (Eq. 6.182).

$$c_l = \frac{c_{l0}}{\sqrt{1 - M_\infty^2}} \tag{7.171}$$

where c_{l0} corresponds to the incompressible lift coefficient. This correction affects only the lift and neglects any changes in drag. Again, such corrections can be useful if other data is not available, and the variations in Mach number are relatively modest. Unfortunately, the Karman-Tsien correction cannot be used as the correction is for pressure coefficients and does not result in a simple proportionality constant that could be factored out of an integral for forces (as does the Prandtl-Glauert method).

7.3.3 Extrapolation

As discussed previously sometimes it is desirable to extend the angle of attack range of the airfoil data all the way from $-180°$ to $180°$. This may be for physical reasons (wind turbine startup/stop scenarios which have high angles), numerical solution approaches (which may

use a large bracket for robustness and simplicity), or optimization robustness (in which intermediate solutions may have large twist angles). Experimental data rarely exists at such high angles, so extrapolation approaches are used. Fortunately at high angles, airfoils behave like a flat plate and so the behavior can be captured in a relatively universal way.

The Viterna method is the most commonly used extrapolation approach.[28] The extrapolation begins at an angle of attack α_s, which corresponds to the angle of attack at stall, the angle of attack at maximum lift (after rotation corrections), or some other location in the stalled region depending on the extent of reliable data. The extrapolation of lift and drag for angles larger than α_s (or less than $-\alpha_{ns}$ where α_{ns} corresponds to stall at negative angles of attack) is:

28. Viterna and Janetzke, *Theoretical and Experimental Power from Large Horizontal-Axis Wind Turbines*, 1982.

$$c_l = \frac{c_{d\,max}}{2}\sin(2\alpha) + A\frac{\cos^2\alpha}{\sin\alpha} \tag{7.172}$$

$$c_d = c_{d\,max}\sin^2(\alpha) + B\cos\alpha \tag{7.173}$$

where A and B are constants defined as:

$$A = (c_{l_s} - c_{d\,max}\sin\alpha_s\cos\alpha_s)\frac{\sin\alpha_s}{\cos^2\alpha_s} \tag{7.174}$$

$$B = c_{d_s} - \frac{c_{d\,max}\sin^2\alpha_s}{\cos\alpha_s} \tag{7.175}$$

The maximum drag coefficient, $c_{d\,max}$, is estimated from flat plate experiments as:

$$c_{d\,max} = \begin{cases} 1.11 + 0.018AR & \text{for } AR < 50 \\ 2.01 & \text{for } AR \geq 50 \end{cases} \tag{7.176}$$

The aspect ratio AR is defined as the blade radius divided by the chord at 75% radius:

$$AR = \frac{R}{c_{0.75R}} \tag{7.177}$$

This method is generally considered reasonably accurate. However, like the rotation corrections, it can sometimes produce nonphysical results with abrupt changes or discontinuities so some care is needed in implementation and usually it is used as a preprocessing step so that the outputs can be inspected. Usually it is applied after rotation corrections, another reason favoring precomputed rotational corrections.

7.3.4 Dynamic Stall

While everything we have discussed so far is based on static aerodynamics, wind turbine and propeller aerodynamics are also subject to

dynamic behavior. This dynamic behavior may arise because of wind fluctuations (e.g., turbulence), motion of the blades (e.g., aeroelasticity) or both. If the dynamic behavior is slow[†], then the steady approache can be used reasonably well with instantaneous dynamic inputs. This approach where static models are used with instantaneous time-varying inputs is known as *quasi-static*. However, as the dynamic behavior increases in speed, then the physical behavior can differ quite significantly from quasi-static predictions. The topic of unsteady aerodynamics is discussed more broadly in a separately chapter. In this section, just a brief overview of the impact on rotors is noted.

[†]What is meant by "slow" is defined more precisely in the next paragraph.

The degree of unsteadiness is quantified by a nondimensional number called the Strohaul number:

$$St = \frac{fL}{V} \tag{7.178}$$

where f is the frequency of the unsteady behavior, L is some characteristic length, and V is the fluid velocity. For aerodynamics the reduced frequency is more commonly used:

$$k = \frac{\omega c}{2V} \tag{7.179}$$

where ω is the circular frequency ($w = 2\pi f$) and a length scale of $c/2$ is used because of results from unsteady thin airfoil theory. If the reduced frequency is small (say, $k < 0.05$) then the behavior can be considered quasi-static. Otherwise, a dynamic model is needed.

The lift, drag, and moment coefficients of airfoils in dynamic stall exhibit hysteresis, meaning that as angle of attack is rapidly increased then decreased the lift and drag curves do not follow the same path back down as they did going up. Figure 7.24 depicts an example, where an airfoil is under going a pitching motion with an amplitude of 4 degrees. Note that the dynamic lift coefficient not only differs from the static lift coefficient, but that the lift coefficient when the angle of attack is increased differs from that when the angle of attack is decreased.

Perhaps the most well known dynamic stall model is the Beddoes-Leishman model, which arose out of the rotorcraft community.[29,30] However, rotorcraft and wind turbine blades have different dynamic stall behavior, as the thin airfoils in rotorcraft are more susceptible to leading edge stall, and travel at speeds where compressibility is critical. Wind turbines on the other hand have much thicker airfoil shapes, and have other unique considerations like lead-lag vibration. Some dynamic stall models that are specific to or commonly used in wind turbine applications include the Øye model[31] or the Risø model.[32]

29. Beddoes, *A synthesis of unsteady aerodynamic effects including stall hysteresis*, 1976.

30. Leishman and Beddoes, *A Semi-Empirical Model for Dynamic Stall*, 1989.

31. Øye, *Dynamic stall simulated as time lag of separation*, 1991.

32. Hansen et al., *A Beddoes–Leishman Type Dynamic Stall Model in State-space and Indicial Formulations*, 2004.

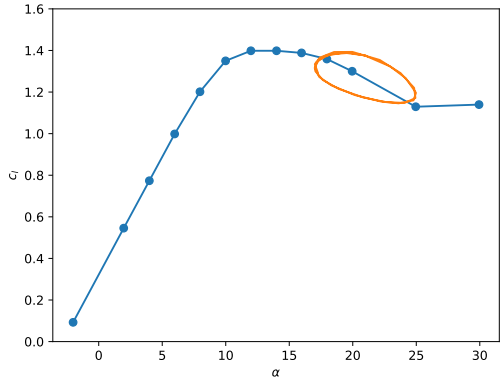

Fig. 7.24 Static airfoil lift coefficient in dotted line. Cyclic behavior created from a pitching airfoil with a reduced frequency of 0.1, and a pitching amplitude of 4 degrees centered at 21 degrees angle of attack.

7.4 Wakes

While the details of wake development behind a propeller or turbine are complex, we can generally obtain reasonable approximations for two scenarios: in the near-field and far-field. In the near field, assuming that the wake does not deform (i.e., moves straight back for a wing, or continues in a rigid helicoidal shape for a rotor), is generally a reasonable approximation. We could, for example, use the induced velocities computed aft of the blade:

$$V_{\text{axial}} = 2V_\infty a \tag{7.180}$$

and

$$V_{\text{swirl}} = 2\Omega r a' \tag{7.181}$$

These velocities are depicted in Fig. 7.25. Note that we don't use the velocities right at the disk. Instead, we are interested in behavior aft of the rotor, which includes a factor of 2 as computed previously. The downstream result of the previous sections is considered near-field in the overall wake development, as the transition occurs quickly. This type of near-field model can work well if we are reasonably close to the rotor disk, typically within about one rotor diameter.

This type of model is sometimes used for tractor configurations with the propeller forward of the wing. The wake of the propeller impinges on the wing and modifies the input velocities (e.g., computed using a VLM Section 4.5). Because the velocities in the propeller wake increase in speed, in a *blown wing* concept multiple propellers can be used to significantly increase the effective freestream velocity as seen by the wing, allowing takeoff with much shorter runways. Sometimes additional corrections are used to modify the effect of the axial and

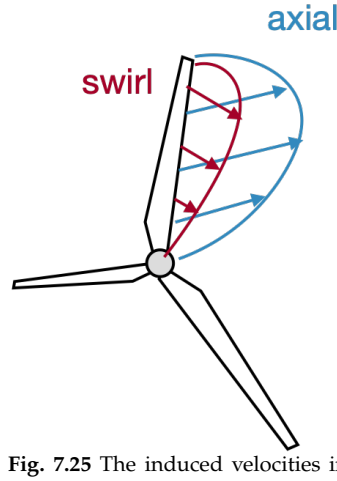

Fig. 7.25 The induced velocities in the near field of the rotor computed based on the induction at the rotor.

swirl velocities on the wing velocities, to better match experimental data.

The other type of approximation that is sometimes used is a far-field wakes. While the former type is more common for propellers, this latter time is common for wind turbines. Far-field wake models are motivated by the observed self-similarity of bluff-body wakes. This means that after some distance, if properly normalized, the velocity deficit profile collapses to a single curve. Thus, we expect that a model can be developed to predict the behavior of a far-field wake in a reasonably universal way. Self-similarity usually begins after a few rotor diameters.

For a turbine, the velocity is decreased in the wake, which reduces the power available to downstream turbines. Furthermore, the wake increases turbulence increasing the fatigue loads on downstream turbines. Thus, in a wind farm, wind turbines are far apart (usually at least 6 diameters spacing) to reduce negative wake interactions. At these separation distances a far-field assumption can be a reasonable approximation.

One of the simplest turbine wake models is the Jensen model.[33] We start a control volume at a point downstream of the rotor and assume that it expands linearly, in a self-similar manner, forward of that point into a far-field wake (Fig. 7.26).

33. Jensen, *A Note on Wind Generator Interaction*, 1983.

We now apply a mass balance to a cylindrical control volume starting downstream of the disk, where we assume the starting wake diameter is identical to that of the rotor disk, and end at an arbitrary location in the farfield. We assume that the mass flow across the side boundaries is negligible in this simplified model.

$$\rho V_s \pi R_d^2 + \rho V_\infty (\pi R^2 - \pi R_d^2) = \rho V_w \pi R^2 \tag{7.182}$$

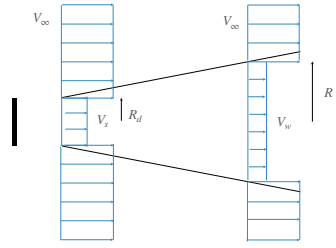

Fig. 7.26 Simple wake model defined by a linearly expanding wake from the rotor disk.

Assuming incompressible flow, we cancel density and π from each term resulting in:

$$V_s R_d^2 + V_\infty (R^2 - R_d^2) = V_w R^2 \tag{7.183}$$

We now solve for the wake velocity:

$$V_w = V_s \left(\frac{R_d}{R}\right)^2 + V_\infty \left(1 - \left(\frac{R_d}{R}\right)^2\right) \tag{7.184}$$

We assume that the starting velocity (V_s) for this analysis is the "far-field" result from momentum theory derived in the previous section (Eq. 7.81). In other words, we assume that $V_s = V_\infty(1 - 2a)$. Making

this substitution and simplifying results in:

$$\begin{aligned} V_w &= V_\infty(1-2a)\left(\frac{R_d}{R}\right)^2 + V_\infty\left(1-\left(\frac{R_d}{R}\right)^2\right) \\ V_w &= V_\infty\left(1+(1-2a-1)\left(\frac{R_d}{R}\right)^2\right) \\ V_w &= V_\infty\left(1-2a\left(\frac{R_d}{R}\right)^2\right) \end{aligned} \tag{7.185}$$

We have already assumed that the radius expands linearly with downstream distance x, starting from the disk, which we express as:

$$R = R_d + kx \tag{7.186}$$

The parameter k is called the *wake growth rate*, and is the slope of the linear wake profile. The rotor diameter (D) is more commonly used than radius, so we also make that change:

$$\begin{aligned} V_w &= V_\infty\left(1-2a\left(\frac{D/2}{D/2+kx}\right)^2\right) \\ &= V_\infty\left(1-2a\left(\frac{D}{D+2kx}\right)^2\right) \\ &= V_\infty\left(1-2a\left(1+\frac{2kx}{D}\right)^{-2}\right) \end{aligned} \tag{7.187}$$

Turbine wake models are typically expressed in terms of the velocity deficit:

$$\delta = \frac{\Delta V}{V_\infty} = \frac{V_\infty - V_w}{V_\infty} = 1 - \frac{V_w}{V_\infty} \tag{7.188}$$

In this case the velocity deficit is:

$$\delta = \frac{2a}{\left(1+\frac{2kx}{D}\right)^2} \tag{7.189}$$

The original Jensen model assumed that the rotor was optimally loaded for maximum power (Eq. 7.87, $a = 1/3$), but a later version generalized to express the induction in terms of the induction factor.[34] We'll keep it general allowing the induction factor to be a function of the thrust coefficient. Solving Eq. 7.83 for the induction factor results in:

$$a = \frac{1}{2}\left(1-\sqrt{1-C_T}\right) \tag{7.190}$$

34. Katić et al., *A simple model for cluster efficiency*, 1986.

In solving the quadratic equation for a, we know that the negative sign is the correct branch based on physically realizable induction factors for this momentum region (Fig. 7.17). We substitute this expression into the velocity deficit:

$$\delta = \frac{1 - \sqrt{1 - C_T}}{\left(1 + \frac{2kx}{D}\right)^2} \tag{7.191}$$

We now have the final model:

$$\delta(x, r) = \begin{cases} \left(1 - \sqrt{1 - C_T}\right) / \left(1 + \frac{2kx}{D}\right)^2 & \text{for } |r| \leq D/2 + kx \\ 0 & \text{otherwise} \end{cases} \tag{7.192}$$

The initial Jensen model assumed an expansion rate of $k = 0.1$ although this is an adjustable constant. Today, more typical values are $k = 0.075$ for onshore turbines, and $k = 0.04$ for offshore.

This was a useful initial model that has served the community well, but is not often used today as it is over-simplistic and has been replaced by better models. The resulting velocity profile contains an unphysical jump, and there is no dependence on other critical parameters like freestream turbulence.

Many turbine wake models exist, we highlight just one more recent model that is well used, which we will call the BP model as it was developed by Bastankhah and Porté-Agel model.[35] The BP model uses a self-similar Gaussian distribution to describe the wake deficit, allowing for a continuous and smooth velocity profile that matches experimental data much better. Additionally, rather than satisfy only a mass balance, both a mass and a momentum balance are used. The wake growth rate is also computed as a function of turbulence intensity. Several parameters in the model are tuned based on LES simulations. The derivation is not discussed here, but we rather provide a summary. The full model allows for changes in yaw angle, wake deflection, variations both laterally and vertically (rather than an axisymmetric model), but we ignore these considerations for simplicity in the expression shown here. The result is:

35. Bastankhah and Porté-Agel, *Experimental and theoretical study of wind turbine wakes in yawed conditions*, 2016.

$$\delta(x, r) = \left(1 - \sqrt{1 - \frac{C_T D^2}{8\sigma^2}}\right) \exp\left(-0.5 \left[\frac{r}{\sigma}\right]^2\right) \tag{7.193}$$

where σ is the wake width (as a standard deviation) defined as:

$$\sigma = k^*(x - x_0) + \frac{D}{2\sqrt{2}} \tag{7.194}$$

Note that k^* is defined slightly differently than the wake growth rate mentioned earlier ($k^* = d\sigma/dx$ as opposed to $k = dD/dx$). A different definition is necessary since a Gaussian distribution has no "edge". The physical effect is the same, both denote a growth rate in the width of the wake, but the actual numbers used will not be the same. The location x_0, the point at which self-similarly is assumed to begin, is computed as:

$$x_0 = \frac{D(1 + \sqrt{1 - C_T})}{\sqrt{2}(\alpha^* I + \beta^*(1 - \sqrt{1 - C_T}))} \tag{7.195}$$

where $\alpha^* = 2.32$, $\beta^* = 0.154$, and I is the turbulence intensity (Eq. 3.148). This model was later extended so the wake growth rate could be computed as a function of turbulence intensity:[36]

$$k^* = 0.3837\, I + 0.003678 \tag{7.196}$$

36. Niayifar and Porté-Agel, *Analytical Modeling of Wind Farms: A New Approach for Power Prediction*, 2016.

Figure 7.27 shows an example comparing the Jensen model and the BP model for some specific parameter choices noted in the figure caption. The main highlight is to contrast the constant wake deficit versus the smooth Gaussian deficit.

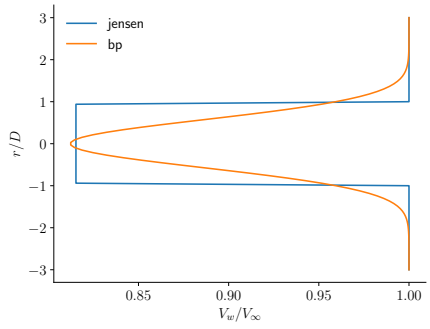

Fig. 7.27 Both wake models are at $x = 6D$ with $C_T = 0.889$. The Jensen model used $k = 0.075$, and the BP used $I = 0.14$.

The above discussion provides only an introduction to turbine wake models. Various additional considerations are needed in a wind farm model. Downstream turbines are often only partially overlapped by an upstream wake, and typically an area overlap ratio is used to modify the velocity deficits. When multiple wakes intersect the velocity deficits must be combined in some way. Some common approaches include a root-mean-square deficit or a linear sum of deficits. As the wind changes direction, typically expressed as a probability distribution called a wind rose, the wakes needed to be recomputed. Some models assume independent calculations, while others require a downstream marching approach to compute the effect of velocity deficits in a

sequential manner. Wind shear, wake deflection, stratification, amongst other considerations, can be important in obtaining good velocity and power predictions in a wind farm.

CFD

8

8.1 Continuum Hypothesis

Before we begin modeling fluids, we must first clarify how we quantify properties that characterize fluids, like density, velocity, and pressure. We know that all matter including fluids are made up of molecules of finite size. A common assumption is to imagine them as rigid spheres buzzing around and bouncing against each other inside the fluid. Unlike solids, most of the space inside a fluid is empty. This means that if we were to measure a property like the density of a fluid using a highly sensitive probe, we would get zero density where there is empty space and spikes when the probe comes across a fluid molecule. In this scenario, the fluid property density, varies like a discrete quantity. This is a perfectly valid model. However, when modeling fluids using mathematical functions, things are a lot easier if we assume that the properties vary continuously. This is called the *continuum hypothesis*.

The continuum hypothesis enables us to describe fluids using continuous functions in space and time and allows us to use differential equations to analyze flow properties. In this scenario, we do not deal directly with exact molecular properties, but an average of such properties. For example, the fluid density at a point is no more dependent on the molecules present at that location, instead it is an average density of the fluid at that point.

8.2 Governing Equations of Fluid Flow

TODO: Derive Convection equation, linear and nonlinear forms. Talk about physical examples of convection and diffusion with say Temperature as an example.

8.3 Finite Difference Method

In Chapter 2, we realized that incompressible inviscid flow is governed by the Laplace equation $\nabla^2\phi = 0$ and computed analytical solutions

to it. Now we shall explore a way to solve such dfferential equations using the numerical method of finite differences.

We know that the Taylor series expansion allows us to represent a function in terms of its derivatives, i.e,

$$f(x+\Delta x) = f(x) + \Delta x f'(x) + \frac{\Delta x^2}{2!} f''(x) + \frac{\Delta x^3}{3!} f'''(x) + \cdots \tag{8.1}$$

We use the big-O notation O to signify the polynomial order of the remaining terms.

$$f(x+\Delta x) = f(x) + \Delta x f'(x) + \Delta x^2 \frac{f''(x)}{2!} + O(\Delta x^3) \tag{8.2}$$

Another way to interpret this is to say that the error when approximating $f(x+\Delta x)$ about x, using the first 3 terms of the Taylor series, is third-order or $O(\Delta x^3)$. This sort of error that occurs when truncating a series representation is called a truncation error.

If we were to use only two terms to represent $f(x+\Delta x)$ about x, we would get a second-order truncation error.

$$f(x+\Delta x) = f(x) + \Delta x f'(x) + O(\Delta x^2) \tag{8.3}$$

We could rearrange the terms and obtain an expression for the first derivative of $f(x)$, as shown in Eq. 8.4. In doing so, we obtain a representation of the first derivative of $f(x)$ with a first-order truncation error. Because we use the value of the function at $x+\Delta x$ to obtain the derivative at x, it is called a *first-order forward difference*.

$$f'(x) = \frac{f(x+\Delta x) - f(x)}{\Delta x} - O(\Delta x) \tag{8.4}$$

If x was the i^{th} discrete step and $x+\Delta x$ the $i+1^{\text{th}}$ discrete step, then we could also write this as,

$$f'(x) = \frac{f_{i+1} - f_i}{\Delta x} - O(\Delta x) \tag{8.5}$$

Conversely, we may also derive the *first-order backward difference* representation of the first derivative using the Taylor series,

$$f(x-\Delta x) = f(x) - \Delta x f'(x) + \Delta x^2 \frac{f''(x)}{2!} - O(\Delta x^3) \tag{8.6}$$

We get,

$$f'(x) = \frac{f(x) - f(x-\Delta x)}{\Delta x} + O(\Delta x) \tag{8.7}$$

Similar to the forward-difference equation, we could write this as,

$$f'(x) = \frac{f_i - f_{i-1}}{\Delta x} - O(\Delta x) \tag{8.8}$$

8.3.1 Linear 1D Advection Equation

In Section 8.2, we saw that the Navier-Stokes equations may be simplified to the non-linear advection equation by making assumptions on the type of flow being considered. We also derived the following linear form of the advection equation,

$$\frac{\partial \phi}{\partial t} + a\frac{\partial \phi}{\partial x} = 0 \tag{8.9}$$

Here, ϕ is the quantity being transported at the velocity a, and the solution to the differential equation is $\phi(x,t)$ or in other words, the variation of ϕ over space and time.

In order to solve it, we first create a finite difference representation of the advection equation. We shall approximate the partial derivatives in space and time using the first-order forward difference. If we denote the value of ϕ at the n^{th} timestep, and i^{th} spatial step as ϕ_i^n, we obtain the expression,

$$\frac{\phi_i^{n+1} - \phi_i^n}{\Delta t} + a\frac{\phi_{i+1}^n - \phi_i^n}{\Delta x} = 0 \tag{8.10}$$

Because the expression is now written out at discrete steps in time and space, it is no more continuous and is called the discrete form. Note that there is only one term that contains the value of ϕ at the $n+1^{\text{th}}$ timestep. All other terms are at the n^{th} timestep. This means we can use the value of ϕ at a certain timestep n to advance the solution to the next timestep $n+1$. To make the solution process easier, we will rearrange Eq. 8.10 to obtain an explicit expression for ϕ_i^{n+1}. Since we used a forward difference in time and a forward difference in space, we call it a forward time forward space (FTFS) finite difference scheme.

$$\phi_i^{n+1} = \phi_i^n - \frac{a\Delta t}{\Delta x}\left(\phi_{i+1}^n - \phi_i^n\right) \quad \text{(FTFS)} \tag{8.11}$$

Alternatively, we may also derive a forward time backward space (FTBS) scheme as shown below,

$$\phi_i^{n+1} = \phi_i^n - \frac{a\Delta t}{\Delta x}\left(\phi_i^n - \phi_{i-1}^n\right) \quad \text{(FTBS)} \tag{8.12}$$

In order to use these finite difference schemes to solve the differential equation, we need to first define our domain and then discretize it. Shown in Fig. 8.1 is a 1D domain discretized using 5 points along the spatial dimension and 6 points along time. We may also say that the solution is modeled using 20 'nodes' and 10 timesteps.

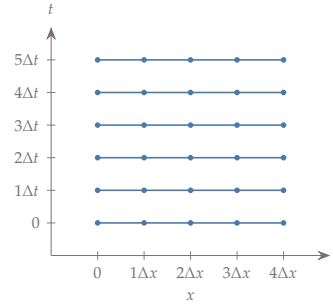

Fig. 8.1 1D domain discretized with 5 nodes in space and 6 timesteps.

We noticed that the solution at each timestep is determined by that at the previous timestep. This means we require an initial solution to

kickstart our iterative process. This is called an initial condition and is $\phi(x, t = 0)$. The advection equation, by its nature, transports the initial condition at the speed a. If we provide an initial condition, we should expect that distribution to have shifted at the advection velocity after a specified period of time as shown in Fig. 8.2. On the discrete $x - t$ plot, this solution would appear as shown in Fig. 8.3.

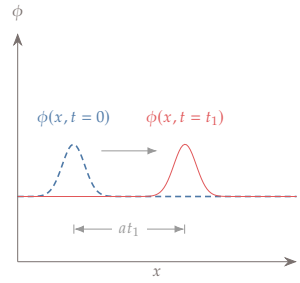

Fig. 8.2 Shifting behavior of 1D advection equation solution.

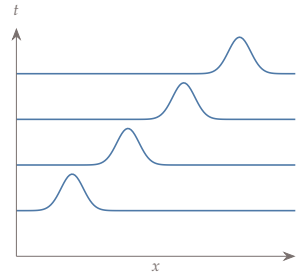

Fig. 8.3 Shifting behavior of 1D advection equation with $a > 0$ depicted on an $x - t$ plot.

Example 8.1 1D Advection Equation using FTFS and FTBS schemes

Let's simulate the advection equation using the FTFS and FTBS schemes described above for a simple initial condition. We shall use the hat function, also known as a piecewise constant function, here.

For an advection velocity of $a = 1.0$ m/s, we shall simulate the 1D advection equation for a time span of 1 s. We will use a timestep of $\Delta t = 0.01$ s and simulate over a distance of 4 m with nodes spaced at $\Delta x = 0.2$ m apart. This gives us 21 nodes in the spatial direction. We can store the solutions for ϕ in a matrix ϕ_i^n where i represents the index for spatial nodes, and n represents the index for timesteps, i.e, $\phi(x_i, t_n) = \phi_i^n$. The size of this matrix would be 21×100 where elements in the first column $n = 1$ would represent the first timestep, which is the initial condition. The initial condition for this example will be,

$$\phi(x, t = 0) = \begin{cases} 0.5 & \text{if } 0.2 \leq x \leq 0.4 \\ 0.0 & \text{if } 0.2 > x > 0.4 \end{cases} \tag{8.13}$$

and is shown in Fig. 8.4. In discrete form, the initial condition could be prescribed as,

$$\phi_i^0 = \begin{cases} 0.0 & \text{for } i = 1 \\ 0.5 & \text{for } i = 2, 3, 4 \\ 0.0 & \text{for } i = 5, 6, \cdots, 21 \end{cases} \tag{8.14}$$

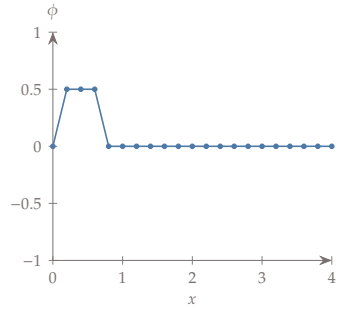

Fig. 8.4 Initial condition for advection problem.

All we need to do now is to use the finite difference scheme given in Eq. 8.11 or Eq. 8.12 to iterate over each spatial node, to obtain the values for ϕ at the next timestep. Provided in Table 8.1 are the values of ϕ_i for the timesteps 2 and 3 using the FTFS and FTBS schemes.

Iterating over 100 timesteps, with the FTFS and FTBS schemes, we will obtain the following final solutions shown in Fig. 8.5. Depicted in these plots are the 20^{th}, 50^{th} and 100^{th} columns of the ϕ_i^n matrix.

Clearly, something has gone wrong with our FTFS simulation! The values have increased rapidly with each iteration and have 'blown up' by three orders of magnitude. The FTBS solution, on the other hand, seems to have captured the expected shift of the initial condition towards the positive x-direction; however, the hat function we started with has been smoothed out and its magnitude has reduced. Additional experimentation will reveal that no matter what timestep size or spatial discretization we use, the FTFS scheme always results in 'unstable' solutions that blow up.

	FTFS		FTBS	
Node	$1\Delta t$	$2\Delta t$	$1\Delta t$	$2\Delta t$
1	-0.025	-0.05125	0.0	0.0
2	0.5	0.5	0.475	0.45125
3	0.5	0.49875	0.5	0.49875
4	0.525	0.55125	0.5	0.5
5	0.0	0.0	0.025	0.04875
6	0.0	0.0	0.0	0.00125
7	0.0	0.0	0.0	0.0
⋮	⋮	⋮	⋮	⋮
21	0.0	0.0	0.0	0.0

Table 8.1 Values of ϕ_i for the second and third timesteps.

Why do these finite difference schemes behave in such odd manners? If we were to visualize these schemes pictorially, we could depict them as shown in Fig. 8.6. The spatial nodes i, $i-1$, and $i+1$ are represented in the horizontal direction, and the timestep n and $n+1$ are represented in the vertical direction similar to the discrete $x-t$ domain like in Fig. 8.1. This representation of a finite difference scheme is typically called a stencil. It shows the nodes that appear in the scheme and we may observe the nodes that influence a solution node at each timestep.

If we study the behavior of the convection equation shown in Fig. 8.3, we will notice that the initial information propagates in the positive x-direction for $a > 0$. This means the solution at a discrete point in space, is determined by the points to its left in the previous timestep. Evidently, there is some sense of direction for the behavior of the advection equation. In fact, in the previous example, if we were to set the advection velocity $a = -1.0$ m/s, we will notice that the FTFS scheme appears to be stable and the FTBS scheme is now unstable. While we were able to intuitively understand it, we have carelessly thrown around the word 'stable' and 'unstable' while describing the solutions of these finite difference schemes. It is high time we define the term 'stability' and learn a more rigorous method to determine if/when a finite difference scheme would be stable.

8.3.2 Von Neumann Stability Analysis

When we talk about stability of a numerical scheme, we are interested in how errors or perturbations introduced into the computations behave. A numerical scheme is said to be stable if the errors introduced remain bounded as the algorithm is executed. These are typically *round-off errors* caused due to the finite precision with which computers represent numbers.

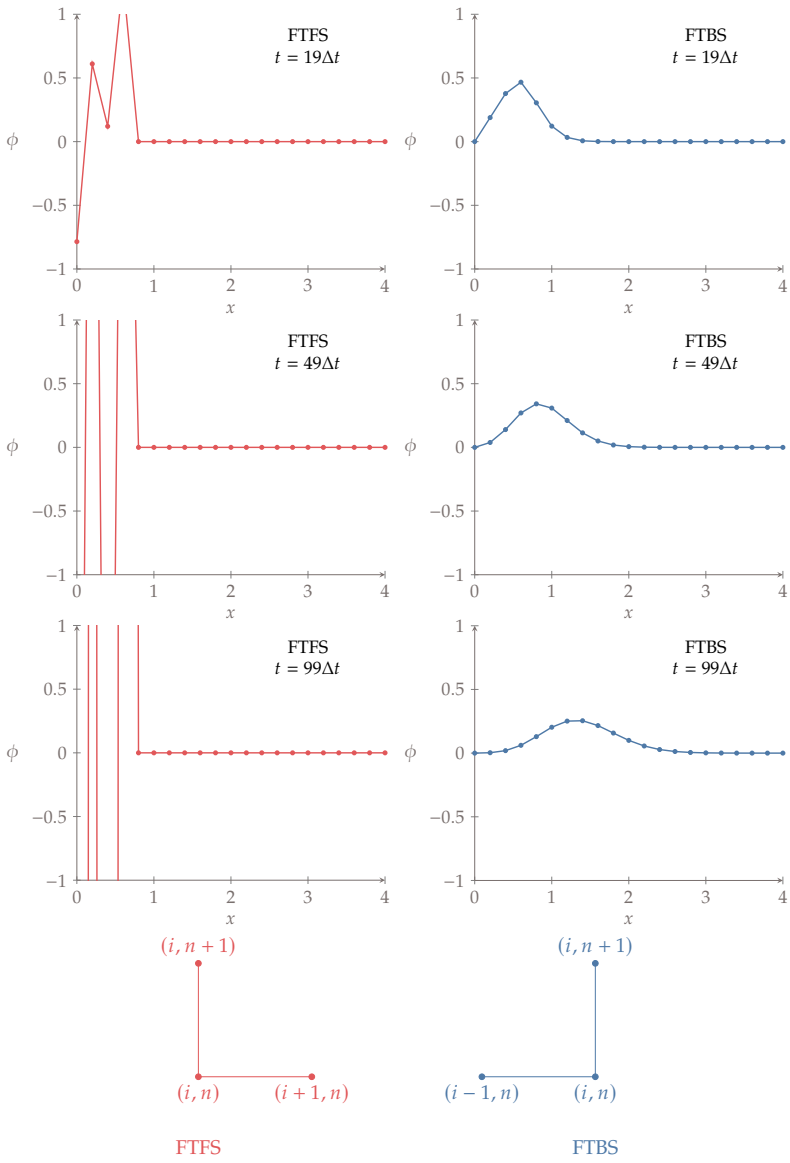

Fig. 8.5 Advection equation solutions using FTFS and FTBS schemes.

Fig. 8.6 FTFS and FTBS finite difference scheme stencils.

The numerical solution ϕ obtained from a finite-difference scheme may be written as the analytical solution $\tilde{\phi}$ with some error ϵ present in it. This applies to each discrete point in the domain; hence,

$$\phi_i^n = \tilde{\phi}_i^n + \epsilon_i^n \tag{8.15}$$

We are interested in the behavior of ϵ_i^n over time. If we were to assume the variation in the error is periodic in space, we could write the error as a Fourier series. The periodic assumption is not far from the truth as

at the boundary conditions the error would reduce to zero. We may expand the error as,

$$\epsilon_i^n = \sum_k E_k(t) e^{j(kx)} \tag{8.16}$$

where $j = \sqrt{1}$ is the imaginary unit. Here, k is the wave number corresponding to each term in the Fourier series and E_k is the Fourier coefficient. Since at each timestep, the variation of error in space could be different, each timestep n would have different Fourier coefficients and are functions of time $E_k(t)$. We could also write this as E_{kn} but then we have too many indices to keep track of. Conveniently, because we are dealing with linear equations, we only need to study an arbitrary term of this Fourier series. We shall henceforth skip the index k of the Fourier coefficient and write,

$$\epsilon_i^n = E_n e^{j(kx)} \tag{8.17}$$

For a uniformly spaced grid, $x = i\Delta x$, and hence,

$$\epsilon_i^n = E_n e^{j(ki\Delta x)} \tag{8.18}$$

As stated before, we are interested in how the error 'evolves' from timestep n to $n+1$. To quantify this, we define an amplification factor, or gain g as,

$$g = \frac{\epsilon_i^{n+1}}{\epsilon_i^n} \tag{8.19}$$

For a stable scheme, we require that $|g| < 1$, so that at each timestep, the error is lesser than that at the previous timestep.

Substituting Eq. 8.18, we get,

$$g = \frac{E_{n+1} e^{j(ki\Delta x)}}{E_n e^{j(ki\Delta x)}} = \frac{E_{n+1}}{E_n} \tag{8.20}$$

We require expressions to define the coefficients E_{n+1} and E_n. Remember that we have expressions, like Eqs. 8.11 and 8.12, for the numerical schemes that govern the behavior of the discrete solution ϕ_i^n. The exact solution $\tilde{\phi}_i^n$ would also satisfy the numerical scheme equation by definition. If we were to write the numerical scheme expression as a linear operator N, this means $N(\phi_i^n) = 0$ and $N(\tilde{\phi}_i^n) = 0$. From Eq. 8.15,

$$N(\phi_i^n) = N(\tilde{\phi}_i^n + \epsilon_i^n) = N(\tilde{\phi}_i^n) + N(\epsilon_i^n) = N(\epsilon_i^n) = 0 \tag{8.21}$$

This provides us the important conclusion that the error satisfies the same numerical scheme expressions when working with linear differential equations. We may hence utilize them to obtain expressions for the Fourier coefficients of the error.

FTFS Scheme Stability

For the FTFS scheme, we re-write the finite-difference expression for the error,

$$\epsilon_i^{n+1} = \epsilon_i^n - \frac{a\Delta t}{\Delta x}\left(\epsilon_{i+1}^n - \epsilon_i^n\right) \quad \text{(FTFS)} \tag{8.22}$$

Substituting Eq. 8.18, we get

$$E_{n+1}e^{j(ki\Delta x)} = E_n e^{j(ki\Delta x)} - \frac{a\Delta t}{\Delta x}\left(E_n e^{j(k(i+1)\Delta x)} - E_n e^{j(ki\Delta x)}\right) \tag{8.23}$$

Dividing through by $E_n e^{j(ki\Delta x)}$,

$$\frac{E_{n+1}}{E_n} = 1 - \frac{a\Delta t}{\Delta x}\left(e^{j(k\Delta x)} - 1\right) \tag{8.24}$$

We have finally obtained the required expression for the Fourier coefficients in the expression for gain. If $k\Delta x = \theta$, we may write,

$$g = 1 - \frac{a\Delta t}{\Delta x}\left(e^{j\theta} - 1\right) \tag{8.25}$$

Using Euler's formula, $e^{j\theta} = \cos\theta + j\sin\theta$, and assuming $\sigma = \frac{a\Delta t}{\Delta x}$,

$$\begin{aligned} g &= 1 - \sigma\left(\cos\theta + j\sin\theta - 1\right) \\ &= (1 + \sigma - \sigma\cos\theta) - j\sigma\sin\theta \end{aligned} \tag{8.26}$$

For stability, we require the amplification factor $|g| < 1$. Since we are dealing with complex numbers, we could state this condition as $|g|^2 < 1$. $|g|^2$ may then be computed as $g\bar{g}$ where $\bar{g}$ is the complex conjugate of g.

Hence,

$$\begin{aligned} |g|^2 &= (1 + \sigma - \sigma\cos\theta)^2 + (\sigma\sin\theta)^2 \\ &= (1+\sigma)^2 + \sigma^2\cos^2\theta - 2(1+\sigma)\sigma\cos\theta + \sigma^2\sin^2\theta \\ &= 1 + 2\sigma(1+\sigma)(1-\cos\theta) \end{aligned} \tag{8.27}$$

For $|g|^2 < 1$,

$$\begin{aligned} 1 + 2\sigma(1+\sigma)(1-\cos\theta) &< 1 \\ \implies 2\sigma(1+\sigma)(1-\cos\theta) &< 0 \end{aligned} \tag{8.28}$$

Since $1 - \cos\theta$ is always positive, we are left with the condition,

$$\sigma(1+\sigma) < 0 \tag{8.29}$$

This is only possible when $-1 < \sigma < 0$.

We had assumed $\sigma = a\Delta t/\Delta x$ and since Δt and Δx have to be positive, $a < 0$ for this condition to be satisfied. If we assume the advection

velocity a in the convection equation to be always positive, we may conclude that the FTFS scheme is *unconditionally unstable*. However, this also means that the solution would be stable if the advection velocity is negative. This is consistent with what we observed in the previous exercise when we used FTFS to model advection with $a < 0$.

FTBS Scheme Stability

Let us now find the stability criterion for the FTBS scheme using the same procedure. Similar to Eq. 8.22, we obtain

$$\epsilon_i^{n+1} = \epsilon_i^n - \frac{a\Delta t}{\Delta x}\left(\epsilon_i^n - \epsilon_{i-1}^n\right) \quad \text{(FTBS)} \tag{8.30}$$

Substituting Eq. 8.18, we get the error expression to be

$$E_{n+1}e^{j(ki\Delta x)} = E_n e^{j(ki\Delta x)} - \frac{a\Delta t}{\Delta x}\left(E_n e^{j(ki\Delta x)} - E_n e^{j(k(i-1)\Delta x)}\right) \tag{8.31}$$

Dividing by $E_n e^{j(ki\Delta x)}$,

$$\frac{E_{n+1}}{E_n} = 1 - \frac{a\Delta t}{\Delta x}\left(1 - e^{-j(k\Delta x)}\right) \tag{8.32}$$

As before, we assume $k\Delta x = \theta$ and $a\Delta t/\Delta x = \sigma$ giving

$$\begin{aligned} g &= 1 - \sigma\left(1 - e^{-j\theta}\right) \\ &= 1 - \sigma\left(1 - \cos\theta + j\sin\theta\right) \end{aligned} \tag{8.33}$$

For $|g|^2 < 1$,

$$\begin{aligned} &(1 - \sigma + \sigma\cos\theta)^2 + (\sigma\cos\theta)^2 < 1 \\ \implies\ &1 + 2\sigma^2 - 2\sigma + 2\sigma\cos\theta - 2\sigma^2\cos\theta < 1 \\ \implies\ &(2\sigma)(\sigma - 1)(1 - \cos\theta) < 0 \end{aligned} \tag{8.34}$$

Again, since $1 - \cos\theta$ is always positive, we are left with the condition,

$$\sigma(1 - \sigma) < 0 \tag{8.35}$$

This is only possible when $0 < \sigma < 1$.

We have arrived at a condition similar to that of the FTFS scheme, but slightly different. In this case, we say that FTFS is *conditionally stable*. Here, σ is required to be always positive for stability. This is again consistent with our observations from the previous example. Additionally, we have also obtained the condition $\sigma < 1$ for stability. This means that for stable solutions, we should take extra care to discretize our domain such that $a\Delta t < \Delta x$.

Note that, we may make Δx extremely small and still arrive at unstable solutions if $a\Delta t > \Delta x$. Hence, it is the relative discretization that is of importance to stability. The fraction $a\Delta t/\Delta x$, typically denoted using σ, constantly appears while analyzing the stability of finite-difference solutions of hyperbolic equations and is called the Courant–Friedrichs–Lewy number or CFL number.

While deriving the first-order backward Euler scheme, you may have noticed that the 'backward expansion' of the Taylor series is an alternating series unlike the forward expansion. This opens up possibilities for deriving higher-order schemes by simple algebraic manipulation of these two series'. We shall derive one such popular scheme called the central-difference scheme next.

Let's subtract the forward Taylor series expansion from the backward expansion,

$$f(x + \Delta x) - f(x - \Delta x) = 2\Delta x f'(x) + O(\Delta x^3) \tag{8.36}$$

Dividing through by $2\Delta x$, we get an expression for $f'(x)$ as,

$$f'(x) = \frac{f(x + \Delta x) - f(x - \Delta x)}{2\Delta x} - O(\Delta x^2) \tag{8.37}$$

We may also write this using the discrete notation as,

$$f'(x) = \frac{f_{i+1} - f_{i-1}}{2\Delta x} - O(\Delta x^2) \tag{8.38}$$

Note that the error for this scheme is second-order. By using values of f on either side of x we have obtained a scheme that has a higher-order error. You can also think of this as an average of the first-order forward and backward schemes; i.e.,

$$\text{Central} = \frac{\text{Forward} + \text{Backward}}{2} = \frac{1}{2}\left(\frac{f_{i+1} - f_i}{\Delta x} + \frac{f_i - f_{i-1}}{\Delta x}\right) \tag{8.39}$$

If you think of this average as a weighted average the weights corresponding to each scheme is 0.5. Researchers often come up with such 'hybrid' schemes with desirable properties using other existing finite-difference schemes by using such weighted averages.

Now that we are aware of the Von Neumann stability analysis method, let's use it to predict the stability of a central-difference based scheme for the advection equation even before running an actual simulation using it.

FTCS Scheme Stability

Similar to the FTFS and FTBS schemes, we shall use a forward-time discretization but with a central difference for the space derivative term.

$$\frac{\phi_i^{n+1} - \phi_i^n}{\Delta t} + a\frac{\phi_{i+1}^n - \phi_{i-1}^n}{2\Delta x} = 0 \tag{8.40}$$

Rearranging for ϕ_i^{n+1}, we arrive at the difference equation,

$$\phi_i^{n+1} = \phi_i^n + \frac{a\Delta t}{2\Delta x}\left(\phi_{i+1}^n - \phi_{i-1}^n\right) \quad \text{(FTCS)} \tag{8.41}$$

The numerical error follows the same difference equation. Hence,

$$\epsilon_i^{n+1} = \epsilon_i^n - \frac{a\Delta t}{2\Delta x}\left(\epsilon_{i+1}^n - \epsilon_{i-1}^n\right) \tag{8.42}$$

Substituting $\epsilon_i^n = E_n e^{j(ki\Delta x)}$, we get,

$$E_{n+1}e^{j(ki\Delta x)} = E_n e^{j(ki\Delta x)} - \frac{a\Delta t}{2\Delta x}\left(E_n e^{j(k(i+1)\Delta x)} - E_n e^{j(k(i-1)\Delta x)}\right) \tag{8.43}$$

Dividing through by $E_n e^{j(ki\Delta x)}$, we obtain,

$$\frac{E_{n+1}}{E_n} = 1 - \frac{a\Delta t}{2\Delta x}\left(e^{j(k\Delta x)} - e^{-j(k\Delta x)}\right) \tag{8.44}$$

Using $k\Delta x = \theta$ and $\sigma = \frac{a\Delta t}{\Delta x}$, and noting that $e^{j\theta} - e^{-j\theta} = 2j\sin\theta$, we get,

$$g = 1 - \frac{\sigma}{2}(2j\sin\theta) = 1 - j\sigma\sin\theta \tag{8.45}$$

Calculating $|g|^2$,

$$|g|^2 = (1 - j\sigma\sin\theta)(1 + j\sigma\sin\theta) = 1 + \sigma^2\sin\theta^2 \tag{8.46}$$

For stability, $|g|^2 < 1$, so we require

$$1 + \sigma^2\sin^2\theta < 1 \tag{8.47}$$

or,

$$\sigma^2\sin^2\theta < 0 \tag{8.48}$$

This condition would never be satisfied, regardless of the value of σ. For this reason, we conclude that the FTCS scheme is *unconditionally unstable*. If we were to simulate the advection equation using the FTCS scheme, our solutions would be unstable regardless of discretization or sign of advection velocity. Although we obtained a finite-difference scheme of higher accuracy, we have interestingly found that the scheme

is unstable. It is relevant at this point to distinguish between accuracy and stability of finite difference schemes. While accuracy determines the magnitude of error in the finite difference solution, stability involves how perturbations or numerical errors are propagated as we iterate over discrete steps using the finite-difference scheme.

With the FTCS scheme giving us disappointing stability characteristics, it is perhaps time to be more adventurous and use a backward difference for the time derivative term. The discrete advection equation at the n^{th} timestep then becomes,

$$\frac{\phi_i^n - \phi_i^{n-1}}{\Delta t} + a\frac{\phi_{i+1}^n - \phi_{i-1}^n}{2\Delta x} = 0 \tag{8.49}$$

If we rewrite this for the $n+1^{\text{th}}$ timestep, we get,

$$\frac{\phi_i^{n+1} - \phi_i^n}{\Delta t} + a\frac{\phi_{i+1}^{n+1} - \phi_{i-1}^{n+1}}{2\Delta x} = 0 \tag{8.50}$$

Rearranging,

$$\phi_i^{n+1} = \phi_i^n - \frac{a\Delta t}{2\Delta x}\left(\phi_{i+1}^{n+1} - \phi_{i-1}^{n+1}\right) \quad \text{(BTCS)} \tag{8.51}$$

Unlike the previous forward-time schemes, here ϕ^{n+1} appears in multiple terms and cannot be 'separated' out. This makes it an *implicit* finite-difference scheme and we cannot use an iterative procedure like before. Instead we will have to resort to a matrix-based solution procedure. Before that, let's first investigate the stability characteristics of the BTCS scheme.

BTCS Scheme Stability

The BTCS scheme for the error can be written as:

$$\epsilon_i^{n+1} = \epsilon_i^n - \frac{a\Delta t}{2\Delta x}\left(\epsilon_{i+1}^{n+1} - \epsilon_{i-1}^{n+1}\right) \tag{8.52}$$

Rewriting, we get:

$$\epsilon_i^{n+1} + \frac{a\Delta t}{2\Delta x}\left(\epsilon_{i+1}^{n+1} - \epsilon_{i-1}^{n+1}\right) = \epsilon_i^n \tag{8.53}$$

Substituting $\epsilon_i^n = E_n e^{j(ki\Delta x)}$, we get:

$$E_{n+1}e^{j(ki\Delta x)} + \frac{a\Delta t}{2\Delta x}\left(E_{n+1}e^{j(k(i+1)\Delta x)} - E_{n+1}e^{j(k(i-1)\Delta x)}\right) = E_n e^{j(ki\Delta x)} \tag{8.54}$$

Dividing through by $E_{n+1}e^{j(ki\Delta x)}$ and using $k\Delta x = \theta$ and $\sigma = \frac{a\Delta t}{\Delta x}$, we get:

$$1 + \frac{\sigma}{2}\left(e^{j\theta} - e^{-j\theta}\right) = \frac{E_n}{E_{n+1}} \tag{8.55}$$

Since $e^{j\theta} - e^{-j\theta} = 2j\sin\theta$, we get:

$$1 + j\sigma\sin\theta = \frac{E_n}{E_{n+1}} \tag{8.56}$$

Thus,

$$g = \frac{1}{1 + j\sigma\sin\theta} \tag{8.57}$$

For stability, we require $|g| < 1$. Calculating $|g|^2$,

$$|g|^2 = \left(\frac{1}{1 + j\sigma\sin\theta}\right)\left(\frac{1}{1 - j\sigma\sin\theta}\right) = \frac{1}{1 + \sigma^2\sin^2\theta} \tag{8.58}$$

For stability, $|g|^2 < 1$,

$$\frac{1}{1 + \sigma^2\sin^2\theta} < 1 \tag{8.59}$$

Since $\sin^2\theta \geq 0$,

$$1 + \sigma^2\sin^2\theta \geq 1 \tag{8.60}$$

This implies the the required condition $g < 1$ is always satisfied for all values of σ. Hence, the BTCS scheme is said to be *unconditionally stable*.

This is exciting news, as we now have a finite-difference scheme where we do not have to worry about the stability of the solution.

The observations on stability of the finite-difference schemes we used to model the advection equation in this section is summarized in Section 8.3.2.

Scheme	Stability Criterion
FTFS	Unconditionally unstable if $a > 0$
FTBS	Conditionally stable for $0 < \sigma < 1$
FTCS	Unconditionally unstable
BTCS	Unconditionally stable

Table 8.2 Stability conditions for different numerical schemes used to model the advection equation

8.3.3 Numerical Dissipation and Dispersion

One question that we have yet to answer is why the FTBS scheme appeared to 'artificially' smoothen the solution of the advection eqution at every timestep.

8.3.4 Linear 2D Laplace Equation

Example with square grid, Tridiagonal system

8.3.5 Lax-Wendroff Scheme and others

8.3.6 Convergence, Consistency and Stability

8.3.7 Non-linear 1D Advection Equation

8.4 Finite Volume Method

8.5 Computational Grids

8.5.1 Types of Grids

8.6 Previous content

This chapter does not overview the CFD process or dive into any theory. We simply visit a few fluid calculations that are relevant to CFD applications.

8.7 Sizing the Prism Layer Mesh

In inviscid CFD an unstructured (or structured) mesh can be used all the way to the body. However, in viscous CFD it is important to use a structured mesh near the body. A structured mesh typically uses quadrilaterals, hexahedrons, or prims cells. We will generically refer to these structured boundary layer cells as prism cells in the below discussion. Prism cells serve multiple purposes. They can more easily be made high aspect ratio, which is important to efficiently capture a boundary layer as flow quantities change much more rapidly normal to the surface as compared to streamwise. Prism cells aligned with the flow in the boundary layer also reduce numerical diffusion allowing for more accurate solutions. This layer is called the *prism layer*. This section discusses some techniques to size the mesh in the prism layer.

First, we need to choose an overall height for the prism layer. As an estimate, we could use the boundary layer displacement thickness

from Schlichting's empirical formulas for turbulent boundary layers (Eq. 3.50):

$$H = \frac{0.046x}{Re_L^{0.2}} \tag{8.61}$$

where H is the total height of the prism layer and $Re_L = V_e L/\nu$ with L the boundary layer length. Since we generally don't know V_e before computing the flow field, we will use the freestream velocity: $Re_L = V_\infty L/\nu$.

Next, we need to determine the height of the first cell. While various wall models exist, in the following we assume that we want to fully resolve the prism layer. In that case our first cell height should give a y^+ value of 1 in order to resolve the viscous sublayer. Recall that y^+ is a Reynolds number applicable near a wall:

$$y^+ = \frac{u_\tau y}{\nu} \tag{8.62}$$

where $u_\tau = \sqrt{\tau_w/\rho}$ is the friction velocity.

If we need y^+ equal to 1 (or some other value like 30 if using a wall model) then we can solve for the y value that is the height of our first cell (which we call h):

$$\begin{aligned} h &= \frac{\nu y^+}{u_\tau} \\ &= \nu y^+ \sqrt{\frac{\rho}{\tau_w}} \\ &= \nu y^+ \sqrt{\frac{\rho}{c_f \frac{1}{2}\rho V_e^2}} \\ &= \frac{\nu y^+}{V_e} \sqrt{\frac{2}{c_f}} \end{aligned} \tag{8.63}$$

The Reynolds number (again using V_∞ instead of the unknown V_e is):

$$Re_L = \frac{V_\infty L}{\nu} \tag{8.64}$$

We solve this for ν and plug into the above equation:

$$h = \frac{y^+ L}{Re_L} \sqrt{\frac{2}{c_f}} \tag{8.65}$$

This provides an estimate for the height of the first cell in the prism layer in order to achieve a desired $y+$ value. We still need an estimate

for c_f but can use the Schlichting formulas for that too.

$$c_f = \frac{0.0592}{Re_L^{0.2}} \tag{8.66}$$

Now that we know the size of the prism layer, and the size of the first cell, we need to determine how many cells span the prism layer. Equivalently, we could determine the growth rate. The growth rate is more fundamental, so it makes more sense to choose a growth rate (e.g., 1.2) and then pick the number of cells accordingly.

CFD packages have different methods to space the cells in the prism layer, but one common approach is geometric progression. The formula for geometric progression is:

$$H = h\left(\frac{r^n - 1}{r - 1}\right) \tag{8.67}$$

where H is the overall height, h the height of the first cell, r the growth rate, and n the total number of cells. In our case, we want to solve for n:

$$n = \log_r\left(\frac{H}{h}(r - 1) + 1\right) \tag{8.68}$$

Thus, we have a procedure to size the mesh in the prism layer.

8.8 Matching Mach and Reynolds Number Simultaneously

Matching Mach number and Reynolds number simultaneously for many aerospace applications is difficult if not impossible experimentally. For CFD applications we can of course match both simultaneously, but this is a source of frequent error if we aren't careful.

In CFD a compressible freestream boundary condition is typically specified with Mach number, pressure, and temperature. Obviously, we set the freestream Mach number to the desired match. But what pressure and temperature do we use in order to match Reynolds number?

Let's start with the definitions of Mach number and Reynolds number (based on chord in this case):

$$M_\infty = \frac{V_\infty}{a}, \quad Re = \frac{\rho V_\infty c}{\mu}$$

How does temperature and pressure affect these equations? The speed of sound and the dynamic viscosity are both functions of temperature, and the density is a function of pressure and temperature through a

thermodynamic equation of state (generally the ideal gas law). In other words:

$$M_\infty = \frac{V_\infty}{a(T)}, \quad Re = \frac{\rho(p,T)V_\infty c}{\mu(T)}$$

The freestream velocity appears in both equations, so we solve for it in one equation and plug it into the other.

$$Re = \frac{\rho(p,T)M_\infty a(T)c}{\mu(T)}$$

We note that we have a degree of freedom. We can either choose a pressure and then solve for the corresponding temperature that satisfies the equation, or we can specify temperature and then choose the corresponding pressure that satisfies the equation. Intuitively that should make sense. We should be able to match Mach and Reynolds Number at any condition by appropriately choosing the other variables.

The density has a simple relationship between pressure and temperature through the ideal gas law:

$$p = \rho RT$$

where the specific gas constant $R = 286.9$ J/(kg-K) for air. Substituting that into our main equation results in:

$$Re = \frac{pM_\infty a(T)c}{RT\mu(T)}$$

The speed of sound also has a simple relationship with temperature:

$$a = \sqrt{\gamma RT}$$

where $\gamma = 1.4$ for an ideal diatomic gases (and air is essentially entirely composed of diatomic gases). Substituting in:

$$Re = \frac{pM_\infty\sqrt{\gamma RT}c}{RT\mu(T)} = \frac{pM_\infty\sqrt{\gamma}c}{\sqrt{RT}\mu(T)}$$

The only thing we haven't substituted in is the dynamic viscosity dependence on temperature. We won't directly substitute in an expression, just because it is a bit long. For an ideal gas, the dynamic viscosity can be found from Sutherland's law:

$$\mu = \mu_{ref}\left(\frac{T}{T_{ref}}\right)^{3/2}\frac{T_{ref}+S}{T+S}$$

where $T_{ref} = 273.15$, $S = 110.4$, $\mu_{ref} = 1.716 \times 10^{-5}$ kg/(m-s).

We can see that the easiest way to solve this equation is to choose T, and then compute p (note that the units for T are Kelvin in all of these equations):

$$p = \frac{Re\ \mu(T)\sqrt{RT}}{M_\infty c\sqrt{\gamma}}$$

By choosing a T, we know everything on the right hand side and can directly solve for p.

The opposite approach is also possible (choose p then solve for T), but is more work. We move everything related to T to the left-hand side.

$$\sqrt{T}\mu(T) = \frac{pM_\infty c\sqrt{\gamma}}{Re\sqrt{R}}$$

We actually can solve for T explicitly through a quadratic function, but it's messy and is easier just to solve the above numerically as a root finding problem:

$$f(T) = \sqrt{T}\mu(T) - \frac{pM_\infty c\sqrt{\gamma}}{Re\sqrt{R}} = 0$$

We use a root finding algorithm to find the T that satisfies $f(T) = 0$ (where again T is in Kelvin).

Either approach is fine, but remember that when you set the temperature and pressure in your boundary condition, you should also use those values to set the initial conditions (or at least something close). If your initial conditions are very far from the steady state solution, you may have numerical issues and a difficult time converging. If you change pressure, it may be easiest to just change the reference pressure and then your gauge pressure can remain at zero elsewhere.

8.9 Richardson Extrapolation

Richardson Extrapolation is a technique to obtain a higher-order solution from multiple lower-order solutions. In this section we will demonstrate usage in a basic CFD example, but it is also a technique used in Rhomberg integration.

Consider a CFD simulation with the goal of predicting predict an output functional f (for example the lift-to-drag ratio of an aircraft). The output we predict depends on the mesh discretization, which we describe by some characteristic mesh length h. In other words, $f = f(h)$. We would like to obtain a "mesh-independent" solution, or the solution as $h \to 0$ thereby eliminating discretization error from our error sources. For a given tolerance we may be able to demonstrate

mesh independence through increasingly smaller mesh sizes until our functional is effectively unchanged. But for more complex geometries or flow conditions, the number of cells required to level out our function may not feasible given our computational resources. In these cases we may still be able to obtain an estimate of the *continuum* solution (solution as $h \to 0$), from multiple coarser solutions.

If f^* is the continuum solution, then the error in our function as a Taylor's series expansion is:

$$\text{error} = f - f^* = c_1 h^p + c_2 h^{p+1} + \dots \tag{8.69}$$

where c are constants, and p is the leading order of the solver error (often second-order for CFD solvers). If we drop the higher-order terms we have:

$$f - f^* \approx c_1 h^p \tag{8.70}$$

Now, let us run our simulation at two different discretizations h_1 and a smaller resolution h_2. Then we would get two different predictions for f.

$$f_1 - f^* \approx c_1 h_1^p \tag{8.71}$$
$$f_2 - f^* \approx c_1 h_2^p \tag{8.72}$$

We can solve these two equations for f^* (eliminating the unknown constant c_1):

$$f^* = \frac{r^p f_2 - f_1}{r^p - 1} \text{ where } r = \frac{h_1}{h_2} \tag{8.73}$$

Note that we have made some significant assumptions here. One is that the constant c_1 is the same between the two simulations. This is only true when we are in the asymptotic range of convergence. This means that h is already sufficiently small that we are actually observing second-order convergence (or whatever the order p is). **??** shows for example the convergence of Newton's method, a second-order method, on a root-finding problem on both a linear and log scale. Only towards the end do we see the second-order convergence. So while we may not be able to refine our mesh all the way to mesh independence, we need to at least be in the asymptotic region.

A good way to increase confidence that we are in asymptotic region is to use more than two simulations. Rearranging Eq. 8.70:

$$f = f^* + c_1 h^p \tag{8.74}$$

we see that plotting f against h^p is the equation of a line with slope c_1. If we run multiple simulations with finer values of h^p and have a straight line, it increases confidence that we are in asymptotic convergence.

A second assumption is that we know what p is. We should of course know what order the solver is, but that is only the theoretical order. The realized order of convergence will, in general, be somewhat less. Careful studies using very fine discretizations on simpler geometries, can help us estimate p. For example, if we call the left-hand side of Eq. 8.70 our error e then taking the log of both sides yields:

$$\log e = \log c_1 + p \log h \tag{8.75}$$

Thus, if we plot the log of the error (where error could be estimated relative to a very fine meshe) versus the log of the step size, for multiple mesh sizes, we can estimate the slope. We would then assume that this is order of convergence is relatively consistent for other geometries using the same solver.

Perhaps the biggest assumption is that we can characterize our mesh with a single number h. The above analysis really only holds if we have uniform refinement, meaning we subdivide every mesh cell by the same factor. That is not typically feasible, but we should still refine globally if attempting Richardson extrapolation (i.e., refining only a selected region may mislead us into thinking we're approaching mesh independence prematurely). Also problematic is that the mesh cell sizes vary drastically throughout the domain and so the use of a single characteristic length is rather crude.

One way to estimate a characteristic length is by using the number of cells. For now, let's assume we use Cartesian cells of the same dimension (h) in all directions: $n_1 h = L_1, n_2 h = L_2, n_3 h = L_3$. The total number of cells is: $N = n_1 \cdot n_2 \cdot n_3$. If we combine these equations we see that: $N = \forall / h^3$. Thus:

$$h \propto \frac{1}{N^{1/3}} \tag{8.76}$$

While, we won't have isotropic cells throughout the entire domain, and may use unstructed grids, this proportionality can still be used as a characteristic length in those cases. We can absorb the proportionality constant into the existing constant in Eq. 8.70 giving:

$$f = f^* + c\left(\frac{1}{N^{1/3}}\right)^p \tag{8.77}$$

For a two-dimensional mesh the equation is the same except the exponent of $1/3$ is replaced by $1/2$.

Bibliography

1 Van Dyke, M., *An album of fluid motion*. Parabolic Press Stanford, 1982, Vol. 176. cited on p. 7

2 Drela, M., "XFOIL: An analysis and design system for low Reynolds number airfoils," *Low Reynolds Number Aerodynamics: Proceedings of the Conference Notre Dame, Indiana, USA, 5–7 June 1989*, Springer, 1989, pp. 1–12. cited on pp. 7, 103

3 Hodge, P. G., "On Isotropic Cartesian Tensors," *The American Mathematical Monthly*, Vol. 68, No. 8, October 1961, p. 793, ISSN: 0002-9890. DOI: 10.2307/2311997 cited on p. 28

4 Buresti, G., "A note on Stokes' hypothesis," *Acta Mechanica*, Vol. 226, No. 10, June 2015, pp. 3555–3559, ISSN: 1619-6937. DOI: 10.1007/s00707-015-1380-9 cited on p. 31

5 Gonzalez, C. and Taha, H. E., "A variational theory of lift," *Journal of Fluid Mechanics*, Vol. 941, May 2022, ISSN: 1469-7645. DOI: 10.1017/jfm.2022.348 cited on p. 74

6 Abbott, I. H. and Doenhoff, A. E. von, *Theory of Wing Sections*. New York: Dover Publications, 1959. cited on p. 82

7 Kulfan, B. M., "Universal Parametric Geometry Representation Method," *Journal of Aircraft*, Vol. 45, No. 1, January 2008, pp. 142–158, ISSN: 1533-3868. DOI: 10.2514/1.29958 cited on p. 83

8 Hess, J. L. and Smith, A. M. O., "Calculation of potential flow about arbitrary bodies," *Progress in Aerospace Sciences*, Vol. 8, 1967, pp. 1–138, ISSN: 0376-0421. DOI: 10.1016/0376-0421(67)90003-6 cited on p. 103

9 Moran, J., *An Introduction to Theoretical and Computational Aerodynamics*. Dover Publications, 1984. cited on pp. 103, 147

10 Lamb, H., *Hydrodyamics*, 6th. Dover Publications, 1945. cited on p. 122

11 Cebeci, T. and Bradshaw, P., *Physical and Computational Aspects of Convective Heat Transfer*, 1st ed. Springer, 1988. ISBN: 978-1-4612-3918-5 DOI: 10.1007/978-1-4612-3918-5 cited on p. 146

12 Wazzan, A. R., Gazley, C., and Smith, A., "The H-Rx method for predicting transition," RAND Corporation, Santa Monica, CA, 1981. cited on p. 152

13 Coder, J. G. and Maughmer, M. D., "Numerical Validation of the Squire–Young Formula for Profile-Drag Prediction," *Journal of Aircraft*, Vol. 52, No. 3, May 2015, pp. 948–955.
DOI: 10.2514/1.C033021 cited on pp. 153, 154

14 Clauser, F. H., "The Turbulent Boundary Layer," *Advances in Applied Mechanics*, Vol. 4, Dryden, H. and von Kármán, T., Eds., 1956, pp. 1–51, ISSN: 0065-2156.
DOI: https://doi.org/10.1016/S0065-2156(08)70370-3 cited on p. 160

15 Anderson, J. D., *Modern Compressible Flow: With Historical Perspective*. 2003.
ISBN: 1259027422 cited on p. 243

16 Ning, A., "Using Blade Element Momentum Methods with Gradient-Based Design Optimization," *Structural and Multidisciplinary Optimization*, May 2021.
DOI: 10.1007/s00158-021-02883-6 cited on pp. 247, 257, 270, 271

17 Glauert, H., *Airplane propellers*, *Aerodynamic Theory*, Springer, 1935, pp. 169–360. cited on pp. 250, 263

18 Ning, A., "A Simple Solution Method for the Blade Element Momentum Equations with Guaranteed Convergence," *Wind Energy*, Vol. 17, No. 9, September 2014, pp. 1327–1345.
DOI: 10.1002/we.1636 cited on pp. 257, 271

19 Glauert, H. and Committee, A. R., *A General Theory of the Autogyro*. HM Stationery Office, November 1926. cited on p. 264

20 Buhl Jr., M. L., "A New Empirical Relationship between Thrust Coefficient and Induction Factor for the Turbulent Windmill State," NREL/TP-500-36834, National Renewable Energy Laboratory, August 2005. cited on p. 264

21 Himmelskamp, H., *Profile investigations on a rotating airscrew*. Ministry of Aircraft Production, 1947. cited on p. 274

22 Snel, H., "Scaling laws for the boundary layer flow on rotating wind turbine blades," *4th IEA symposium on aerodynamics for wind turbines, Rome*, 1991. cited on p. 276

23 Snel, H., Houwink, R., and Bosschers, J., "Sectional prediction of lift coefficients on rotating wind turbine blades in stall," ECN-C-93-052, Netherlands Energy Research Foundation (ECN), December 1994. cited on p. 276

24 Lindenburg, C., "Investigation into Rotor Blade Aerodynamics: Analysis of the stationary measurements on the UAE phase-VI rotor in the NASA-Ames wind tunnel," ECN-C–03-025, July 2003. cited on pp. 276, 277

25 Du, Z. and Selig, M., "A 3-D Stall-Delay Model for Horizontal Axis Wind Turbine Performance Prediction," *1998 ASME Wind Energy Symposium*, ser. AIAA-1998-21, January 1998. cited on p. 276

26 Laino, D. J., Hansen, A. C., and Minnema, J. E., "Validation of the AeroDyn Subroutines Using NREL Unsteady Aerodynamics Experiment Data," *Wind Energy*, Vol. 5, 2002, pp. 227–244. DOI: 10.1002/we.69 cited on p. 277

27 Eggers Jr, A. J., Chaney, K., and Digumarthi, R., "An Assessment of Approximate Modeling of Aerodynamic Loads on the uae Rotor," *41st Aerospace Sciences Meeting and Exhibit*, ser. AIAA-2003-0868, January 2003. DOI: 10.2514/6.2003-868 cited on p. 277

28 Viterna, L. A. and Janetzke, D. C., "Theoretical and Experimental Power from Large Horizontal-Axis Wind Turbines," DOE/NASA/20320-4, National Aeronautics and Space Administration, Lewis Research Center, September 1982. cited on p. 280

29 Beddoes, T., "A synthesis of unsteady aerodynamic effects including stall hysteresis," *Vertica*, Vol. 1, No. 2, 1976, pp. 113–123. cited on p. 281

30 Leishman, J. G. and Beddoes, T. S., "A Semi-Empirical Model for Dynamic Stall," *Journal of the American Helicopter Society*, Vol. 34, No. 3, July 1989, pp. 3–17, ISSN: 2161-6027. DOI: 10.4050/jahs.34.3 cited on p. 281

31 Øye, S., "Dynamic stall simulated as time lag of separation," *Proceedings of the 4th IEA Symposium on the Aerodynamics of Wind Turbines*, Vol. 27, Rome, Italy, 1991, p. 28. cited on p. 281

32 Hansen, M. H., Gaunaa, M., and Madsen, H. A., "A Beddoes–Leishman Type Dynamic Stall Model in State-space and Indicial Formulations," Risø-R-1354, Risø National Laboratory, Roskilde, Denmark, 2004. cited on p. 281

33 Jensen, N. O., "A Note on Wind Generator Interaction," RISØ-M-2411, Risø National Laboratory, November 1983. cited on p. 283

34 Katić, I., Højstrup, J., and Jensen, N. O., "A simple model for cluster efficiency," *Eurorpean Wind Energy Association Conference and Exhibition*, Rome, Italy, October 1986. cited on p. 284

35 Bastankhah, M. and Porté-Agel, F., "Experimental and theoretical study of wind turbine wakes in yawed conditions," *Journal of Fluid Mechanics*, Vol. 806, October 2016, pp. 506–541, ISSN: 1469-7645. DOI: 10.1017/jfm.2016.595 cited on p. 285

36 Niayifar, A. and Porté-Agel, F., "Analytical Modeling of Wind Farms: A New Approach for Power Prediction," *Energies*, Vol. 9, No. 9, September 2016, p. 741, ISSN: 1996-1073. DOI: 10.3390/en9090741 cited on p. 286